Understanding the physics of perovskite solar cells for stable and efficient multijunction photovoltaics

Jarla Thiesbrummel

Wolfson College

A thesis submitted for the degree of

Doctor of Philosophy

at the University of Oxford

Trinity Term 2023

Voor mama en papa

Abstract

Over the past decade, metal halide perovskites have significantly stirred up the field of photovoltaic research. Despite the remarkable increase in efficiency, there is still a lack of comprehensive understanding regarding the device physics and stability of perovskite solar cells. This is problematic because to unlock the full potential of perovskite solar cells and push them towards commercialisation, it is imperative that researchers understand the physical underlying mechanisms that determine whether a solar cell can reliably operate at high efficiency levels over long timescales. This thesis, therefore, concentrates on gaining a better understanding of the device physics and stability of perovskite solar cells, with specific emphasis on two aspects: investigating the effect of mobile ions on the performance and stability of these devices, and understanding performance losses in perovskite-based tandems.

Many perovskite solar cells still suffer from current losses that cannot be attributed to suboptimal device optics and light harvesting. The origin of these losses is investigated, using a combination of voltage-dependent photoluminescence time series and various charge extraction measurements. It is demonstrated that the perovskite devices suffer from a reduction in the charge extraction efficiency within the first few seconds of operation, which leads to a loss in current and lower maximum power output. In addition, the emitted photoluminescence from the device rises on the exact same timescales due to the accumulation of electronic charges in the active layer. Using transient charge extraction measurements, it is shown that these observations cannot be explained by doping-induced electronic charges but by the movement of mobile ions towards the perovskite/transport layer interfaces, which inhibits charge extraction due to band flattening. These findings are generalised to a variety of metal-halide perovskites, showing that the loss mechanism is universal. This elucidates the negative role mobile ions play in perovskite solar cells and paves a path toward understanding and mitigating a key loss mechanism.

Abstract

Hereafter, the impact of such ion-induced loss mechanisms on the device performance upon ageing of perovskite solar cells is investigated. An increased mobile ion density with a corresponding increased field screening leads to a decrease in the steady-state power conversion efficiency mainly due to a large reduction in current density, while the efficiency at high scan speeds ($>$1000 V/s) where the ions are immobilised is much less affected. Interfacial recombination does not increase upon ageing, yet the open-circuit voltage decreases as a result of an increase in the mobile ion density upon ageing. Furthermore, similar ionic losses appear under different external stressors, in particular when there are free charges present in the absorber layer. We thus reveal a key degradation mechanism, providing new insights into initial device degradation before chemical or extrinsic mechanical device degradation effects manifest, and highlight the critical role mobile ions play therein.

The second part of this thesis, then, shifts focus towards perovskite-based tandem photovoltaics. Understanding performance losses in all-perovskite tandem photovoltaics is crucial to accelerate advancements toward commercialisation, especially since these tandem devices generally underperform in comparison to what is expected from isolated layers and single junction devices. The individual sub-cells in all-perovskite tandem stacks are selectively characterised to disentangle the various losses. It is found that non-radiative losses in the high-gap subcell dominate the overall recombination in the baseline system, as well as in the majority of literature reports. Through a multi-faceted approach, the open-circuit voltage of the high-gap perovskite subcell is enhanced, and employing a novel (quasi) lossless indium oxide interconnect, this enables all-perovskite tandem solar cells with 2.00 V open circuit voltage and 23.7% stabilised efficiency. Reducing transport losses as well as imperfect energy alignments could boost efficiencies to 25.2% and 27.0% as identified via subcell selective electro- and photo-luminescence. Finally, it is shown how, having improved the open circuit voltage, improving the current density of the low-gap absorber pushes efficiencies even further, reaching 25.9% efficiency stabilised, with an ultimate potential of 30.0% considering the bulk quality of both absorbers measured using photo-luminescence. These insights not only show an optimisation example but also a generalisable evidence-based optimisation strategy utilising optoelectronic sub-cell characterisation.

In 2-terminal perovskite-based tandem photovoltaics, mobile ions play an important role as well, as these devices rely on a carefully engineered current balance. Ageing of such devices, and the corresponding mobile-ion-induced current losses, can be detrimental to device performance. Therefore, it is important to not only understand voltage losses but also ion-induced current losses subcell selectively. To this end, we demonstrate the use of current-voltage scans and current decay measurements as well as photoluminescence measurements to investigate the effect of mobile ions subcell-selectively. Finally, the relationship between radiative and non-radiative losses at short circuit conditions is investigated in an ultimate attempt to directly and subcell-selectively quantify current losses from photoluminescence at short circuit.

Overall, the results of this thesis provide a crucial understanding of mobile ions and their role in performance loss and device degradation. We show that it is important to gain further understanding of how to reduce the mobile ion density, or how to engineer the devices so that the charge collection is insensitive to the redistribution of the ions.

These findings also pave the way towards accelerated ageing tests of perovskite solar cells, which can be used to identify losses and test potential mitigation mechanisms. At the same time, we highlight the importance of subcell-selective measurements in perovskite-based tandem devices to understand which factors are limiting the efficiency, and design evidence-based optimisation approaches. These findings combined will ultimately enable us to move closer to the radiative efficiency limit, while at the same time improving stability, which is a key for the commercialisation of perovskite-based solar cells.

Acknowledgements

This thesis would not have been completed without the contribution and support of a great many people. Possibly the most difficult, but definitely the most enjoyable part of writing this thesis, is trying to express my gratitude on paper.

Henry, thank you for giving me the freedom to pursue my dreams, for allowing me to carry out my research wherever I feel I can get the best results, and for trusting that I will eventually also produce some output. I think not many supervisors would say 'yes' to their student when they ask if they can move to Svalbard during their DPhil, but I am very thankful you did. I would like to thank you for your inexhaustible enthusiasm and for having me be part of the group.

Next, I would like to thank the most important person in the group in Oxford: Clare. Thank you for all you do for us every day. I am always amazed how you manage to be on top of so many things at the same time. Thank you for all your support and advice over the years, and for always being ready to do your magic, even when I was far away.

Emil and Manuel, thank you for being the best labmates! Thanks to you I still felt very much part of the group in Oxford, whilst away. Also, thank you for always having my back and reminding me of all the deadlines, forms to fill in and other things which I was generally blissfully unaware of. Besides amazing labmates, you are also great friends. I would have loved to spend more time with you guys in Oxford.

Thanks also go to Mike for making up the other half of the pre-covid team lead-tin, and to Suhas for guidance and mentoring.

Acknowledgements

While it may normally take a lab to raise a Dr., in my case it took two. Having spent the majority of my DPhil in the labs in Potsdam, PwM has played a vital role in the establishment of this thesis. Dieter, thank you for allowing me to come to Potsdam as a visitor, and basically adopting me into your group. I feel very privileged to have been able to spend so much time in your amazing labs, and very much appreciate the great research environment you foster. Martin, thank you for teaching me how to do research and how to write papers, and for sharing with your students your inexhaustible enthusiasm about science, I have learnt a lot from you. Felix, I truly admire the way you lead your group and supervise your students. Thank you for your mentoring and support.

Having such amazing labs to do research in is only possible because of the people who help out every day to keep everything running. I am extremely grateful to PwM's 'dream team', and would like to extend a heartfelt thanks to its present and former members: Elke, Frank, Thomas, Apu, Andreas, Florian and Burkhard. I would like to specifically thank Thomas for all his practical support and help. Even though you say you do not do the science, your contributed ideas are generally much better than mine. It is truly amazing to have an idea for a measurement, and get so much support from you to be able to actually carry it out. Without your contributions, there would have been a lot less successful experiments carried out at PwM. Special gratitude goes also to Apu, for his endless efforts designing, building and repairing the various electronic components of the different setups I used intensively during my time at PwM.

I owe thanks to all of the PwM members I have gotten to know during my time in Potsdam, not only for their scientific contributions and for the various collaborations, but also for their company and support. A few people deserve a special mention: Vincent, thank you for having been the best office mate. Your advice, both scientific as well as personal, has been really valuable. Also, thank you for always taking time to teach me things! Lucas also deserves some additional thanks. It was probably not easy for you to have a supervisor who just disappeared to the Arctic, but you did an amazing job for your bachelor thesis and it has been a pleasure working with you. I am sure that, if you want, you have a great scientific career ahead of you. Sahil, thank you for being a great office mate, and for your contributions to the ageing paper. Fellow visitor Fangyuan, your optimism, genuine laughter and wise words always cheered me up, it was truly a pleasure to be your labmate for a while!

There are also many people outside the labs in Potsdam and Oxford that I have head the pleasure to get to work with during the course of the last four years. Specifically, I would like to thank Kai for making all of our tandem projects possible, and for being ready to discuss science no matter the time of day. I also owe thanks to Fengjiu, for helping me weigh chemicals at HZB, and for all the times we shared thoughts, ideas and struggles regarding lead tin perovskites.

Special thanks go to Guilherme, Atul, Thomas, Andreas, Kai, Laura and Akash for proofreading the various chapters of this thesis.

Next, I would like to thank my friends and family for all their support and encouragement over the past four years.

Thank you Anna, Mahdi, Ali and Minru for making Lausanne still feel like a place to come home to. Our adventures in Switzerland, little or big, have meant a lot to me! Thomas, I am grateful to have met such a kind-hearted adventure buddy and friend. Fabien, thank you for the encouragement and wise words throughout the years!

I also am very grateful to my friends in Oxford for sticking around after I snuck away to Potsdam, and for all the good moments we had together in Oxford. I would have liked to spend more time with you all! Max, thank you for teaching me how to roll! Theodor, whether it is playing games or having deep discussions, it is always a joy to get to spend time with you. Special thanks go to Csabi, Toby and Eduardo for providing distraction and keeping me sane during the long lockdown in Oxford. I would also like to extend my sincere gratitude to the porters and kitchen staff of Wolfson for taking care of those students who were stuck in Oxford during the first lockdown. Fellow Wolfie and sort-of lab mate Andreas, thank you for all the encouragement and advice over the years, and for being there to listen whenever I needed to blow off some steam.

Leaving Oxford and moving to Germany, I was very lucky to meet some wonderful new people who made me feel at home here. Thank you Balázs and Marlene for having been the best flatmates! Your never ending support and encouragement has meant a lot. Thank you Laura, Jorge, Sabela, Dinara, Kapio and Guilherme for all the fun trips, dinners, board games and company over the past years. Additional thanks go to Guilherme for the many (even more) board games we played, and for all of the support (both morally and practically) especially during the last part of me writing of this thesis.

B2 family: although I only met you towards the end of my PhD, you played an essential role in the last part of this shady journey. It is hard to express in words how grateful I am for having met you, and I look forward to all the adventures we will be embarking on in the coming years. I feel honoured to be able to call you my friends. Thank you Kai-Ming, Håvard, Idunn, Jani, Rob, Anne, Pierre, Sunniva, Justin and Sondre for all you do! I would also like to thank the walrus of Ekmanfjorden for its encouragement and for allowing me to finish writing my thesis.

Svea, ondanks dat we af en toe van mening verschillen over dingen, waardeer ik je enorm, en ben ik trots dat ik jouw (kleine) grote zus ben. Bedankt dat je er altijd bent.

Als laatste wil ik mijn ouders bedanken voor hun onvoorwaardelijke steun, aanmoediging en betrokkenheid. Ik had me geen betere ouders kunnen wensen. Deze thesis is voor jullie.

Det vanskelige kan man gjøre med en gang,
det umulige tar bare litt lengre tid.

– Fridtjof Nansen

Wat niet kan, kan toch.

– Marian Thiesbrummel

Foreword

Nowhere on earth are temperatures rising as fast as on Svalbard. With an average temperature increase of 6 °C compared to 30 years ago, the situation in the archipelago provides a gloomy insight into how rapid climate change will affect the rest of the earth. The island group is, in a way, the canary in the coal mine.

I got to see with my own eyes how fast the glaciers here are disappearing. How there is barely any sea ice left in many of the fjords that used to be frozen each winter. Within 50 years, the Arctic sea will be completely ice-free during the summer, and it will be possible to simply reach the geographic north pole by boat. If we are unlucky, this scenario might even become reality already by 2035.

The rapidly changing climate is not only noticeable from the disappearance of ice, both on land and on sea. Longyearbyen, worlds northernmost town, has become increasingly under threat of mudslides and avalanches, which can be linked directly to climate change. But by letting climate change get out of control, we as humans do not only ruin our own prospects of surviving on this planet in the long run, we also take down a large part of the earths flora and fauna with us, and put those species who might be able to adapt under a lot of pressure.

Living on Svalbard, learning about sea-ice, glaciers, and the precarious future of the Arctic, and especially going out on the ice for fieldwork has opened my eyes further to the results of climate change, but also made me realise more than before that technology alone will not be enough to get society to transition to a more sustainable one. Even in Longyearbyen, the most rapidly warming town on earth, coal is still the main energy source for heating and electricity. Public awareness, political leadership and vision, might, at this point in time, be more important than innovations

in photovoltaic technology that push power conversion efficiencies a couple percent higher. This thesis should therefore be read with this global context in mind. I hope I managed to contribute a bit to the understanding of the physics of perovskite solar cells, but to fight climate change, action is needed on a completely different scale.

The Arctic is the most fascinating, beautiful place I have seen in my life. Roald Amundsen described the serene beauty of the Antarctic in 'Sydpolen', stating "We see many fine sunsets here, unique in the splendour of their colour. No doubt the surroundings in this fairyland of blue and white do much to increase their beauty." Its northern counterpart, I believe, is equally stunning with all its snow and ice. Let us hope some of this beauty will be preserved for future generations to dream about and explore.

Longyearbyen, 2023

Photo: Pierre Lefevre, Bjørndalen, February 2023

Contents

List of Figures

List of Tables

List of Publications

1. J. Thiesbrummel*, S. Hu*, J. Pascual*, M. Stolterfoht, A. Wakamiya, H. J. Snaith, "Narrow bandgap perovskites for all-perovskite tandem photovoltaics", under review, 2023

2. J. Zhu, Y. Luo, R. He, C. Chen, Y. Wang, J. Luo, Z. Yi, J. Thiesbrummel, C. Wang, F. Lang, H. Lai, Y. Xu, J. Wang, Z. Zhang, W. Liang, G. Cui, S. Ren, X. Hao, Y. Wang, L. Wu, J. Zhang, M. Stolterfoht, F. Fu, D. Zhao, "A donor–acceptor-type hole-selective contact reducing non-radiative recombination losses in both subcells towards efficient all-perovskite tandems", Nature Energy, 2023, https://doi.org/10.1038/s41560-023-01274-z

3. F. Yang, P. Tockhorn, A. Musiienko, F. Lang, D. Menzel, R. Macqueen, E. Köhnen, K. Xu, S. Mariotti, D. Mantione, L. Merten, A. Hinderhofer, B. Li, D. R. Wargulski, J. Zhang, F. Scheler, J. Thiesbrummel, A. Al-Ashouri, K. O. Brinkmann, T. Riedl, F. Schreiber, D. Abou-Ras, H. Snaith, D. Neher, L. Korte, M. Stolterfoht, S. Albrecht, "Reduced recombination losses and defect densities of wide-bandgap perovskite for 27.2% efficiency all-perovskite tandem solar cells", under review, 2023

4. J. Diekmann, F. Peña-Camargo, N. Tokmoldin, J. Thiesbrummel, J. Warby, E. Gutierrez-Partida, S. Shah, D. Neher, M. Stolterfoht, "Determination of mobile ion densities in halide perovskites via low-frequency capacitance and charge extraction techniques", J. Phys. Chem. Lett., 2023, 14, 18, 4200–4210, https://doi.org/10.1021/acs.jpclett.3c00530

5. J. Warby, S. Shah, J. Thiesbrummel, E. Gutierrez-Partida, H. Lai, F. Lang, F. Fu, D. Neher, M. Stolterfoht, "Mismatch of quasi-Fermi level splitting and V_{OC} in perovskite solar cells", under review, 2023

6. F. Yang, R. W. MacQueen, D. Menzel, A. Musiienko, A. Al-Ashouri, J. Thiesbrummel, S. Shah, P. Karunanantharajah, D. Abou-Ras, L. Korte, M. Stolterfoht, D. Neher, I. Levine, H. J. Snaith, S. Albrecht, "Rubidium iodide reduces recombination losses in methylammonium-free tin-lead perovskite solar cells", Adv. Energy Mater. 2023, 13, 2204339, https://doi.org/10.1002/aenm.202204339

7. J. Thiesbrummel*, S. Shah*, E. Gutierrez-Partida, F. Zu, F. Peña-Camargo, S. Zeiske, J. Diekmann, F. Ye, K. Peters, K. O. Brinkmann, J. Warby, Q. Jeangros, F. Lang, Y. Wu, S. Albrecht, T. Riedl, A. Armin, D. Neher, N. Koch, V. M. Le Corre, H. J. Snaith, M. Stolterfoht, "Ion induced field screening governs the early performance degradation of perovskite solar cells", Submitted, 2023

8. R. He, W. Wang, Z. Yi, F. Lang, C. Chen, J. Luo, J. Zhu, J. Thiesbrummel, S. Shah, Y. Luo, C. Wang, H. Lai, H. Huang, J. Zhou, B. Zou, X. Yin, S. Ren, X. Hao, L. Wu, J. Zhang, M. Stolterfoht, F. Fu, W. Tang, D. Zhao, "Improving interface quality for 1 cm^2 all-perovskite tandem solar cells", Nature, 2023, 618, 80–86, https://doi.org/10.1038/s41586-023-05992-y

9. P. Caprioglio, J. Smith, R. Oliver, A. Dasgupta, S. Choudhary, M. D. Farrar, A. Ramadan, Y-H. Lin, M. G. Christoforo, J. Ball, J. Diekmann, J. Thiesbrummel, K-A. Zaininger, X. Shen, M. Johnston, D. Neher, M. Stolterfoht, H.J. Snaith, "Open-circuit and short-circuit loss management in wide-gap perovskite p-i-n solar cells", Nature Communications, 2023, 14, 932, https://doi.org/10.1038/s41467-023-36141-8

10. J. Thiesbrummel, F. Peña-Camargo, K. O. Brinkmann, E. Gutierrez-Partida, F. Yang, J. Warby, S. Albrecht, D. Neher, T. Riedl, H. J. Snaith, M. Stolterfoht, F. Lang, "Understanding and minimizing V_{OC} losses in all-perovskite tandem solar cells", Advanced Energy Materials, 2023, 13, 2202674. https://doi.org/10.1002/aenm.202202674

11. H. Lai, J. Luo, Y. Zwirner, S. Olthof, A. Wieczorek, F. Ye, Q. Jeangros, X. Yin, F. Akhundova, T. Ma, R. He, R. K. Kothandaraman, X. Chin, E. Gilshtein, A. Müller, C. Wang, J. Thiesbrummel, S. Siol, J. M. Prieto, T. Unold, M. Stolterfoht, C. Chen, A. N. Tiwari, D. Zhao, F. Fu, "High-Performance Flexible All-Perovskite Tandem Solar Cells with Reduced V_{OC}-Deficit in Wide-Bandgap Subcell", Advanced Energy Materials, 2022, 12, 2202438. https://doi.org/10.1002/aenm.202202438

12. F. Peña-Camargo, J. Thiesbrummel, H. Hempel, A. Musiienko, V. M. Le Corre, J. Diekmann, J. Warby, T. Unold, F. Lang, D. Neher, and M. Stolterfoht , "Revealing the doping density in perovskite solar cells and its impact on device performance", Applied Physics Reviews 9, 021409 (2022) https://doi.org/10.1063/5.0085286

13. V. M. Le Corre, J. Diekmann, F. Peña-Camargo, J. Thiesbrummel, N. Tokmoldin, E. Gutierrez-Partida, K. P. Peters, L. Perdigón-Toro, M. H. Futscher, F. Lang, J. Warby, H. J. Snaith, D. Neher, M. Stolterfoht, "Quantification of efficiency losses due to mobile ions in perovskite solar cells via fast hysteresis measurements", Solar RRL, 2022, 6: 2100772. https://doi.org/10.1002/solr.202100772

14. J.Thiesbrummel, V. M. Le Corre, F. Peña-Camargo, L. Perdigón-Toro, F. Lang, F. Yang, M. Grischek, E. Gutierrez-Partida, J. Warby, M. D. Farrar, S. Mahesh, P. Caprioglio, S. Albrecht, D. Neher, H. J. Snaith, M. Stolterfoht, "Universal current losses in perovskite solar cells", Advanced Energy Materials, 2021, 11, 2101447. https://doi.org/10.1002/aenm.202101447

In preparation

1. J. Thiesbrummel, E. Beier, L. Holte, F. Ye, J. Warby, K. O. Brinkmann, F. Lang, "All-perovskite tandem photovoltaics for indoor applications", in preparation

2. J. Thiesbrummel, M. Kober-Czerny, J. Lim, O. Gunawan, M. Stolterfoht, H. Snaith, "On the oxidation of lead-tin perovskite solar cells", in preparation

3. Z. Iqbal, R. Félix, A. Musiienko, J. Thiesbrummel, E. Gutierrez-Partida, T. W. Gries, E. Hüsam, A. Saleh, R. G. Wilks, J. Zhang, M. Stolterfoht, D. Neher, S. Albrecht, H. Köbler, M. Bär, A. Abate, Q. Wang, "Surface and Interface Characterization for Dry and Ambient Air Processed $CsPbI_3$ Films in Perovskite Solar Cells", in preparation

4. J. C. Blakesley, R. S. Bonilla, M. Freitag, A. M. Ganose, N. Gasparini, P. Kaienburg, G. Koutsourakis J. D. Major, J. Nelson, N. K. Noel, B. Roose, J.S. Yun, ..., J. Thiesbrummel, ..., S. D. Stranks, R. L. Z. Hoye, "Roadmap on Photovoltaic Absorber Materials for Sustainable Energy Conversion", in preparation

List of Abbreviations

AFM atomic force microscopy

ALD atomic layer deposition

AZO aluminium zinc oxide

BACE bias assisted charge extraction

BCP bathocuproine

CD current decay

CELIV charge extraction by linearly increasing voltage

CU charge capacitive (electrode) charge

C_{60} Fullerene-C60

EDX energy dispersive x-ray spectroscopy

EL electroluminescence

ELQY electroluminescence quantum yield

ETL electron transport layer

EQE external quantum efficiency

FA formamidinium

FACs formamidinium/cesium double cation perovskite

FAPI formamidinium lead triiodide

FF fill factor

FH fast hysteresis

FTIR Fourier-transform infrared spectroscopy

FTO fluorine-doped tin oxide

HG high bandgap perovskite

HTL hole transport layer

iPLQY intensity dependent photoluminescence quantum yield

ITO indium-doped tin oxide

$J_{\mathbf{0,gen}}$ generation current

$J_{\mathbf{nrad}}$ non-radiative recombination current

$J_{\mathbf{rad}}$ radiative recombination current

$J_{\mathbf{SC}}$ short-circuit current

$J_{\mathbf{0,rad}}$ radiative dark current

LG low bandgap perovskite

LiF lithium fluoride

MA methylammonium

MAPI methylammonium lead triiodide perovskite

MPP maximum power point

OC open circuit

P3HT poly(3-hexylthiophene-2,5-diyl)

PbSn low bandgap, mixed metal lead-tin perovskite

PC$_{60}$BM phenyl-C$_{61}$-butyric acid methyl ester

PCE power conversion efficiency

PCE$_{\mathbf{rad}}$ radiative efficiency potential

PEDOT:PSS poly(3,4- ethylenedioxythiophene) polystyrene sulfonate

PL photoluminescence

PLQY photoluminescence quantum yield

PMMA poly(methyl methacrylate)

PolyTPD poly(4-butyl-triphenylamine-4',4''-diyl)

PSC perovskite solar cell

PTAA Poly[bis(4-phenyl)(2,4,6-trimethylphenyl)amine

$_{\mathbf{PS}}$**FF** pseudo fill factor

$_{\mathbf{PS}}$**PCE** pseudo power conversion efficiency

$_{\mathbf{PS}}V_{\mathbf{OC}}$ pseudo open circuit voltage

PV photovoltaics

QFL quasi Fermi level

QFLS quasi Fermi level splitting

RPV rising photovoltage

SAM self-assembled monolayer

SC short circuit

SEM scanning electron microscopy

Spiro-OMeTAD 2,2',7,7'-tetrakis-(N,N-di-4-methoxyphenylamino)-9,'-spirobifluorene

SPO steady-state power output

TC triple cation perovskite

TFT thin film transistor

TH triple halide perovskite

TL transport layer

TPC transient photocurrent

TRMC time-resolved microwave conductivity

TRPL time-resolved photoluminescence

$V_{\mathbf{OC}}$ open circuit voltage

$V_{\mathbf{BI}}$ built-in voltage

XPS X-ray photoelectron spectroscopy

XRD x-ray diffraction

2-PACz [2-(9H-Carbazol-9-yl)ethyl]phosphonic Acid

2T 2-terminal

CHAPTER 1

Introduction

1.1 Climate change

The findings presented in the most recent report of the Intergovernmental Panel on Climate Change (IPCC) are alarming - temperatures are rising quickly, and every region of the world is now experiencing changes in the climate system[1]. The climate changes we are currently experiencing are unprecedented in recent human history. Average temperatures worldwide have risen 1.1 °C already, and along with these rising temperatures comes an increasing number of extreme weather events. And while 1.1 °C is a global average, some areas in the world are warming at an even more disturbingly fast pace. The Arctic as a whole has warmed nearly 4 times faster than the global average - and due to local amplification, specific regions, around the Barentz Sea, are even experiencing temperature increases up to 7 times faster than the global average[2].

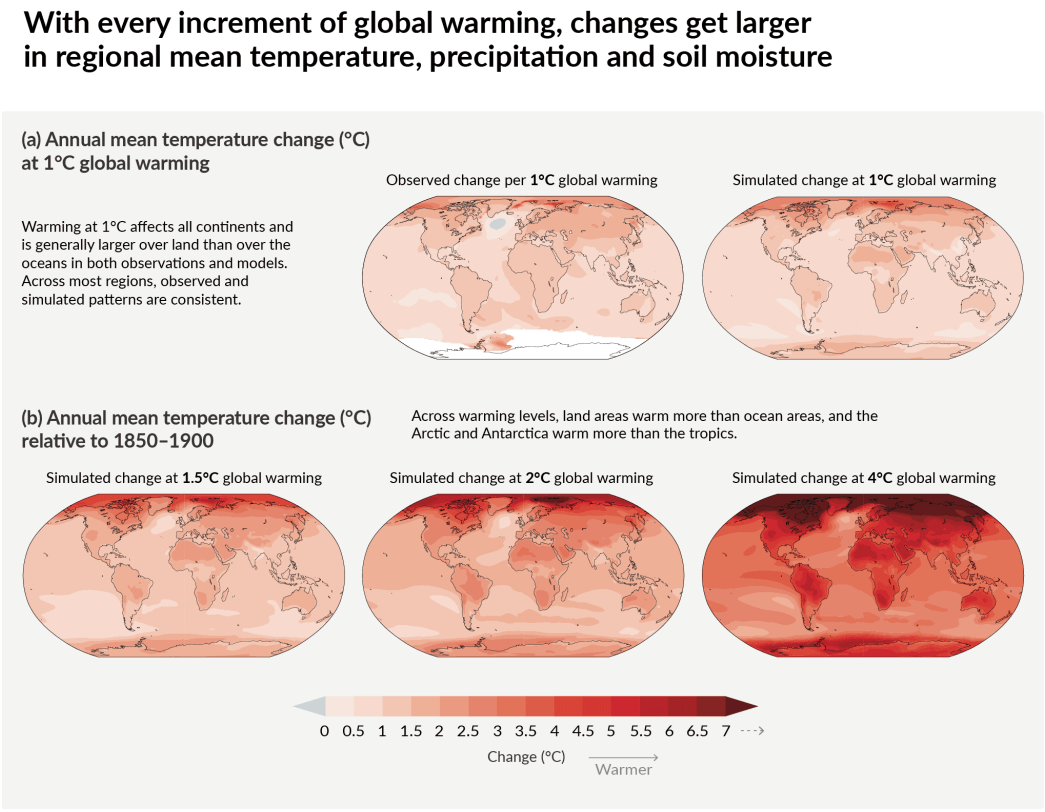

Figure 1.1: Measured and simulated average yearly temperature increase around the globe. Reproduced from IPCC[1]

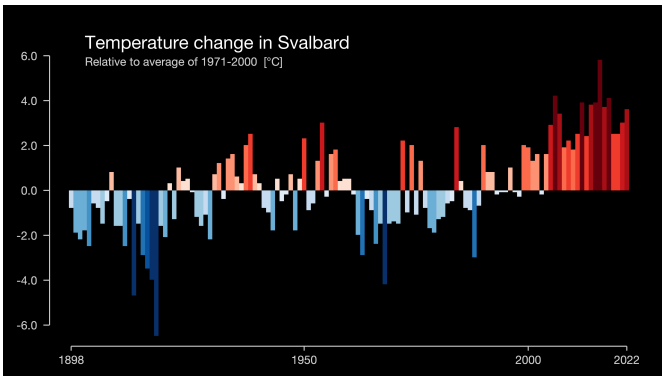

Figure 1.2: Anomalies in average yearly temperature in Longyearbyen, Svalbard, with reference to the period 1971-2000. Temperatures have increased so strongly in Svalbard, that the standard colour scale, going up to $\pm$ 2.6 the standard deviation of the period 1900-2000, did not suffice, and had to be enhanced. Graphic obtained from https://showyourstripes.info, created by Professor Ed Hawkins, University of Reading

The effects of climate change on the environment, besides the increased temperatures and changes in weather patterns, are also becoming more and more clear. Sea levels are rising faster than in the past millennia[3]. And not only are sea

levels rising, the oceans are also warming up and acidifying rapidly[4]. According to the IPCC, the impact of climate change on both humanity and the environment is not only more severe but also more widespread than expected. Some of the climate change impacts are already so severe they are impossible to adapt to, rendering formerly inhabited regions of the world uninhabitable[1].

Climate change has directly been linked to the increase in CO_2 concentrations in the atmosphere, with every 10 ppm of CO_2 roughly causing a 0.1 °C increase in global average temperature (see Figure 1.3) [i]. Even if the world rapidly decarbonises and cuts emissions, the greenhouse gases which are already in the atmosphere mean we will still experience worsening impacts of climate change through the next twenty years. Limiting global temperature rise to 1.5 °C, the most optimistic scenario described in the IPCC report, is still possible, but requires immediate action. In order to have a chance at achieving this goal, greenhouse gas emissions should be halved by 2030 and reach net zero by 2050. This can be achieved by a combination of retiring existing fossil fuel infrastructure, while scaling up renewable energy sources. In addition, all pathways that would limit global warming to 1.5 °C require some extent of carbon removal.

1.2 Renewable energy sources and their viability

The IPCC stated once more what has been known for a while now - we need to abandon fossil fuels, and move to sustainable power sources. The sun provides plenty of energy - the earth receives about 173 000 TW [ii]. With an average global power

[i] This is a rough estimate, because although CO_2 is the main contributor to global warming, it is not the only driver. Furthermore, the earth's climate system exhibits some inertia, which is also the reason why global warming would continue for a bit, even if we stop emitting any greenhouse gasses today. However, I find that linking CO_2 concentrations in the atmosphere directly to temperature provides more relatable results than looking, for example, at the amounts of total emitted greenhouse gasses

[ii] This number relates to the energy reaching the upper atmosphere - about 30% of this is directly reflected back into space from there.

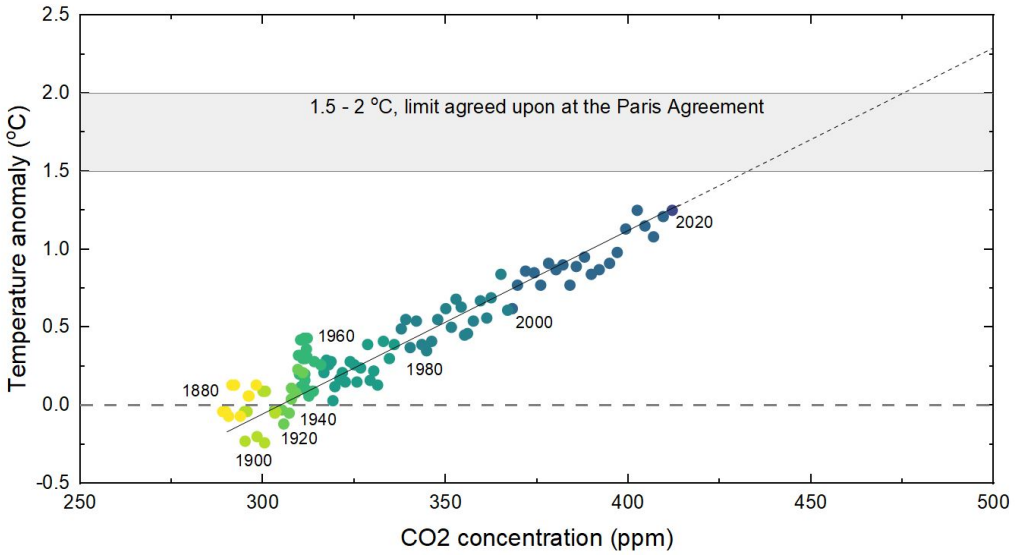

Figure 1.3: Global average temperature anomaly versus carbon dioxide concentration in the atmosphere. Every coloured circle depicts a year - yearly global average temperature is plotted versus the yearly average global CO_2 concentration. Data for this plot was obtained from the Goddard Institute for Space Studies (GISS - NASA) and the National Oceanic & Atmospheric Administration (NOAA)[5–7]

consumption of 18.4 TW[8], this means we receive nearly 10,000 times as much energy as we need on average to power the world. So, energy provided by the sun is plentiful. The difficulty, however, lies in efficiently harnessing it.

There are a variety of renewable energy sources which all, in one way or another, are powered by the sun. Wind energy, hydropower and biomass, for example, are all renewable energy sources that indirectly are also forms of solar energy. However, harnessing solar power directly should in principle enable to use the sun's energy most efficiently, and this thesis will therefore focus on photovoltaic energy conversion of sunlight. However, due to the intermittent nature of solar power, a mixture of different energy sources will be needed to power the world sustainably. On top of that, energy storage will play an important factor - both to cushion fluctuations in power supply and demand, as well as to provide sustainable energy solutions for mobility.

1.3 Photovoltaics - viability and upscaling

Photovoltaics (PV), the direct conversion of light into electricity using semiconductors, have been around since the early 1900's, when the first 'Sun Electric Generators' based on Selenium were developed[9] and installed as a proof of concept [iii]. Much later, in the 1940's and 50's, the first silicon-based solar cells were developed at Bell labs [iv][12]. Reaching a power conversion efficiency of 6%, these solar cells were the first that were efficient enough to be suitable for practical applications. The potential of this invention was widely recognised, with the New York Times writing that it 'may mark the beginning of a new era, leading eventually to the realization of one of mankind's most cherished dreams – the harnessing of the almost limitless energy of the sun for the uses of civilization'[13]. Although it would still be a while until photovoltaics were widely implemented (not least due to the high cost of these early solar cells), they were quickly adopted to power communication devices as well as satellites [v]. As costs dropped, and device efficiencies increased from the 1980's on, interest in silicon photovoltaics to power households grew. Today, silicon-based photovoltaics are omnipresent in our society, with an estimated total installed capacity of over 1.1 TW[15].

1.4 Future outlook

Crystalline silicon photovoltaics, with best performing devices today reaching efficiencies of about 26 %, are still continuously being improved, slowly approaching the theoretical efficiency limit[16]. A couple of solar panels on a roof can easily provide for the electricity consumption of an average household. However, in order to truly make a difference in the effort to slow down climate change, PV needs to go beyond just powering the

[iii] In fact, there is an interesting mystery surrounding the world's first rooftop solar panel, and whether its invention should be accredited to George Cove, or Charles Fritts[10]

[iv] A development which was actually kickstarted by the accidental creation of a p-n junction in a cracked silicon sample by Russel Shoemaker Ohl, who later patented his invention[11].

[v] Starting of with Vanguard, the first solar-powered satellite, photovoltaics truly revolutionised space technology[14].

electricity need of households. Sectors like industry and transport, which account for about 24 and 16 percent of greenhouse gas emissions, respectively, also need to be decarbonised. In order to achieve this, a new generation of photovoltaics is required. This new generation of solar cells requires higher efficiencies, such that the levelised cost of electricity is lowered. One option to achieve this is the use of multi-junction solar cells, which more efficiently utilise the photons coming from the sun. Besides more efficient solar cells which could lower the levelised cost of electricity, there is also a growing demand for solar cells that can be used in situations where conventional silicon-based PV is less suitable. Some examples of such niche applications include indoor PV (for example to power the Internet of Things (IoT)), flexible solar cells, and light-weight solar cells, for example for aerospace and satellite applications. Thin film perovskite solar cells, with their easy fabrication, short energy payback time, and tuneable bandgaps have gained considerable interest in the framework of '3rd generation PV'. They have the potential to form a powerful synergy with silicon in the form of perovskite-silicon multi-junction solar cells, which can surpass the theoretical efficiency limit of single-junction silicon solar cells. At the same time, single junctions perovskite solar cells on their own are also highly efficient while cheap to fabricate, rendering them interesting candidates for the above-mentioned niche applications.

1.5 Thesis outline

This thesis focuses on understanding the physics of perovskite solar cells, in order to enable more effective, evidence guided optimisation of single-, and ultimately multi-junction devices. In the first part of the thesis, mobile ions, and their implications for the efficiency and stability of perovskite solar cells are discussed. Thereafter, the focus shifts towards multi-junction solar cells, and how the study of subcell behaviour in these cells can guide optimisation approaches.

The introduction and motivation to this thesis in Chapter 1 are followed by an in-depth explanation of perovskite solar cells, as well as some more fundamental

theory on photovoltaics in Chapter 2. Chapter 3 then describes the experimental methods used in this thesis, from sample fabrication to different measurements and drift-diffusion simulations.

Chapter 4 investigates the origin of the relatively low short circuit current observed in low-bandgap lead-tin perovskite solar cells, using a combination of voltage dependent photoluminescence (PL) time series and various charge extraction measurements. These current losses are linked to the presence of mobile ions, which inhibit efficient charge extraction, and thereby lead to enhanced recombination, and reduced output currents. Upon investigation of other conventionally used metal halide perovskite systems, it is found that these (lead-based) perovskites suffer from the same loss mechanism.

Next, Chapter 5 explores the role of mobile ions in the (performance) degradation of perovskite photovoltaic devices. We reveal that an increase in the mobile-ion-induced field screening, discussed in Chapter 4, is responsible for the early onset performance degradation in perovskite solar cells. In addition, the device open circuit voltage also suffers from increased mobile-ion densities, which cause an increased quasi Fermi level splitting (QFLS) - V_{OC} mismatch. We also show that these ionic losses appear under different stressors, especially when additional free charges are present in the perovskite absorber layer.

The second part of the thesis focuses more directly on perovskite-based tandem devices. In Chapter 6, several different subcell selective measurements are used to investigate V_{OC} losses in all-perovskite tandem solar cells. After the identification of the main losses, an evidence-based optimisation approach is developed, strongly enhancing the performance of the tandem devices, with the best devices reaching stabilised power outputs of 25.9%. Finally, photo- and electroluminescence measurements provide insights into the efficiency potential of these devices.

Chapter 7, then, combines knowledge and methods from Chapters 4, 5 and 6 to study the presence and impact of mobile ions in perovskite-based tandem solar cells subcell-selectively. Both 'fast hysteresis' and current decay measurements, as well as

voltage-dependent photoluminescence time series are employed to investigate, and try to quantify, the mobile-ion-induced current losses in the subcells. The chapter then raises the question whether non-radiative losses in tandem subcells at short circuit conditions can be determined directly through luminescence measurements, and several different measurements are carried out in an effort to try to answer this question.

Chapter 8 presents some preliminary results from ongoing research, investigating the effect of oxidation on the device performance of low-bandgap lead-tin perovskites. Remarkably, we find that vacuum treatment can partially reverse oxidation effects. This leads us to postulate that it is possible to extract some SnI_4 from the perovskite surface through vacuum treatment, thereby reducing trap densities.

Finally, Chapter 9 summarises the work presented in this thesis and places it in perspective. We provide a future outlook, and point out how the results and insights presented in this thesis pave the way towards more efficient, stable, perovskite solar cells.

CHAPTER 2

Fundamentals

In this chapter, the fundamental physics that provide the foundations for the study of solar cells are discussed. Starting from semiconductor physics and energy band theory, the generation of charges by the photovoltaic effect is explained. Next, different types of recombination as well as other loss mechanisms are discussed, and the concept of the fundamental efficiency limit is introduced. Thereafter, the working principles of different concepts to overcome this efficiency limit, such as multijunction solar cells, are discussed. Finally, the material class of metal halide perovskites is introduced, with a special emphasis on low bandgap, mixed metal lead-tin perovskites. The theory presented here is largely based on 'Introduction to Solid State Physics' by Charles Kittel, as well as 'Physics of Solar Cells' by Peter and Uli Würfel[17,18].

2.1 Semiconductor physics

Utilising the photovoltaic effect, solar cells are based on semiconductors, materials with a conductivity value in between that of an insulator and a metal. The electrical

properties, and specifically the conductivity of semiconductors can be modified by applying external stimuli such as for example an electric field, heat, or light. This property makes them ideally suited for use in applications such as transistors, laser diodes, and solar cells[19].

In order to understand why semiconductors display the special behaviour they do, and how this can be utilised in applications, the underlying quantum mechanics needs to be discussed, at least to some extent. Quantum mechanics is based on the concept of wave-particle duality, that is, quantum entities possess both wave-like and particle-like characteristics. Light, traditionally described as electromagnetic waves, can also be described as particle-like, consisting of 'quanta' with a discrete energy - photons. Both photons and electrons are elementary particles that exhibit wave-particle duality.

In a crystal lattice, every atom (comprised of an atomic core plus electrons) is surrounded by multiple other atoms. The Born-Oppenheimer approximation allows to consider the atomic cores to be stationary, while the electrons move around and interact. Electrons in the crystal lattice experience a periodic potential, which dictates the energy levels these electrons can be at. This results in a density of states (DOS) of the material, which describes the number of states that are available at each energy level for an electron to occupy. Since electrons are Fermions, the actual electron distribution across this density of states is determined by the Fermi-Dirac distribution:

$$f(E) = \frac{1}{\exp\left(\frac{E-E_F}{k_B T}\right) + 1} \tag{2.1}$$

where k_B is the Boltzmann constant and T the temperature. E_F is the Fermi level - the energy level at which half of the available states are occupied. For an undoped semiconductor in the dark, the Fermi level would be in the middle of the bandgap. However, under illumination, the semiconductor is no longer in thermal equilibrium, and the electron and hole populations in the conduction and valence bands, respectively, both increase. Consequently, the Fermi level splits: the Fermi energy describing the

electron population must be closer to the conduction band, while the Fermi energy describing the hole population must be closer to the valence band. Electrons can then be described with:

$$f(E) = \frac{1}{\exp\left(\frac{E-E_{F,e}}{k_B T}\right) + 1} \tag{2.2}$$

and holes with:

$$f(E) = \frac{1}{\exp\left(\frac{E-E_{F,h}}{k_B T}\right) + 1} \tag{2.3}$$

Electron and hole densities can then be defined as

$$n_e = N_C \cdot \exp\left(\frac{-(E_C - E_{F,e})}{k_B T}\right) \tag{2.4}$$

and

$$n_h = N_V \cdot \exp\left(\frac{-(E_V - E_{F,h})}{k_B T}\right) \tag{2.5}$$

where N_C and N_V are the effective densities of states at the conduction and valence band, respectively, and E_C and E_V the energy level of the conduction and valence band edges. The product of the electron and hole densities then becomes:

$$\begin{aligned} n_e n_h = N_C N_V \cdot \exp\left(\frac{-(E_C - E_V)}{k_B T}\right) \exp\left(\frac{E_{F,e} - E_{F,h})}{k_B T}\right) \\ = n_i^2 \cdot \exp\left(\frac{E_{F,e} - E_{F,h})}{k_B T}\right) \end{aligned} \tag{2.6}$$

The difference between the quasi Fermi level for electrons and holes, $E_{F,e} - E_{F,h}$ is known as the quasi Fermi level splitting (QFLS). This quantity can directly describe the population of free charges in a semiconductor. Furthermore, since the electrochemical potential of electrons and holes relate to the quasi Fermi levels through

$$\eta_e = E_{F,e} \text{ and } \eta_h = -E_{F,h} \tag{2.7}$$

the QFLS is directly related to the maximum amount of free energy that can be delivered by the semiconductor upon dissociation of an electron-hole pair.

2.1.1 Charge carrier generation

When an incoming photon has an energy $h\nu$ that is higher than the bandgap (E_G) of the semiconductor, it can be absorbed, generating an electron-hole pair by promoting an electron from the valence band, where it normally resides, to an excited state in the conduction band. When carriers are excited to energy levels that are higher than the valence band maximum (conduction band minimum), they lose their excess energy through thermalisation, and relax down to the valence band minimum (conduction band maximum) (see Figure 2.1). The absorption coefficient α describes how far photons on average travel into a material before getting absorbed through the Lambert-Beer relation: $I = I_0 \cdot e^{-\alpha d}$, with high α values indicating strong absorption. Here, I is the intensity of the transmitted light, I_0 the initial intensity of the incident light, and d the thickness of the material.

2.1.2 Recombination

Once free charge carriers are generated in a semiconductor, they can either be extracted out of the semiconductor, or recombine. Extraction occurs when the charges, either through drift or diffusion move out of the semiconductor and into a neighbouring material (for example, an electrode or another charge transport layer). If free charges are not extracted from a semiconductor, they will eventually recombine. Recombination can take place through several pathways, which are illustrated in Figure 2.1. When carriers recombine directly, in a bi-molecular manner, they do so radiatively, i.e. they emit light [i]. When recombination takes place defect-assisted, or as a three-body process (Auger), no light is emitted, hence these types of recombination are non-radiative.

[i] Although bimolecular recombination can in principle be non-radiative as well, such as in organic solar cells[20], for perovskites this process is mostly radiative. Since this thesis focuses on perovskites, we will consider bimolecular recombination to be radiative in this thesis.

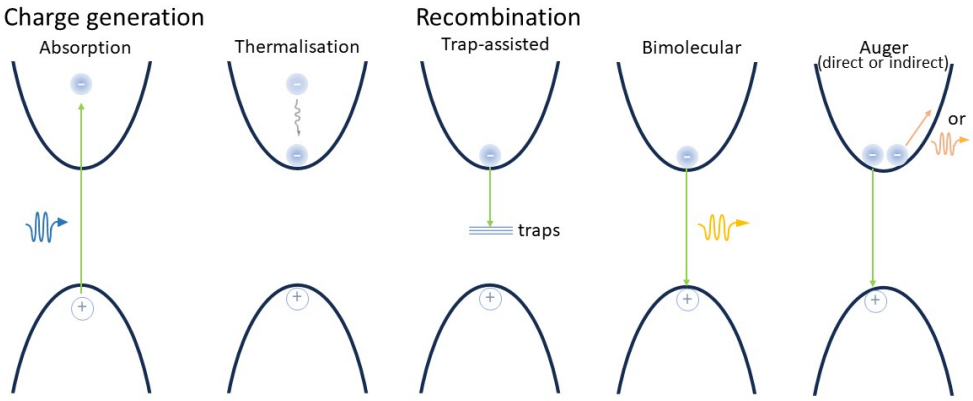

Figure 2.1: Schematic overview of charge generation and the different recombination pathways in semiconductors.

2.1.2.1 Radiative recombination

When an electron-hole pair recombines directly through band-to-band recombination, the excess energy is released in the form of the emission of a photon, i.e. $e + h \rightarrow \gamma$. Since this process depends on the simultaneous presence of both an electron and a hole in an excited state, the radiative recombination rate depends on the product of the hole and the electron density: $R_{\text{rad}} = B_{\text{rad}} \cdot n \cdot p$. In thermal equilibrium, this equation can be simplified to $R_{\text{rad}} = B_{\text{rad}} \cdot n_i^2$.

2.1.2.2 Non-radiative recombination

Shockley-Read-Hall recombination (SRH)

The dominant recombination pathway in perovskite solar cells is trap-assisted recombination. In this process, either electrons or holes get 'trapped' at defects [ii], which have a certain energy level. Generally, traps are divided into two categories: 'shallow traps' and 'deep traps', depending on their energy level. Shallow traps for electrons (holes), which occur close to the conduction (valence) band, are less detrimental to solar cell performance than deep traps, since carriers can relatively easily 'escape' from shallow traps.

[ii] Dopants can also act as trap states - which includes mobile ions or vacancies left behind by mobile ions

Trap-assisted recombination only depends on the carrier density of either electrons or holes, rather than the product of both as is the case for radiative recombination. Therefore, the trap-assisted recombination rate can be written as $R_{\text{nonrad}} = B_{\text{nonrad}} \cdot n \cdot N_{\text{trap}}$. Here, N_{trap} is the trap density. The value of prefactor B_{nonrad} depends on the 'capture coefficient' of the traps, that is, how effectively the traps capture free charges. This capture coefficient C is defined as $C = \sigma\nu_{\text{th}}$ and depends on the capture cross section σ, as well as the thermal velocity of the carrier ν_{th} [21,22].

When trap-assisted recombination occurs at interfaces, it is referred to as 'surface recombination'. Atoms located at surfaces do not have the same bonding structure as bulk atoms since they lack neighbouring atoms. This causes some of the valence orbitals to not form any chemical bonds. Instead, these partially filled electron orbitals, or dangling bonds, turn into divergent electronic states that can be located within the bandgap of the material, where they act as recombination centers.

Auger recombination

Auger recombination is a three-body process, which takes place when a recombining electron-hole pair transfers its excess energy to another electron that is already present in the valence band, facilitating its transition to a higher energy level. Since this process is a three-body process, it normally only becomes significant under circumstances where carrier densities are (very) high, for example in concentrator photovoltaics, but also in silicon solar cells. It is less relevant for perovskite solar cell operation under normal, 1-sun equivalent illumination. The recombination rate for Auger recombination can be described as $R_{\text{Auger}} = C_{\text{Auger}} \cdot n \cdot p^2$ or $R_{\text{Auger}} = B_{\text{Auger}} \cdot p \cdot n^2$.

2.1.2.3 Photoluminescence and carrier lifetimes

Recombination in semiconductors can be investigated by looking at the carrier lifetimes. The different recombination processes take place at different rates, with rate constants

denoted by k_1, k_2 and k_3 for trap-assisted, bimolecular and Auger recombination, respectively. The dynamics of charge carrier generation and recombination, in a system where there is no extraction, can then be described as

$$\frac{dn}{dt} = G \overbrace{-k_1 n - k_2 n^2 - k_3 n^3}^{\mathrm{R}}$$

where G is the charge carrier generation and R is recombination.

Using this relation, at equilibrium conditions (no extraction, and $G = R$), photoluminescence measurements can provide insights into the extent of the different recombination processes. The ratio of the radiative recombination versus the total recombination, that is, $\frac{J_{\mathrm{rad}}}{J_{\mathrm{rad}}+J_{\mathrm{nrad}}}$, is the photoluminescence quantum yield (PLQY). This quantity provides insight into how effectively carriers recombine radiatively in a semiconductor - important, because Rau's reciprocity states that 'In fact, a solar cell that has the theoretical maximum power conversion efficiency will also act as an LED with the maximum possible luminescence efficiency'[23]. High PLQY values are indicative of good solar cell performance, since they indicate low levels of non-radiative recombination, which is detrimental to solar cell performance. Time resolved photoluminescence (TRPL), furthermore, can also be used to investigate recombination rates in a semiconductor. A short light pulse excites (a known number of) carriers, and the radiative decay that follows can be used to investigate carrier lifetimes, and determine the mono- and bimolecular recombination rates. The effective carrier lifetime τ_{eff} is the result of a combination of decay mechanisms, and can be defined as $\frac{1}{\tau_{\mathrm{eff}}} = \frac{1}{\tau_{\mathrm{rad}}} + \frac{1}{\tau_{\mathrm{SRH}}} + \frac{1}{\tau_{\mathrm{surf}}} + \frac{1}{\tau_{\mathrm{Auger}}}$, where τ_{rad} is the radiative lifetime, τ_{SRH} the Shockley-Read-Hall lifetime, τ_{surf} the surface lifetime, which includes recombination at the front and back side of the semiconductor film and also depends on the electron and hole mobilities[24,25]. The Auger lifetime τ_{Auger} is also included here for completeness, but since Auger recombination only becomes relevant at high carrier densities, this term can normally be omitted for perovskite films.

Quasi Fermi level splitting

PLQY and electroluminescence quantum yield (ELQY) measurements can also be used to calculate the quasi Fermi level splitting (QFLS) in a material. As described above, the QFLS, which equals $E_{F,e} - E_{F,h}$ is a measure of the population of free carriers in a semiconductor. As such, it can be used to calculate the (maximum achievable) open circuit voltage in a solar cell, since its value equals the maximum amount of work an electron-hole pair in a semiconductor can do (and thus how much of the incoming radiative energy the solar cell can convert into electrical energy). The QFLS is directly related to the PLQY value, through $\text{QFLS} = k_B T \ln(\text{PLQY} \cdot \frac{J_G}{J_{0,\text{rad}}})$, where J_G is the generation current, and $J_{0,\text{rad}}$ the radiative dark current. Calculating the QFLS at different charge injection densities (EL) or light intensities (PL) can also be used to reconstruct 'pseudo-JV curves', which can provide important information on losses and potential efficiencies in solar cells. More information regarding the reconstruction of such pseudo-JV-curves can be found in Chapter 3.

2.1.3 Thermodynamic efficiency limits and power loss in solar cells

Even ideal solar cells, which do not suffer from traps, energy level misalignments, or series and shunt resistances, display losses. Most importantly, these losses come from thermalisation (causing voltage losses) and photons with below-gap energy (leading to current losses). However, there are some additional losses that occur in ideal solar cells. Carnot losses, stemming from the fact that a solar cell essentially is a heat engine, limited by the Carnot efficiency, make up for some additional voltage losses[26]. Furthermore, Boltzmann losses, due to entropy, also cause a reduction in the output voltage of the solar cell. Finally, there are some emission losses, which slightly reduce the current output from the cell[27]. Figure 2.2 displays the usable power, as well as the different losses, for an ideal solar cell depending on its bandgap.

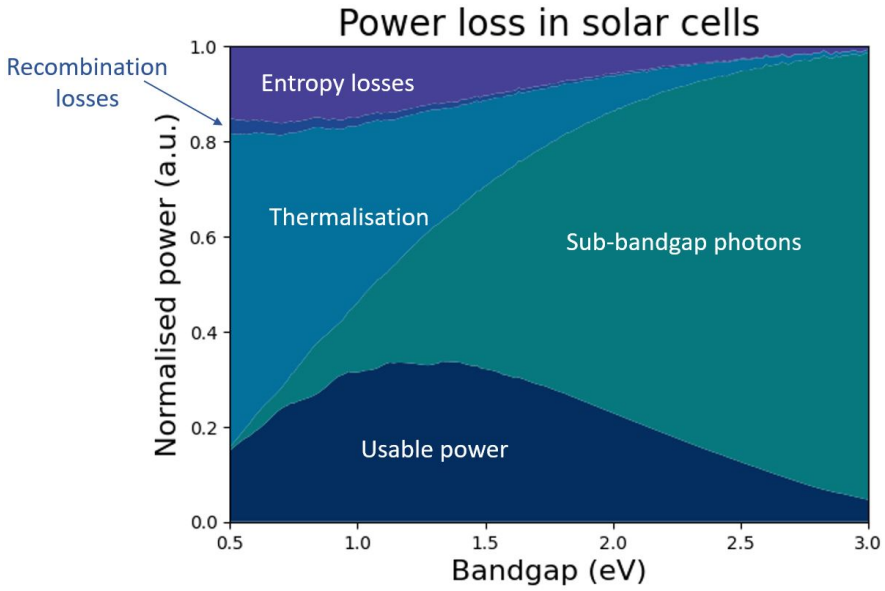

Figure 2.2: Usable power and losses in an ideal solar cell. Calculations based on[27]

Multi-junction solar cells

To overcome this fundamental efficiency limit, several strategies have been developed, including hot carrier extraction, singlet fission, and the use of multiple junctions with different bandgaps[28]. Particularly important to this thesis are the multi-junction solar

cells, which can overcome the efficiency limit through the use of multiple subcells. This allows for more efficient conversion of incoming light into electricity by reducing thermalisation losses while maximising absorption (Figure 2.3 depicts a schematic explanation of the working mechanisms of multijunction solar cells). To date, this is the only approach aimed at overcoming fundamental efficiency limits which has been demonstrated to work efficiently and practically. This has led multi-junction solar cells to become of great interest for commercialisation.

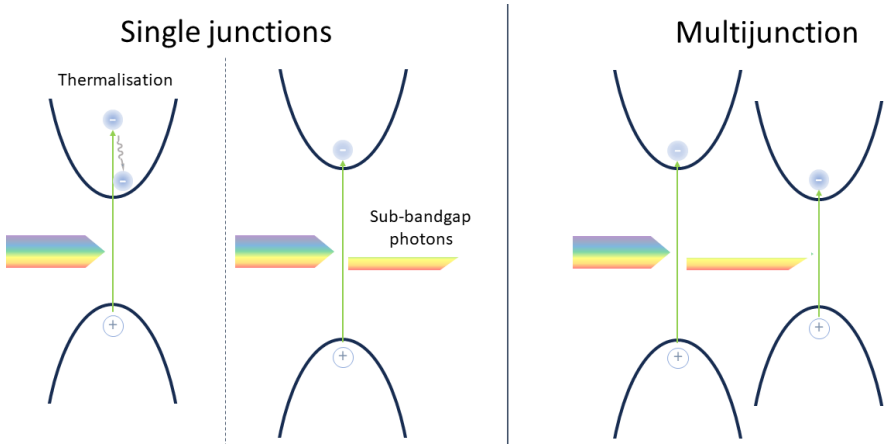

Figure 2.3: The working principle of multi-junction solar cells. On the left, energy is lost in single junctions due to thermalisation and photons not being absorbed. The multi-junction device reduces these losses by making use of 2 different bandgaps, absorbing high energy photons in the first subcell, while lower energy photons are absorbed in a second subcell.

There are different strategies when it comes to the construction of multi-junction cells. The working principle of 2-Terminal (2T) devices, where the subcells are processed directly on top of each other and are connected in series, is based on current matching between the different subcells [iii]. However, the design does allow for the devices to be integrated into the power system without additional electronics compared to single junctions. Processing can be challenging, however, and the recombination layer, where the subcells are connected electronically, can introduce losses. 4-Terminal (4T) devices, on the other hand, are a bit easier to process but require additional effort for integration into the power system. 3-Terminal (3T)

[iii] Although in some cases, a slight current mismatch is introduced on purpose, for example to improve the fill factor of 2T tandem solar cells

devices, finally, can overcome some of the limitations of 2- and 4-terminal tandems, but come with some additional complexity and their operation is less straightforward[29]. For efficient multi-junction solar cells, the bandgap energies of the different subcells are of vital importance, since the enhanced efficiency comes from a careful balance between increased photon absorption and reduced thermalisation losses. Figure 2.4 shows the maximum efficiency that can be achieved in a 2-terminal and 4-terminal tandem for different bandgap combinations. It can be seen that both in 2-T, as well as 4-T tandems, the bandgap of the bottom cell needs to be rather low to enable maximum efficiencies.

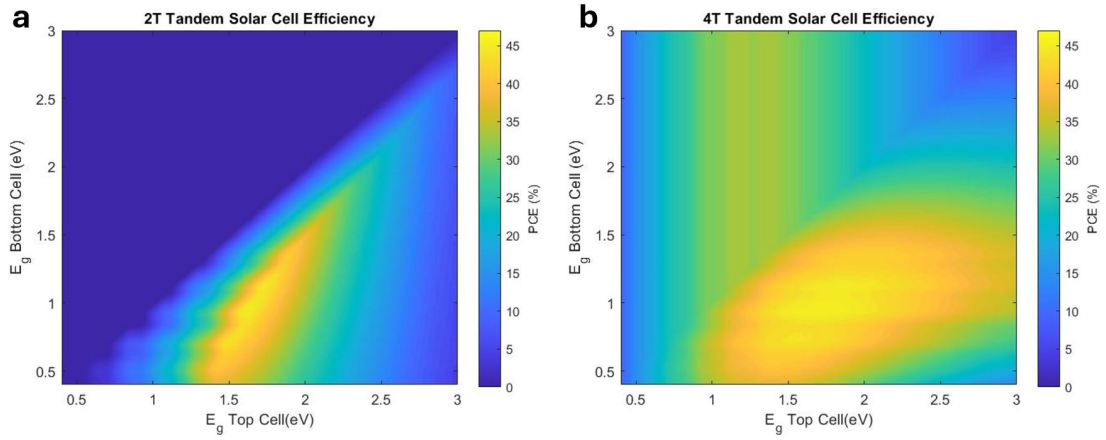

Figure 2.4: The maximum theoretically achievable efficiency for a) 2T and b) 4T tandems as a function of the bandgap of the top and bottom subcells. Calculated based on[18].

Losses in real solar cells

Real solar cells, in addition to the intrinsic losses described above, also suffer from additional losses. Imperfect absorption and reflection of incoming light and (nonradiative) recombination all lower the device PCE. Furthermore, additional losses can arise from non-ideal carrier transport. Such transport losses are linked to issues extracting the carriers from the device, as well as the series resistance in the device. This series resistance can have a profound impact on the fill factor of devices, and hence the series resistance should be kept as low as possible. High series resistance in devices can arise from low-mobility transport layers, for example. On top of this, there can be internal

short circuits, which run parallel to the solar cell junction, leading to a loss of voltage and fill factor. To prevent these shunt losses, the shunt resistance should be as high as possible. Low shunt resistances often result from defects that are formed during fabrication, such as pinholes or inhomogeneities in absorber or transport layers. Figure 2.5 displays the simulated impact of shunt resistance (a) as well as series resistance (b) on a JV curve. Furthermore, in Chapter 6, we will show how low shunt resistances in 2T tandem devices can also impact current matching requirements and have a profound impact on the tandem device performance.

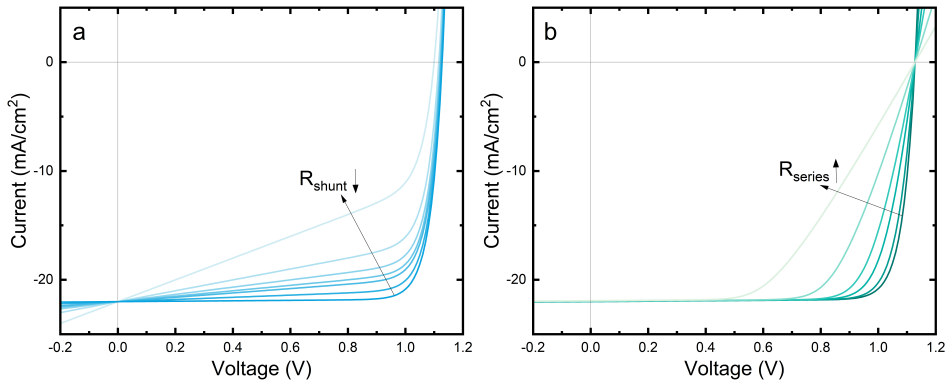

Figure 2.5: Simulated JV curves for varying shunt (a) and series (b) resistances, simulated using LTspice.

2.2 Metal halide perovskites

2.2.1 Composition and structure

Perovskites are a class of compounds that have the same crystal structure as calcium titanate ($CaTiO_3$). Calcium titanate was first discovered by the German mineralogist Gustav Rose, who named the mineral 'perovskite' after his Russian colleague Lev Perovski[30].

Perovskites exhibit a near cubic structure with the general chemical formula ABX_3, where the A-site ion is located in the centre of the lattice, with B-site ions situated at the corners and the X-site ions at the face-centred positions. In this structure, the

A- and B-site ions are positively charged cations, whereas the X ions are negatively charged anions. Naturally found materials that assume a perovskite structure are often oxides, where the negatively charged oxygen ions on the X-site are combined with positively charged metal ions on the A- and B-site. However, there is a plethora of different options available for the different ionic sites, which can generally form stable perovskite structures as long as the Goldschmidt tolerance factor[31], t, is in the range of 0.75 and 1. Assuming the ions to be hard spheres, this formula can be used to predict the structural stability based on the ionic radii of the ions at the different positions.

$$t = \frac{R_{\mathrm{A}} + R_{\mathrm{X}}}{\sqrt{2}(R_{\mathrm{B}} + R_{\mathrm{X}})} \tag{2.8}$$

Here, $\mathrm{R_A}$ is the radius of the cation on the A site, $\mathrm{R_B}$ the radius of the cation on the B site, and $\mathrm{R_X}$ the radius of the anion on the X site.

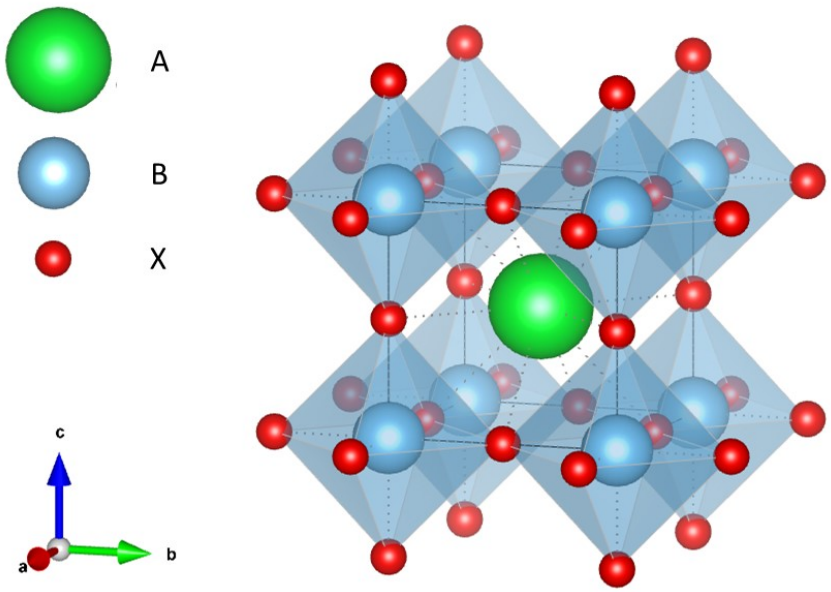

Figure 2.6: $\mathrm{ABX_3}$ perovskite crystal structure. The structure displayed here is cubic, that is, unit cell dimensions a = b = c. However, perovskites do not have to occur in cubic form, a, b and c can have different lengths.

Different perovskite materials display a wide variety of interesting physical properties, such as charge ordering, giant and colossal magnetoresistance, piezoelectricity,

(high temperature) superconductivity and spin-dependent transport[32–41]. These properties make this material class interesting for applications in microelectronics - attracting considerable research interest.

Stable metal halide perovskites, where a halide on the X position replaces the commonly found oxygen anion, although not found naturally, can be fabricated using for example cesium as the A-site cation. Christian Moller first characterised such *caesium plumbohalides* to have a perovskite structure in 1958[42] [iv], and also found these materials to be photoconductive. Later, in 1978, Dieter Weber replaced the A-site cesium with methylammonium, thereby creating the first organic-inorganic halide perovskites, demonstrating both lead-based, as well as tin-based systems[44,45]. Although metal halide perovskites were studied more in-depth afterward, they only first found their application in solar cells in 2009, when researchers led by Tsutomu Miyasaka first used metal halide perovskite nanocrystals as sensitisers in dye-sensitised solar cells[46]. With the discovery in 2012 that these metal halide perovskites could be employed not just as sensitisers, but as absorbers with long enough charge-carrier lifetimes such that charge carriers could reach their respective electrodes, research into metal halide perovskite solar cells kicked off[47].

For solar cell applications, the role of the monovalent A-site cation is often fulfilled by either methylammonium (CH_3NH_3), formamidinium ($CH(NH_2)_2$) or cesium (Cs). The bivalent B-site is usually composed of either lead (Pb) or tin (Sn). Finally, the anionic X-site is usually filled by a halide, commonly chloride (Cl), bromide (Br) or iodide (I) [v]. The occupation of the different sites in the crystal lattice is not limited to only one type of ion - there exists a wealth of different perovskite compositions with different combinations of cations and anions on the A, B and X positions. Through changing the perovskite composition, not only can the bandgap of the perovskite be tuned[48,49](metal halide perovskite bandgaps span a range from about 1.2 to 3.2

[iv] Although the materials themselves had already been reported as early as in 1893[43]

[v] There are, of course, other anions and cations which are also being investigated for their use in perovskite, such as the monovalent rubidium (Rb) for the A-site and the bivalent germanium (Ge) for the B site. However, due to their relatively limited usage, they are not discussed in further detail in this thesis.

eV, which also makes them ideal candidates for use in perovskite-based multijunction solar cells [vi]), but also other relevant material characteristics such as the dielectric constant and charge transport properties can be altered, and tuned to serve specific applications[51,52].

Metal halide perovskites can easily be deposited, generally either from solution (spin coating, blade coating, slot-die coating, inkjet printing, spray coating) or through thermal evaporation [vii]. This variety of available deposition methods allows for flexibility in the development of upscaling strategies[53].

2.2.2 Material properties and physics

Metal halide perovskites exhibit several properties that make them ideally suited for use in solar cells. They have moderately high absorption coefficients in the range of 10^5 cm^{-1}, which, combined with their direct bandgaps, allow them to efficiently utilise incoming photons for charge generation[54]. Furthermore, they generally exhibit good (and balanced) carrier mobilities and long charge diffusion lengths, which, combined with their relatively high 'defect tolerance'[55,56] [viii] enables effective charge transport. Finally, perovskites also exhibit low exciton binding energies, which also contributes to low efficiency losses[57]. Beyond these favourable optoelectronic properties that are directly important for the initial photovoltaic performance of perovskite solar cells, the material group exhibits some other characteristics which turn out to be advantageous in the long run. For example, the relatively low atom displacement energy combined with weak binding which causes perovskites to classify as 'soft semiconductors', leads these materials to display some self-healing properties, and makes them relatively radiation tolerant[58,59].

[vi] Not all perovskite compositions are very stable, and especially the halides on the X site have a tendency to de-mix, leading to halide segregation[50]. Some bandgaps are therefore more easily achieved with stable perovskite compositions than others - but more about that later.

[vii] Or a combination thereof in a two-step process

[viii] Perovskites have relatively high defect densities compared to, for example, silicon, but since many of these defects are not deep traps, the perovskite solar cell performance is relatively unaffected.

Furthermore, facile and cheap deposition of perovskites as well as easy options for recycling provide additional benefits for eventual commercialisation of perovskite solar cells.

Mobile ions

However, although metal halide perovskites are often glorified for their outstanding optoelectronic properties, the materials also exhibit some less favourable characteristics. The 'soft semiconductor' characteristics mentioned before which enable self-healing, also allow ionic charges to move through the material[60] and wreak havoc. Ions can move to interfaces and react with materials there, causing permanent degradation of devices[61–63]. And, as will be discussed in Chapters 4 and 5, even when they do not degrade devices through chemical reactions, large amounts of mobile ions can also strongly negatively impact photovoltaic device performance[64–67]. Organic A-site cations, especially methylammonium, can relatively easily decompose and leave the perovskite - leaving vacancies behind, leading to destabilisation and degradation[68,69]. Furthermore, polar solvents also pose an issue for metal halide perovskites - due to the highly ionic nature of the crystal, in combination with low binding energies, polar solvents, including water, easily degrade the perovskite[70,71]. Stability and the prevention of degradation, generally, are the biggest challenges that still need to be overcome to make the widespread use of perovskites in commercial applications a reality[72–74].

Lead-tin perovskites

Besides the general unfavourable metal halide perovskite characteristics described above, some specific perovskite compositions bring along additional challenges. Especially relevant for this thesis is the oxidation of Sn(II) to Sn(IV) in (partially) tin based perovskites. Oxidation of the tin can occur before, during, and after perovskite deposition, and both through direct exposure to oxygen in air, as well as through reactions with solvents[75–77]. This oxidation has a number of direct and indirect effects.

Mobile ion densities, as well as doping densities in the perovskite can (strongly) increase, impacting the device performance [ix]. The additionally created free charges can thereafter also accelerate further degradation. Several strategies have been designed to prevent oxidation (or reduce its impact)[79–83], but it still remains challenging to fabricate high-quality tin-based perovskites, and processing is less straight-forward than for other perovskite compositions [x] [xi]. This is also because, in addition to the oxidation issue, tin-based perovskites crystallise much faster than their fully lead-based counterparts, making it more challenging to control the crystallisation process, and causing the perovskite film quality to be more dramatically impacted by small changes in for example temperature or solvent atmosphere during processing[84–86].

[ix] Although there is also some evidence that the presence of Sn itself in the lattice, when not oxidised, might be beneficial in preventing some ion migration due to lattice distortion[78]

[x] Although good, air- and solvent-atmosphere-free gloveboxes may help a great deal to overcome some of the challenge.

[xi] However, even with great equipment, fabricating lead-tin perovskites involves a lot of 'I did everything exactly the same as last time, why does this recipe suddenly not work anymore' situations.

CHAPTER 3

Experimental Methods

This chapter describes the characterisation methods utilised in this thesis. It also provides background information regarding the drift-diffusion simulations presented in this thesis. Device fabrication methods, as well as simulation parameters, can be found in Appendix A.1.

3.1 Characterisation

3.1.1 Optical and Spectroscopic Characterisation

3.1.1.1 Steady State Photoluminescence

Photoluminescence measurements were obtained by illuminating an encapsulated device or perovskite comprising stack with a 520 nm CW laser (for HG perovskites) or an 808 nm CW laser (for LG perovskites). The resulting PL spectra were measured using an Andor Solis setup with a DU420A-BR-DD Si detector. A calibrated Oriel 63355 lamp was used to correct the spectral response of the spectrometer. All

measurements were repeated several times to check for consistency.

For absolute PL measurements, the sample was placed in an integrating sphere, which the laser light was coupled into using an optical fibre. A second optical fibre was used to guide light from the integrating sphere to the Andor Solis SR393i-B spectrometer. The intensity of the laser light was adjusted to 1 sun equivalent using a calibrated silicon photodiode under the sphere (photodiode 2). However, this photodiode can only be used when there is no sample present in the integrating sphere, and hence the intensity of the laser should be adjusted before the sample is placed into the sphere. Intensity-dependent photoluminescence measurements were performed similarly, using a neutral density filterwheel to attenuate the laser light, measuring the PL for different light intensities (in an increasing or decreasing manner). The applied light intensities were monitored continuously with a Si photodiode (photodiode 1). Impurities in the integrating sphere, as well as attenuation in the optical fibres, slightly alter the spectrum of the light passing through, hence a correction needs to be applied during the data processing. Furthermore, long-pass filters, used within the spectrometer to cut out the excitation light, cause some further changes in the spectrum, which, especially when the PLQY of the sample is low, can significantly impact results and should be corrected for.

Voltage-dependent PL measurements were carried out using a slightly different setup. Instead of using the integrating sphere, laser light was directed directly onto the device active area using a free-space setup, which includes a lens to allow to focus the incoming light. Thereafter, a lens was used to focus the outcoming light on the entrance slit of the Andor Solis SR393i-B spectrometer. For these voltage-dependent, linear PL measurements, the intensity of the laser light was adjusted using the J_{SC} of the perovskite device, as determined under AM1.5G illumination. During the measurement, the devices were masked, ensuring that only the active device area could be illuminated by the incoming laser light. A schematic overview of both the setup for absolute PL measurements, as well as linear, voltage-dependent PL measurements can be found in Figure 3.1

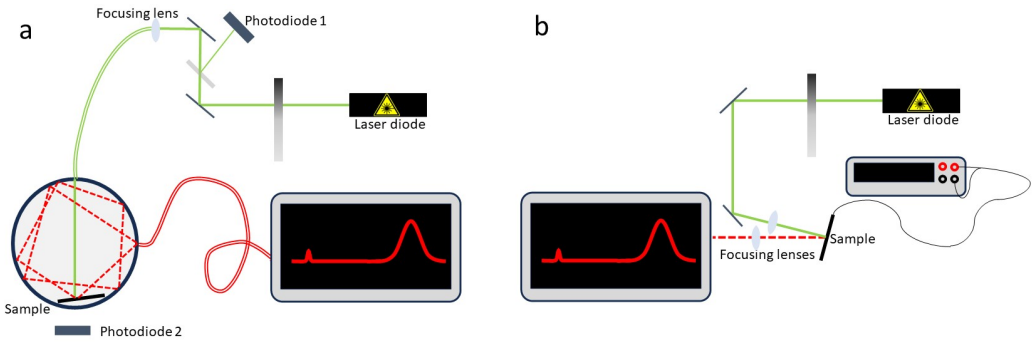

Figure 3.1: A schematic overview of the setups used for absolute (a) and linear (b) photoluminescence measurements.

3.1.1.2 QFLS calculations

The quasi-Fermi level splitting in the individual subcells was calculated following detailed balance, linking the radiative recombination density of free charges (J_{rad}) with the chemical potential per free electron-hole pair (μ) or the quasi-Fermi level splitting (QFLS) in the respective active material[87,88]:

$$J_{\text{rad}} = J_{0,\text{rad}} \exp\left(\frac{\text{QFLS}}{k_B T}\right) \tag{3.1}$$

Here, $J_{0,\text{rad}}$ is the radiative thermal recombination current density in the dark, k_B is the Boltzmann constant, and T is the temperature. Equation 3.1 is a simplification of Würfel's generalised Planck law and is valid for a QFLS that is a few $k_B T$ smaller than the bandgap, $\mu < E_G - 3k_B T$[18]. (If radiative recombination comes only from free charges, the radiative recombination current is identical to the photoluminescence flux times the elementary charge, i.e., $J_{\text{rad}} = \phi_{\text{PL}} \cdot e$.) Moreover, we can define the photoluminescence quantum yield (PLQY) as the ratio of radiative to total recombination ($J_{R,\text{tot}}$), where the latter is identical to the generation current density (J_{G}) under open-circuit conditions (V_{OC}):

$$\text{PLQY} = \frac{J_{\text{rad}}}{J_{R,\text{tot}}} = \frac{J_{\text{rad}}}{J_{\text{G}}} \tag{3.2}$$

The QFLS is then given by:

$$\mathrm{QFLS} = k_B T \ln\left(\mathrm{PLQY} \cdot \frac{J_\mathrm{G}}{J_{0,\mathrm{rad}}}\right) \tag{3.3}$$

With $T = 300$ K and the measured PLQY values. For a PLQY = 1, we further get the radiative limit of the QFLS ($\mathrm{QFLS_{rad}}$) via:

$$\mathrm{QFLS_{rad}} = k_B T \ln\left(\frac{J_\mathrm{G}}{J_{0,\mathrm{rad}}}\right) \tag{3.4}$$

We note that equations 3.2 and 3.4 are only valid if the spectral dependence of J_rad is identical to $J_{0,\mathrm{rad}}$, meaning recombination goes through the same channels regardless of the QFLS.

The generation current density J_G was approximated with the short-circuit current density of the complete solar cell. The $J_{0,\mathrm{rad}}$ was estimated by integrating the overlap of the external quantum efficiency (EQE) of the respective subcell with the black body spectrum ϕ_BB at 300 K over the energy:

$$J_{0,\mathrm{rad}} = \int \mathrm{EQE} \cdot \phi_\mathrm{BB}\, d\epsilon \tag{3.5}$$

with

$$\phi_\mathrm{BB} = \frac{1}{4\pi^2} \frac{\hbar^3 c^2 \cdot E^2}{\exp\left(\frac{E}{k_B T}\right) - 1} \tag{3.6}$$

3.1.1.3 Time-Resolved Photoluminescence Spectroscopy

Time resolved photoluminescence measurements were carried out using a FluoTime 300 time-correlated single photon counting (TCSPC) setup from PicoQuant. A 634 nm centre wavelength pulsed laser was used to excite lead-tin perovskite samples, and a 505 nm centre wavelength pulsed laser to excite lead-based perovskite samples. The response of the lead-tin sample was measured using a H10330C-75 photomultiplier tube unit from Hamamatsu.

3.1.1.4 UV Vis Absorbance, Transmittance, and Reflectivity

In order to analyse reflection parasitic absorption losses as well as to improve tandem device architecture, absorbance, transmittance and reflectivity were measured for several full or partial device stacks. These measurements were carried out using a Cary 5000 UV-Vis-NIR spectrophotometer with an integrating sphere.

3.1.1.5 X-ray Photoelectron Spectroscopy

The X-ray photoelectron spectroscopy (XPS) measurements presented in Chapter 5 were conducted in a JEOL JPS-9030 ultrahigh vacuum system (base pressure of 1 x 10^{-9} mbar) using monochromatised Al K-alpha (1486.6 eV) radiation. All samples were transferred to the UHV chamber using a transfer rod under a rough vacuum (1 $\times$ 10^{-3} mbar). XPS measurements were carried out by Fengshuo Zu.

3.1.2 Material Characterisation

3.1.2.1 Scanning Electron Microscopy

Scanning Electron Microscopy images were obtained by Emilio Gutierrez-Partida using a Zeiss Ultra Plus SEM (Chapter 6) and myself using a FEI Quanta 600 FEG system (Chapter 4).

3.1.2.2 X-ray Diffraction

The X-ray diffraction measurements presented in Chapter 5 were obtained by Fengshuo Zu, and conducted in air using a Bruker D8 Advanced diffractometer at a wavelength of 0.154 nm (Cu k-alpha).

3.1.3 Photovoltaic Device Characterisation

3.1.3.1 Current-Voltage Characteristics

In order to investigate the performance of a solar cell, the device is illuminated with light of a specific intensity and spectrum, while its output current density is measured as a function of the applied voltage. The resulting JV characteristics allow for the determination of key performance metrics, including the power conversion efficiency, fill factor, J_{SC} and V_{OC}. JV curves presented in this thesis were measured using a Keithley Standard Series 2400 Source Measure Unit (SMU), connected to the sample in a 2-wire configuration. Unless indicated otherwise, JV characteristics were measured in a nitrogen filled glovebox, with the sample temperature kept at 25 °C through the use of a Peltier element. The device was illuminated with simulated AM1.5G irradiation at 100 mWcm^{-2}, from a filtered Oriel Class AAA Xenon lamp. The sun simulator was calibrated using a certified KG3 filtered silicon solar cell (calibrated and certified by Fraunhofer ISE). On top of that, during measurements, the light intensity was continuously monitored using a Si photodiode.

3.1.3.2 Fast hysteresis and current decay

Fast JV-curves were obtained by applying a triangular voltage pulse to the cells by holding the cells at the open-circuit voltage for several seconds, then going gradually to 0 V and directly back to the open-circuit voltage. The scan speed time of the voltage sweep was varied and the voltage response of the cell measured with an Agilent DSO9054H High-Definition Oscilloscope, using an external load resistance of 10 Ω. The voltage pulse was supplied by an Agilent 33220A function generator in combination with a home-built amplifier (4x), which minimised the output resistance of the function generator to avoid external resistances. A schematic overview of this setup can be seen in Figure 3.3.

We note that during the JV scans the device was continuously illuminated and that the measurement of the full scanrate-dependent hysteresis takes about 15 minutes.

Current decay measurements were obtained using the same setup, switching the bias applied to the illuminated device from V_{OC} to 0 V while measuring the output voltage, using an external load resistance of 50 Ω.

3.1.3.3 External Quantum Efficiency

The photovoltaic external quantum efficiency (EQE_{PV}) is a measure of the number of electrons extracted per incident photon (therefore, this measurement is also known as incident photon to current efficiency (IPCE)). All EQE_{PV} measurements presented in this thesis were measured in a nitrogen-filled glovebox, unless stated otherwise. Light from a broadband light source (250W Osram Projection lamp, type 64655HLX) is chopped at a desired frequency and coupled into a Oriel Cornerstone 74100 monochromator. Thereafter, the resulting monochromatic light is coupled into an optical fibre, and directed into the glovebox and onto the device. To calibrate, the light coming out of the fibre at the different wavelengths is measured using Newport 818-UV Newport 818-IR photodiodes. The modulated signal from the sample is lock-in-amplified and consequently measured by a lock-in-amplifier (SR 830). A schematic overview of the setup is displayed in Figure 3.2.

For perovskite-based tandems, bias light was used as follows: for measurements of the perovskite top cell, infrared bias light was applied while for measurements of the perovskite bottom cell, blue bias light was applied using appropriate LEDs. For perovskite-based triple junctions, bias light was used as follows: for the measurement of the perovskite top cell, infrared bias light as well as red bias light were applied, for measurements of the perovskite middle cell, infrared bias light as well as blue bias light were used, and for measurements of the perovskite bottom cell, red bias light as

well as blue bias light were used.

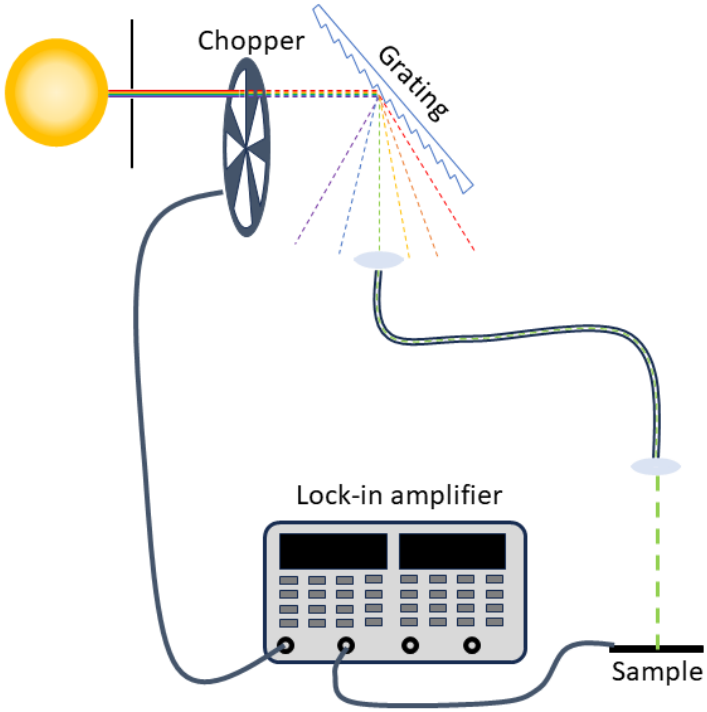

Figure 3.2: A schematic overview of the setup used for EQE_{PV} measurements

3.1.3.4 Electroluminescence Quantum Yield

Electroluminescence measurements were obtained by applying a bias voltage to the cell, and recording the electroluminescence emitted by the cell with a silicon photodiode (Newport). To distinguish between the emission of the different subcells, short- and long-pass filters were used. Calibration measurements were performed to account for the extra distance introduced by the filters between the cell and the photodiode. These electroluminescence measurements were performed on unencapsulated cells in a N_2 filled glovebox. To account for the spectral response of the photodiode, the EL spectra were recorded using an Andor Solis setup with a Si detector. A bias voltage was applied to the encapsulated cell, after which the spectrum was recorded. All measurements were repeated several times to check for

consistency and changes over time.

3.1.3.5 Ageing and Stability Testing

3.1.3.5.1 Light ageing Light aging under open-circuit conditions was initialy performed by placing the device under AM1.5G in a N_2 filled glovebox, using a peltier-cooled device holder which ensured the temperature of the cell was being kept constant and limited to 25 °C. Later, additional ageing experiments were carried out by placing samples in a dedicated aging box in the glovebox under N_2 atmosphere under using white LED array illumination providing a 1 sun equivalent intensity by matching the initial current of the cell to the J_{SC}. The intensity of the LED was checked using a photodiode and remained stable over the course of the course of the measurement timescale ($\sim$24 h) in a sample holder. The cells were cooled to 25 °C over the course of the measurement, however, no significant changes in the degradation was observed without additional cooling.

3.1.3.5.2 Voltage and temperature ageing Voltage ageing was performed by applying a voltage slightly above the open-circuit voltage (V_{pre}) to the cell at which the injected charge equals the initial short-circuit current. Over the course of the ageing test, the applied voltage was slightly adjusted to maintain an injection current of roughly J_{SC}. Temperature ageing was conducted by placing the cell on a hotplate at $\sim$80 °C for the given amount of time. Both voltage and temperature ageing were carried out while the device was being kept in the dark.

3.1.3.5.3 Steady-state Power Output (SPO) tracking Long-term steady-state power output tracking measurements were performed with a Botest multichannel analyser system (Botest Systems GmbH, EMU-8/ v2.3) with a constant applied voltage (initial VMP) using a white light LED (3000K Cree CXB3590) illumination providing a 1 sun equivalent intensity by matching the initial current of the cell to the J_{SC} under AM1.5G illumination. The temperature during the tracking was T=40 °C and the measurements were performed in ambient atmosphere on encapsulated cells.

3.1.3.5.4 Maximum Power Point (MPP) tracking In addition to the SPO tracking, long-term MPP tracking was performed on reference cells under 1 Sun equivalent white LED irradiation in air (25% relative humidity) for several days. The cell was continuously held at 25 °C. Using a Keithley Standard Series 2400 SMU, maximum power output was enforced by applying a small voltage perturbation ($\pm$ 5 mV) to the cell every 5 seconds, and adapting the voltage applied for the next 5 seconds accordingly. Depending on which voltage gave a higher power output, the applied voltage was either increased or decreased by 5 mV and then held at this voltage for the next 5 seconds. The intensity of the white LED was monitored using a silicon photodiode. All data was recorded using a home-built LabView program.

3.1.4 Charge Extraction Measurements

A range of different charge extraction measurements is carried out using a combination of a function generator (Agilent 33220A), home-built amplifier, variable resistance and oscilloscope (Agilent DSO9054H High-Definition Oscilloscope). Figure 3.3 shows a schematic illustration of this setup, and the pulses that are applied to the sample for the different measurements. Where indicated in the text, an alternative, automated setup was used for charge extraction measurements. This setup, although using the

same basic building blocks, employs a different function generator (Siglent SDG 1032X) and oscilloscope (Siglent SDS 1202X-E). A Python-based user interface is used to input the different measurement parameters, after which measurements and data processing are carried out fully automatically. This setup is now being commercialised and distributed under the name 'FastChar'.

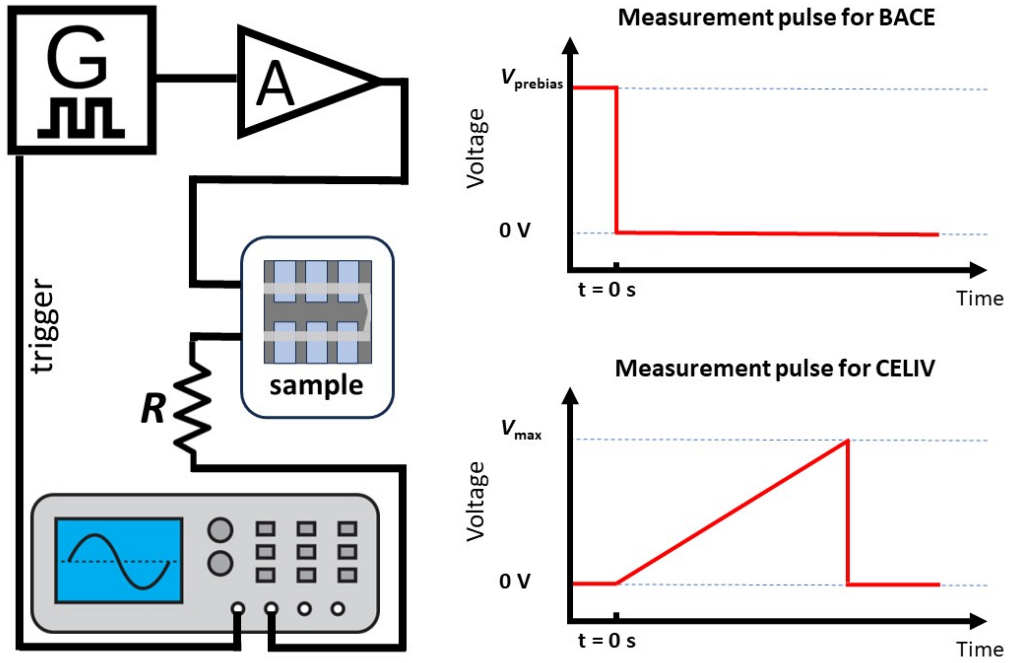

Figure 3.3: A schematic overview of the setup used for the different charge extraction measurements employed in this work. A pulse from a function generator (G) is amplified by a dedicated amplifier (A), after which it is input into the sample. The output signal from the sample is recorded by an oscilloscope.

3.1.4.1 Bias Assisted Charge Extraction (BACE)

For BACE measurements, the sample is kept in dark conditions while a constant pre-bias V_{pre} is applied. At t = 0, the applied bias changes, as a step function, to the collection voltage V_{coll}. A schematic representation of this measurement pulse can be seen in Figure 3.3. When the pre-bias is set to be equal to the built-in voltage, and at t=0 the bias is changed to 0 V, BACE measurements can be used to estimate the

mobile ion density in the device from the integrated displacement current. BACE measurements performed using an oscilloscope often suffer from a small offset in the recorded voltage, which can be problematic when trying to integrate the displacement current to estimate mobile ion densities. Alternatively, BACE can also be measured using a Keithley SMU. This solves the issues with the offset, however, this does come at the cost of lower time resolution.

3.1.4.2 Charge Extraction by Linearly Increasing Voltage (CELIV)

For CELIV measurements, the sample is kept in dark conditions while a pre-bias of 0V is applied. At t = 0, the voltage is ramped up linearly to 400 mV, as is schematically displayed in Figure 3.3. The slope of the voltage ramp is varied to probe different timescales. The current transients were recorded with an oscilloscope (Agilent DSO9104H) and measured with a variable load resistance (50 Ω at short 10 µs pulse and up to 10 kΩ at 100 ms pulses) to keep the voltage response approximately constant. The increased load resistance reduces the time resolution at short times but allows to record the response for long pulses. The continuous increase of the electrode charge leads to a step-like voltage response. The voltage response step of the cell is given by from which we calculated the capacitance of the cell (C). Equilibrium charges in the active layer (doping-induced electronic charge or mobile ions) lead to an additional bump in the voltage response. CELIV measurements can therefore used to estimate the lower bound of the mobile ion density in the device.

3.1.4.3 Rising Photovoltage (RPV)

Rising photovoltage measurements were obtained using an EKSPLA NT242-500 nanosecond laser to apply a short laser pulse to a device, after which the transient photovoltage is recorded across a large (1MΩ) resistance using an Agilent DSO9054H

High-Definition Oscilloscope, oscilloscope. This large resistance is used to create a large RC time, which enables visualisation of the transit time of the carriers through the photovoltaic device. The wavelength of the laser light was adapted for the different samples, and both single junctions as well as subcells in tandem devices could be measured. IR laser light was used to measure the low gap subcell in all perovskite tandems, and green light to measure the high gap subcell in all-perovskite tandems. Single junctions were also measured for comparison - using the same laser wavelength as was used to measure their corresponding subcells. The measurements were repeated for different laser fluences.

3.1.4.4 Transient Photocurrent (TPC)

Transient photoconductivity measurements were carried out using a home-built setup, described in further detail in ref[89]. Using a Nd:YAG laser (Ekspla NT342A), tuned to a wavelength of 470 nm and pumped at 10 Hz with 3.74 ns pulses to illuminate the sample, in between the in-plane electrodes deposited on the perovskite, and a digital oscilloscope to record the change in photoresistance, this method allows to estimate long-range charge carrier mobilities.

3.1.4.5 Photo-Hall measurements

Photo-Hall measurements were carried out using an IBM parallel dipole line (PDL) Hall setup as described in[90]. To this end, 6-terminal perovskite Hall-bars were fabricated, with an active area of 2 mm $\times$ 4 mm. After the deposition of gold contacts, the samples were oxidised in a dry air box for fixed amounts of time, and encapsulated. Finally, measurement pins were glued to the sample, and electronically connected to the gold contacts using silver epoxy. Photo-Hall measurements and analysis were carried out by Oki Gunawan at the Thomas J. Watson Research Center, IBM.

3.1.5 Drift-diffusion simulations

Several types of numerical simulations were used throughout this thesis to support experimental findings, provide explanations for observed effects, or investigate routes towards improved device stability and efficiency. Steady-state drift-diffusion simulations were carried out using SCAPS, an open-source software capable of simulating one-dimensional solar cells. This simulation software was developed at the Department of Electronics and Information Systems (ELIS) of the University of Gent, Belgium.[91] Transient drift-diffusion simulations, as well as some additional steady-state simulations were carried out using Setfos, a commercial simulation software for organic and perovskite solar cells and LEDs. Importantly, Setfos simulations can take into account the effects of mobile ionic charges on the electrical behaviour of solar cells.

The basis of both simulation softwares are the continuity equations,

$$\frac{\partial n(x)}{\partial t} - \frac{1}{q}\frac{\partial J_n(x)}{\partial x} = G(x) - R(x) \tag{3.7}$$

$$\frac{\partial p(x)}{\partial t} - \frac{1}{q}\frac{\partial J_p(x)}{\partial x} = G(x) - R(x) \tag{3.8}$$

where G(x) is the generation rate, R(x) the recombination rate, n and p are electron and hole densities, J_n and J_p are the electron and hole current densities and q the elementary charge. Mobile charged species (so electrons, holes, mobile anions and mobile cations) move through the system through a combination of drift and diffusion, therefore the current densities can be expressed as

$$J_n = q \cdot n(x)\mu_n \frac{\partial \phi}{\partial x} - qD_n \frac{\partial n(x)}{\partial x} \tag{3.9}$$

$$J_p = q \cdot p(x)\mu_p \frac{\partial \phi}{\partial x} + qD_p \frac{\partial p(x)}{\partial x} \tag{3.10}$$

where μ_n and μ_p are the electron and hole mobilities, and D_n and D_p the diffusion constant of electrons and holes, which are related through $D = \mu \cdot \frac{k_B T}{q}$.

Together, these continuity equations describe coupled charge transport species obeying the Poisson equation, which describes the electric potential

$$\frac{\partial^2 \Phi(x)}{\partial x^2} = \frac{q}{\varepsilon_r \varepsilon_0}[n(x) - p(x)] \tag{3.11}$$

where ε_r is the relative dielectric permittivity, and ε_0 the vacuum permittivity.

Taking into account the presence of mobile ions as well as donors and acceptors, this equation turns into

$$\frac{\partial^2 \Phi(x)}{\partial x^2} = \frac{q}{\varepsilon_r \varepsilon_0}[n(x) - p(x) + N_d^+ - N_a^- + n_a(x) - n_c(x)] \tag{3.12}$$

where N_d^+ and N_a^- are the concentration of ionised donors and acceptors, $n_a(x)$ the anion density and $n_c(x)$ the cation density.

When simulations include mobile ions, we note we make two important assumptions. First of all, whenever simulations are carried out in which only type of ionic species is mobile (for example, considering halide vacancies, mobile cations), an equal density of immobile ions with the opposite sign (which, in the case of mobile halide vacancies, would be static anions) is introduced in the bulk of the perovskite to maintain charge neutrality. Second, while it is assumed that all mobile ions are created in the bulk of the perovskite, they can move through the whole device (including both the electron and hole transport layers, unless explicitly stated otherwise). We note that simulations presented throughout this thesis were carried out assuming mobile halide vacancies (positive charges/anion vacancies). Chapter 4 forms an exception, where simulations were carried out assuming anions (negative charges) to be mobile instead.

Both in SCAPS as well as in Setfos, transport is only considered in one dimension. There are different pathways to attempt to solve the set of coupled equations described above, but in both softwares, a Gummel iteration scheme is used.

For the simulations of all-perovskite tandem solar cells in SETFOS, which are described in Chapter 6, the recombination layer which connects the two subcells is simulated as an electronic interface, where charges from both subcells can recombine through hopping. A schematic overview of the energy levels used for these simulations can be found in Figure 3.4

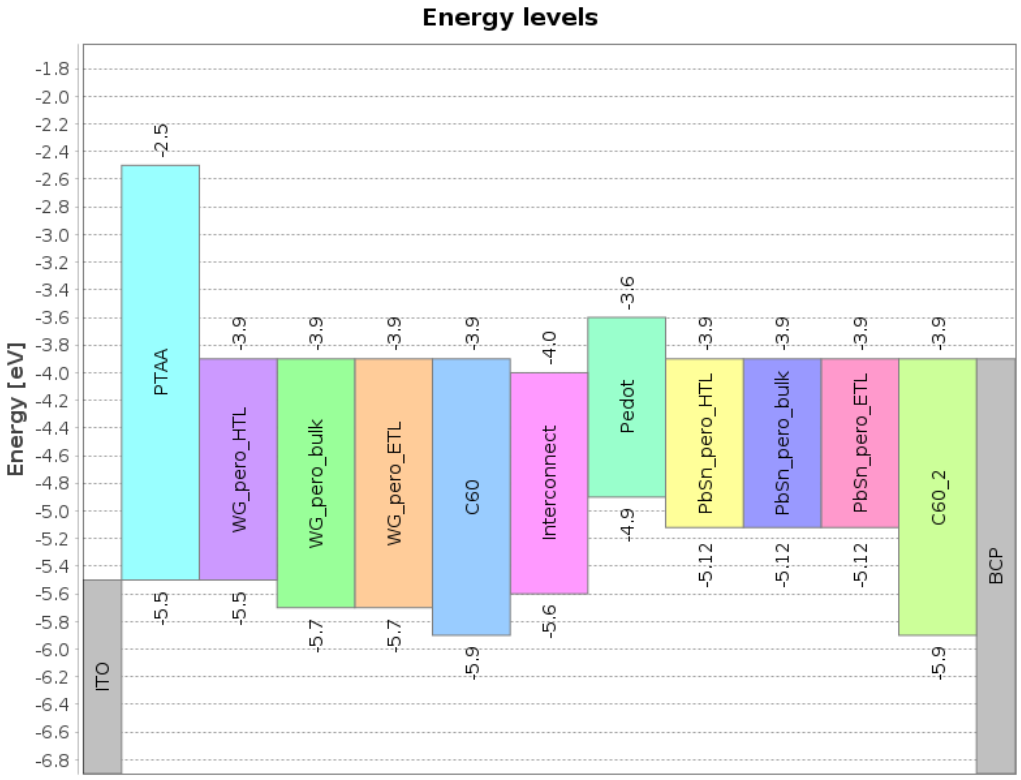

Figure 3.4: A schematic overview of the energy levels used to simulate an all-perovskite tandem solar cell stack as described in Chapter 6.

Absorption simulations, coupled to the drift-diffusion simulations, were also carried out in Setfos, to enable full opto-electronic simulation of solar cells, and allow for stack optimisation. These optical simulations are based on the transfer matrix method, where each of the different layers and interfaces in the stack is assigned a transfer

matrix, which describes how electromagnetic waves propagate in this layer or at this interface. Using continuity equations, the transmission and reflection at each interface can be determined. This allows for the simulation of complicated stacks with multiple interfaces using a system matrix, which is the product of the individual layer matrices. For more details regarding the use of the transfer matrix method for the optical simulation of perovskite solar cells, we refer the reader to[92].

Input parameters for the simulations are, wherever possible, based either on measured- or literature values. In case no values were available, experimentally obtained, steady-state JV curves were used to determine the missing input parameters through fitting. Table A.1 in Appendix A.2 lists the input parameters used to simulate the lead-tin perovskites from Chapter 4 in Setfos, with Table A.2 in Appendix A.2 listing input parameters used to simulate the triple cation perovskites from Chapter 5.

CHAPTER 4

Universal current losses in perovskite solar cells due to mobile ions

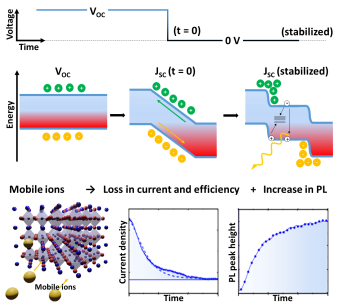

The work presented in this chapter is based on:

J.Thiesbrummel, V. M. Le Corre, F. Peña-Camargo, L. Perdigón-Toro, F. Lang, F. Yang, M. Grischek, E. Gutierrez-Partida, J. Warby, M. D. Farrar, S. Mahesh, P. Caprioglio, S. Albrecht, D. Neher, H. J. Snaith, M. Stolterfoht, "Universal current losses in perovskite solar cells", Advanced Energy Materials, 2021, 11, 2101447. https://doi.org/10.1002/aenm.202101447

4.1 Introduction

Perovskite solar cells have undergone major development from their first discovery in 2009, to a viable technology that is approaching commercialisation.[46] One of their most interesting assets is the wide range of bandgaps which can be fabricated by changing the perovskite composition, opening up the possibility to produce all-perovskite multijunction cells that can overcome the Shockley-Queisser (SQ) limit of single junctions. For a tandem cell, the ideal bandgaps for the top and bottom cell are 1.7-1.9 and 0.9-1.2 eV, respectively.[93] Fully lead-based perovskites are widely investigated and have reached power conversion efficiencies (PCEs) of up to 25.5%.[94] In order to achieve ideal bandgaps for the low-gap cell in all-perovskite tandem photovoltaics, a mixture of lead and tin atoms at the B-site of the ABX_3 perovskite structure is required. This allows metal halide perovskites to reach bandgaps as low as 1.2 eV.[95,96]

While many studies in the literature focus their efforts on improving the open circuit voltage (V_{OC}) and fill factor (FF) of perovskite solar cells (PSCs), there are fewer reports that investigate the loss in short-circuit current density (J_{SC}). In fact, high-performing perovskites have been shown to have "only" moderate (≈5-15%) J_{SC} losses compared to the SQ limit, making them competitive in this regard with established technologies such as c-Si and GaAs, as shown in Figure 4.1a. In many cases, this loss is quickly overlooked and treated as a result of suboptimal light management in the cell which could be solved by optimising the thickness of the solar cell stack or by using more complex light management strategies such as, for example, textured substrates,[97,98] cavities & plasmon resonances,[99] or carefully designed anti-reflective layers.[100,101] However, as we will show, suboptimal light management is not the only cause of J_{SC} losses in perovskite solar cells, even in well performing mixed-cation mixed-halide perovskite cells. Tin-based and mixed PbSn perovskite solar cells are particularly affected by short-circuit current losses and their efficiencies lag behind those of their full-lead equivalents, despite having a bandgap closer to the ideal for

single junctions, with the best mixed lead/tin cells only reaching certified PCEs of a bit over 20%.[79,80,96,102]

Considering reported bandgaps of 1.22 eV for a 50:50 Pb:Sn mixture, this would allow a maximum short-circuit current density of ≈37.1 mA cm^{-2} if we assume that an average external quantum efficiency of 95% can be achieved as demonstrated in the best Pb-perovskite cells.[103,104] However, even the best $APbSnI_3$ perovskites achieve significantly lower currents, for example, 32 mA cm^{-2} have been demonstrated for a bandgap of 1.22 eV in ref.[79]. In most other reports, PbSn perovskites with similar bandgaps delivered even lower short circuit current (30 mA cm^{-2}).[105–107] This discrepancy between two apparently similar technologies is not often discussed and it is currently not clear why Sn(II) containing perovskites cannot achieve as high currents as their lead counterparts relative to their SQ limits.

Generally, it is well known that Sn(II)-containing metal halide perovskites are more prone to oxidation to Sn(IV) than their Pb(II) counterparts, due to the inert pair effect stabilising the 6s electrons in Pb(II). This propensity to oxidise has led researchers to conclude that this is likely the origin of performance losses in PbSn perovskites. In turn, significant efforts have been undertaken to prevent this oxidation, or reduce its negative effects, such as the addition of metallic Sn to the solution to reduce Sn^{4+} through comproportionation,[79] addition of antioxidants and reducing agents,[80,108,109] or addition of excess Sn^{2+} by using salts such as SnF_2, which also acts as a reducing agent.[110] Recently, it was also proposed to move away from using dimethylsulfoxide (DMSO) as a co-solvent, as this could oxidise Sn^{2+} to Sn^{4+} in solution.[76] However, the exact effect of the increased concentration of "oxidation-induced" mobile charges in the system has only been investigated by a few researchers.[111–113]

On the one hand, there has been substantial evidence of a large increase in the dark conductivity of Sn-based perovskites upon exposure to oxygen, which is most likely due to electronic doping. For example, in ref.[114,115], a background hole carrier concentration of 10^{15} to 10^{16} cm^{-3} has been reported. This led to the conclusion that it is largely the p-doping that is responsible for the significant current losses.[102,116]

For example, a high concentration of doping-induced carriers could reduce the lifetime and diffusion length of photoinduced charge or screen the built-in field, which would in turn reduce the charge extraction efficiency, thereby causing short-circuit current losses.[114,117,118] Although it is expected that high levels of doping can undermine the device performance, the exact underlying mechanisms have not been studied thoroughly experimentally, and the concentration of charge carriers required to induce detrimental effects is not precisely known. Moreover, the charge collection losses at short-circuit conditions in Sn-based perovskites can be caused by an insufficient charge carrier diffusion length due to electronic defects, which would also negatively affect the open-circuit voltage.

On the other hand, the performance losses could be caused by mobile ions, which may cause screening (or more precisely, a redistribution) of the internal field. Several groups have attempted to quantify mobile ion concentrations in different perovskites, and their outcomes are generally in the range of 10^{15} to 10^{19}cm^{-3}.[119–122] Indeed, the presence of mobile ions is expected in PbSn perovskite thin films. For example, Leijtens et al.[75] recently investigated the mechanism of oxidation of Sn and PbSn perovskites through X-ray diffraction (XRD), thermogravimetric analysis (TGA), and UV-vis, and demonstrated that mobile ions such as FA+ or I- are likely formed. However, the effect of mobile ions on the short-circuit current losses in perovskites has, in general, not been investigated as intensively as, for example, their effect on the V_{OC},[123] the hysteresis,[64,124,125] and device stability.[61,126,127] In order to further improve PbSn and Pb-based perovskite solar cells and other electronic devices,[128,129] it is vital to gain a more detailed understanding of the mechanism causing short-circuit current losses and the exact effects of electronic doping and mobile ions on the device operation.

In this work, we investigated short-circuit current losses in low bandgap, mixed PbSn ($FA_{0.83}Cs_{0.17}Pb_{0.5}Sn_{0.5}I_3$) and other lead-based perovskite cells. In particular, we first aimed to understand whether the charge transport losses under short-circuit conditions in mixed metal PbSn perovskites ($FA_{0.83}Cs_{0.17}Pb_{0.5}Sn_{0.5}I_3$) are a result of electronic doping or mobile ions, before generalising the results to other Pb-based

systems. To this end, we recorded the temporal evolution of the current transient and determined a concurrent rise in the photoluminescence (PL) emission intensity after switching the voltage from V_{OC} to short-circuit, which implies an accumulation of electronic charge in the perovskite bulk. We hence attribute the reduced current density to a reduced charge extraction efficiency. The decay in current directly translates into a loss of the steady-state maximum power point output of the device on the same timescales and to a current loss at slow scan speeds. To distinguish whether background doping or mobile ions are responsible for this loss, we performed bias assisted charge extraction (BACE) and charge extraction by linearly increasing voltage (CELIV) measurements, which allowed us to investigate the density and dynamics of extracted electronic and ionic charges. Overall, these measurements underline the extraction of electronic (bias-induced injected) charges on the µs-timescales, while the characteristic features of mobile ions appear on the ms-s timescales, as observed in the current decay transients. Importantly, the ionic charge density ($>1 \times 10^{17}$ cm^{-3}) was found to exceed the injected and photogenerated electronic charge density (5 $\times 10^{15}$ cm^{-3}) present at V_{OC} by several orders of magnitudes, therefore dominating the observed recombination losses in the transient current decay. Moreover, the density of doping induced equilibrium charges ($\approx 6 \times 10^{14}$ cm^{-3}) was found to be negligible compared to the capacitive charge density (6 $\times 10^{15}$ cm^{-3}), hence the density of doping-induced charge, in contrast with the mobile ion density, is insufficient to screen or redistribute the built-in potential. Furthermore, we could reproduce both the transient and steady-state performance of the device using numerical simulations, which further corroborated the understanding obtained from the experimental results. Finally, we demonstrated that PbSn based perovskites are not unique with respect to ion-induced current losses, but the same losses appear in various other perovskite compositions and architectures. Overall, the mobile ion induced losses limit the power conversion efficiency of our devices by 1-3% absolute. As such, this work underlines the importance of"ion management" to overcome band flattening and minimise the recombination losses under maximum power point losses and improve device stability

Neat-lead-based perovskite solar cells investigated in this work were fabricated by Francisco Peña-Camargo, Emilio Gutierrez-Partida and Max Grischek.

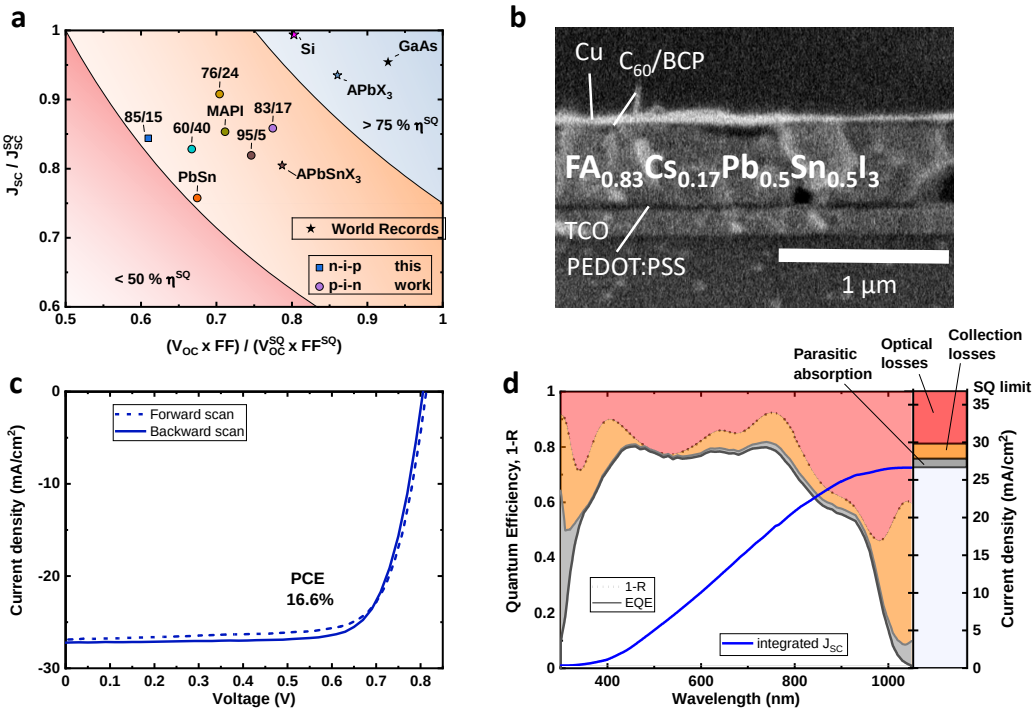

Figure 4.1: a) Comparison of short-circuit current losses in world-record Si, GaAs, Pb-, and PbSn-based perovskites (stars) taken from ref.[79,130,131], as compared to the perovskite cells studied in this work (filled circles). The graph was inspired by ref.[132]. Generally, PbSn-perovskites have larger current losses compared to Pb-perovskites, including $MAPbI_3$ and several triple cation $Cs_{0.05}(FA_xMA_y)_{0.95}Pb(I_xBr_y)_3$ devices made from different (x:y) ratios of $FAPbI_3$ and $MAPbBr_3$. b) A cross-sectional scanning electron microscopy image of a typical $FA_{0.83}Cs_{0.17}Pb_{0.5}Sn_{0.5}I_3$ perovskite pin-type solar cell device. c) Forward and reverse JV scan at a scan rate of 60 mV s^{-1} under AM1.5G illumination. d) Device absorption (1 - reflectance) and external quantum efficiency spectra of a $FA_{0.83}Cs_{0.17}Pb_{0.5}Sn_{0.5}I_3$ perovskite pin-type solar cell, with a graphical representation of the different current losses that occur in the system. It can be seen that, besides parasitic absorption and optical losses that stem from the sample being too thin to absorb all the light, there are also significant charge collection losses

4.2 Results

Here we studied low bandgap $FA_{0.83}Cs_{0.17}Pb_{0.5}Sn_{0.5}I_3$ perovskite photovoltaic devices. The device stack is comprised of spin-coated poly(3,4-ethylenedioxythiophene) polystyrene sulfonate (PEDOT:PSS) hole transporting layer (HTL) on a glass substrate coated with an indium-doped tin oxide (ITO) conductive layer. On top of that, the perovskite layer with a thickness of 470 nm is deposited via spin-coating. The stack is

completed by an electron transporting layer (ETL) comprised of evaporated C60 (30 nm) and bathocuproine (BCP) (8 nm), with a copper (Cu) electrode on top. A detailed description of the device preparation can be found in Chapter 3. A cross-section of a complete device is displayed in Figure 4.1b. A JV scan of a characteristic efficient device can be seen in Figure 4.1c, while more detailed characteristics and statistics can be found in Figure 4.2. From the device absorption and the external quantum

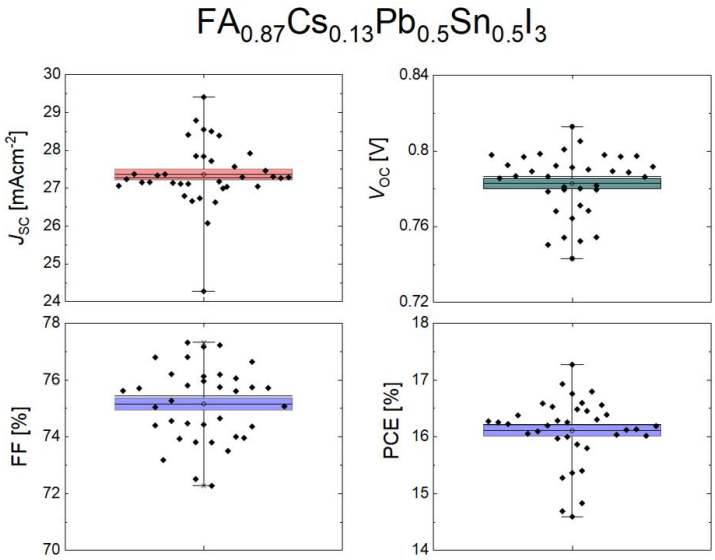

Figure 4.2: JV parameter and cell statistics for the studied PbSn-perovskites.

efficiency (EQE), displayed in Figure 4.1d, the different current losses in the device can be determined. First of all, the optical losses of the device, as determined from the total reflectance R of the device, are significant. This is caused by the relatively low absorption coefficient of the lead-tin perovskite near the band edge (Figure 4.3) and the absorber layer being too thin to absorb all the incident photons with energies above the bandgap. On top of that, the lead-tin perovskite devices suffer from significant additional collection losses ($\approx$2 mAcm^{-2}), which can be determined from the difference between the device absorption minus parasitic losses in the ITO, PEDOT:PSS and copper (i.e., 1-R-$A_{parasitic}$), and the device EQE. The parasitic losses were estimated using a transfer matrix code developed by McGehee, et al.[133]. Although the optical losses can be largely reduced in thicker $\approx$800 nm devices (Figure 4.4), the J_{SC} cannot

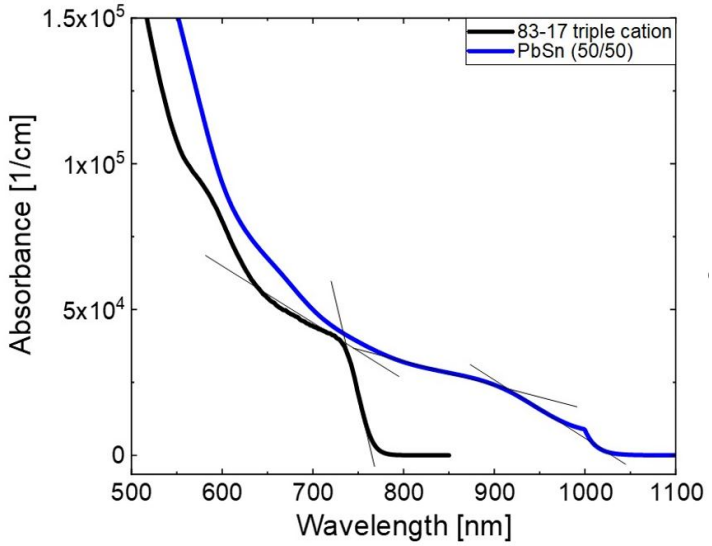

Figure 4.3: Absorption coefficient in PbSn and a Pb-based perovskite, e.g. 83-17 triple cation. PbSn data provided by Suhas Mahesh

be improved due to enhanced collection losses. Therefore, it can be concluded that the combination of relatively large optical losses in 470 nm thick devices and the large collection losses in our thicker devices (e.g., ≈800 nm), possibly due to traps resulting in an insufficient carrier diffusion length, are among the main reasons for the relatively low J_{SC} of the PbSn-perovskite as compared to Pb-based perovskites, with respect to what is expected from their different bandgaps. In the following, however, we focus on understanding the observed charge collection losses at 0 V in the optimum 470 nm-thick devices, which are poorly understood and also significantly contributing to the J_{SC} loss.

To investigate these collection losses at 0 V, we first measured the time dependence of the photoluminescence quantum yield (PLQY) and the short-circuit current density (J_{SC}) immediately after switching from V_{OC} to 0 V, while the sample remains under continuous illumination. As can be seen in Figure 4.5a, the J_{SC} falls during the initial few seconds of operation at 0 V before eventually reaching a steady state. On average, we find that freshly prepared $FA_{0.83}Cs_{0.17}Pb_{0.5}Sn_{0.5}I_3$ devices experience current density losses of 1.4 mA cm^{-2}. This equals about 5% of the initial current density. To reveal the reason for the loss in current, we simultaneously measured the emitted PL from

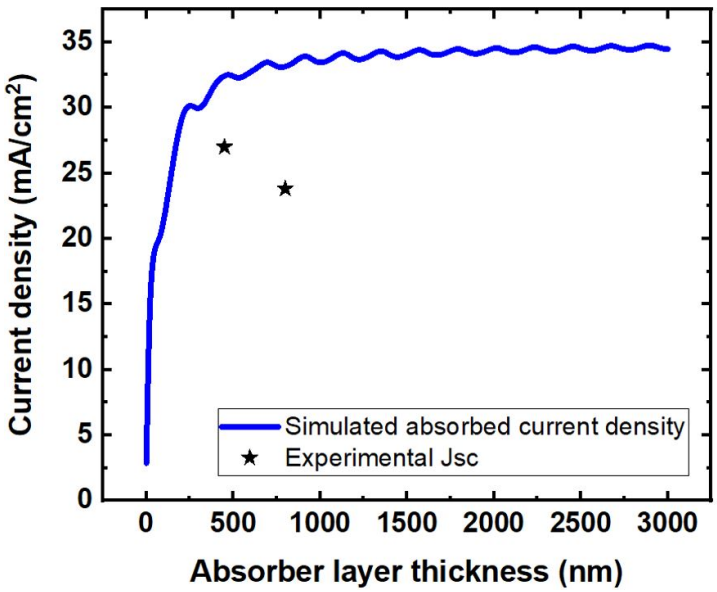

Figure 4.4: The absorbed current density as a function of perovskite layer thickness, as determined from transfer matrix simulations, taking into account parasitic absorption and reflection losses. The graph highlights that the optical losses can be minimised upon increasing the perovskite thickness. The symbols show the obtained J_{SC} from the JV-characteristic for cells with different thicknesses. While the collection losses are a more important problem in the devices with thicker active layers, in the main text we focus on the comparatively thin devices, with which we were able to achieve a higher efficiency.

the cell as a function of time. The temporal evolution of the PL spectra is displayed in Figure 4.5b, while the corresponding peak height is displayed in Figure 4.5c. It can be seen that, when the device bias is changed to 0 V at t = 0 s, the PL is initially nearly completely quenched. Considering that the PL yield is directly proportional to the product of the electron and hole density (n × p), the strong reduction of the PL at 0 V with respect to V_{OC} indicates an efficient initial extraction of electronic charges.[134] However, after the initial quench, the PLQY starts to quickly rise again despite the fact that the device is still kept under short-circuit conditions. This indicates that the efficiency of the charge extraction is gradually reduced, causing charges to accumulate in the device until the PL and the charge carrier distribution stabilise after about 3 s. Therefore, the loss of current is not consistent with a deteriorating interface quality or defects. At the time of stabilisation, the PL has increased to up to ≈6% of the PLQY value at open circuit conditions. Importantly, the decrease in current density and increased PL yield leads also to a direct loss in efficiency, that is, in the initial phase

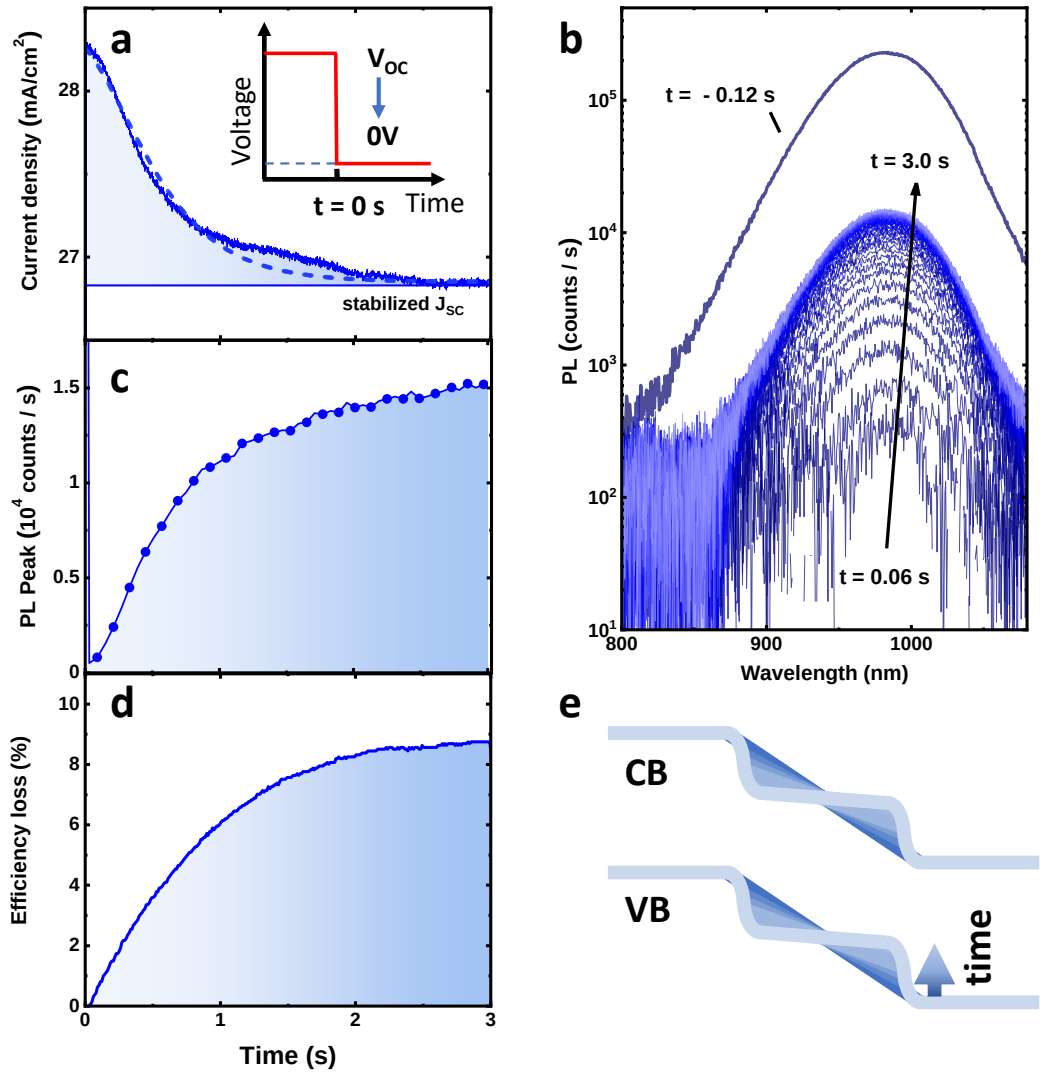

Figure 4.5: a) The measured (blue line) and simulated (dashed blue line) current decay of a $FA_{0.83}Cs_{0.17}Pb_{0.5}Sn_{0.5}I_3$ perovskite pin-type solar cell device after switching from open-circuit (OC) to short-circuit (SC) at t = 0 s as shown in the inset. b) The photoluminescence (PL) trace over the same time, taken while switching from OC to SC. c) The maximum height of the PL peak as a function of time, where t = 0 is the moment where the bias of the device was switched from OC to SC. It can be seen that the PL is initially almost completely quenched, due to efficient charge extraction. However, it quickly comes back up again, indicating that the charge extraction is becoming less efficient and that photogenerated charges accumulate in the perovskite layer. d) The corresponding temporal evolution of the relative device efficiency loss under maximum power point tracking under AM1.5G illumination. e) A schematic representation of the band flattening that is presumably causing the decay in current upon switching to SC conditions. A more elaborate overview of the change in band structures can be found in Figure 4.6. Comparing panels (a), (c), and (d) highlights that the decay of the current and the MPP happens on the same timescales as the PL increases

of maximum power point (MPP) tracking measurements, as displayed in Figure 4.5d.

This has important implications as it indicates that the observed effect also influences

cell performance under steady-state working conditions. Figure 4.5e displays the field screening due to the accumulation of mobile ions at the interfaces over time, which is expected to cause the observed J_{SC} and MPP losses and the increase of the PL on the same timescales. The simplified time dependent band structures displayed in Figure 4.5e are extracted from our numerical device simulations (details about the simulations are discussed further below). The corresponding time-dependent simulated band structures are presented in Figure 4.6, which also includes a more detailed description of the movement of mobile ions in the performed experiments. Interestingly, as shown

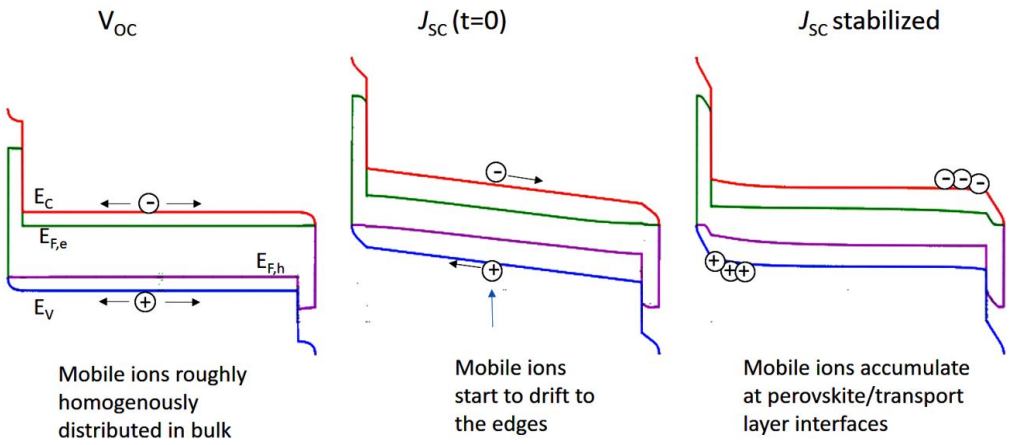

Figure 4.6: Simulated band structures at V_{OC} conditions (left), at J_{SC} conditions right upon the switch to 0 V (middle), and at J_{SC} conditions after stabilising (right). After the rapid switch to 0 V , the mobile ions drift to the edges of the active layer or to the perovskite/transport layer interfaces. After some time, a new equilibrium condition is established after the mobile ions accumulated at the interfaces. As shown in the right panel, this causes a screening/redistribution of the internal field (or band flatting) in the perovskite bulk, which is initially present directly after the switch to 0 V and visible from the gradient of the valence (E_V) and conduction band (E_C) in the middle panel. Note, the screening of the internal field causes an accumulation of electronic charge in the bulk (not shown), which causes the observed increase in the PL and transient current decay. In the left panel, $E_{F,e}$ and $E_{F,h}$ denotes the quasi-Fermi level for electrons and holes.

in Figure 4.7, we find that there is an approximately linear relationship between the current decay and the increase in PL at 0 V. To explain this, we consider that the PL yield is proportional to the radiative recombination current ($J_{rad} = e\varphi PL$), while the current decay is mostly governed by non-radiative recombination (as the overall PLQY yield of the sample is only 10^{-4}). Therefore, a linear relationship between the current decay and the PL increase implies that the radiative and non-radiative

recombination losses are directly proportional to each other. In other words, the field screening-induced accumulation of electronic charges in the active layer increases the radiative and non-radiative recombination losses in the same way, which is consistent with the findings of our previous study.[134]

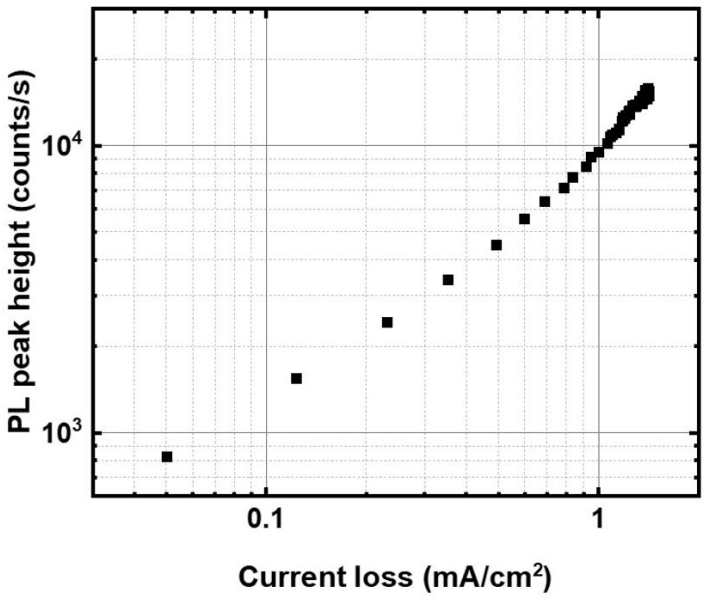

Figure 4.7: The PL peak height versus the observed current loss directly after the switch from open-circuit (OC) to short-circuit (SC), i.e. time = 0. The graph highlights an approximately linear relationship between the emitted PL and the total current loss, which shows that the radiative and non-radiative recombination losses increase proportionally, as the internal field is screened by the mobile ions.

It is important to note that the current losses can occur even if the charge carrier diffusion length in the perovskite exceeds the film thickness. This is because the transport layers can limit the extraction from the device and also interfacial recombination can increase if more charges accumulate in the active layer. To describe the current decay more quantitatively, we performed numerical drift-diffusion simulations of the cell, using the commercially available Setfos 5.1 software package provided by FLUXiM. The input parameters for the simulations shown in Table A.1, were partially based on our previous simulation work of pin-type triple cation perovskites,[135,136] and parameters tailored for lead-tin using the literature specified in Table A.1, and our own extraction measurements, as discussed further below. The fit from the numerical simulations is shown in Figure 4.1a by the dashed line, which

highlights that both the kinetics of the decay can be reproduced with the experimentally obtained effective ion diffusion coefficient (≈10^{-10} cm^2 s^{-1}) and density (≈10^{17} cm^{-3}) as well as the overall magnitude of the current losses. Figure 4.8, demonstrates the simulated current decay for other mobile ion densities.

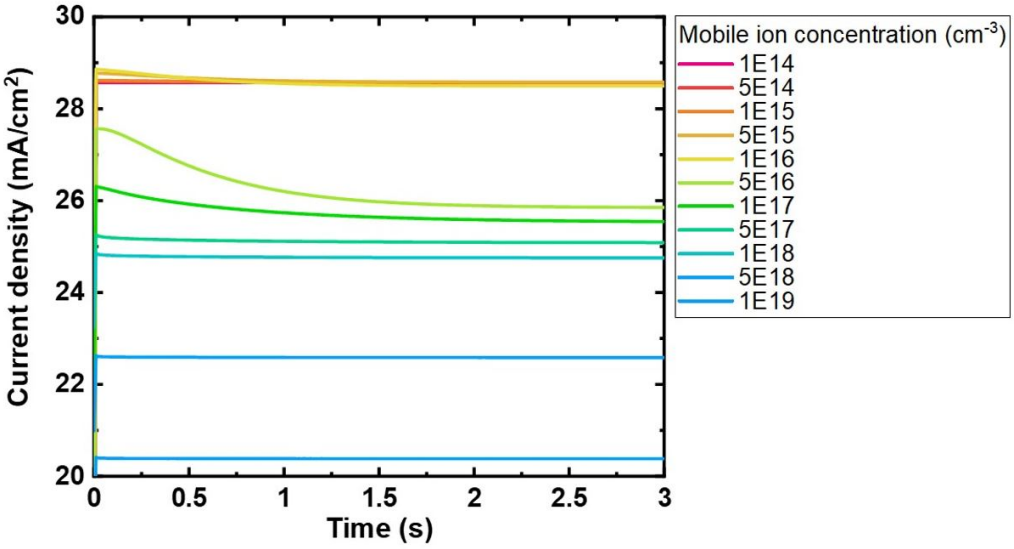

Figure 4.8: The simulated current decay upon switching from open-circuit to short-circuit as a function of mobile ion density. Simulations were performed using the software Setfos and the parameters in Table A.1 for different mobile ion densities. As highlighted in the main text, the best fit of the current decay is found for a mobile ion density of 3.2×10^{16} cm^{-3}, which matches roughly the charge density obtained in the charge extraction measurements (Figure 4.12).

In the following, we demonstrate that the time dependent losses of the short-circuit current are also present in JV hysteresis measurements at slow scan speeds. To clearly visualise this important fact, we performed "fast hysteresis" measurements, where the JV is measured in forward and reverse direction over several orders of magnitude in scan speed (100 mV s^{-1} to 800 V s^{-1}) after keeping the cell under open-circuit conditions and constant AM1.5G illumination. The details of this measurement are presented in Chapter 3 and in[137]. Figure 4.9 plots the short-circuit current density obtained as a function of scan speed. At the fastest scan speeds (here, 1 ms per scan, or 800 V s^{-1}), the mobile ions do not have enough time to react to the change in the external voltage, hence an "ion-free current density" is obtained if the ions are roughly homogeneously distributed at the starting voltage (V_{OC}). However, at slower scan

speeds (e.g., 1 s per scan), the mobile ions are able to follow the change in internal field by moving from their equilibrium positions toward the transport layers, where they start to screen the field causing the losses in the J_{SC}. Indeed, at the slowest scan speeds (10^{-1} V s^{-1}), a decrease in J_{SC} of about 1.5 mA cm^{-2} is observed with respect to the fast scan (800 V s^{-1}). As such, both the timescale (1 ms to 10 s) and the magnitude of the current decay (1.5 mA cm^{-2}) in the hysteresis measurements is consistent with the temporal current decay shown previously in Figure 4.5a.

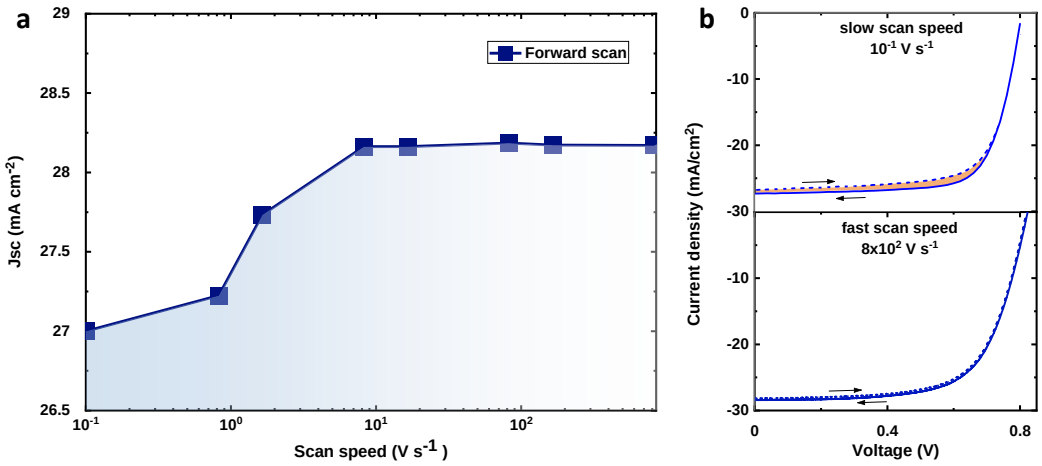

Figure 4.9: a) The current density as obtained from JV scans in forward and reverse direction as a function of scan speed (100 mV s^{-1} to 800 V s^{-1}). b) exemplifies the JV scans in forward and reverse directions at the slowest (top) and fastest scan speed (bottom). At fast enough scan speeds (scan time « ion transit time), the mobile ions in the perovskite layer are not able to react to the change in the applied voltage, and hence the obtained efficiency can be regarded as a proxy of the ion-free efficiency. At slow scan speeds, however, mobile ions are able to screen the built-in field. This lowers the device efficiency, primarily through increased short-circuit current losses in the case of the studied cells. Panel (a) shows lower current density for JV scans taken at slower scan speeds, as opposed to the "mobile-ion free" JV scans taken at the fastest scan speeds. Hence, the current losses also appear in the JV measurements at slow scan speeds that are representative for steady-state conditions, as shown in Figure 4.5

In order to distinguish between different processes that could cause the observed current losses and the suspected band flattening, and to elucidate the density and kinetics of free electronic and ionic charge, we performed different charge extraction measurements. Figure 4.12a shows the extracted charge as a function of time from bias assisted charge extraction (BACE), where the (displacement) current is recorded upon a switch from V_{OC} to 0 V. The charge inside the active layer is thereby obtained

by integrating the displacement current over time. It is important to note that mobile ions are not extracted from the device but rather transported to the transport layers or electrodes, which, however, causes an external displacement current. As can be seen in Figure 4.12a, the obtained temporal evolution of the charge density displays two features; an initial rise at ≈1 µs and a second rise at ≈300 ms. The initial rise consists itself of two contributions, the extraction of electronic charges that were injected by applying a voltage equal to V_{OC} while the device was kept in the dark, and the RC decay due to the electrode (capacitive) charge (CU, where U is the V_{OC}). As shown

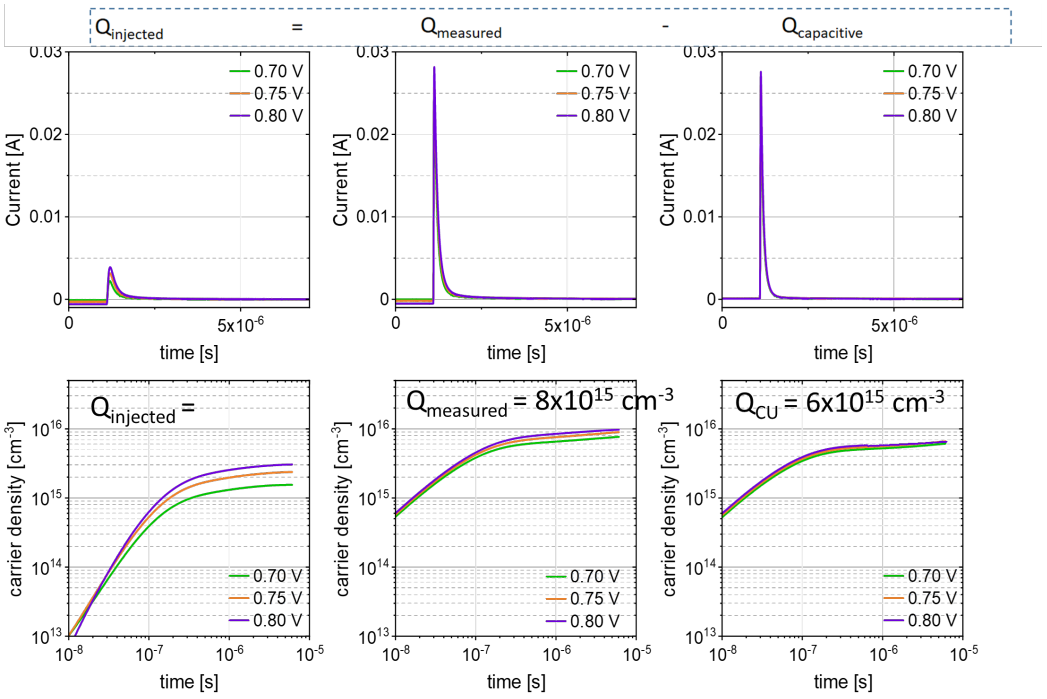

Figure 4.10: The current transients and obtained charge carrier density from bias-assisted charge collection measurements in the dark, upon a switch from different pre-biases around the V_{OC} to 0 V. The contribution of the capacitative charge to the total extracted charge can be obtained by doing a reference measurement from 0 V to minus V_{OC}. Subtracting the capacitive charge carrier density from the measured charge carrier density yields this the injected charge carrier density at the different pre-biases as indicated on the top. Measurement and analysis by Lorena Perdigón Toro

in Figure 4.10, using a separate setup with a home-built amplifier with a relatively low resistance (≈ 5 Ω), we can distinguish the contribution of these two initial processes to the first bump. As shown in Table 4.1, we obtain an injected charge carrier density of 2×10^{15} cm^{-3}, while the electrode charge divided by the perovskite volume equals

6×10^{15} cm^{-3} at 0 V (if the V_{OC} is equal to the built-in field). Furthermore, upon applying a constant background illumination with a 1-sun equivalent intensity, the same measurement allows us to quantify the photogenerated charge carrier density that is present at V_{OC}, Figure 4.11. The details of these measurements are discussed more elaborately in the captions of the corresponding figures.

Table 4.1: Charge concentrations (cm^{-3})

Charge	Charge Concentration
Dark injected charge @ V_{OC}	2×10^{15}
Electrode charge @ 0V	6×10^{15}
Photogenerated charge @ 0V, 1 sun	3×10^{15}
Doping density	6×10^{14}
Mobile ionic charge	2×10^{17}

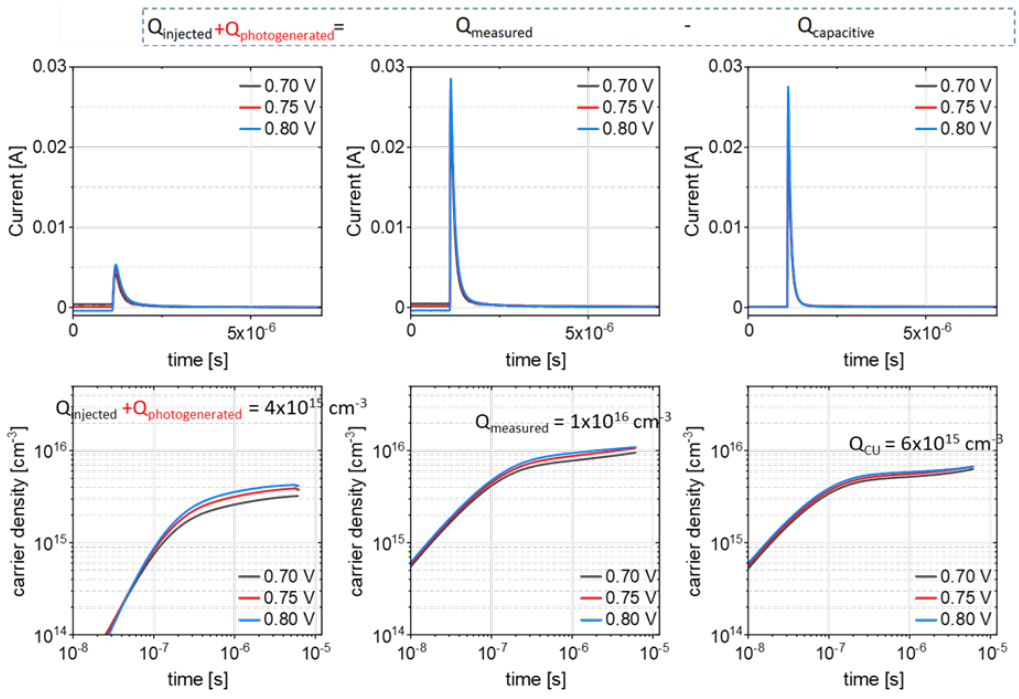

Figure 4.11: The current transients and obtained charge carrier density from bias-assisted charge collection measurements under a 1 sun equivalent illumination at a wavelength of 638 nm, upon a switch from different prebiases around the V_{OC} to 0 V. The capacitative contribution to the extracted charge can be obtained by doing a reference measurement from 0 V to minus V_{OC} in the dark. Subtracting the capacitive charge carrier density from the total measured charge carrier density thus yields the injected + photogenerated charge carrier density at the different pre-biases as indicated on the top. Measurement and analysis by Lorena Perdigón Toro.

Coming back to Figure 4.12a, the second increase in the extracted (or transported)

charge is assigned to the mobile ion density in the system with a characteristic effective displacement time of 300 ms. This corresponds to the timescale observed in the current decay and PL increase. Note, this corresponds to an effective ion mobility of 4 $\times 10^{-9}$ cm^2 V^{-1} s^{-1} and a diffusion coefficient of $\approx$1 $\times 10^{-10}$ cm^2 s^{-1}. Importantly, the obtained mobile ion density in the system is $\approx$2 $\times 10^{17}$ cm^{-3}, which is significantly larger than the electronic charge in the system, including the electrode charge (per volume) that creates the built-in potential. Hence, a significant redistribution of the built-in field is expected due to the obtained mobile ion density (as already shown above in Figure 4.5e). We note again, that the obtained ion diffusion coefficient and density was used as input parameters for the numerical simulations, which allowed us to fit the current decay shown in Figure 4.5a.

In order to further corroborate the BACE measurements, we performed charge extraction by linearly increasing voltage (dark-CELIV) measurements, which are shown in Figure 4.12b. In this measurement, the linearly increasing voltage leads to a constant charging current of the electrodes. For a dielectric capacitor in the absence of mobile charges in the active layer, the response to the CELIV voltage pulse is a step function.[138] Any additional charge present, for example, doping induced equilibrium charges or mobile ions (or photogenerated charges with background light), will cause a "bump" in the transient response, which allows us to estimate their density with respect to the electrode charge (CV_{max}, where V_{max} = -0.4 V is the maximum applied voltage of the triangular pulse in this case). Hence, the absence of an initial bump in the dark CELIV response, shown in Figure 4.12b, indicates that the doping density is insignificant with respect to CV_{max} per cell volume ($\ll$ 5 $\times 10^{15}$ cm^{-3}). To further highlight this important point, we performed a photo-CELIV measurement, where we intentionally photogenerated a charge carrier density of e.g. 1 $\times 10^{15}$ cm^{-3} in the perovskite cell. As shown in Figure 4.12c, this photogenerated charge carrier density can nicely be seen in the current response and is roughly in the correct ratio compared to the CV_{max} charge. Moreover, the extraction of the photogenerated charge carrier density happens on the order of 1 µs, which further confirms the timescale of

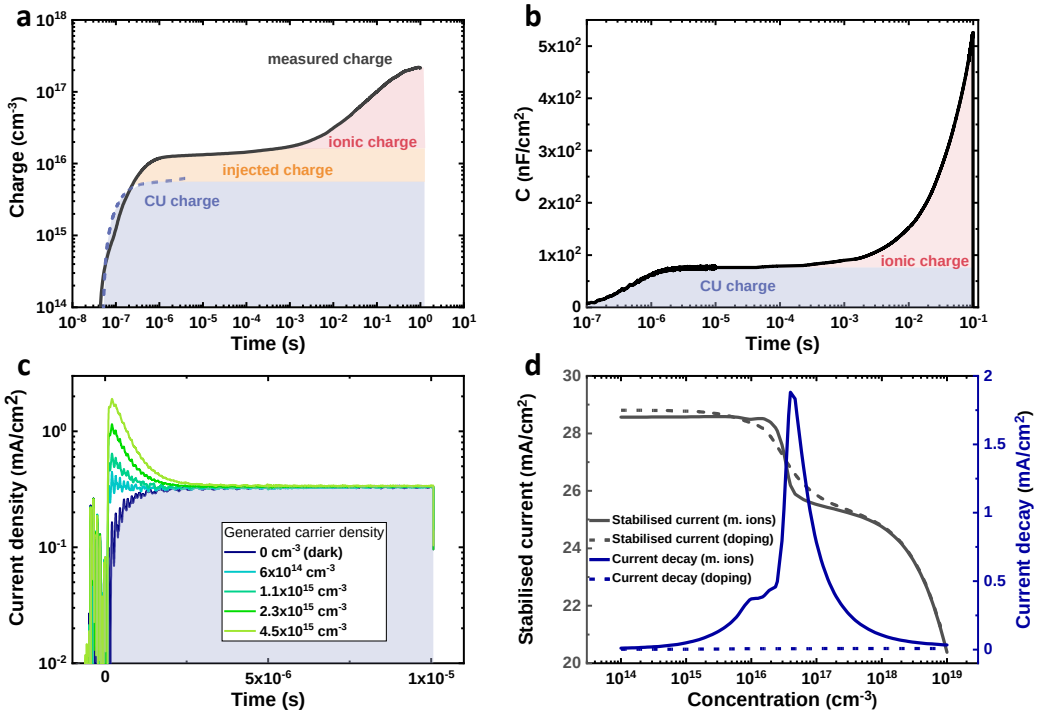

Figure 4.12: a) Bias assisted charge extraction (BACE) measurement (solid line) upon a switch from open-circuit to short-circuit, including the associated change in the electrode charge (i.e., the capacitance-voltage product 6 $\times$ 10^{15} cm^{-3}) and the injected charge at open-circuit conditions (2 $\times$ 10^{15} cm^{-3}). The extraction of both electronic charge and ionic charge occurs at very different timescales, where the extraction of mobile ions coincides with the current decay observed in Figure 1. b) Current extraction by linearly increasing voltage (CELIV) measurements confirm the results from the BACE measurements, showing that electronic charge extraction occurs much faster than ionic charge, and that the latter occurs on timescales of ms. c) Photo-CELIV transients after a laser excitation with given photocarrier concentrations. The graph demonstrates that a (photogenerated) carrier density of about 1 $\times$ 10^{15} cm^{-3} would create an initial bump in the transient response. Considering that the bump is absent in the dark measurement confirms that the doping-induced equilibrium carrier density is significantly lower than this threshold which is consistent with lateral conductivity measurements. d) Simulated stabilised current and current decay as a function of the mobile ion concentration (solid lines) and the doping concentration (dashed lines), respectively

electronic charge transport. We note the relatively long extraction time is likely limited by the transport layers rather than bulk transport through the perovskite layer, as has been previously shown.[139] To quantify the doping density in the PbSn perovskite, we performed lateral conductivity measurements which revealed a dark conductivity of 9 $\times$ 10^{-5} S cm^{-1} (Figure 4.13). Assuming a long-range charge carrier mobility of roughly 1 cm^2 V^{-1} s^{-1} (which is lower than the short-range charge carrier mobility as obtained from optical-pump terahertz-probe spectroscopy measurements in ref.[106], since we consider grain boundaries), this would correspond to a doping-induced charge carrier

density of ≈6 × 10^{14} cm^{-3}, which is consistent with the absence of a doping-induced feature in the CELIV response.

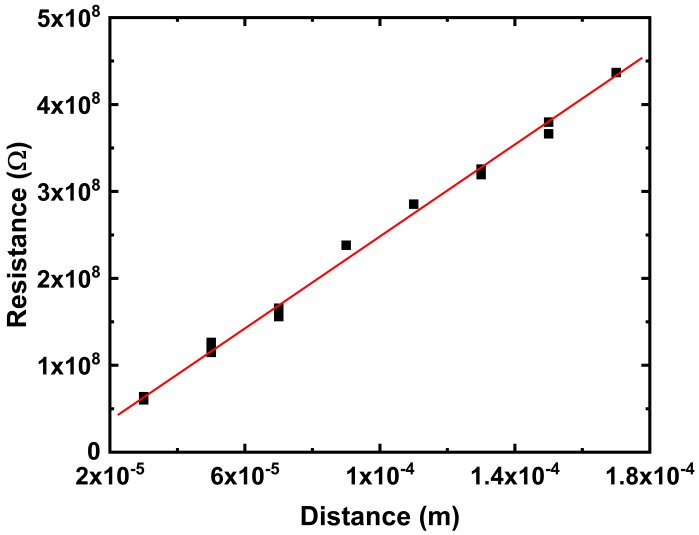

Figure 4.13: The conductivity in 50/50 mixed-metal lead-tin perovskite, which can be used to estimate doping levels. The conductivity was found to be 9x10^{-5} S/m, which, assuming a mobility of 1 cm^2/Vs would correspond to a doping density of 5.6x10^{14} cm^{-3}. The results of these 2-point-probe measurements were crosschecked against previously obtained 4-point-probe conductivity measurements, and the values turned out to be consistent.

Turning our attention again to the dark-CELIV transient in Figure 4.12b, after ≈1 ms the signal rises again just as observed in the BACE measurements due to the presence of mobile ions until beyond 100 ms, which represents the detection limit of our current setup. Considering that the current does not saturate, only a lower mobile ion density of 1.5 × 10^{16} cm^{-3}, can be specified upon integration of the dark-CELIV signal. Therefore, these transient measurements demonstrate that the mobile ion concentration is much larger than the photogenerated charge carrier density, the injected charge at V_{OC} and the doping induced charge, and sufficiently large to redistribute the built-in electric field of the device. In contrast, it is important to note that the doping density is much smaller than the CU charge per cell volume (6 × 10^{15} cm^{-3}), which is too low to screen the electric field. To further highlight this point, we performed numerical simulations, the results of which, displayed in Figure 4.12d, demonstrate that the doping density will only start to make a significant impact at densities exceeding ≈1 × 10^{16} cm^{-3}, at which point the built-in field becomes

screened. Moreover, it can be seen that electronic doping, although it can affect the device performance at higher concentrations, as is displayed in Figure 4.14, never leads to a temporal current decay, whereas for mobile ions, temporal current decays are observed for a range of concentrations.

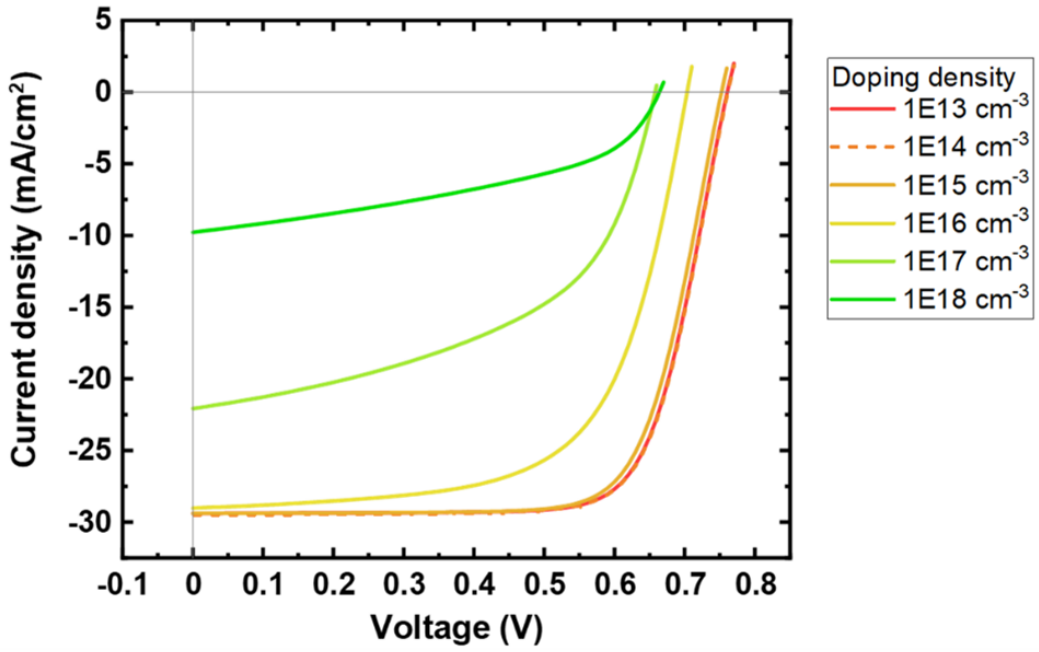

Figure 4.14: Simulated JV curves for a mixed-metal lead-tin perovskite cell with different doping concentrations. It can be seen that doping density only starts to affect the performance of the device once the doping density becomes higher than the electrode charge per perovskite volume that creates the built-in field at 0V. These JV curves were simulated using SCAPS-1D, a software developed at the Department for Electronics and Information Systems (ELIS) at the University of Gent, Belgium [91]. This software is freely available upon request to the developers.

Interestingly, we also found that when the mobile ion concentration reaches a certain threshold, the stabilised current still decreases with increasing mobile ion densities, but the temporal decay disappears. We attribute this to the fact that at these high mobile ion densities, the mobile ion concentrations at the TL interfaces are already large enough at t = 0 s to fully screen the field. The simulation results displayed here are for the case of only one mobile ionic species. In Figure 4.15, results for the case where there are two types of mobile ion present are displayed. Overall, the experimentally measured timescales and carrier densities allow us to conclude that

the collection losses of the current stem from the ionic movement in the perovskite causing a redistribution of the internal field, rather than from electronic doping.

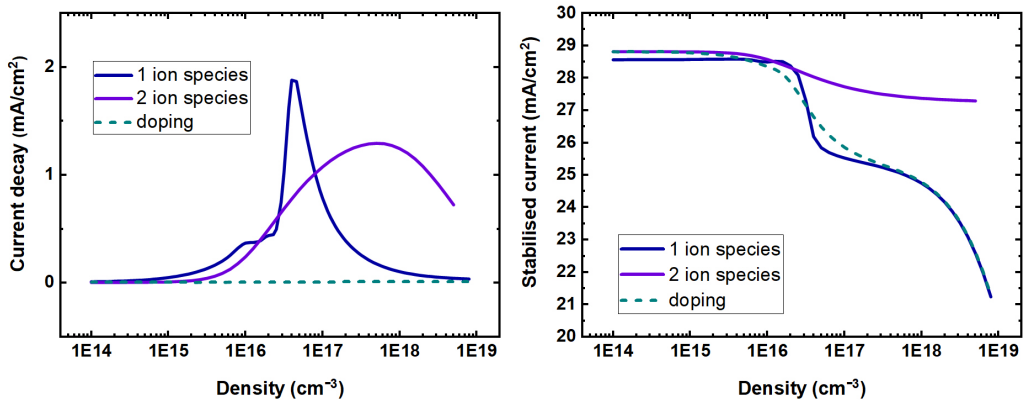

Figure 4.15: Simulated current decay (a) and stabilised current (b) for a system with either electronic doping, mobile anions, or mobile anions + mobile cations. It can be seen that, though doping can cause a decrease in stabilised current with increasing concentration, it never leads to a transient current decay. In both cases where mobile ions were present, a current decay is observed. We note that the presence of a second mobile ion species seems to have a mitigating effect both on the temporal current decay observed, but also, importantly, on the reduction of the stabilised current. These simulations were carried out with Setfos.

In order to find out whether the loss mechanism described above is unique for tin-containing perovskites, or if it also occurs for other perovskite compositions or architectures, we investigated several different lead-based perovskite systems. Surprisingly, as shown in Figure 4.16a, we observed that the exact same charge transport losses are indeed present for all other studied lead-based perovskites, including methyl ammonium lead triiodide, two triple cation perovskites ($Cs_{0.05}(FA_xMA_y)_{0.95}Pb(I_xBr_y)_3$), with different x/y ratios as well as for a triple cation perovskite in a nip-configuration based on TiO_2 and Spiro-OMeTAD. Further details of the device fabrication are presented in chapter 3. Also for these systems, as displayed in Figure 4.16b, the transient current decay is accompanied by an increase in PL over time at 0 V, while the timescales of the current loss and deterioration in charge extraction efficiency correspond to the timescales at which the ions move in the respective systems. Figure 4.16c displays the effects of different scan speeds on the obtained short-circuit current confirming that the current at slow scan speeds is significantly lower than the "ion-free" J_{SC} fast-scan speeds. This confirms that the finding that ionic charge movement is responsible for

the observed current losses can be generalised beyond tin-based perovskites to lead halide perovskites. The formation of field-free regions in the perovskite bulk due to mobile ions is thus not only responsible for the JV hysteresis, but also for significant current and efficient losses under realistic operating conditions. The latter is shown in Figure 4.16d, which highlights the MPP tracking of several devices with a high time resolution (≈10 ms). Each of these devices displays a quick initial decrease in maximum power output (which might be easily overlooked when tracking the device efficiency over longer times).

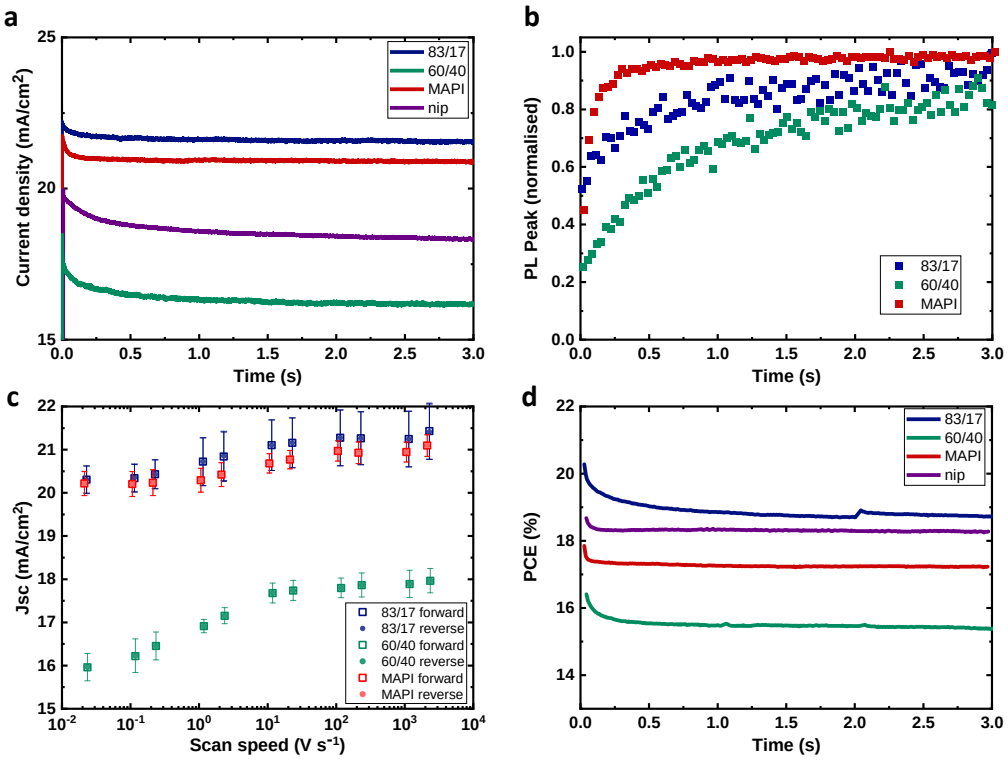

Figure 4.16: a) Current decay upon switching from open-circuit (OC) to short-circuit (SC) at t = 0 s, depicted for devices from several different perovskite compositions including $MAPbI_3$ ("MAPI") and two triple cation $Cs_{0.05}(FA_xMA_y)_{0.95}Pb(I_xBr_y)_3$ devices made from different (x/y) ratios of $FAPbI_3$ and $MAPbBr_3$ ("83/17" and "60/40") in a pin-structure, as well as one device with a $FA_{0.85}MA_{0.15}Pb(I_{0.85}Br_{0.15})_3$ perovskite in a nip-structure ("nip"). b) Analogous to the mixed lead-tin devices, the current decay takes place on the same timescale as the increase in the PL after the initial quench. c) Short-circuit current as a function of scan-speed depicted for different compositions, d) the efficiency decay on short timescales as obtained through maximum power point measurements. Data for c) provided by Vincent Le Corre.

We point out that light soaking has also been shown to have an impact on ion migration and hysteresis.[140] In order to distinguish between light soaking effects

and the current losses studied here, we checked whether the scan-rate dependent hysteresis is reversible, or if there are permanent/light-induced changes in the device performance. Figure 4.17 shows that for the pin-type perovskite cells studied here, the current losses observed are not linked to light-soaking-induced changes in the device performance. However, on longer timescales, light soaking may have more pronounced effects. Finally, we note that we found the mobile-ion-induced losses were overall quite similar in PbSn- and Pb-perovskite, hence we attribute the difference in the J_{SC} loss in these two systems more to the difficulties in obtaining thicker active layers in PbSn-perovskites, which are required due to their lower absorption coefficient at the band edge. Nevertheless, preventing the fast-field screening and the corresponding current losses by minimising the mobile ion density in all studied perovskites, would thus allow a significant improvement of the current in steady-state and in turn a substantial PCE improvement of between 1.5-3% absolute, even in our optimised devices.

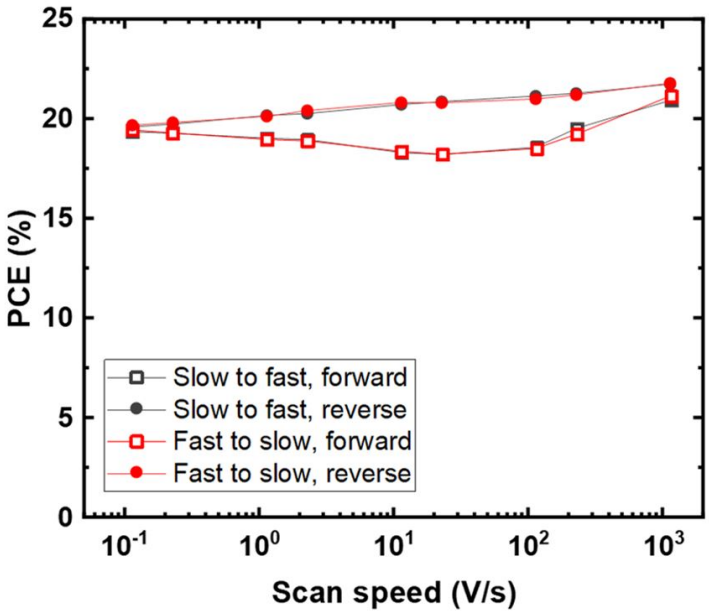

Figure 4.17: PCE as a function of scanspeed for an '83/17' Pb-based perovskite solar cell. The JV scans were taken at different scan speeds, while the cell was left on the light in between the different scans. In order to check whether light soaking effects could account for the current losses observed, the measurements were performed twice - once starting with the slowest scan speeds and scanning progressively faster, and once starting with the fastest scan speeds and scanning progressively slower. Similar current losses were observed in both scan directions, hence ruling out light soaking is the underlying cause.

4.3 Conclusion

To summarise, we have demonstrated that the charge collection losses in mixed lead-tin perovskites are caused by an accumulation of electronic charge in the active layer due to a reduction in the charge extraction efficiency over the first few seconds of operation, which simultaneously increases the emitted PL from the device. Through a series of transient electronic measurements and numerical modelling, we identified this collection loss to be due to the presence of mobile ions in these systems which redistribute the internal field within the first few seconds of operation, rather than a recombination rate of photogenerated carriers with doping-induced background charges or increased defect densities. As far as we could assess in this work, doping of (non-oxidised) mixed lead-tin perovskite is not directly causing current losses through band flattening as the doping density is too low to screen the electric field. Going beyond mixed lead-tin systems, to lead-based perovskites, we show that the same process also occurs for a range of different mixed-ion lead-based perovskite solar cells. As with the low bandgap materials, we again find that the timescales of the current loss correspond to the timescales of ion motion in these different systems. Our findings demonstrate that even in what appear to be "hysteresis-free" perovskite solar cells at typical scan speeds ($\approx$100 mV s^{-1}), the role of mobile ions cannot be neglected, since they still have a large and negative impact on device performance. Considering that the ion-free current (measured at fast scan speeds) is typically $\approx$1.5 mA cm^{-2} larger, this constitutes a significant PCE loss. In order to reduce charge collection losses both in mixed lead-tin perovskites, but also in neat lead-based perovskites, it is important to gain further understanding of how to reduce the mobile ion density, or how to engineer the devices so that the charge collection is insensitive to the redistribution of the mobile ions. This will then enable us to move closer to the radiative efficiency limit.

CHAPTER 5

On the relationship between mobile ions and device degradation in perovskite solar cells

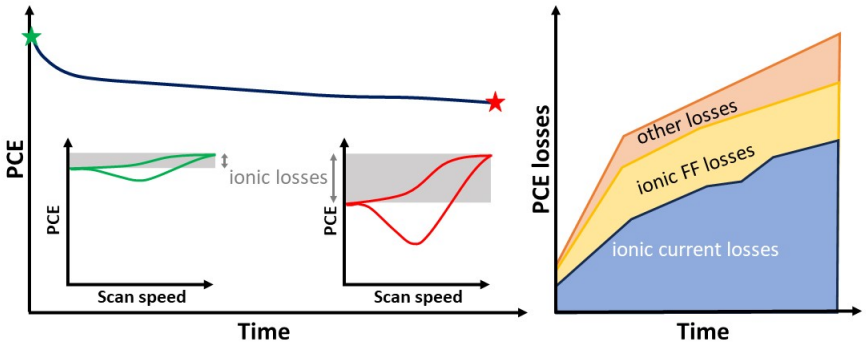

The work presented in this chapter is largely based on:

J. Thiesbrummel, S. Shah, E. Gutierrez-Partida, F. Zu, F. Peña-Camargo, S. Zeiske, J. Diekmann, F. Ye, K. Peters, K. O. Brinkmann, J. Warby, Q. Jeangros, F. Lang, Y. Wu, S. Albrecht, T. Riedl, A. Armin, D. Neher, N. Koch, V. M. Le Corre, H. J. Snaith, M. Stolterfoht, "Ion induced field screening governs the early performance degradation of perovskite solar cells", Submitted, 2023

5.1 Introduction

Despite the impressive progress in terms of photovoltaic performance of perovskite solar cells over the last decade there still remain many issues regarding the stability. This has considerable implications for their real-world energy yield, and the levelised cost of electricity.[72,141,142] These challenges include various degradation pathways including material decomposition under light[143,144], heat[145,146], oxygen[147,148], humidity[149,150], and a combination thereof. Efforts to improve device stability include, amongst many others, compositional engineering, e.g. omission of methylammonium iodide[151,152], the use of additives[153,154], transport layer (TL)[155–157] and interface engineering[158], using a mixture of 2D and 3D perovskites[159–161], the incorporation of diffusion barriers to the metal electrode (e.g. SnO_2[162–164], CuSCN[165], or bismuth[166]) and more effective encapsulation methods[167]. However, the stability reported in the academic literature remains far below the targeted values required for commercial viability (IEC standards and $>$ 25 years operational lifetime). It is thus essential to gain a more comprehensive understanding of the underlying chemical and physical processes occurring during device ageing, and their effects on device performance.

In general, perovskites can also degrade over time without the presence of a specific external stressor, for example due to strain within the material which leads to a reduced shelf lifetime[168,169]. Other challenges, more specifically related to perovskite-based tandem photovoltaics include the phase segregation in mixed-halide Br-rich perovskites[170–173] as well as mechanical concerns, for example instabilities on top of (textured) Si substrates due to strain and potential delamination of charge transport and contact materials[174]. However, many of the intrinsic stability limitations are related to the presence of mobile ions in the perovskite layer, which behaves like a solid electrolyte with low-activation energies for ionic transport[175]. For methylammonium lead iodide (MAPI), density functional theory simulations have predicted a mobile ion density of 1x10^{19} cm^{-3} due to the low activation energy of the mobile ions ($\approx$ 100 meV)[176]. However, from an experimental and numerical perspective, such high

mobile ion densities are very difficult to reconcile in well-performing devices and are controversial with most recent works narrowing the mobile ions density to 1x10^{15}-1x10^{17} cm^{-3} in devices with low levels of hysteresis[122,177–180]. Halide vacancies and interstitial iodine are usually considered to be the dominant species of mobile ions and they are particularly harmful since they can form I_2 - a solid that easily sublimes above room temperature, leading to a loss of absorber layer material, potentially causing electrode cracks and critical device failure[181]. The migration and accumulation of halide defects due to lateral variation in the electric field also triggers the degradation of laboratory-scale solar cells at their edges and at the position of external impurities[182]. The formation of halide vacancies has also been linked to oxidation reactions at transport layers and metal electrodes[183]. Moreover, mobile ions and vacancies on both the A-site cations and the X-site halides have been shown to be able to diffuse into the transport layers, with halide ions being localised in the device electrodes[163,181,183–186]. This effect may cause a range of problems, for example, loss of charge selectivity due to a change of the electrode work function, oxidation/corrosion, the formation of insulating layers, and the de-oxidation of doped transport layers.

Although tackling stability issues has always been a main priority for perovskite researchers, the community still lacks to some extent the experimental methodologies required to quantitatively characterise mobile ions in perovskite semiconductors to overcome these limitations. For example, besides the above-discussed degradation pathways which are chemical and mechanical in nature, it is not yet possible to quantitatively determine the ageing-induced performance loss due to mobile ions and to differentiate these losses from those due to defects and other device and material parameters. In this regard, we have recently presented a method to determine the contribution of mobile ion-induced efficiency losses to the device performance and we have shown that the presence of mobile ions leads to moderate efficiency losses in fresh devices with low levels of apparent hysteresis (typically 1-3% absolute). The underlying mechanism of these ion-induced losses is the movement of mobile ions to

the perovskite-transport layer interfaces, leading to current losses due to field screening and a reduction in charge extraction efficiency[64,187].

In this chapter, we determine the contribution of mobile ion-induced degradation losses to the total degradation loss in the presence of external stressors for a range of different perovskite solar cells. Using JV measurements at different scan speeds, we first demonstrate that these losses can be directly linked to the movement of mobile ions and an increase in mobile ion density which dominates the initial performance losses of perovskite solar cells, thereby confirming the hypothesis of Tress et al.[64]. In particular, we show that an increased mobile ion density upon prolonged illumination leads to a substantial decrease in the steady-state power conversion efficiency (PCE), mainly due to a significant reduction in short circuit current (J_{SC}) from fast to slow scan speeds that can exceed 10 mAcm^{-2}. We attribute this result to increased field screening - a phenomenon that has not been previously discussed in relation to the degradation of perovskite solar cells. We also show that interfacial recombination does not increase upon ageing, yet there is an increasing mismatch between open-circuit voltage (V_{OC}) and the quasi-Fermi level splitting (QFLS) which can also be attributed to an increased accumulation of mobile ions in the contact regions. As such, the increasing mobile ion density dominates the early ageing stages of perovskite solar cells. Finally, we show the general validity of this result for a range of different perovskite compositions, including methylammonium lead iodide ("MAPI"), a formamidinium caesium lead iodide ("CsFA"), a mixed-halide wide gap perovskite ("1.8 eV WG"), and a formamidinium-rich triple halide perovskite ("95:5 TH"). This chapter establishes key insights into the process of device degradation and the critical role mobile ions play therein and lays the foundation for accelerated ageing tests to predict the long-term stability of perovskite devices based on a quantitative analysis of ion-induced losses.

The devices investigated in this chapter were provided by Francisco Peña-Camargo, Emilio Gutierrez-Partida, Fangyuan Ye and Sahil Shah.

5.2 Results

In order to investigate the effects of illumination-induced degradation in the perovskite solar cells, we started off investigating the commonly used triple cation $Cs_{0.05}(FA_{0.83}MA_{0.17})_{0.95}Pb(I_{0.83}Br_{0.17})_3$ perovskite composition with a bandgap of 1.63 eV in a pin-type architecture (referred to as "83:17 TC" throughout the rest of this thesis). The following cell architecture was used: ITO/PTAA/PFN-Br/perovskite/C_{60}/BCP/Cu, ITO is indium tin oxide, PTAA is poly[bis(4-phenyl)(2,4,6-trimethylphenyl)amine], PFN-Br is Poly(9,9-bis[30-(N,N-dimethyl-N-ethylammonium)-propyl]-2,7-fluorene-alt-2,7-9,9-di-n-octylfluorene) dibromide, and BCP is bathocuproine[188]. The cells were subjected to three different external stressors: light, heat, and electrical bias, with a focus on light-induced ageing. During the light-induced ageing, devices were exposed to 1 sun illumination at open circuit and cooled such that the device temperature remained at 25 °C. Measurements under (MPP) maximum power point conditions are discussed further below. In Figure 5.1a, the stabilised JV curves (without hysteresis) at slow scan speeds (10 mV/s) after different illumination times under V_{OC} are exemplified. Figure 5.1b shows how the different device parameters change over time with ageing. In these cells, the increasing J_{SC} losses over time dominate the degradation losses, although FF losses are also significant, and the V_{OC} decreases slightly as well. Based on the work presented in the previous chapter[187], we suspect that the increased current losses observed here might be caused by an increase in the mobile ion density in the perovskite.

In order to quantify the impact of mobile ions on the light-induced performance degradation we performed fast-hysteresis (FH) JV measurements at different points in time during the ageing process. While details are presented in Chapter 3 and in the work by Le Corre et al.[137], we note that the cell is initially held slightly above the initial V_{OC} (pre-bias), followed by a reverse and forward sweep with variable frequency or scan speed. The duration of the pre-bias was 5 times longer than the total scan time of the voltage sweep. This methodology allows us to determine the efficiency in

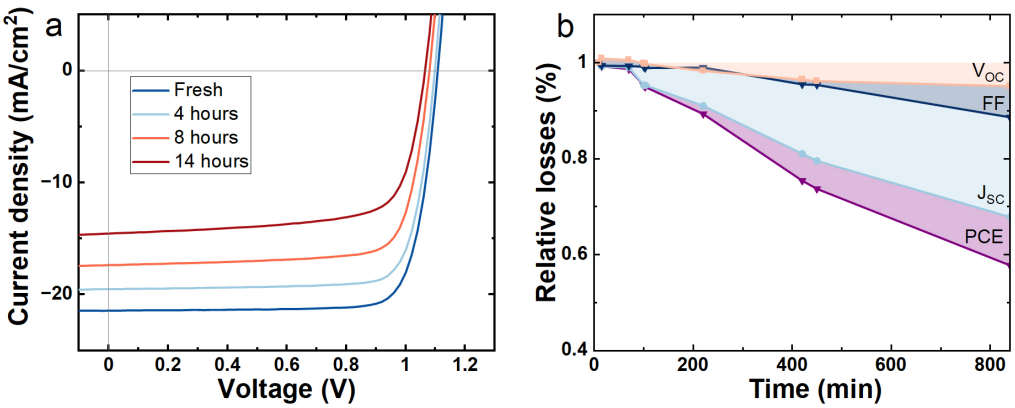

Figure 5.1: a) Representative stabilised current-voltage (JV) characteristics at slow scan speeds (10 mV/s) measured on a fresh $Cs_{0.05}(FA_{0.83}MA_{0.17})_{0.95}Pb(I_{0.83}Br_{0.17})_3$ perovskite solar cell as well as after continuous illumination at V_{OC} for the specified time. b) Relative steady-state losses of the different PCE parameters as a function of ageing time.

steady state and the "ion-freeze" efficiency, which refers to the condition at which the ions are effectively immobilised when the scan rate is much quicker than the diffusion rate[137]. The difference in the JV curve between slow (steady-state) and fast-scan speeds can be directly attributed to the movement of mobile ions. In the following, these losses are referred to as mobile ion-induced PCE losses. However, it should be noted that the presence of mobile ions can still affect the PCE even when they are immobilised depending on their distribution and accumulation throughout the device and at the interfaces[137,189]. This effect will be small if the mobile ions are homogeneously distributed in the bulk at the start of the scan which is discussed further below. The results, displayed in Figure 5.2a, reveal once again that the steady-state efficiency drops significantly with ageing. Conversely, the ion-freeze efficiency, determined at fast scan speeds of around 2500 V/s experiences a much smaller, almost negligible reduction. Next, we investigated the effects on each of the three JV metrics: the V_{OC}, J_{SC} and fill factor (FF), displayed in Figure 5.2b-d. It can be seen that the illumination-induced performance losses are largely related to a drastic loss of the steady-state current output with respect to the ion-freeze J_{SC} (for longer ageing times, and for some other perovskite compositions, current losses exceeding 10 mA cm^{-2} can be observed). However, the V_{OC} and the FF are also affected to some extent.

Furthermore, the "peak hysteresis'" i.e. the maximum difference between the PCE determined from the forward versus the reverse scan increases significantly with ageing. Overall, the remarkable difference in the PCE between the fast and slow scan speeds (Figure 5.2e and f) indicates that the dominant loss mechanism upon ageing affects the device performance much more significantly at the slower timescales.

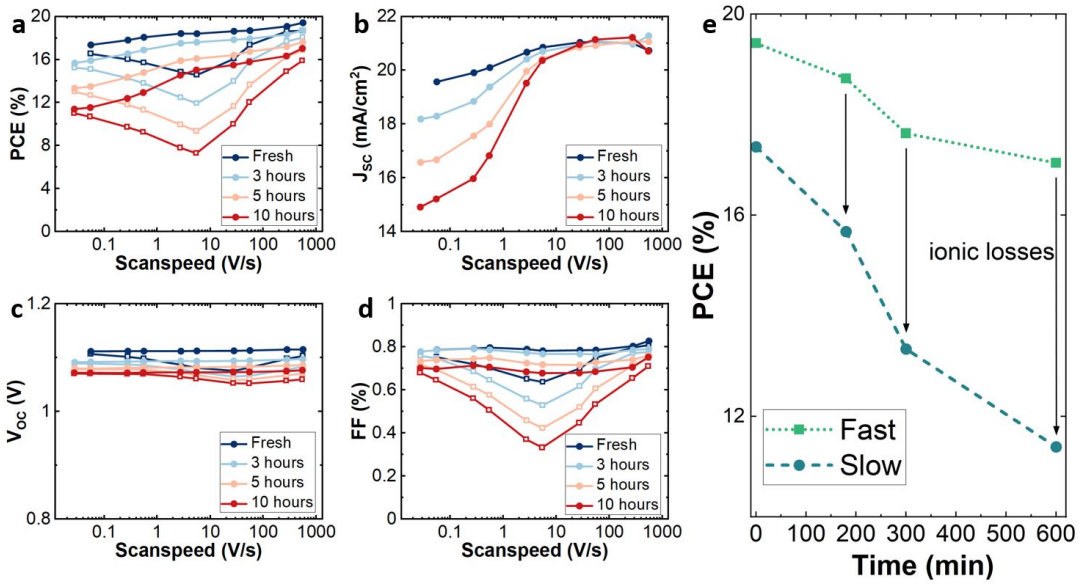

Figure 5.2: a) The power conversion efficiency (PCE), b) short-circuit current density (J_{SC}), c) open-circuit voltage (V_{OC}) and d) fill factor (FF) from current-voltage characteristics measured at different scan speeds for $Cs_{0.05}(FA_{0.83}MA_{0.17})_{0.95}Pb(I_{0.83}Br_{0.17})_3$ perovskite solar cells after different ageing times. Data for reverse (closed symbols) and forward (open symbols) scans. e) PCE at fast and slow timescales versus ageing time demonstrating the losses induced by the movement of mobile ions and small additional losses at fast scan speeds.

To get some understanding of the chemical changes of the perovskite film during light exposure, we performed absorption spectroscopy (Figure B.1, Appendix B), X-ray diffraction (XRD) measurements on fresh and aged perovskite layers (Figure B.2, Appendix B), scanning electronic microscopy (SEM) and atomic force microscopy (AFM) measurements (Figure B.3, Appendix B). As discussed in Appendix B, while these measurements indicate possible changes in the morphology, these changes are considered to be relatively small on the timescale of the measurements (up to 24 h of illumination). This chapter focuses on early onset degradation, before more structural and chemical changes take place in the perovskite.

To generalise these findings, we then investigated the mobile ion-induced ageing loss in a range of different perovskite compositions beyond the "83:17" model system. These perovskite systems include a standard 1.6 eV methyl ammonium lead iodide $MAPbI_3$ ("MAPI"), a double cation perovskite $FA_{0.85}Cs_{0.15}Pb(I_{0.77}Br_{0.23})_3$ ("CsFA") with a bandgap of 1.69 eV relevant for Silicon/perovskite tandems, a wide-bandgap $Cs_{0.05}(FA_{0.60}MA_{0.40})_{0.95}Pb(I_{0.60}Br_{0.40})_3$ ("1.8 eV") relevant for all-perovskite tandems and a high performance (22% PCE) 1.57 eV formanidinum lead iodide rich ("95:5 TH") triple halide perovskite $Cs_{0.05}(FA_{0.95}MA_{0.05})_{0.95}Pb(I_{0.95}Br_{0.05})_3$ + 20 wt% MACl). The FH results on all systems are shown in Figure B.6 - B.9, Appendix B. These results demonstrate that the increase of the ionic loss (L_{ion} =PCE_{fast}/PCE_{slow}) contributes significantly to total degradation loss for all systems (Figure 5.3a). Moreover, we find that the reduced J_{SC} is the most important factor contributing to the ion-induced loss in all systems (Figure B.10 and B.11). Figure 5.3b exemplifies the large reduction of the steady-state J_{SC} after several hours of illumination (5h for most compositions, except for MAPI which was measured after 12h) with respect to the initial current. Figure 5.3c shows that the mobile ionic losses also emerge in the much more stable 95:5 TH perovskite system which degraded to roughly 68% of its initial PCE (21%) after tracking the MPP over 1630 h. The FH measurements taken initially and after the MPP tracking reveal a nearly unchanged ion-freeze PCE, indicating that the observed power output losses can be attributed to mobile ionic losses. We note that other factors, such as shunt formation, moisture ingress or electrode corrosion can cause an early device failure. However we observe that the mobile ionic losses are very prominent if these "extrinsic" issues are mitigated.

Having established that the mobile ionic losses dominate the overall performance decrease upon device degradation, we now set out to try to understand the origin of these increasing losses by further investigating the example of the 83:17 triple cation perovskite. At this point, it is important to note that the increase of the ionic loss with ageing time could be related to many other factors[137]. This is because for a given mobile ion density, the magnitude of the mobile-ion-induced losses depends

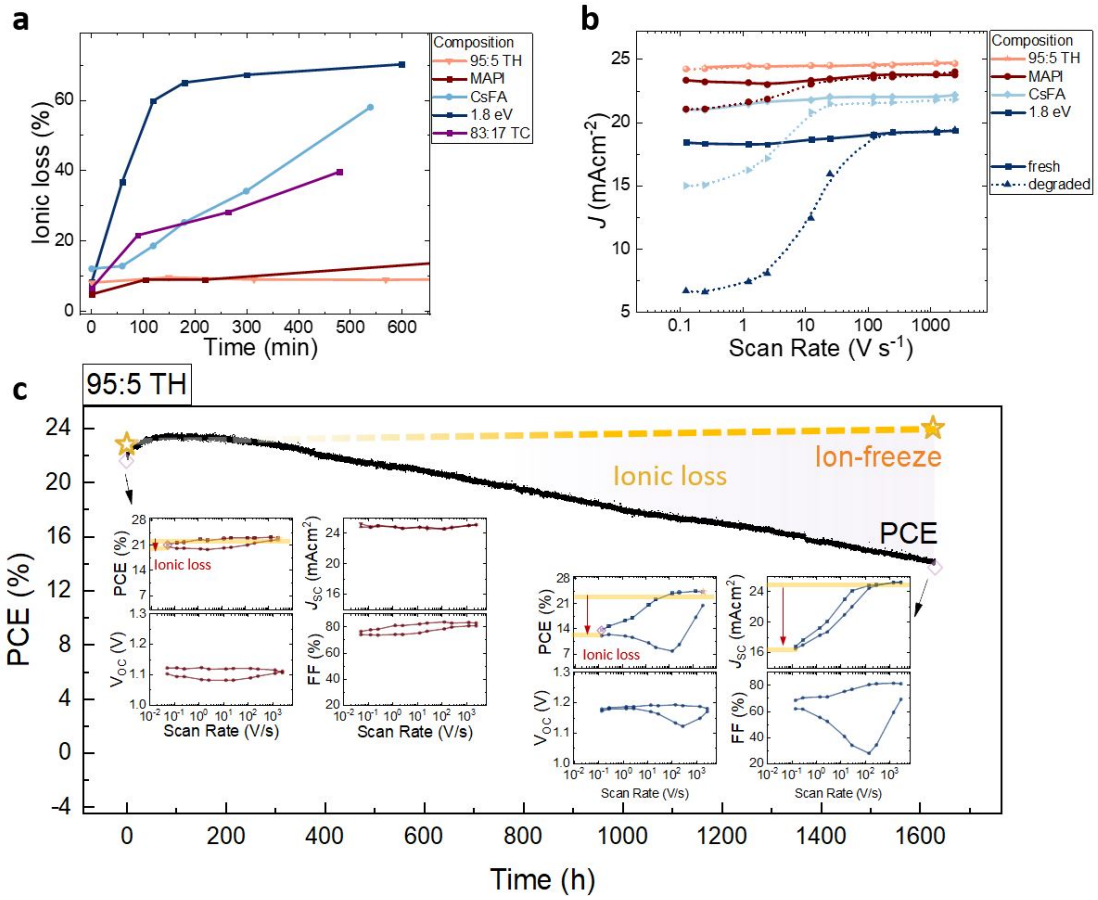

Figure 5.3: a) The ageing-induced relative ionic loss (L_{ion} = PCE_{fast}/PCE_{slow}) as a function of ageing time demonstrating increasing mobile ionic losses in all systems though with varying magnitude depending on the individual composition. Highest ageing-induced mobile ionic losses are found in the $Cs_{0.05}(FA_{0.60}MA_{0.40})_{0.95}Pb(I_{0.60}Br_{0.40})_3$ ("1.8 eV") cell, followed by $FA_{0.85}Cs_{0.15}Pb(I_{0.77}Br_{0.23})_3$ ("CsFA"), and 83:17 TC with the smallest losses found in $MAPbI_3$ ("MAPI") and the $Cs_{0.05}(FA_{0.95}MA_{0.05})_{0.95}Pb(I_{0.95}Br_{0.05})_3$ + 20 wt% MACl ("95:5 TH") cell, where the ion-induced ageing losses do not increase on these timescales. b) The J_{SC} from JV curves measured at different scan speeds for fresh and aged cells after 5h hours of ageing (12h for MAPI) with additional PCE parameters shown in Figure B.6-B.9, Appendix B. c) Steady-state power point tracking on the 95:5 TH device with enhanced stability compared to the 83:17 TC reference cell. The insets show the fast-hysteresis measurement before and after the degradation demonstrating that the observed degradation stems from mobile ionic losses while the ion-freeze PCE remains nearly unchanged.

on various device and material parameters. For example, recombination rates at the interface, as well as doping densities in the transport layers can affect to what extent mobile ions in the device lead to decreased device performance. To identify the underlying mechanisms we now discuss, simulate, and analyse distinct scenarios. For the simulations, we employed the drift-diffusion software Setfos from FLUXiM. Parameters used for the simulations can be found in Table A.1 in Appendix 3.

We identify two possible origins of the increased mobile ionic losses. In our first hypothesis, the concentration of mobile ions increases with ageing, which leads to enhanced mobile ionic losses as shown by the simulation results in Figure 5.4a (see Figure 5.5, Figure 5.6 and Table A.1 for simulated JVs and the corresponding PCE parameters and the simulation parameters, respectively). In this case, the increased mobile ion density causes an enhanced screening of the internal electric field in the absorber layer, which leads to a continuous reduction in charge extraction efficiency due to band flattening (Figure 5.7). The details of this loss process are discussed below in more detail. Another possible explanation for the enhanced mobile ionic losses are degrading perovskite/transport layer interfaces, which lead to higher recombination velocities (S). As shown by the scan-rate dependent PCE in Figure 5.4b, such an increased recombination velocity also leads to a reduced steady-state PCE and increased peak hysteresis. However, in contrast to the case of an increased mobile ion density (Figure 5.4a), the ion-freeze PCE at fast scan speeds decreases as well. Finally, we also investigated the impact of an increased energy level offset on the FH results, as well as the impact of an increased bulk defect density. However, we found that both (i.e. increased energetic offset and reduced bulk lifetime) lead to a parallel downshift of the scan-rate dependent PCE rather than an increase in the mobile ionic losses, which is not consistent with the experimental results (Figure 5.8).

To further investigate the impact of potentially worsening interfaces or absorber layer quality on the enhanced mobile ionic losses, photoluminescence (PL) measurements of different partial cell stacks were recorded as a function of illumination time. From the PL yield the quasi-Fermi level splitting (QFLS) was calculated following our previous methodology[135,188]. Surprisingly, the results displayed in Figure 5.4c, suggest that the interfaces do not significantly worsen as the QFLS of all partial device stacks increases slightly over time, while the QFLS of the neat perovskite layer is nearly unchanged. Yet, the device V_{OC} decreases, resulting in an increasing QFLS-eV_{OC} mismatch[135] upon ageing. While increased interfacial defects (leading to an enhanced S) are not consistent with the increased QFLS and can be likely ruled

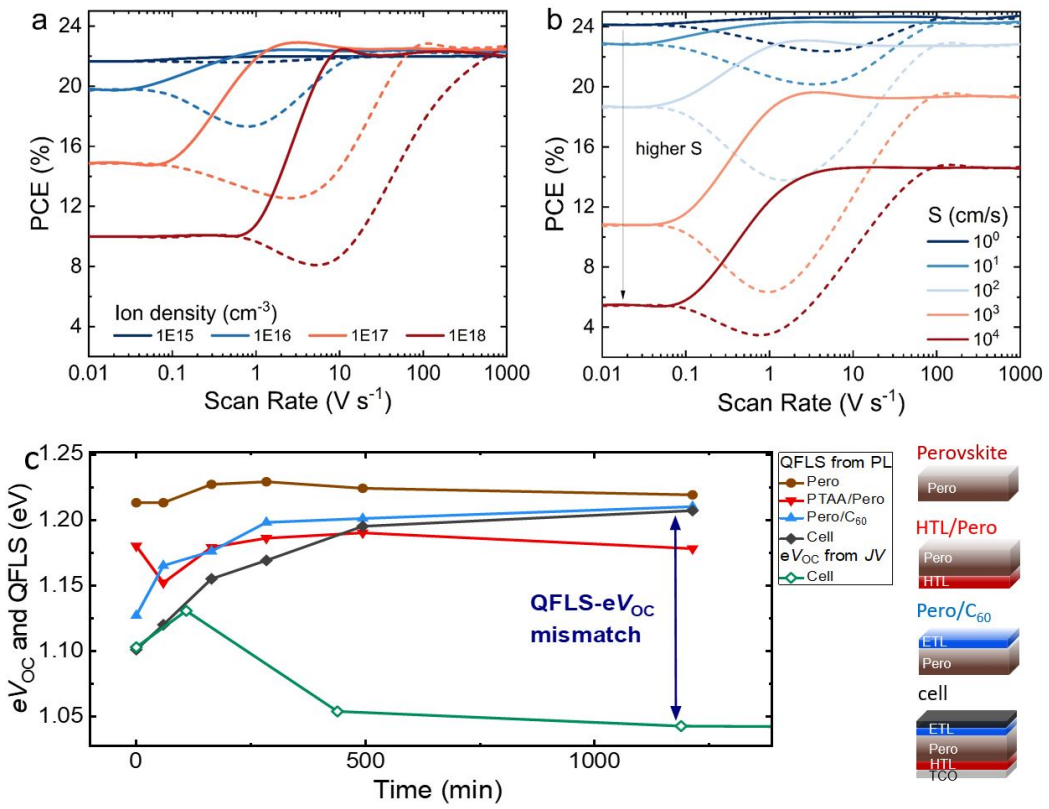

Figure 5.4: a) The simulated PCE from JV curves at different scan speeds for a range of different mobile ion densities. We note that we consider halide vacancies as the mobile ionic species in our simulations, however, the observed trend does not depend on the sign of the dominant mobile ion species, or on whether there are 1 or 2 mobile species. b) Simulated PCE from JV curves at different scan speeds for a range of different recombination velocities (S) at both perovskite-transport layer interfaces. c Device V_{OC} and the QFLS measured with photoluminescence on bare triple cation films, partial and complete cell stacks as a function of illumination time. Data from c) measured by Sahil Shah.

out as a dominant factor of the light-induced degradation in this cell, the increased QFLS-V_{OC} mismatch is intriguing. Although this requires further investigation, the QFLS-V_{OC} mismatch provides clues about the effect of mobile ions at fast scan speeds. The FH simulations displayed in Figure 5.9 show that if the built-in field is not offset with the pre-bias of the FH measurement (i.e. $V_{pre} < V_{BI}$), the V_{OC} decreases with increasing mobile ion density. Considering that such a V_{OC} decrease (and QFLS-eV_{OC} mismatch) is observed in various systems, the most likely scenario is that mobile ions accumulate in an unfavourable position under open-circuit conditions (e.g. cations at the hole selective interface)[189]. This is discussed further below.

Having ruled out an increased recombination velocity at the interfaces, an increased

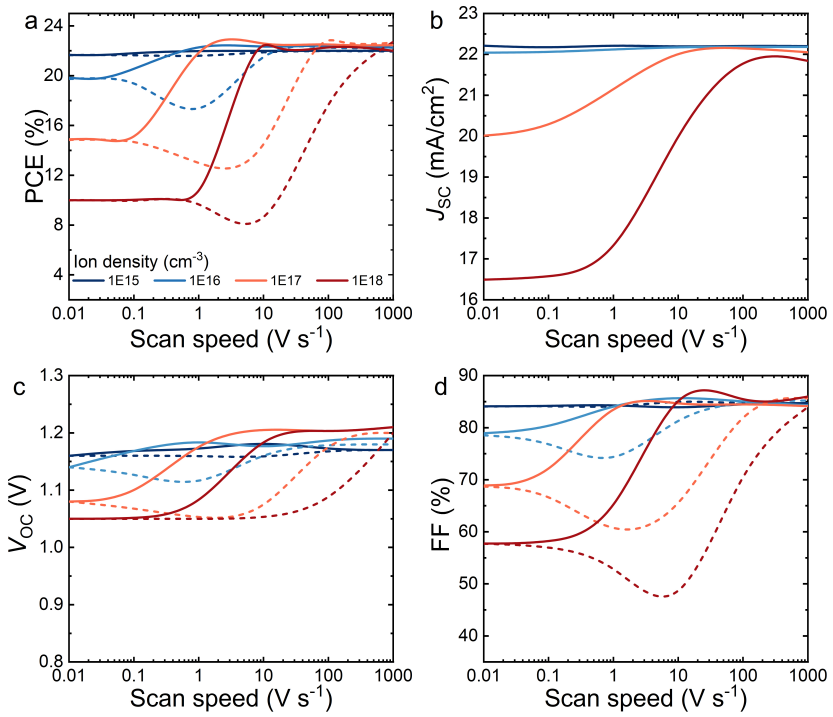

Figure 5.5: Simulated performance metrics PCE (a), J_{SC} (b), V_{OC} (c) and FF (d) for a range of different scan speeds for $Cs_{0.05}(FA_{0.83}MA_{0.17})_{0.95}Pb(I_{0.83}Br_{0.17})_3$ perovskite solar cells with varying mobile ion densities. The pre-bias (1.3 V) was chosen to establish flat band conditions in the perovskite for a device built-in voltage of 1.5 V. The flat band condition can be identified from the point at which the V_{OC} at fast scan speeds remains unaffected even in case of large mobile ion densities.

mobile-ion density seems likely to be the root cause of the observed ageing-induced losses. In order to directly assess whether the mobile ion density increases with degradation, we performed bias assisted charge extraction (BACE) measurements and charge extraction by linearly increasing voltage (CELIV) at the same points in time when we also performed fast hysteresis measurements. Both transient charge extraction techniques can be used to estimate the mobile ion density by integrating the external current. In BACE, the cell is held under "quasi" open-circuit conditions, where the injection current equals the short-circuit current density at which the mobile ions are distributed throughout the absorber layer before the voltage is switched to 0 V, at which point the mobile ions drift to the contact layers. However, we note that if the ionic charge is larger than the electrode charge ($Q_{ion} < CV_{BI}$), the formation of zero field regions should limit the displacement of mobile ions in excess of CV_{BI}. Thus,

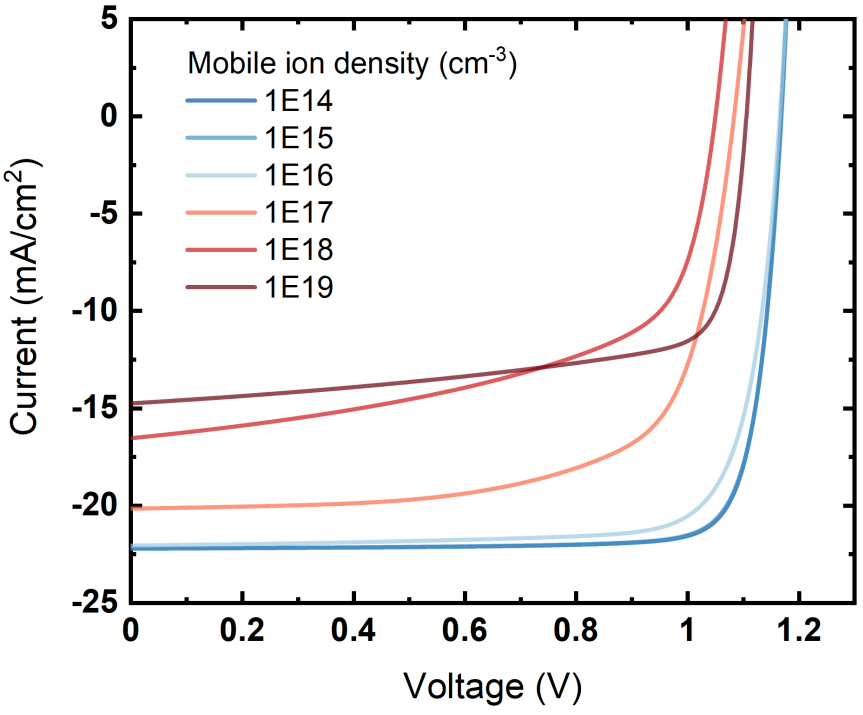

Figure 5.6: Simulated steady-state JV curves for $Cs_{0.05}(FA_{0.83}MA_{0.17})_{0.95}Pb(I_{0.83}Br_{0.17})_3$ perovskite solar cells with varying mobile ion densities. It can be seen that increasing mobile ion densities lead to significant current losses once the mobile ion densities pass the threshold of about 10^{15} cm^{-3}.

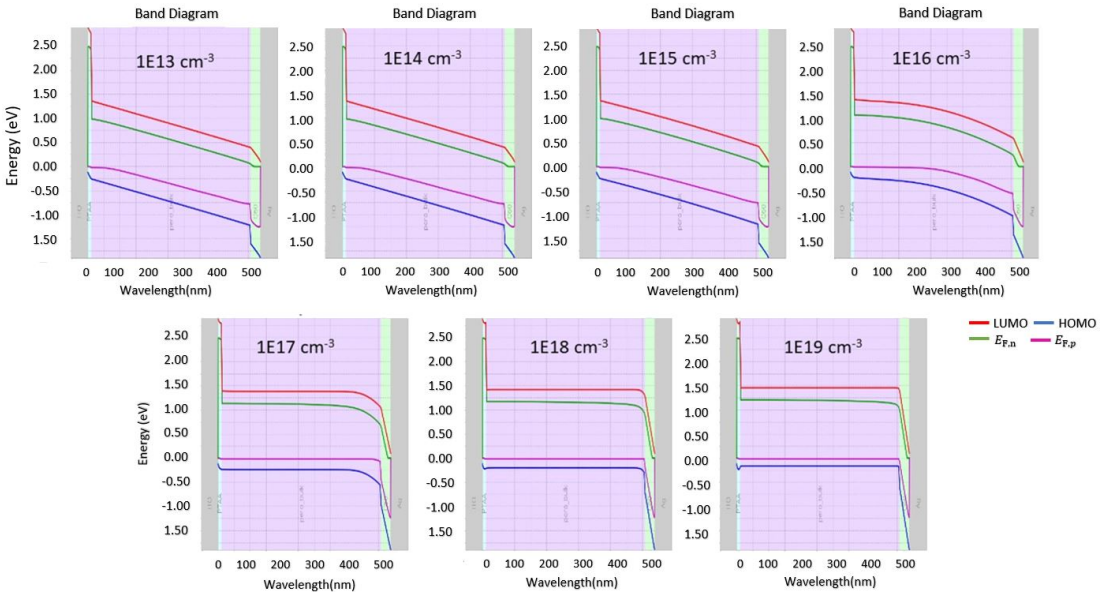

Figure 5.7: Simulated band diagrams at 0V for devices with different mobile ion densities. It can be seen that increasing mobile ion densities lead to significant flattening of the bands, which in turn causes a reduced charge carrier extraction efficiency and leads to the current losses observed in the JV curves displayed in Figure 5.6

the CV_{BI} is expected to be a natural limit for the externally detectable mobile ionic charge. Moreover, the ratio of the drift length of charges versus the film thickness (d_{drift}/d) limits the externally integrated charge. Therefore, the mobile ions should be roughly homogenously distributed under the pre-bias condition to maximise the drift length and to avoid an underestimation of the mobile ionic density[190].

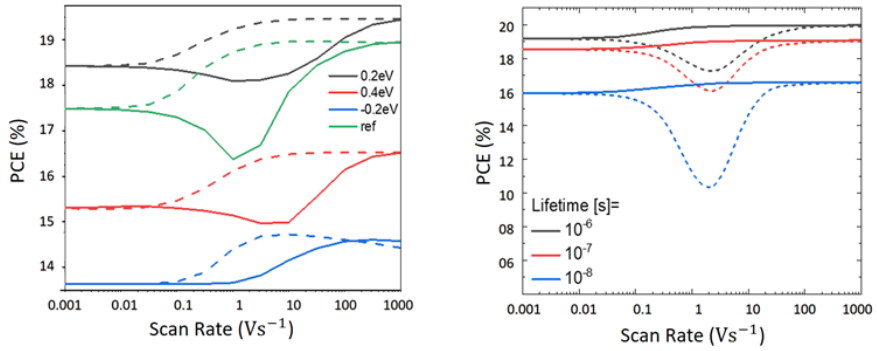

Figure 5.8: Simulated performance metrics PCE for a range of different scan speeds for $Cs_{0.05}(FA_{0.83}MA_{0.17})_{0.95}Pb(I_{0.83}Br_{0.17})_3$ perovskite solar cells with varying interfacial energy offsets and bulk lifetimes.

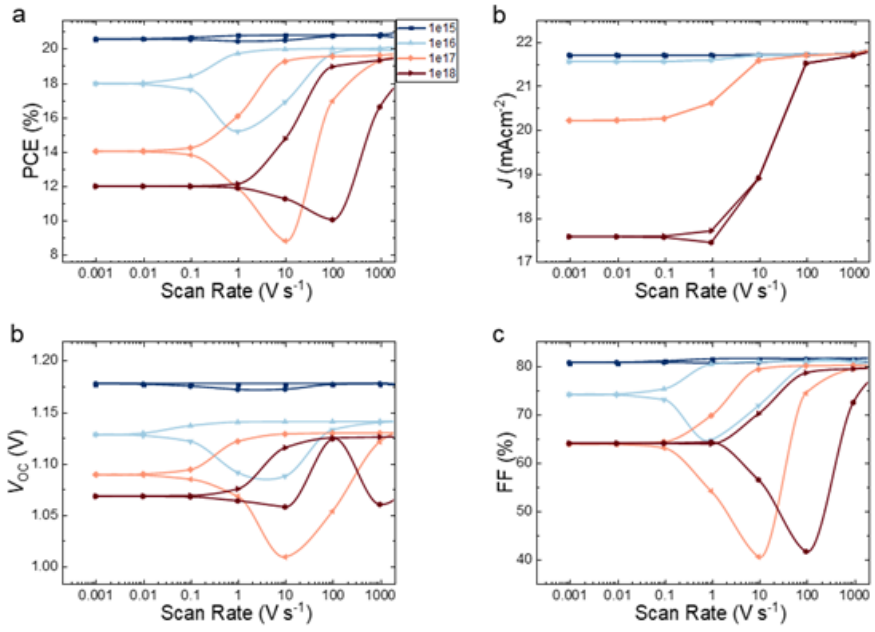

Figure 5.9: Simulated performance metrics PCE (a), J_{SC} (b), V_{OC} (c) and FF (d) for a range of different scan speeds for $Cs_{0.05}(FA_{0.83}MA_{0.17})_{0.95}Pb(I_{0.83}Br_{0.17})_3$ perovskite solar cells with varying mobile ion densities. The pre-bias was chosen to match the initial V_{OC} (1.18 V) for a device with a built-in voltage of 1.5 V.

The results of the BACE measurements are displayed in Figure 5.11a and b. It

can be seen that the externally measured compensation current strongly increases for samples that have been exposed to light ageing for longer times. Notably, the ionic "time of flight" in the fresh device at around 50 ms (Figure 5.10) matches nearly perfectly the scan time at the peak hysteresis observed in averaged FH on fresh devices (50 ms). Due to the associated diffusion constant (D = 7x10^{-10} cm^2/s) and ionic mobility (μ = 2x10^{-8} cm^2/Vs), these results indicate that the responsible mobile ion species are consistent with halide vacancies[122,191]. Therefore, these measurements link the transient charge extraction with the scan rate dependent JV results. It is also interesting to note that with prolonged ageing time, an increased amount of slower species are extracted, which could point to A-site vacancies[122,191]. Notably, this could also explain why the peak hysteresis does not shift to faster scan rates as obtained in the FH simulations (Figure 5.4a) for a given ion diffusion coefficient. As shown in Figure 5.11b, by integrating the external current, a rough estimate for the mobile ion density can be obtained. Plotting the mobile ionic losses obtained through FH as a function of the mobile ion density determined from BACE in Figure 5.11c, we observe a linear dependence after an initial dwell time. It can be seen that the mobile ion density increases significantly, even within the first hour of device ageing, and reaches values over 10^{18} cm^{-3} after 20 h of ageing. Although the reason why such large densities can be obtained in BACE is not yet clear considering the above-discussed limit of the detectable mobile ionic density which requires further investigation, the observed increase in mobile ion densities does make sense qualitatively. As shown in Figure 5.4a, simulations can reproduce the observed losses at the given mobile ion densities well. For example, a mobile ion density of 5x10^{18} cm^{-3} approximately halves the initial steady-state PCE due to enhanced mobile ionic losses [i]. From CELIV measurements a similar picture is obtained, where the increased mobile ion density after ageing is reflected in a strong increase in the signal on slower timescales, starting at roughly 1x10^{-4} s (Figure 5.12). The substantial additional signal above the CV_{BI}

[i] We note that we do not exclude some collection of mobile ions from the side of the pixel takes place[182], which could increase the mobile ion density within the active device area.

charge is consistent with the large increase in the mobile ionic density observed in BACE. Finally, we note that an increase of the mobile ion density with increasing ageing time, consistent with the results on the triple cation cells, was also confirmed for the other studied systems based on different perovskite compositions[192].

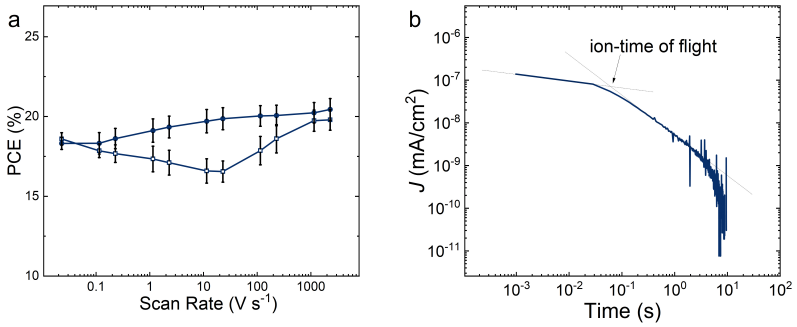

Figure 5.10: b) Ion-time of flight transient in a charge extraction experiment (BACE) measured on a fresh $Cs_{0.05}(FA_{0.83}MA_{0.17})_{0.95}Pb(I_{0.83}Br_{0.17})_3$ perovskite solar cell with increased time resolution. The efficient transit time of the mobile ions is 50 ms which matches the peak hysteresis in averaged FH measurements on 5 fresh devices (50 ms scan time) (b). The associated effective ion mobility is $\mu = 2\text{x}10^{-8}$ cm^2/Vs and the diffusion coefficient D = 7x10^{-10} cm/s. Data from a) measured by Vincent Le Corre

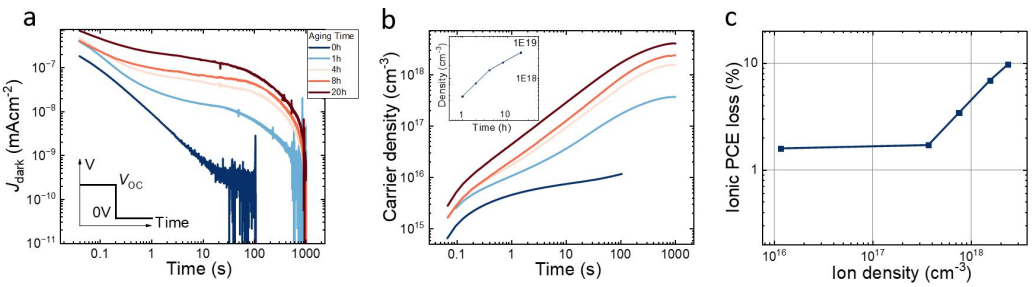

Figure 5.11: a) Current transients from Bias Assisted Charge Extraction (BACE) measurement for both fresh and aged devices and b) integrated charge carrier density from the transients in a. The applied voltage pulse to the device is illustrated in the inset. Considering that the capacitive (dis-) charging effect after the voltage switch and the extraction of electronic charges takes place on the µs-timescales, the contribution to the total extracted charge in these transients is nearly entirely given by mobile ions[137]. We note the integrated charge was multiplied by a factor of 2 to take into account the fact that the drift length is on average half of the active layer thickness. c) The ionic loss obtained for a $Cs_{0.05}(FA_{0.83}MA_{0.17})_{0.95}Pb(I_{0.83}Br_{0.17})_3$ triple cation device as a function of the mobile ion density reveals a linear dependence after an initial dwell ageing time. Measured by Emilio Gutierrez-Partida.

In order to investigate whether the devices would age similarly under real-world conditions and to better understand the dominant factor triggering the degradation, we expanded our measurements to other ageing conditions. The FH results for degradation

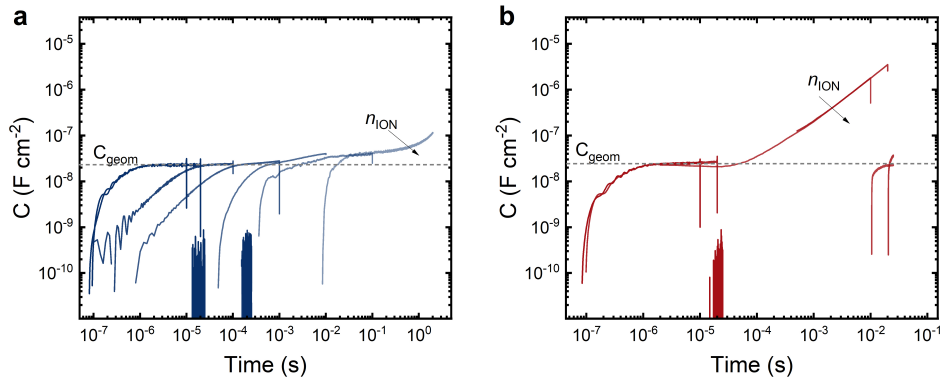

Figure 5.12: Charge Extraction by Linearly Increasing Voltage (CELIV) measurements on a) fresh and b) 8-hour aged $Cs_{0.05}(FA_{0.83}MA_{0.17})_{0.95}Pb(I_{0.83}Br_{0.17})_3$ perovskite solar cells revealing a huge increase of the capacitance (as calculated from C =V/(SR_{Load}), where V is the recorded voltage on the oscilloscope, S the slope of the applied voltage pulse and R_{Load} the load resistance) at long timescales on the aged device.

at elevated temperatures (75 °C) in the dark (Figure B.12, Appendix B), under MPP conditions at 1 sun illumination (Figure B.13, Appendix B), and under electrical bias (V_{OC}) in the dark (Figure B.14, Appendix B) can be seen in Appendix B. From these results, it becomes clear that the mobile ion induced performance loss is a general degradation mechanism, that is also triggered by electrical bias. Nevertheless, the ageing at elevated temperatures does not show the characteristic step-function like scan-rate dependent J_{SC} (Figure B.12, Appendix B), nor displays a very large increase of the mobile ion density on these timescales. This might point towards a different path of degradation or a slower evolution of the mobile ionic losses. While determining the exact rates of degradation requires a much more focused investigation that goes beyond the scope of the present work, our measurements indicate that mobile ions are easily created under different stressors with different rates, in particular in the presence of electrical charges in the active layer. The fact that the increase of mobile ionic losses behaves qualitatively similar under V_{OC}, regardless of the presence of light, but differs at elevated temperatures in the dark (and 0 V) is consistent with the interpretation that halide vacancies are generated by injected or photo-generated free holes[183,193]. In particular, it has been previously shown that iodine ions can be oxidised and kicked out of the lattice by photogenerated holes, creating halide vacancies via $I_I^x + h^+ = I_i^x + V_I^+$,

where I and i refer to the regular and the interstitial lattice site, respectively and x to the neutral charge[175,183,193]. Another possible mobile ion source is unreacted lead halide PbI_2 (Figure B.2, Appendix B), which can decompose into metallic lead and mobile iodine under illumination[194]. Both of these mechanisms are consistent with additional X-ray photoelectron spectroscopy (XPS) measurements which reveal the presence of iodine on top of the C_{60} layer after illuminating the triple cation perovskite for approximately 10 h, demonstrating the possibility of iodine diffusion through fullerenes in line with previous reports (Figure B.4, Appendix B)[163,195–197]. Moreover, we could detect iodine from the perovskite film on a Si substrate that was placed 1 mm above the sample (in N_2) during illumination, hence highlighting the egress of volatile iodine species (I_2) (Figure B.5, Appendix B).

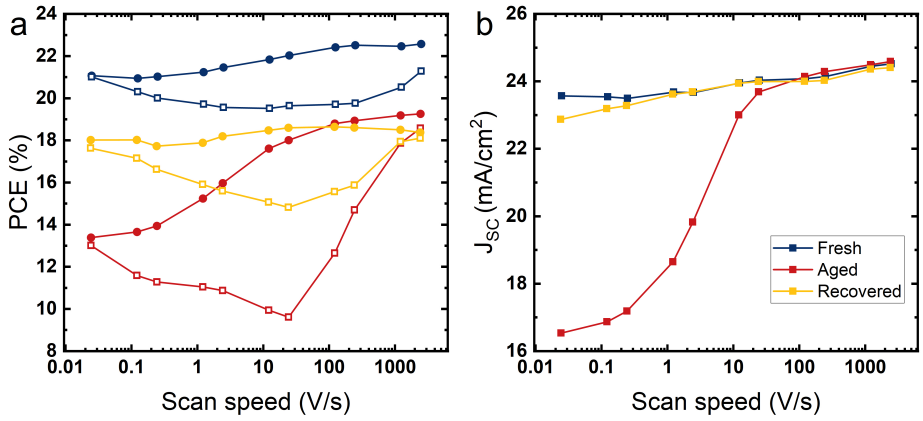

Figure 5.13: a PCE and b J_{SC} as a function of scan speed for a fresh, aged and recovered device

Interestingly, we observe that the mobile-ion-induced losses, which result from light- and bias-induced ageing, are, to some extent, reversible. Once the stressor is removed, and devices are kept in the dark, ion-induced losses can decrease, with resulting steady-state PCEs sometimes even reaching pre-ageing values. Figure 5.13 shows an example of such a recovery effect, where a device, after having been aged under light for 20 hours and displaying significant ion-induced losses, is left to recover in the dark for 8 hours. Such a recovery effect has been observed before[198,199], with the latter work also linking the effect to mobile ions. We observe that the revived

performance in these devices is accompanied by lower mobile ion densities determined from BACE measurements (Figure 5.14). The existence of such a recovery effect has interesting implications for the degradation of perovskite solar cells, as most devices, under realistic operating conditions, will experience a light-dark cycle, during which ion-induced losses may partially recover. We note, however, that once these recovered devices are subject to subsequent additional ageing, mobile-ion-induced losses increase more rapidly than they did when the devices were exposed to stressors for the first time. This may indicate that the mobile ions, once they have become mobile for the first time, require a lower activation energy to be released again.

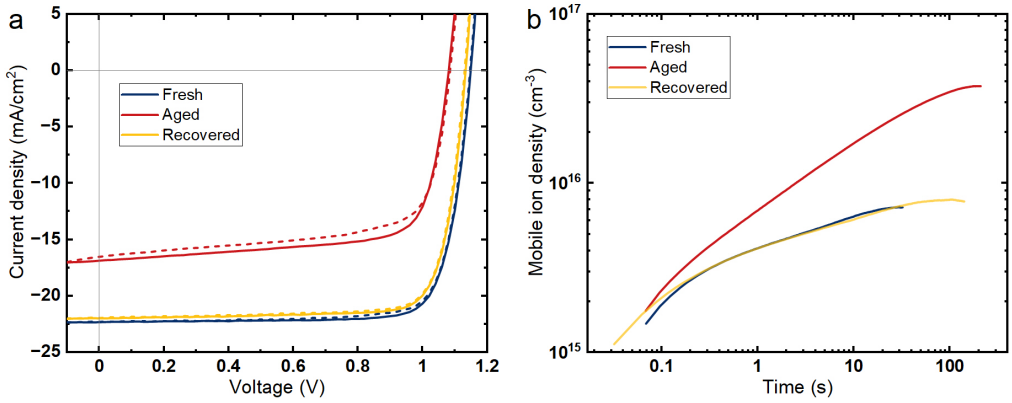

Figure 5.14: a) Steady-state JV scans and b) corresponding BACE results of a fresh, aged and recovered device. We note that these measurements were performed on a different device than was used in Figure 5.13. The device measured here was aged under light for 7 hours, and subsequently left to recover in the dark for 12 hours.

To recap, the mobile ion induced efficiency losses observed in the FH measurements dominate the early degradation loss in the here-tested halide perovskite compositions. Based on various measurements such as PL and BACE, we attribute these enhanced mobile ionic losses to an increasing mobile ion density upon ageing. Figure 5.17a shows a breakdown of the identified degradation losses under illumination for the 83:17 triple cation system. The J_{SC} and FF loss due to the movement of mobile ions is attributed to the field screening effect, the loss due to the QFLS-V_{OC} mismatch which is likely also a mobile-ion-induced loss, and other, yet unspecified loss processes.

Figure 5.17b-d schematically illustrates a possible explanation of the observed J_{SC} and FF losses and the QFLS-V_{OC} mismatch. The increased mobile ion density during the ageing successively screens the internal (built-in) field, thus increasing the fraction of the active layer which is effectively under V_{OC} (or flat band) conditions. The formation of the zero-field region under short-circuit conditions leads to an increased accumulation of electronic charges (e^- and h^+) at the hole selective interface. This charge accumulation leads in turn to enhanced recombination at the hole transport layer and in the bulk. We note that the reason why the p-interface is more affected than the electron-selective interface is that we consider positively charged mobile ions (halide vacancies) which screen the field at the hole transport layer. Likewise, the electron-selective interface would be more strongly affected in the case of a dominant negative mobile ion species.

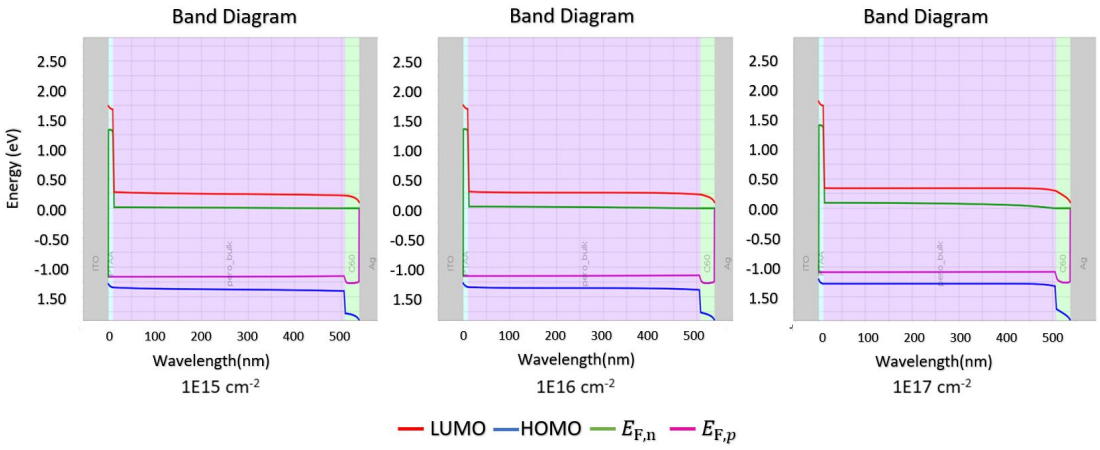

Figure 5.15: Simulated band diagrams at V_{OC} for devices with a V_{BI} of 1.5 V with different mobile ion densities. It can be seen that increasing mobile ion densities lead to a stronger QFLS bending closer to the perovskite – C_{60} interface. We attribute this effect to a mobile ion induced barrier which reduces the electron density. The QFLS in the bulk remains nearly constant (1.167 eV, 1.162 and 1.154 eV) for mobile ion densities of 10^{15}, 10^{16} and 10^{17} cm^{-3} respectively. However, despite the near-constant QFLS, the V_{OC} of the simulated JV curves is strongly reduced with increasing mobile ion densities, dropping from 1.165 through 1.140 to 1.077 V.

To explain the observed QFLS-V_{OC} mismatch with increased mobile ion densities, we analyse the band diagrams at V_{OC} conditions displayed in Figure 5.15 for devices with different mobile ion densities. The graph shows that higher mobile ion densities

cause a larger electron QFL bending ($\vec{\nabla}E_{f,e}$) at the C_{60} interface. The bending of the electron QFL can be explained by a population inversion of electronic charges at the electron selective interface, i.e. enhanced hole accumulation and depletion of electrons, in case of an enhanced cation vacancy concentration (Figure 5.16 d). Considering that at V_{OC}, $\vec{\nabla}E_{f,e}$ depends on the electron and hole conductivities and the gradient of the hole QFL, i.e. $\vec{\nabla}E_{f,e} = \frac{\sigma_h}{\sigma_e} \cdot \vec{\nabla}E_{f,h}$[18,200,201], allows us to conclude that the mobile ions are likely also responsible for the observed QFLS-V_{OC} mismatch and the reduction of the V_{OC}. Finally, while there might be some small bulk recombination losses at short-circuit conditions depending on the diffusion length in the absorber layer as shown in Figure 5.17d, the recombination at the interfaces increases more rapidly with enhanced cation vacancies at 0 V. Moreover, the interfacial recombination current scales faster with the applied forward bias voltage than the bulk losses, thus affecting the FF more significantly (Figure 5.17d).

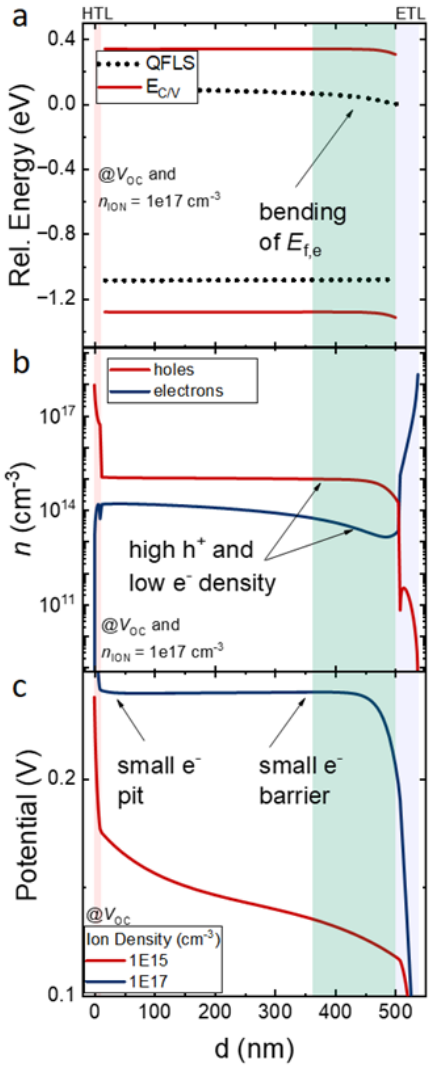

Figure 5.16: a The band diagram showing the conduction and valence band as well as electron and hole quasi-Fermi levels (QFLs) for a device with a V_{BI} of 1.5 V at its V_{OC} (1.14) reveals a bending of the electron QFL at the C_{60} interface. b The carrier density profile at V_{OC} shows an excess of holes in the device, while the electron density drops in the vicinity to the C_{60} layer. This is due to the screened internal field in case of the higher mobile ion density which is shown in panel c. Considering that the total (electron and hole) current depends on the conductivity and the gradient of the QFL, i.e. $J_{e/h} = \sigma_{e,h}/e * \nabla E_{f,e/h}$ and that the electron and hole current have to be equal at V_{OC}, follows that: $\frac{\sigma_h}{\sigma_e} = \frac{\nabla E_{f,e}}{\nabla E_{f,h}} \rightarrow \nabla E_{f,e} = \frac{\sigma_h}{\sigma_e} \cdot \nabla E_{f,h}$.[18,200,201] Because the conductivity of holes is greatly enhanced at the electron-selective interface, while the electron conductivity is strongly decreased (inversion population) allows us to conclude that the electron QFL bends at the C_{60} interface.

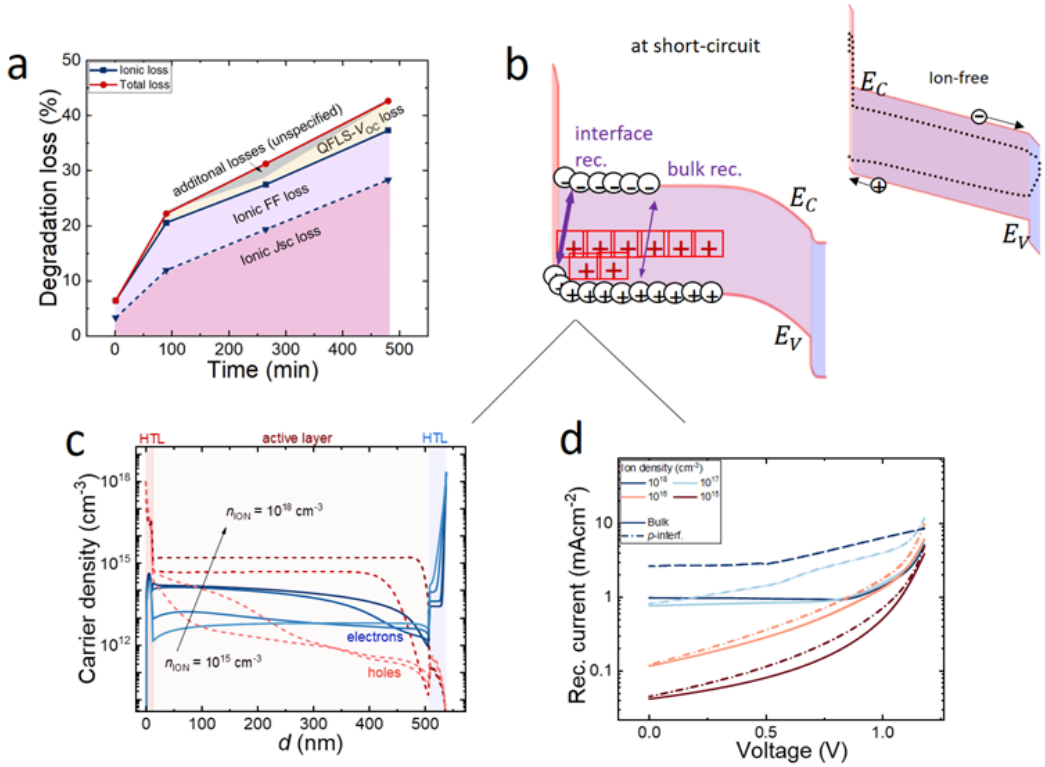

Figure 5.17: a) Breakdown of loss processes: mobile-ion-induced J_{SC} and FF losses, mismatch of the QFLS and V_{OC} that we also attribute to accumulation of mobile ions at the interfaces and other losses. b) Schematic band diagram at short-circuit conditions highlighting the accumulation of cation vacancies at the HTL interface (p-interface) that leads to enhanced hole accumulation (red dashed lines) and electron accumulation (blue solid lines) close to the HTL as shown in c. d) The recombination current at the p-interface and in the bulk as a function of applied voltage for different mobile ion densities. The inset in (b) reveals the ion-free case.

5.3 Conclusion

In this chapter, we investigated the impact of mobile ions on the ageing-induced performance degradation of perovskite solar cells under different external stressors, with a focus on light-induced degradation and we thoroughly studied the underlying mechanisms behind the observed losses. We reveal a new degradation mechanism as a dominant factor in the early intrinsic degradation that has previously not been clearly identified, namely mobile-ion-induced field screening. The mobile ionic losses manifest as a strongly reduced J_{SC}, which overall suffers most significantly under the illumination in the studied compositions while the FF and the V_{OC} are also affected by

the mobile ions. With regard to the voltage losses, we found that they are caused by an increased QFLS-V_{OC} mismatch, and not due to increased interfacial defects at the perovskite-transport layer interfaces. This QFLS-V_{OC} mismatch occurs in various systems and can also be explained by an increased mobile ion density. Using different transient charge extraction techniques, we then linked the increasing current and fill factor losses upon ageing to an increase in the concentration of mobile ions in the perovskite. We showed that the increase of mobile ion concentrations upon ageing is a general degradation mechanism, which occurs also when devices are aged through exposure to other stressors, such as electrical bias. However, the ion-induced losses are more significant in the presence of free electrical charges and less under elevated temperatures, consistent with previous findings of halide vacancy generation through holes. In the future, perovskite solar cells need to be engineered to minimise both the mobile ion densities that can be generated during ageing as well as their impact on the device performance. For example, our results highlight the key role of the hole selective interface for the initial degradation in case of large halide vacancy concentrations. By providing a crucial understanding of mobile ions and their role in device performance degradation, this work paves the path for the development of accelerated ageing tests based on ionic characteristics. This will allow us to identify stable conditions as well as potential mitigation routes more rapidly, which is key for the commercialisation of perovskite-based solar cells.

CHAPTER 6

Understanding and minimising V_{OC} losses in all-perovskite tandem solar cells

The work presented in this chapter is based on:

J. Thiesbrummel, F. Peña-Camargo, K. O. Brinkmann, E. Gutierrez-Partida, F. Yang, J. Warby, S. Albrecht, D. Neher, T. Riedl, H. J. Snaith, M. Stolterfoht, F. Lang, "Understanding and minimizing V_{OC} losses in all-perovskite tandem solar cells", Advanced Energy Materials, 2023, 13, 2202674. https://doi.org/10.1002/aenm.202202674

6.1 Introduction

With the discovery that mixed-metal halide perovskites enable much lower bandgaps than their neat-lead or neat-tin based counterparts, significant efforts commenced on the development of all-perovskite tandem solar cells.[61,93,96,202,203] Combining low-bandgap (LG) and high-bandgap (HG) perovskites in tandem solar cells overcomes the fundamental efficiency limits of their single junction counterparts, without the need for combining with more traditional low-bandgap materials used previously such as Si or copper indium gallium selenide.[204–208] All-perovskite tandems promise highest efficiencies, on par with perovskite/silicon tandem technologies, while using much thinner absorber layers, and move away from the energy-intensive production of crystalline silicon. They can also be much lighter, which makes them a promising option for a range of different applications: from building- or vehicle-integrated photovoltaics (PV) to high-altitude and even space PV where they also benefit from their radiation hardness.[144] Their energy-efficient processability, either from solution or by thermal evaporation at ambient temperatures, is roll-to-roll compatible and could allow a much more cost-efficient technology with shorter energy payback times compared to current technologies, or even perovskite/Si tandem PV.[209]

The solar to electrical power conversion efficiency (PCE) for 2-Terminal all-perovskite tandems has increased from 17% for the first attempts, to the current record of 26.4%.[79,93,210] We give an overview of this rapid progress in Figure 6.1a, by plotting the employed bandgap combinations and the achieved power conversion efficiencies, alongside a realistic efficiency potential of $\approx 0.75 \times \mathrm{PCE}_{\mathrm{rad}}$. Here $\mathrm{PCE}_{\mathrm{rad}}$ is the radiative efficiency from the detailed balance limit assuming a step function absorption profile for each bandgap. A large focus has been on improving the efficiency and stability of the low-bandgap lead-tin perovskite.[61,79,80,115,211] However, as we illustrate in Figure 6.1b, the high-gap perovskites dominate the open-circuit voltage (V_{OC}) losses for most tandem devices, especially after significant improvement of low bandgap perovskites over the past 3 years. Overcoming the V_{OC} losses in the high-gap

perovskite subcell, which typically increase for higher bandgap perovskites,[170,172,212] therefore offers room for further improvements. Moreover, the incorporation of the high-gap and low-gap perovskites in a tandem device often leads to significant additional V_{OC} penalties. This can be due to degradation of the underlying subcell or layers during subsequent layer deposition, be it via sputtering or from solution, additional interfacial recombination induced by the interconnecting layer, or processing issues and inhomogeneities. We highlight several of those cases with a "D" in Figure 6.1b.

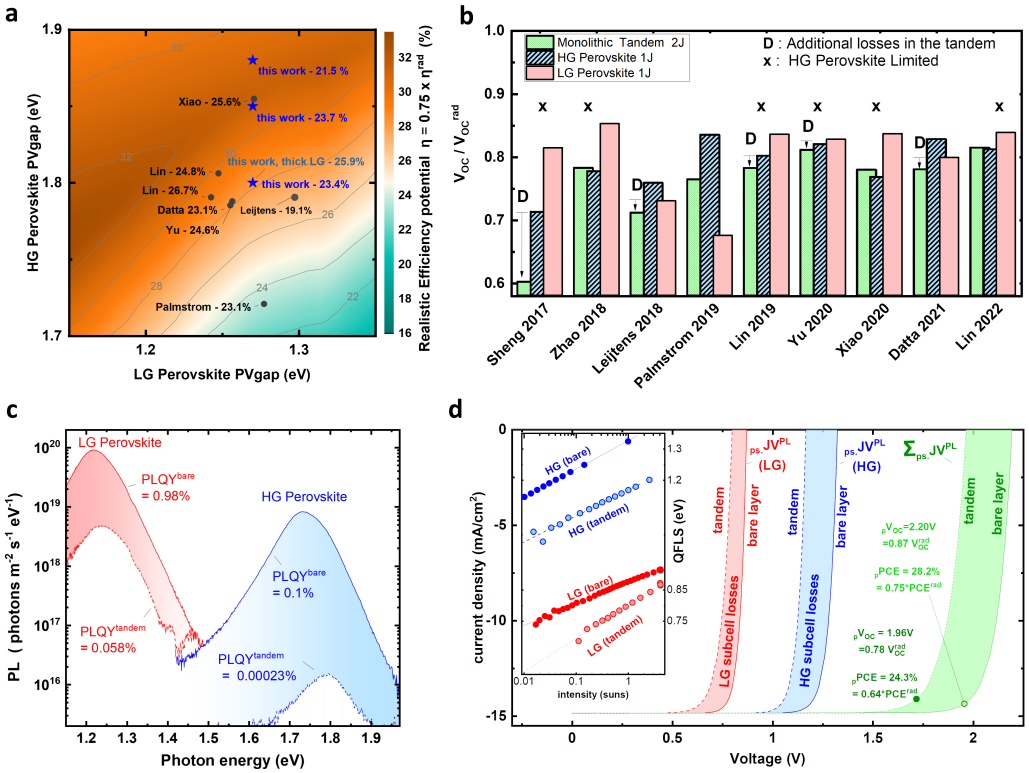

Figure 6.1: a) Literature overview of various all-perovskite tandem solar cells indicating the achieved efficiency, plotted as a function of the employed high-and low-bandgap perovskites. For consistency, we determined the individual bandgaps from reported external quantum efficiencies (EQE), via d(EQE)/dE, and denoted this as PVgap. The colour map displays the realistic efficiency potential for specific bandgap combinations (defined as 75% of the radiative efficiency limit). b) Relative V_{OC} losses in monolithic all-perovskite tandems from (a), as well as the corresponding high-gap and low-gap single junction devices.[75,79,80,213–219] c) Photoluminescence (PL) of high- and low-gap perovskites fabricated individually on glass (isolated bare layers) and incorporated in a monolithic tandem. d) Pseudo-JV curves reconstructed from intensity-dependent PL measurements highlighting V_{OC} losses.

To understand where these losses come from and how they can be reduced, it is important to not just look at the overall tandem performance and single junction cells,

but characterise the behaviour of both subcells when incorporated in the complete tandem device. Traditional electrical characterisation of the monolithic tandem, however, provides little information on the behaviour of the individual subcells. Current-voltage JV measurements performed on corresponding single junction devices that are often reported alongside tandem results and used in Figure 6.1b, do not necessarily reflect subcell performance once integrated in the tandem accurately. Quantitative measurements that provide information on the different subcells within the monolithic tandem stack individually are therefore crucial to understand performance-limiting layers and mechanisms. Electro- and photo-luminescence (EL & PL) can be measured from each subcell selectively in monolithic interconnected tandem devices. These techniques have previously been employed by the III/V solar cell community to investigate subcell performance in multijunction solar cells.[220–223] We recently extended these approaches to reveal efficiency limits in perovskite/silicon tandems.[144] However, although 2-terminal all perovskite tandem cells have become a topic of great interest, and subcell selective characterisation can provide valuable insights to accelerate development, such an extensive subcell selective characterisation has to date never been carried out for these systems.

Herein, we conduct extensive PL and EL characterisation of isolated perovskite films, single-junction devices, and complete all-perovskite tandem cells, in order to identify the factors limiting the performance in these cells in comparison with the thermodynamic efficiency limit. We reveal that the high-bandgap subcell is predominantly responsible for the V_{OC} losses in our own complete tandem devices, as well as in many tandem devices from literature at the moment. We employ a threefold optimisation strategy for the high-bandgap perovskite, consisting of; i) addition of oleylamine to the perovskite in combination with, ii) a lithium fluoride (LiF) layer between the perovskite and the electron transport layer (ETL) and, iii) the use of the self-assembled monolayer (SAM) 2PACz instead of the frequently used hole transport layer (HTL) poly[bis(4-phenyl)(2,4,6-trimethylphenyl)amine (PTAA). We apply our threefold optimisation approach to triple cation-based high-gap perovskites with bandgaps ranging from 1.80

through 1.85 to 1.88 eV and find a robust reduction of V_{OC} losses for all tested bandgaps. This is important since the latter two bandgaps promise highest power conversion efficiencies in combination with the 1.27 eV perovskite used herein (Figure 6.1b). We thereafter use the optimised high-gap perovskites to fabricate efficient all-perovskite tandem solar cells, reaching steady-state efficiencies of up to 23.4%, 23.7%, and 21.5% for 1.80 eV/1.27 eV, 1.85 eV/1.27 eV and 1.88 eV/1.27 eV bandgap combinations, respectively. Coming back to the subcell characterisation, we then characterise these optimised all-perovskite tandems, and are able to determine the efficiency potential that could be achieved if transport losses and energy-level mismatches in the stack were eliminated. Furthermore, we also show that the interconnect we employed is lossless. Overall, our versatile subcell characterisation approach will facilitate evidence-based optimisation of future all-perovskite tandem cells.

All tandem devices presented in this chapter were fabricated through collaboration, with Francisco Peña-Camargo fabricating the HG subcell, Kai O. Brinkmann fabricating the interconnect, and myself fabricating the LG subcell. Optimisation of the HG subcell was carried out by Francisco Peña-Camargo. Measurements were carried out with Felix Lang.

6.2 Results

6.2.1 Assessing the limiting junction in the tandem cells

In order to investigate whether the V_{OC} losses in our all-perovskite tandems are dominated by the high- or the low-gap perovskite subcells, we measured the photoluminescence quantum yield (PLQY) selectively by excitation with 520 and 818 nm in a monolithic all perovskite tandem (based on a 1.27 eV low-gap and 1.80 eV high-gap combination with an efficiency of 20.9% under AM1.5G) and compared it to the PLQY of identically prepared isolated high-gap (PLQY = 0.1%) and low-gap (PLQY = 0.98%) perovskite layers on glass (Figure 6.1c). Interestingly, the PLQY

of the high-gap perovskite is reduced by three orders of magnitude in the tandem device, compared to the isolated layer, whereas the low-gap perovskite is only reduced ≈20-fold. Since the quasi-Fermi level splitting (QFLS) is directly given by the PLQY and the radiative limit of the semiconducting material ($QFLS_{rad}$, see Chapter 3) via Equation 6.1, we conclude that the high-gap perovskite strongly dominates V_{OC} losses also in our system.

$$QFLS = QFLS_{rad} + k_B T \cdot \ln(PLQY) \tag{6.1}$$

To further understand the potential of our tandem with the given absorbers, we now measure intensity-dependent photoluminescence yields (iPLQY) which allows us to determine a QFLS at each intensity. We then construct "pseudo-JV curves" by plotting the total recombination current at each excitation intensity minus the generation current (J_{SC}) on the y-axis versus the QFLS on the x-axis (Figure 6.1d). Comparison of pseudo-JV curves derived from iPLQY measurements on isolated films versus measurements in the monolithic tandem stack exemplifies V_{OC} losses present in the tandem configuration. It also shows that these losses are dominated by the high-gap perovskite. Summing the QFLS obtained for the high-gap and low-gap perovskite isolated layers and subcells further allows us to construct pseudo-JV curves of corresponding tandems that are free of resistive losses and, in case of the isolated layers, additionally free of interface recombination from the various contact layers, processing damage, etc. This efficiency potential constructed from isolated layer measurements reaches 28.2%, a value that corresponds to the practical efficiency potential of around 0.75 × PCE_{rad}. We present a more detailed analysis as well as strategies to reach this potential at the end of this chapter.

6.2.2 Minimisation of V_{OC} Losses in HG Perovskites

To understand the origins of V_{OC} limitations in our high-gap perovskite we measured the PLQY of 1.80 eV bandgap triple-cation based perovskites

($Cs_{0.05}(FA_{0.60}MA_{0.40})_{0.95}Pb(I_{0.60}Br_{0.40})_3$) with and without the hole and electron transport layers (HTL and ETL respectively). Comparing the PLQY of a perovskite layer prepared on glass and on PTAA, our standard HTL, as displayed in Figure 6.2a, reveals that the PTAA is strongly limiting the PLQY. This limitation is known and has been addressed in the past by using self-assembled monolayer (SAM) HTLs instead of conventional HTLs.[224,225] Their use as a hole selective contact can strongly reduce non-radiative losses at the perovskite—HTL interface compared to the conventionally used PTAA,[224] which is particularly a problem for wide-gap perovskites (>1.75 eV).[172]

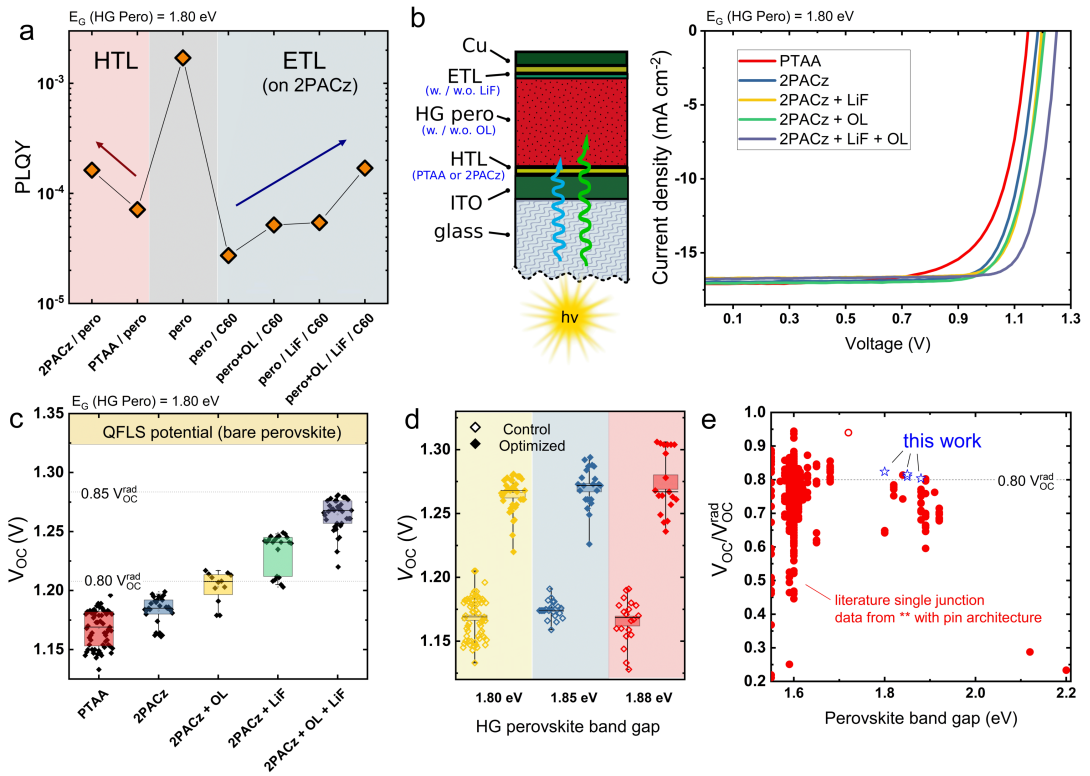

Figure 6.2: a) PLQY measured on different partial stacks. b) Schematic overview of the HG single junction solar cell and JV curves for 1.80 eV $Cs_{0.05}(FA_{0.60}MA_{0.40})_{0.95}Pb(I_{0.60}Br_{0.40})_3$ perovskite solar cells for various optimisation steps. c) The V_{OC} from the solar cells in (b), plotted as a function of the different optimisation steps. The dashed line displays the radiative V_{OC} limit (V_{OC}rad), which is 1.51 V for perovskites with a 1.80 eV bandgap. d) V_{OC} statistics for optimised and control HG perovskite solar cells with bandgaps of 1.80, 1.85, and 1.88 eV. e) The V_{OC} divided by the radiative V_{OC} limit for recent pin perovskites with a range of different bandgaps, extracted from The Perovskite Database.[212] The open circle indicates a device with an ETL based on an alternative fullerene blend.[226] The stars indicate our results and show optimised (champion) solar cells based on perovskites bandgaps at 1.80, 1.85, and 1.88 eV. HG optimisation was performed by Francisco Peña-Camargo.

Changing the HTL from PTAA to 2PACz significantly improves the PLQY of our 1.80 eV triple-cation based perovskites (Figure 6.2a), indicating a reduction of interfacial recombination at the HTL side, which was strongly limiting before. Having removed the dominating HTL-Pero-interface limitation now allows us to address the perovskite-ETL interface. We first try inserting a thin layer of LiF between the perovskite and the ETL, which is suggested to be forming a strong surface dipole that repels minority carriers away from the interface, thereby reducing interfacial recombination.[188,225,227] In order to reduce the recombination losses further, we then added oleylamine into the perovskite precursor solution, which has previously been shown to improve the efficiency of lead-based perovskite solar cells through both grain- and interface modifications.[228] Interestingly when we tested a combined approach of adding oleylamine to the perovskite precursor and inserting a thin LiF layer we found that they worked in an additive fashion, increasing the QFLS to exactly the sum of the individual improvements (Figure 6.2a).

We subsequently fabricated single junction solar cells with the structure glass/ITO/PTAA or 2PACz/1.80 eV bandgap triple-cation based perovskite w/ or w/o oleylamine and w/ or w/o LiF/ETL/Cu to test our threefold optimisation approach prior to its incorporation into tandem devices. Looking at the JV curves displayed in Figure 6.2b, it can be seen that the improvement in PLQY directly translates into an increased V_{OC} in devices. As seen in Table 6.11, summarising device parameters and statistics (more statistics can be found in Figure C.6, Appendix C), the V_{OC} improves ≈90 mV for the fully optimised device compared to control devices, which equals the sum of the individual gains. Figure 6.2c shows that every step of our threefold optimisation brings the V_{OC} significantly closer toward the limit imposed by the bulk quality of the perovskite absorber, which is 1.32 V as determined from PLQY measurements of isolated perovskite absorbers. Notably, the threefold optimised devices reach an average V_{OC} of 1.26 V (max 1.29 V) which is around 83% of the radiative V_{OC} limit of 1.51 V for devices with a 1.80 eV bandgap. Ultimately, we tested the long-term stability of our threefold passivation approach step by step by tracking

the efficiency under AM1.5G or equivalent illumination conditions and found that fully passivated devices outperform control devices, see Figures C.8 and C.9, Appendix C.

	V_{OC} [V]	J_{SC} [mA cm^{-2}]	FF [%]	PCE [%]	ΔV_{OC} [mV]	ΔFF [%]
PTAA device	1.17 $\pm$ 0.02	17.0 $\pm$ 0.5	75.6 $\pm$ 2.9	15.0 $\pm$ 1.0	-	-
2PACz device	1.18 $\pm$ 0.01	17.2 $\pm$ 0.7	78.8 $\pm$ 1.4	16.1 $\pm$ 0.6	10	3.2
2PACz + OAm	1.20 $\pm$ 0.01	17.1 $\pm$ 0.2	77.2 $\pm$ 2.0	15.9 $\pm$ 0.7	30	1.6
2PACz + LiF	1.23 $\pm$ 0.02	17.1 $\pm$ 0.5	78.9 $\pm$ 2.0	16.6 $\pm$ 0.6	60	3.3
2PACz + OAm + LiF	1.26 $\pm$ 0.01	16.6 $\pm$ 0.5	79.1 $\pm$ 2.0	16.6 $\pm$ 0.6	90	3.5

Table 6.1: Device parameters and statistics for the different optimised and control single junction devices using a 1.80 eV HG perovskite absorber. ΔV_{OC} and ΔFF indicate the improvement in these respective values compared to the unoptimised control device on PTAA

We tested the robustness of this threefold optimisation route with various high-bandgap perovskite compositions by varying the Br-ratio from the initial 0.4 to 0.45 and 0.5. This allowed us to vary the perovskite bandgap from 1.80 eV to 1.85 and 1.88 eV respectively, as determined from EQE. Control devices based on the 1.85 and 1.88 eV perovskites both reached 1.17 V V_{OC} on average, see Figure C.7, Appendix C. Using our threefold optimisation significantly improved the V_{OC} to 1.27 V and 1.28 V, thereby achieving remarkable $V_{OC}/V_{OC,rad}$ ratios of 0.82 and 0.81, respectively, as can be seen in Figure 6.2d. This improvement becomes even more apparent when comparing our achieved V_{OC} with data obtained from literature. In Figure 6.2e we display the ratio of the V_{OC} divided by the $V_{OC,rad}$ as a function of the perovskite bandgap for a large number of perovskite pin devices, extracted from The Perovskite Database.[212] Clearly visible is a general trend of decreasing $V_{OC}/V_{OC,rad}$ with increasing bandgap.[229] This effect has been assigned to different phenomena, from halide segregation (or Hoke effect), to interface recombination, improper energy alignment, or high defect densities at the surface of the perovskite.[170,172,230] There is also evidence to suggest that the use of C60 as an ETL is the cause of the limited V_{OC}s, with other fullerenes (or fullerene blends) showing promise to overcome these issues (open circle in Figure 6.2e).[226]

Our optimised 1.80, 1.85, and 1.88 eV perovskite based single junction devices (blue stars) thereby reach comparatively high $V_{OC}/V_{OC,rad}$ ratios, well above 0.8. This

highlights that our threefold optimisation route which was initially developed for the HG perovskite with a bandgap of 1.80 eV, is applicable to a wider range of perovskite compositions. A robust passivation strategy is critical for future all-perovskite tandem development to unlock highest efficiencies with optimal HG - LG bandgap combinations, as shown in Figure 6.1a.

6.2.3 Implementation in tandems

In the next step, we integrated our threefold optimised high-gap perovskites into monolithic all-perovskite tandems. For this purpose, we use a 1.27 eV (as determined by d(EQE)/dE) low-gap $FA_{0.83}Cs_{0.17}Pb_{0.5}Sn_{0.5}I_3$ perovskite subcell, which we deposited on top of the high-gap subcells. The complete layer stack comprises glass/ITO/PTAA or 2PACz/HG-Perovskite/C60/AZO-nanoparticles/ALD-SnOx/ALD-InOx/PEDOT:PSS/LG-Perovskite/C60/BCP/copper as shown in Figure 6.3a alongside a cross-sectional scanning electron microscopy image of the all-perovskite tandem structure. Our recombination layer comprises an ultrathin (≈1.5 nm) layer of indium oxide, like we have reported previously for perovskite/organic tandem solar cells.[231] This indium oxide layer is deposited by atomic layer deposition (ALD) on top of a hybrid AZO-NP/ALD SnOx layer that functions as an internal barrier layer, stabilising and protecting the layers underneath from follow-up processing.[162,163] This is the first time that such an interconnect is implemented in a perovskite/perovskite tandem structure.

As seen in the JV characteristics in Figure 6.3b, our all-perovskite tandems with optimised HG perovskite subcells reach a much higher V_{OC}, than the non-optimised control tandems. The improvement in V_{OC}, of ≈120 mV, is consistent with the improvement observed in the optimised HG single junctions, and we present a more detailed subcell analysis later on. Optimised tandems reach 78% of their radiative V_{OC} limit, see Figure 6.3c and maximum power point (MPP) tracking, displayed in

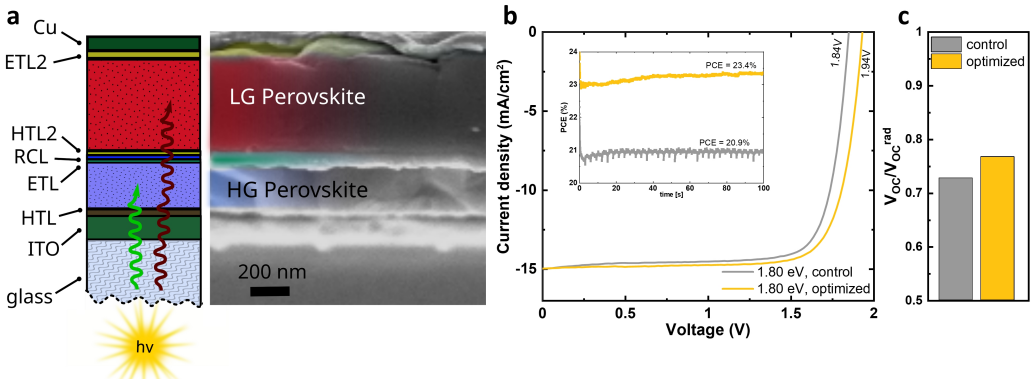

Figure 6.3: a) Schematic overview of the all-perovskite tandem structure alongside a cross-sectional scanning electron microscopy (SEM) image of an all-perovskite tandem with optimised HG perovskite. b) JV curves of a tandem with optimised 1.80 eV HG perovskite subcell, and a control tandem. In the inset, MMP tracking is displayed for both of these devices. The optimised wide-gap cell directly translates into improved tandem cell devices with efficiencies reaching over 23%. c) $V_{OC}/V_{OC,rad}$ ratios for the control and optimised tandems displayed in (b). SEM by Emilio Gutierrez-Partida.

the inset of Figure 6.3b, shows that the optimised all-perovskite tandems reach PCEs of 23.4%, an improvement of ≈2.5% absolute compared to the control tandems.

In order to optimise the efficiency of the tandems further, we then implemented the three previously optimised high-gap perovskite compositions. The bandgap shift from 1.80 to 1.85 eV and 1.88 eV can be well seen in external quantum efficiency (EQE) spectra in all-perovskite tandems made thereof (Figure 6.4a). Naturally, the three different high-gap subcells also influence the absorption onset of the LG perovskite. Using different bandgaps allowed us to improve the current matching between the HG and LG subcells, which is crucial for a monolithic tandem interconnection (see Figure C.1 and Figure C.5, Appendix C for integrated EQE values and the current mismatch between HG and LG subcells, respectively).

As shown in Figure 6.4b, the V_{OC} of fabricated all-perovskite tandems increases with increasing HG-perovskite bandgap, and best performing all-perovskite tandems based on a 1.85 eV HG-perovskite reach 23.7% according to MPP tracking with a champion V_{OC} of 2.00 V. The forward and reverse JV of this champion device can be found in Figure 6.5.

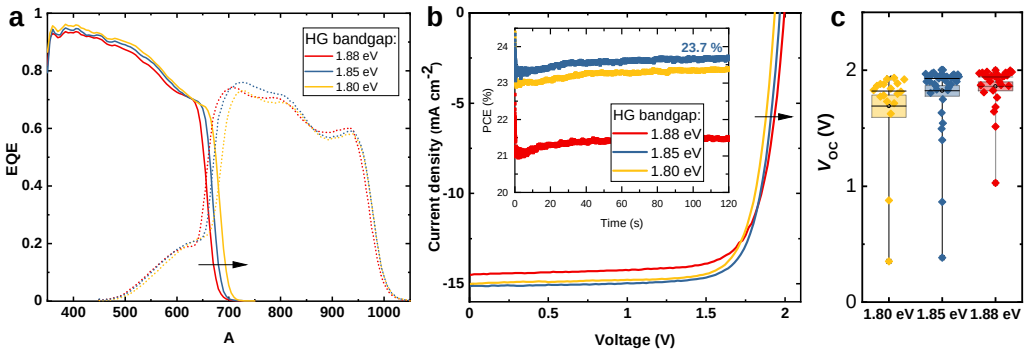

Figure 6.4: a) EQE spectra for all-perovskite tandems fabricated using three different HG perovskite bandgaps. These spectra alongside the integrated J_{SC} values are shown in Figure C.1, Appendix C . We note that the high EQE at low wavelengths can be explained by light incoupling from ITO due to the high refractive index of the perovskite absorber material.[232] b) JV curves for representative tandems with three different HG perovskite bandgaps. Best performing MPP tracking is displayed in the inset. c) Statistical overview of the V_{OC} for the different tandem systems. Further device statistics can be found in Figure 6.6. EQE measured with Felix Lang and Francisco Peña-Camargo.

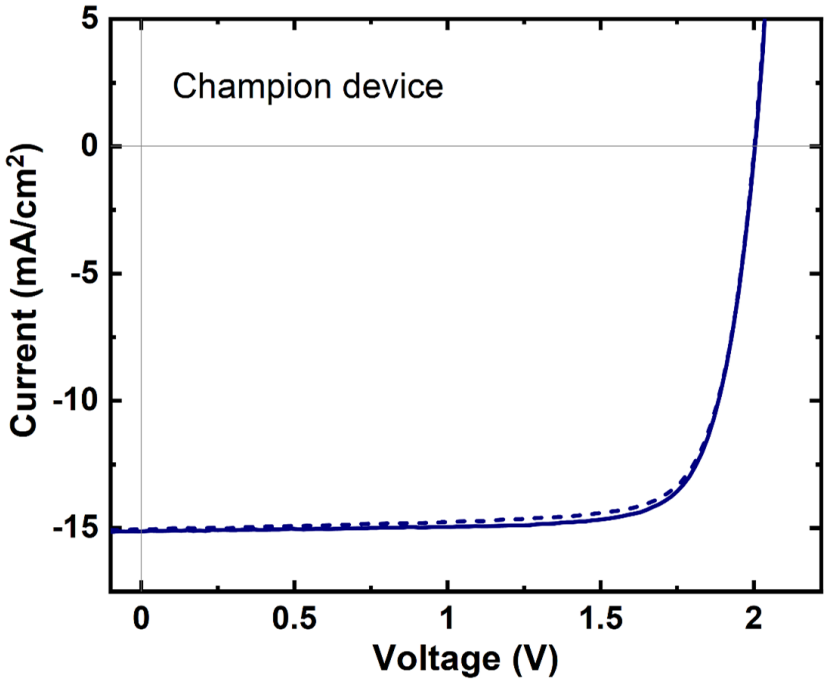

Figure 6.5: Forward and reverse JV scan of the champion device, based on a 1.85 eV HG perovskite in combination with a 1.27 eV LG perovskite. Device parameters are: J_{SC} = 15.1 mA/cm^2, V_{OC} = 2.00 V, FF = 78.6 %, PCE = 23.8 % (reverse) and J_{SC} = 15.0 mA/cm^2, V_{OC} = 2.00 V, FF = 77.8 %, PCE = 23.4 % (forward).

Interestingly, the J_{SC} of our 1.80/1.27 eV tandem combination exhibits a relatively high J_{SC} equal to the integrated EQE from the HG subcell, although this tandem combination should be limited by the LG subcell producing a somewhat lower integrated

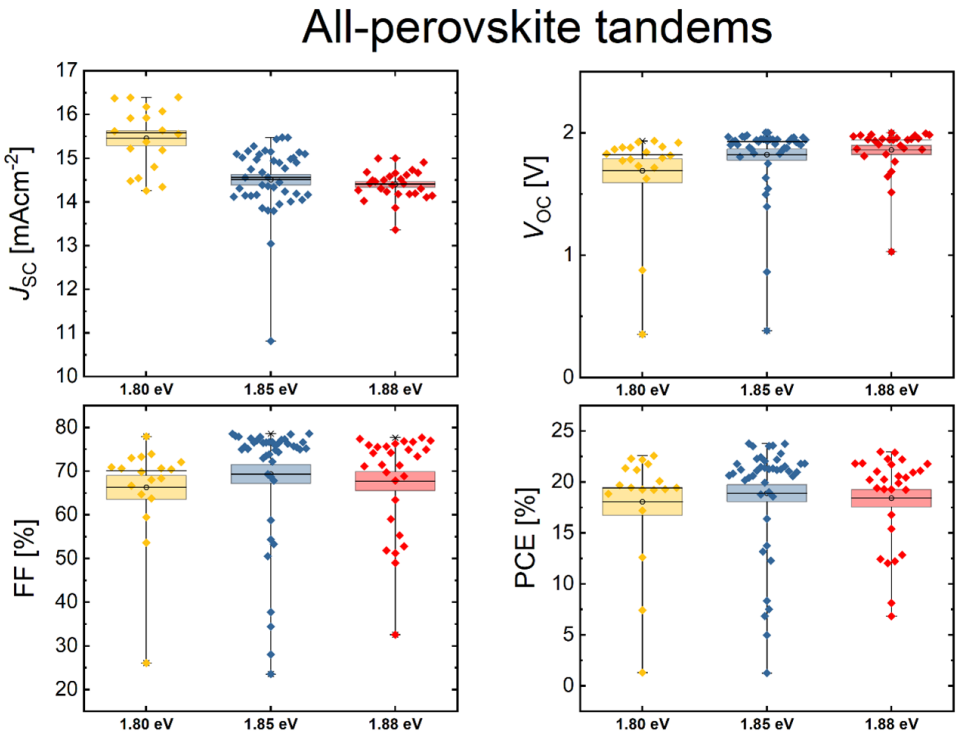

Figure 6.6: Cell statistics for the optimised all-perovskite tandem solar cells based on 1.80, 1.85 and 1.88 eV high gap perovskites.

EQE current. We performed all measurements with an illumination mask and confirmed that the spectral mismatch between our sun simulator and AM 1.5G is very small (see Figure C.4, Appendix C) to exclude potential overestimations and thereby confirm that the J_{SC} measured from JV is correct and not overestimated. Device statistics, displayed in Figure 6.6, further corroborate that our tandems—especially the 1.8/1.27 eV HG/LG combination - can operate at output currents which are higher than would be expected with a strict current matching, as the output current of the tandem exceeds that of the LG subcell (which has the lower output of the two subcells, and should therefore normally be current limiting). We believe this is caused by a rather low shunt resistance within the LG subcell, and show electrical simulations and subcell selective resistive photovoltage measurements highlighting the existence and the impact of low shunt resistances in the LG subcell on tandem solar cell operation and performance in the Appendix (see the note on current matching in Appendix C

as well as Figures C.2 and C.3, Appendix C). Importantly, Figure C.3, Appendix C , also shows that while the observed shunts in the LG cell can lift the current matching condition, the shunts will still reduce the PCE due to a concurrent reduction in FF, thus not causing an overestimation of the PCE. Indeed, looking at a statistical analysis of our fabricated devices we observe that the 1.80/1.27 eV tandem combination exhibits a larger J_{SC} but lower FF in comparison to the better current matched 1.85/1.27 eV and 1.88/1.27 eV combinations (see Figure 6.6).

6.2.4 Subcell analysis

In order to get a deeper insight into the factors limiting the performance of these optimised tandem solar cells, we performed more detailed subcell selective EL measurements. Hereby we apply a forward bias to the tandem device that injects a current into both subcells. EL within both subcells then can be measured in the dark and easily distinguished by their corresponding photon energy, for example, around 1.80, 1.85, and 1.88 eV for the HG-perovskite subcells and 1.27 eV for the LG-subcell respectively, see also EL spectra displayed in Figure 6.7. In order to measure the EL quantum yield (ELQY) as a function of injection current, we used appropriate long-pass and short-pass filters together with a large-area Silicon-photodiode. Analogous to the PL, we can calculate the $QFLS_{EL}$ from the measured ELQY for each injection current J_{inj} using Equation 6.2.

$$QFLS_{EL} = k_B T \cdot \ln\left(\frac{ELQY \cdot J_{inj}}{J_{0,rad}}\right) \tag{6.2}$$

Sample/Condition	HG Pero	LG Pero
1.27/1.85eV optimized	2.64E-24	3.37E-15
1.27/1.85eV control	2.76E-24	2.86E-15
1.27/1.80eV control	8.90E-24	3.08E-15

Table 6.2: Values of the radiative dark recombination current $J_{0,rad}$, as calculated from EQE. Calculation details are given in Chapter 2, see Equations 3.5 and 3.6.

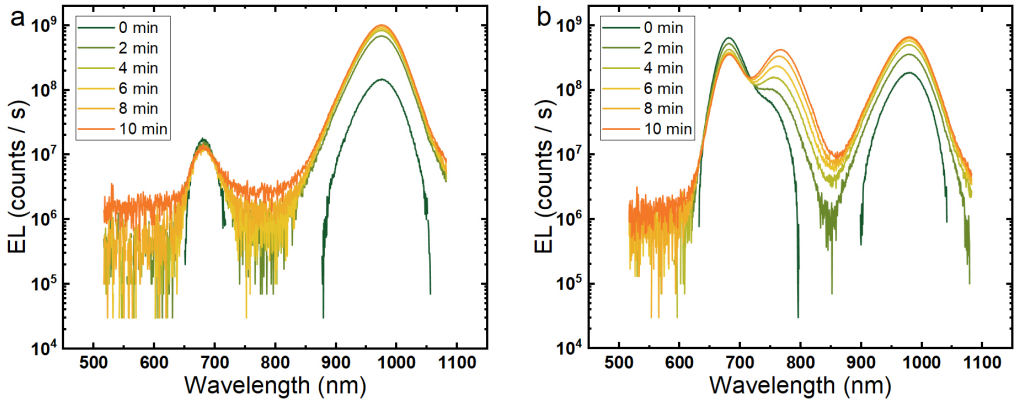

Figure 6.7: EL spectra while continuously applying V_{OC} to the cell for a) a tandem with the control HG perovskite and b) a tandem with the optimised HG perovskite. The optimised HG perovskite displays an increased EL, but also a stronger halide segregation. The emission from the segregated phase was not considered in the determination of the QFLS. The reasons for this were recently discussed in ref.[233].

Radiative dark current $J_{0,\mathrm{rad}}$ values were calculated from EQE measurements, as detailed in the experimental methods, and we summarise results in Table 6.2 for the different perovskites. Plotting the implied or pseudo-voltage ($_{\mathrm{ps}}V_{EL} = \mathrm{QFLS}_{\mathrm{EL}}/e$) on the x-axis and the J_{inj} current minus J_{SC} ($J = J_{\mathrm{inj}} - J_{\mathrm{SC}}$) on the y-axis allows us to derive pseudo-light-JV curves from the measured ELQY values. The derived pseudo-JV-characteristics are not only free of parasitic transport losses but most importantly reveal pseudo-JV-characteristics of the individual subcells, which cannot be accessed using standard JV measurements under illumination. We show EL-pseudo-JV curves of the individual subcells for all-perovskite tandems based on the 1.85/1.27 eV bandgap combination in Figure 6.8a alongside the summarised pseudo-JV curves representing the resulting tandem as well as standard JV characteristics under AM1.5G. Open and closed symbols refer to control and threefold optimised HG subcells that we prepared within the same batch to avoid batch-to-batch variations. Comparison of the subcell pseudo-JVs clearly shows that the improvement in the tandem V_{OC} of ΔV_{OC}tandem $\approx$ 120 mV between control and optimised devices, directly results from the optimised HG subcell featuring an improvement of 120 mV. Both values are corroborated by the mean V_{OC} improvement of 0.10 V we observe when evaluating statistics as shown as inset in Figure 6.8a.

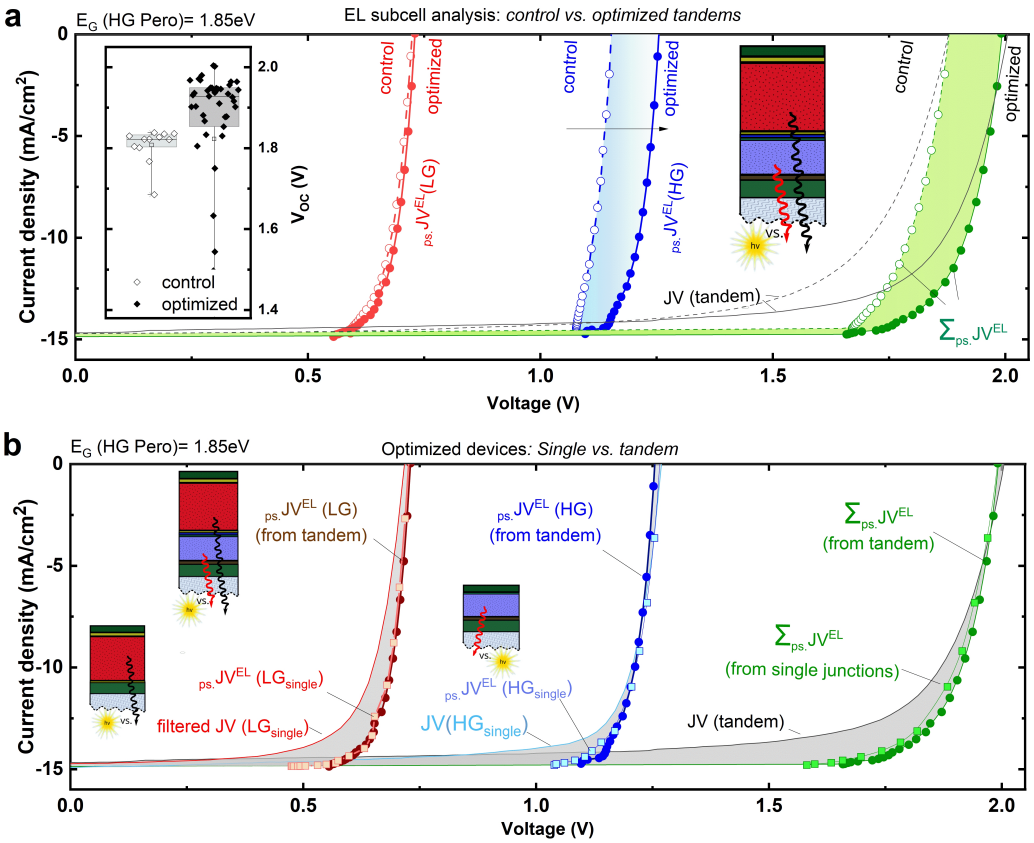

Figure 6.8: a) Pseudo JV curves from EL for an optimised and control tandem based on a 1.85 eV HG $Cs_{0.05}(FA_{0.55}MA_{0.45})_{0.95}Pb(I_{0.55}Br_{0.45})_3$ perovskite. Shown are the individual subcell pseudo-JV curves as well as the resulting (added) tandem pseudo-JV curves in comparison with traditional JV curves measured under AM1.5G. The inset displays V_{OC}s obtained from the JV curves of optimised and control tandems employing a 1.85 eV HG perovskite. b) Comparison between pseudo-JV curves obtained from an optimised 1.85/1.27 eV tandem and pseudo-JV curves obtained from single junctions based on the same perovskites. Corresponding JV curves for both single junction and tandem devices are plotted alongside to highlight FF losses. Measured with Felix Lang.

To analyse this V_{OC} improvement further, we compare in Figure 6.8b pseudo-JV characteristics of the optimised tandem (closed circles) to the corresponding EL-pseudo-JV characteristics of identically prepared single junctions (open square symbols). Notably, the LG perovskite pseudo-JVs in the tandem and in the single junction are identical, indicating that there are no V_{OC} losses stemming from the integration in the tandem device. The optimised HG perovskite shows a slight (≈20 mV) decrease in V_{OC} upon incorporation in a tandem device. This could be caused by the processing of the LG perovskite on top of the HG subcell, but the difference is so small it could also be the result of device-to-device variation. On

the other hand, the pseudo-FFs ($_{ps}$FF) and pseudo-PCEs ($_{ps}$PCE) of the HG subcell are improved in the tandem compared to $_{ps}$FF and $_{ps}$PCE of identically prepared HG single junctions. Our interconnect—comprising an ultrathin layer of indium oxide and a layer of tin oxide, both deposited by atomic layer deposition on top of a spin coated layer of Al doped ZnO nanoparticles previously only applied in perovskite/organic tandem[231]—therefore can be considered quasi lossless.

Finally, we compare in Figure 6.8b, the pseudo-JVs (symbols) to regular JV curves for HG and LG single junctions (lines) measured under AM1.5 and HG-filtered AM1.5G, respectively. It can be seen here that the V_{OC} and pseudo-V_{OC} ($_{ps}V_{OC}$) match very well. The FFs on the other hand are much lower than their corresponding pseudo-FFs, especially for the LG perovskite. This indicates that the cells suffer from severe transport losses, while the EL pseudo-JV measurements are only sensitive to the total non-radiative recombination losses analogously to a dark-JV curve and are barely affected by resistive losses.[234] Overall, we can conclude that the FF can be improved from 74.6% to 84.6% by optimising the charge transport in both subcells, which could enable an efficiency of 25.2%. (Table 6.3)

		$_{ps}V_{OC}$ [V]	$_{ps}$FF [%]	$_{ps}$PCE [%]
HG subcell	From EL	1.26	88.2	16.4
LG subcell	From EL	0.73	80.6	8.8
Tandem	From EL	1.99	84.6	25.2
Tandem	AM1.5	2.00	74.6	21.4
HG single junction	From EL	1.27	84.3	15.9
HG single junction	AM1.5	1.27	78.7	15.6
LG single junction	From EL	0.73	81.3	8.8
LG single junction	HG filtered AM1.5	0.72	71.2	7.6

Table 6.3: Summary of implied V_{OC} and efficiency potentials from EL for optimised 1.85/1.27 eV HG/LG based perovskite tandems, compared to device parameters measured under AM1.5G. Note that the comparison presented here was made on one exemplary device, while we summarise further device parameters and statistics in Figure C.1, Appendix C. J_{SC} in all cases was equal to J_{gen} of 14.87 mA

We further note that when using EL, a measurement that is performed in the dark, care has to be taken on transient effects that are barely present under full AM1.5G

illumination. Especially for the LG perovskite, the ELQY can increase upon light soaking of the cell as well as upon keeping the cell biased at V_{OC} in the dark. We show examples of this effect in Figures 6.7 and 6.9, as well as the impact on extracted pseudo-JV characteristics from EL measurements in Figure 6.10. Pseudo-JV characteristics we analysed here were taken after the cell reached a steady state comparable to standard JV measurements under AM1.5G. We note that the derived ${}_{ps}V_{OC}$ at $J_{inj.} = J_{gen}$ conditions must equal the device V_{OC} if Rau´s reciprocity is fulfilled.[23] This is generally observed for perovskite cells,[135,235] and therefore a good sanity check of the EL and derived pseudo-JV characteristics. If done properly, injection-dependent ELQY measurements reveal accurate pseudo-light JV characteristics that allow us to obtain a comprehensive overview of the limiting factors.

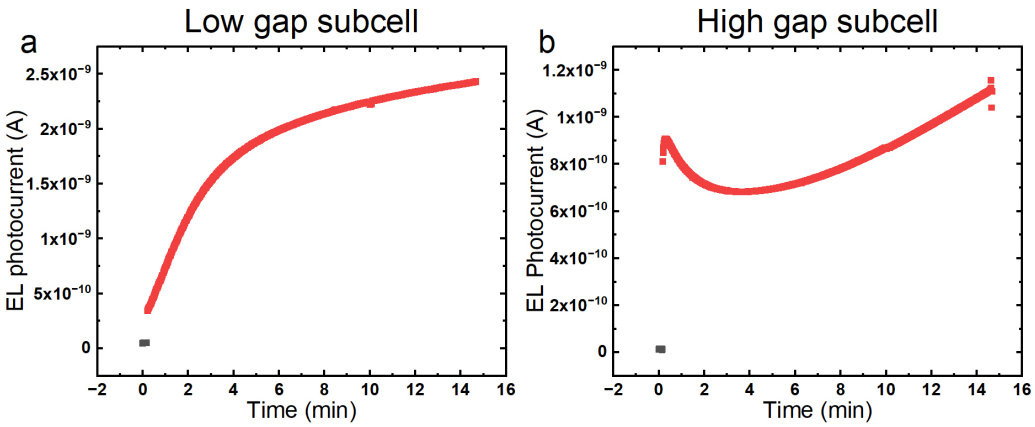

Figure 6.9: EL photocurrent as a function of time while applying V_{OC} to the cell for both the LG (a) and the HG (b) subcell.

Finally, we also perform intensity-dependent PL measurements on the optimised tandems, and compare the results to those from ELQY. Figure 6.11a displays the QFLS as a function of the equivalent injected current (ELQY) or generated current density (PLQY). If plotted on a semi-logarithmic scale the data follows a linear slope given by the subcell/tandem ideality factor. And while the ideality factors are relatively similar we notice significantly higher QFLS for PLQY measurements compared to ELQY for both the LG and the HG subcells. The discrepancy between these two values indicates energy level offsets present in the device stack, causing a difference

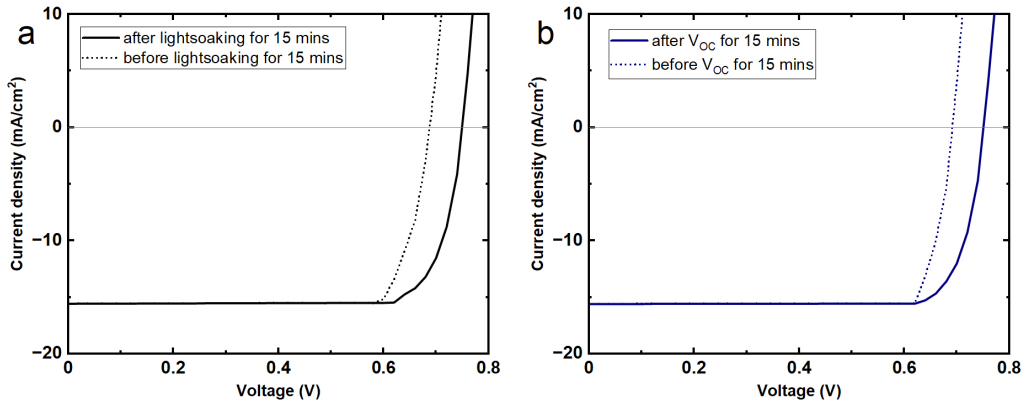

Figure 6.10: a) Pseudo-JVs for the LG subcell obtained from EL before and after light soaking, as well as b) pseudo-JVs obtained before and after applying a bias that equals the device V_{OC} to the cell in the dark for 15 minutes.

between QFLS generated under illumination (i.e., from PLQY) and the device V_{OC}. Note that the QFLS from EL equals the device V_{OC} if Rau's reciprocity is fulfilled.[23] In Figure 6.12, simulated energy diagrams alongside a simulated JV curve corroborate the impact of potential energy level offsets. We note that the discrepancies between QFLS determined by EL and PL are also present in our single junction devices (see Figure 6.13), and thus stem from energy level offsets already present in the single junction stacks, rather than energy level offsets introduced by incorporation in the tandem cell or the recombination layer. Reducing such energy level offsets would enable us to minimise the QFLS discrepancy between ELQY and PLQY results, and push the efficiencies up further toward the potential indicated by the PLQY measurements at 27.0% versus 25.2% from ELQY. Corresponding intensity-dependent PL measurements, as well as a comparison between pseudo-JVs obtained from EL and PL measurements, can be found in Figures 6.14 and 6.15, respectively.

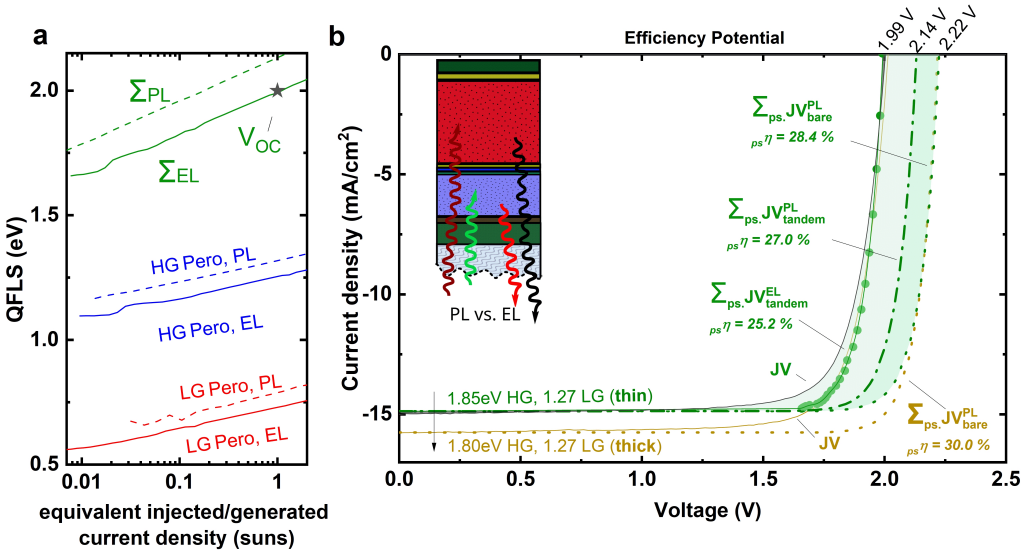

Figure 6.11: a) QFLS of the HG and LG perovskite subcells in a 1.85 eV/1.27 eV tandem calculated from ELQY or PLQY as a function of the equivalent injected current density (ELQY) or generated current density (PLQY) respectively. Summed QFLS representing the actual tandem are further shown alongside the V_{OC} obtained from JV characteristics under AM1.5G b) Pseudo-JVs reconstructed from EL (solid line) and PL (dashed line) tandem measurements, displayed alongside a pseudo-JV reconstructed from a PL measurement of isolated perovskite layers. The latter indicates the material efficiency potential. Displayed for tandems based on a standard thin (green) LG absorber and an optimised thick (golden) LG absorber, with improved current density. Measured with Felix Lang.

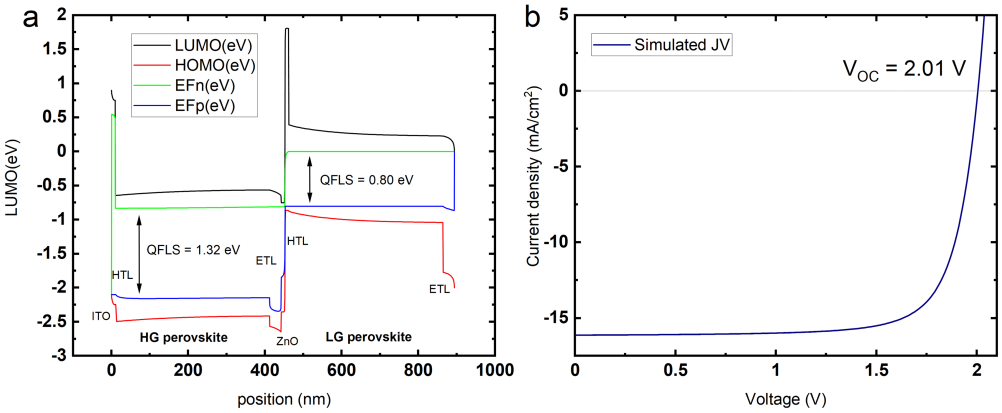

Figure 6.12: Simulated band structure (a) and JV curve (b) for an all perovskite tandem with bandgaps of 1.27 eV and 1.85 eV for the LG and HG, respectively. It can be seen that the QFLS of the individual subcells add up to 2.12 V, while the V_{OC} of the tandem is limited to 2.01 V. In the simulations, this was reproduced by implementing an energy level offset at the HTL/perovskite interfaces, although we note that we do not exclude that there are other factors that lead to a QFLS-V_{OC} mismatch.[201,236] Simulations were carried out using Setfos 5.2.5., with parameters summarised in A.2 and[237].

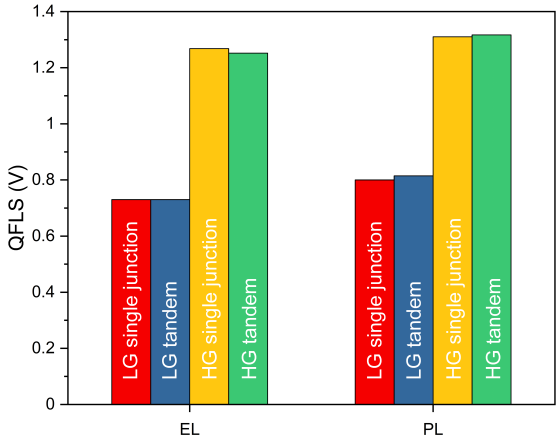

Figure 6.13: QFLS determined from EL (left) and PL (right) for single junctions as well as tandem subcells.

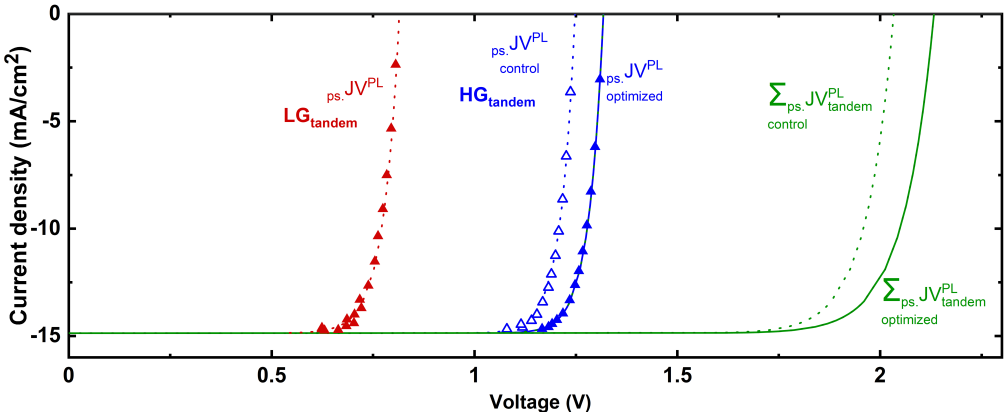

Figure 6.14: Pseudo-JVs obtained from iPLQY measurements for the optimised and control tandems.

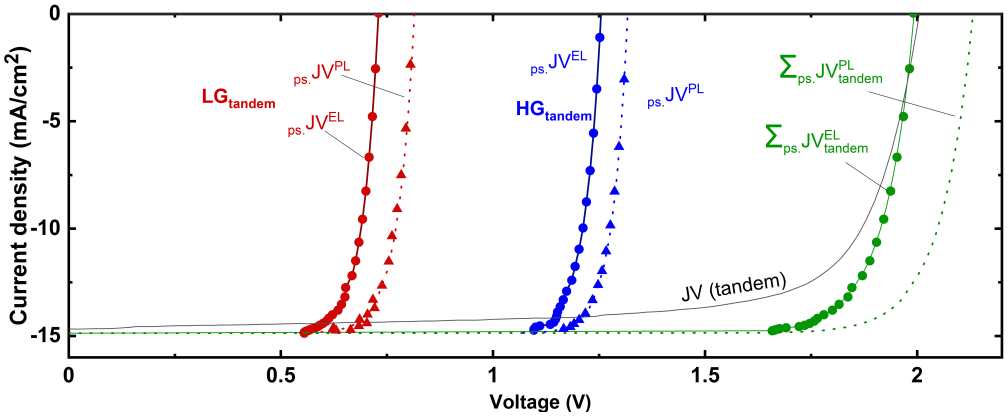

Figure 6.15: Comparison between pseudo-JV curves obtained from iPLQY and EL measurements, alongside JV curves of the tandem and corresponding single junctions. Measured with Felix Lang.

Looking beyond the transport losses and QFLS-V_{OC} mismatch, we ultimately also investigate the efficiency potential of the isolated absorber materials through intensity-dependent PLQY measurements. Figure 6.11b displays pseudo-JV curves from ELQY and PLQY measurements on the tandems, alongside the pseudo-JV characteristics from PLQY measurements on the isolated perovskite layers, and clearly shows the limitations imposed by the transport layers. The combination of our 1.27 eV LG perovskite with the 1.85 eV HG perovskite reaches an absorber efficiency potential of 28.4% with an implied V_{OC} of 2.22 V. Notably our threefold optimised 1.85/1.27 eV HG/LG champion tandem with a V_{OC} of 2.00 V already reaches 84% of this material potential. Although we have now optimised the device V_{OC} by focusing on improving the HG perovskite, we note that the tandems still suffer from a limited short circuit current due to the lead-tin perovskite not being thick enough to absorb all the light. Therefore, as an ultimate optimisation step, we increase the thickness of the LG perovskite, using a fabrication method adapted from Hu et al.[238] thereby reaching higher EQE values at long wavelengths (see Figure 6.16a for EQE). In combination with our optimised 1.80 eV HG subcells, this increases the tandem current and ultimately boosts the device efficiency to 25.2% (JV) and 25.9% stabilised (MPP tracking in Figure 6.16b). With this increased tandem current, the material potential determined from isolated absorber layers reaches 30.0%, as can be seen in Figure 6.11b, thereby exemplifying the enormous potential of this PV technology.

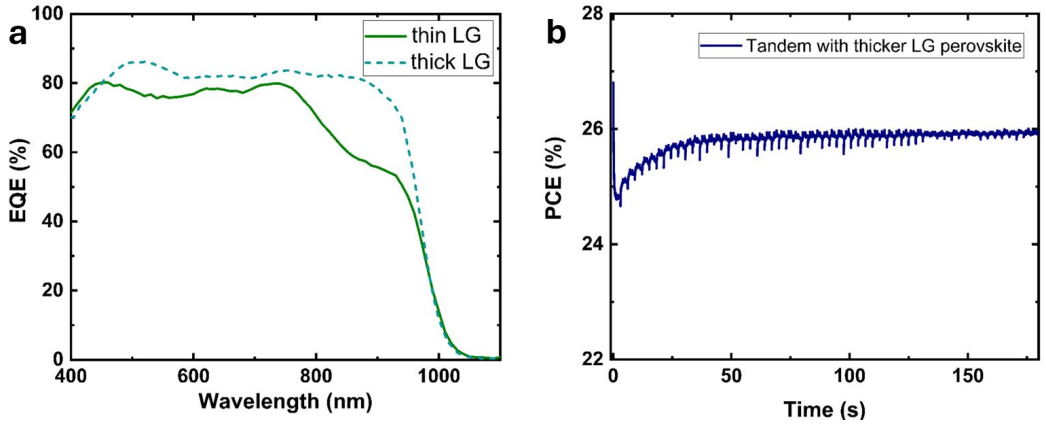

Figure 6.16: a) External quantum efficiency (EQE) of a low gap perovskite solar cell with the standard, thin, absorber layer, as well as of a low gap perovskite solar cell with the optimised, thicker, absorber layer. It can be seen that the latter absorbs more light, especially in the (near) infrared. b) Maximum power point (MPP) tracking of a tandem device, based on a 1.80 eV HG perovskite in combination with a thicker (800 nm) 1.27 eV LG perovskite.

6.3 Conclusion

In this chapter, we identified V_{OC} losses in all-perovskite tandem solar cells and show that in our present material set, as well as many literature devices, nonradiative recombination within the high-bandgap perovskite subcell dominates V_{OC} and performance losses. We developed a multifaceted optimisation route to improve the high-bandgap subcell by replacing the HTL PTAA with 2PACz, adding oleylamine to the perovskite in combination with including a thin LiF layer between the perovskite and the ETL. In an additive manner, our combined approach enables high-gap perovskite absorbers with high QFLS and an improved V_{OC} potential, reaching 83% of their radiative V_{OC} limit. The high V_{OC} potential translated directly to the V_{OC} of the all-perovskite tandems that were subsequently fabricated, and improved their steady-state power conversion efficiency to 23.7% for our champion combination of 1.85/1.27 eV HG/LG perovskite subcells. We performed a thorough subcell analysis to disentangle further factors limiting the performance of these tandem devices and found that although there is still room for improvement of the V_{OC}s of both individual subcells, our ultra-thin InOx based interconnect is quasi-lossless, and both subcells reach V_{OC}s equally high to those in their respective single junctions. The FF on the other hand is significantly lower than the pseudo-FF obtained from EL measurements, indicating significant transport losses. Reducing such transport losses would allow us to approach efficiencies of 25.2%, which is the efficiency potential for our 1.85/1.27 eV HG/LG perovskite tandem combination extracted from EL-based pseudo-JV characteristics. We also observe a discrepancy between the pseudo-V_{OC} obtained from EL measurements, and the QFLS obtained from PLQY measurements, the latter being significantly higher. This indicates there are energy barriers present in the stack, which, when reduced, will provide a significant additional optimisation potential, enabling efficiencies of up to 27.0%. Concluding, the indium oxide interconnect that was used in these tandems is quasi-lossless, but both individual subcells, specifically the low-gap after the optimisation of the high-gap perovskite, can still be improved to reach better performances, as we demonstrate

with a proof-of-concept device which, due to a thicker LG absorber, reaches 25.9% stabilised efficiency, with an ultimate efficiency potential of 30%. The insights of this extensive subcell-selective characterisation provide crucial feedback and allow us to develop evidence-based optimisation routes to improve the tandem efficiencies further in the future.

CHAPTER 7

Mobile ions in perovskite-based tandem photovoltaics

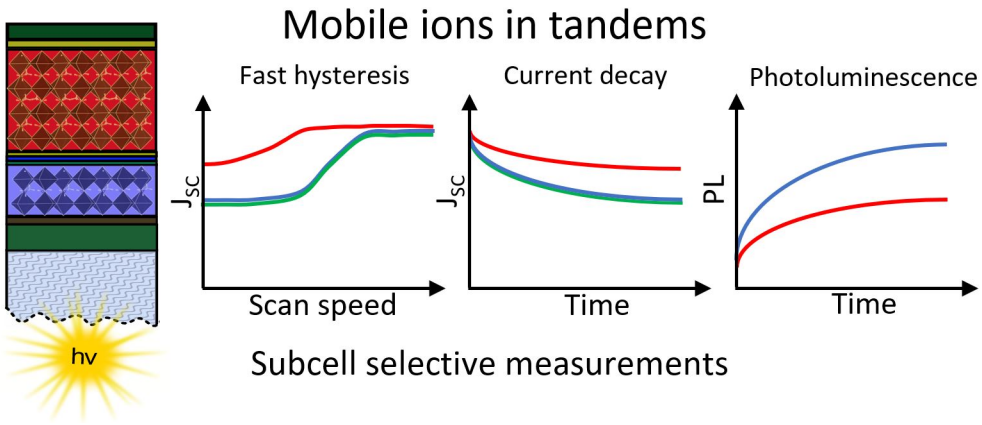

7.1 Introduction

In Chapter 4, the impact of mobile ions on the performance of perovskite solar cells was described. From the results presented there, it is clear that mobile ions in the

perovskite can negatively impact the output current of perovskite solar cells through field screening. Later, in Chapter 5, early performance degradation in perovskite solar cells upon ageing was linked to increasing mobile ion concentrations. We showed that different external stressors can increase the concentration of mobile ions in the perovskite, especially when there are free charges present in the absorber layer.

In 2-terminal (2T) tandem solar cells, the two subcells are connected in series. For optimal operation, the current delivered by the two subcells should be matched - as the overall output current of the tandem device will be limited by the lowest current produced by one of the subcells. Although there are some pathways which can relax current matching requirements[237,239], it is crucial to design perovskite-based 2T tandems keeping in mind that the current output from the different subcells might change with ageing of the device. The increase of mobile ion densities in the perovskite upon ageing described previously can alter the current outputs of perovskite subcells, undermining the carefully engineered current matching of tandem devices in the long run and bringing the subcells in disbalance. In order to design perovskite-based solar cells to be robust and optimise long-term performance, it is therefore crucial to study the ageing of the tandem subcells.

However, subcells in perovskite-based tandems might not degrade at the same rate as their single junction counterparts, for example due to the presence of additional free charges, exposure to a different light spectrum[240] caused by filtering and back-reflection, and due to the presence of materials which are different from those in single junctions, such as the interconnect which electronically connects both subcells. Because of this, it is important to study the evolution of mobile ion concentrations and their impact on the device performance subcell-selectively.

In a similar fashion to the methods presented in Chapter 6, this chapter explores different options for the subcell-selective investigation of the impact of mobile ions on device performance in 2T tandems. Several different measurement setups are presented, and data obtained from subcells in different types of perovskite-based

tandems (perovskite-organic, perovskite-silicon and perovskite-perovskite) is compared with data from their single-junction counterparts.

7.2 Results

7.2.1 Subcell-selective fast hysteresis measurements and current decay

In order to gain insight into the extent to which the presence of mobile ions in the absorber layer affects the device performance of a solar cell, fast hysteresis, as well as current decay measurements (described in more detail in Chapter 3 and 4) can be carried out. In theory, the fact that the output current in 2T tandem cells should be solely determined by the current-limiting subcell, can be exploited to investigate mobile-ion-induced current losses subcell selectively. By artificially making one of the two subcells current-limiting, the effects of mobile ions on the current of that subcell can be studied by simply looking at the output current of the tandem.

There are two options to make sure a specific subcell is limiting the output current of the 2T tandem. For the first option, starting with a 1 sun equivalent illumination of the tandem device at AM1.5G, the light intensity in the wavelength range that will be absorbed by the subcell to be studied can be reduced, using a colour filter. Alternatively, starting with the same base illumination of AM1.5G at 1 sun equivalent, additional light can be added to flood the other subcell. A schematic displaying the two methods used to limit the current in a specific subcell can be seen in Figure 7.1.

Both methods have their advantages and disadvantages. Using colour filters is simple and allows for efficiently taking multiple measurements using an existing, calibrated sun simulator setup in a N_2 filled glovebox. However, in practice, it can be complicated to obtain colour filters which solely reduce the light intensity in the wavelength range of one of the subcells, without reducing light intensity so far that the current imbalance between the subcells becomes unrealistic. Using LEDs to add

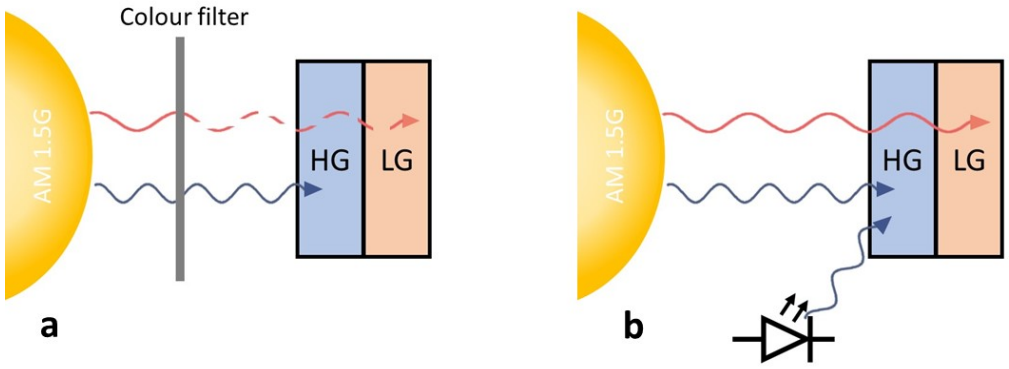

Figure 7.1: A schematic overview of two different methods to limit the current in one of the subcells, enabling subcell-specific investigation of mobile-ion-induced current losses. Current can be limited by reducing incoming light for one of the subcells using a colour filter (a) or by adding additional (LED) light to the other subcell (b). In this example, the low gap (LG) subcell becomes the current limiting cell.

additional light at a certain wavelength for one of the cells allows for more flexibility as the intensity of the LEDs can be easily controlled, however, such a setup requires more time to calibrate, and may not be compatible with a calibrated sun simulator setup in a glovebox. In order to confirm that both methods (reducing light intensity for wavelengths absorbed by the subcell that is to be limited, versus increasing light intensity for wavelengths absorbed by the subcell that is not to be limited) provide trustworthy results, both methods have been tested and the results compared. Once one of the subcells is artificially made to be current-limiting in the tandem cell, fast hysteresis measurements as well as current decay measurements were carried out as described in Chapter 3, without any further modifications.

In Figure 7.2, current decay upon switching device bias to short circuit, as well as as short-circuit current density obtained as a function of scan speed range are displayed for both subcells, measured using both the 'filter method' and the 'LED method'. It can be seen that the results obtained using both methods are similar, without significant deviations in the trends observed. Furthermore, the current losses upon switching to short circuit conditions equal the mobile-ion-induced losses which can be determined from the short-circuit-current difference between the 'ion-freeze' and the steady state JV scans. Besides showing the extent of the mobile-ion-induced losses in

both subcells, these measurements also directly reveal which subcell is current-limiting in the tandem device. The results displayed in Figure 7.2 show that for this particular tandem device, the HG subcell suffers from stronger ion-induced current losses than its LG counterpart. Furthermore, it can be seen that the HG is presently the current limiting subcell in this tandem device.

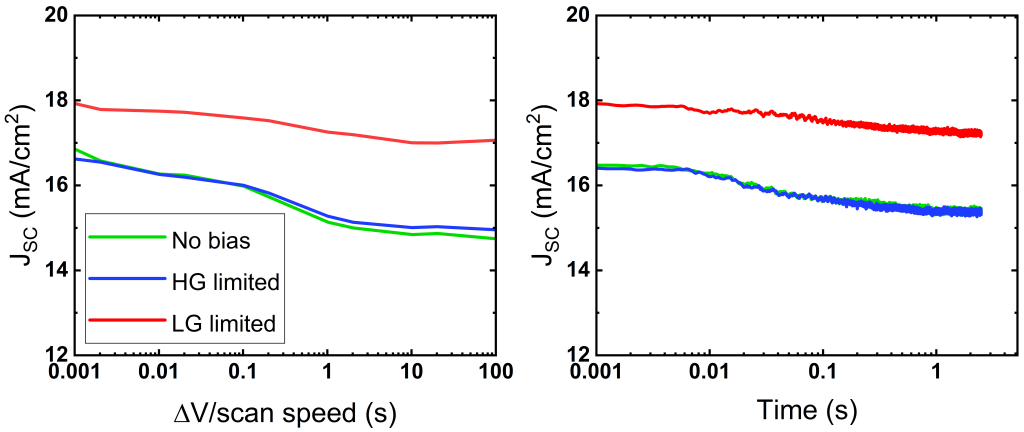

Figure 7.2: Subcell-selective short circuit current from fast-hysteresis measurements (a) and current decay measurements (b). Measurements were carried out using a coloured LED to selectively increase illumination for one of the subcells, rendering the remaining subcell current-limiting. Measured with assistance of Lucas Holte.

Figure 7.3, moreover, shows that, for fresh tandem devices, the subcell-selectively determined mobile-ion-induced losses correspond with the losses identified in their single-junction counterparts. This further suggests that the methods presented here to obtain subcell-selective measurements of mobile-ion-induced current losses in 2T tandems provide accurate results.

Although current losses in the subcells can in principle be measured successfully using the techniques presented above, these measurements do rely on the subcells having a relatively high shunt resistance. The method is based on the principle that the total current output of the tandem is equal to the current produced by the current limiting subcell. However, as we have shown in Chapter 6, when shunt resistances are low, current matching in 2T tandems may be lifted at the cost of a reduction in FF, and the current output of the tandem can be higher than the output current of the limiting subcell, which would immediately render our subcell-selective current loss

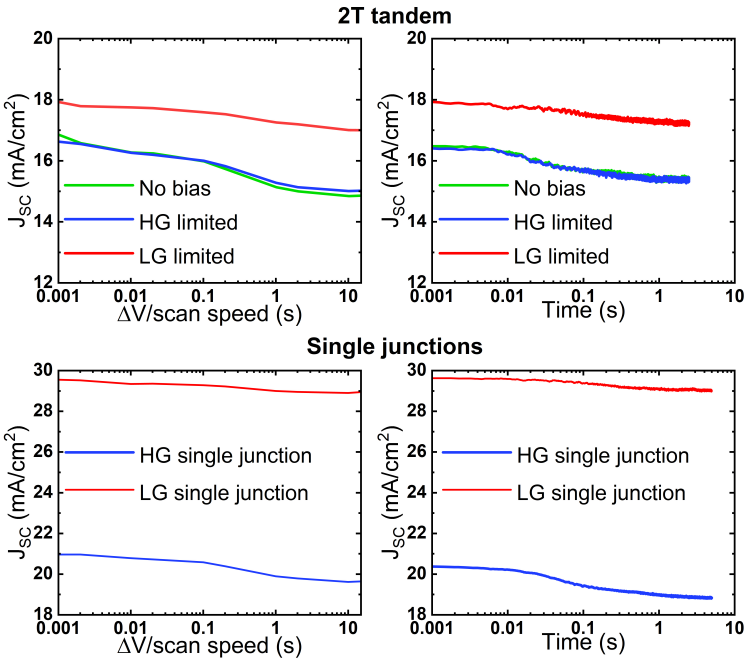

Figure 7.3: Subcell-selective short circuit current from fast-hysteresis measurements (a) and current decay measurements (b), as well as short circuit current for the corresponding single junctions from fast hysteresis measurements (c) and current decay measurements short circuit current from single junction measurements (d). a) and b) measured with assistance of Lucas Holte.

measurement technique invalid. An example of such an effect is displayed in Figure 7.4, where the fast hysteresis results of an organic-perovskite tandem are displayed. It can be seen that in this case, the organic subcell shows exactly the same current behaviour as the perovskite subcell and the overall tandem, despite the fact that the organic photovoltaics do not suffer from mobile-ion-induced current losses. As shunt resistances in perovskite solar cells generally decrease with device degradation[198,241], this issue presents a significant limitation to the technique and its viability for the subcell-selective measurement of mobile-ion-induced losses in 2T tandems. Based on equivalent circuit simulations, as a rule of thumb, mobile ion-induced losses can only be measured without significant crosstalk between the two subcells if the shunt resistance is at least 5000 Ω. [i]

[i]The shunt resistance of each subcell can be measured by applying a light bias solely to one of the subcells, and measuring the resulting current as a function of voltage[242].

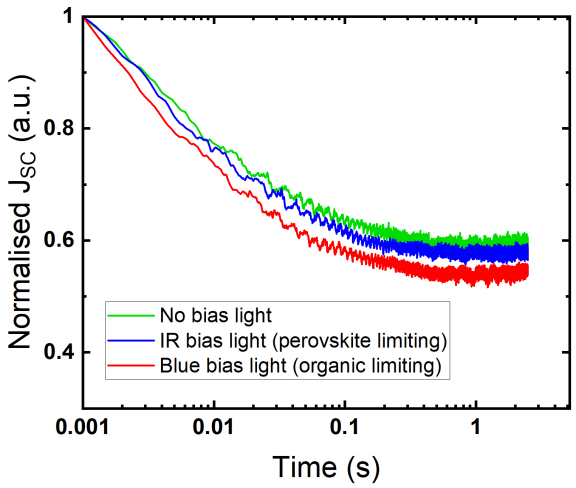

Figure 7.4: Normalised current decay results of an organic-perovskite tandem device, seemingly displaying effects of mobile-ion-induced losses in the organic subcell-selective measurements due to a low shunt resistance. We note that this device was over one year old at the date this measurement was taken, which probably is the reason behind the low shunt resistance observed. Measured with assistance of Lucas Holte.

Furthermore, we also note that in significantly degraded 2T devices, occasionally an effect is observed which causes a sudden, strong increase in output current at higher scan speeds. An example of this effect can be seen in Figure 7.5, where a JV curve from a silicon-perovskite device, scanned at 390 V/s is displayed. We also note that this effect is reproducible between measurements, and not a one-off measurement artefact. The exact origins of this effect are not yet understood, however, it is clear that this effect provides additional limitations for the measurement of mobile-ion-induced losses in ageing perovskite-based 2T devices.

Unfortunately, although the mobile-ion-induced current losses in the subcells can be determined within the limitations mentioned above, it is not possible to use methods such as BACE, CELIV or other charge extraction measurements to get an idea of the mobile ion density in the different subcells. I.e. the effect of mobile ions on the current of the subcells can be determined, but the amount of mobile ions themselves, which cause this effect in the first place, cannot. This problem is inherent to the 2T architecture, as the subcells are electrically connected through the interconnect, where electrons from one subcell recombine with the holes from the other subcell.

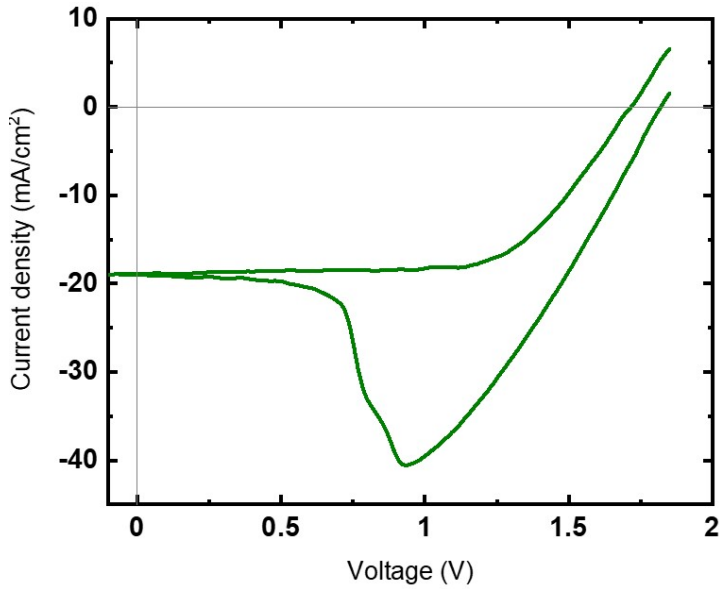

Figure 7.5: JV curve of a silicon-perovskite 2T tandem device, measured at 390 V/s, displaying a sudden increase in current density at fast scan speeds. Measured with assistance of Lucas Holte.

However, although charge extraction measurements cannot be used to determine mobile ion densities, the use of photoluminescence measurements might be able to provide additional insights into how the ions affect device performance.

7.2.2 Subcell-selective voltage-dependent photoluminescence time series

Similar to the work presented in Chapter 4, the temporal PL response of the two different subcells in the 2T tandem can be measured upon switching the bias that is applied to the device from V_{OC} to 0 V. Since both subcells will emit light at a different peak wavelength, the PL response of the different subcells can easily be distinguished. Figure 7.6a displays a schematic overview of the experiment. The spectrometer, which was initially used for these measurements (Figure 7.6 b), has a rather limited time resolution. In order to enable faster measurements, with better time resolution, the photoluminescence can also be measured with a photodiode connected to an oscilloscope (Figure 7.6c). A long- or short-pass filter (or a combination of both) is

then used to filter out reflected laser light, as well as the photoluminescence of one of the two subcells.

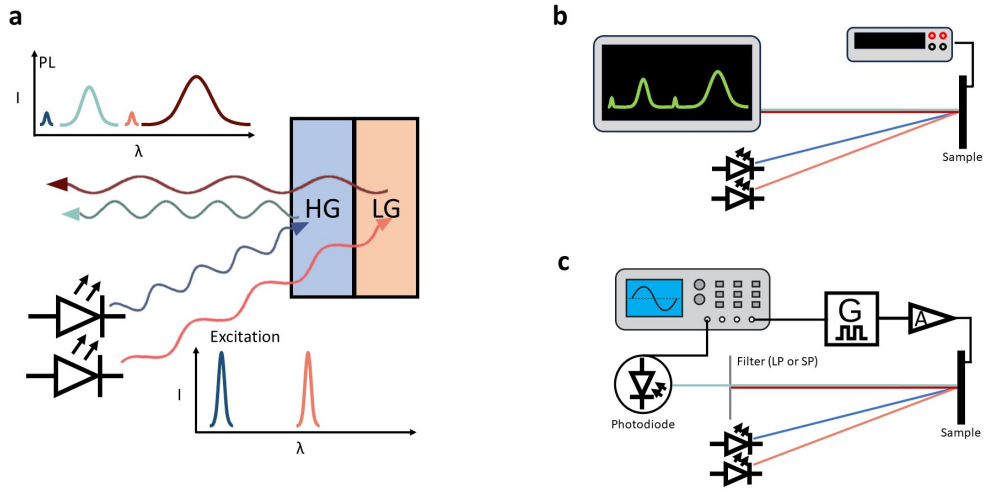

Figure 7.6: Schematic overview of the experimental setups used for subcell-selective temporal PL measurements. (a) Shows a schematic of the measurement principle. (b) Displays a schematic overview of the experimental setup where a source meter unit (SMU) is used to apply a bias to the device, with a spectrometer recording the PL coming from the device. In (c), an alternative setup is displayed, where a combination of a photodiode with an oscilloscope is used to measure the PL with an improved temporal resolution.

In Figure 7.7, an example of the temporal PL response upon switching from OC to SC conditions is displayed for a low gap and a high gap subcell of an all-perovskite tandem cell (similar to the devices presented in Chapter 6). It can be seen that, in both subcells, an initial efficient charge extraction (signified by a very low PL signal, which indicates there are few charges left in the device to recombine) is followed by a significant reduction in charge extraction efficiency (signified by an increase in PL signal over the first couple of seconds upon switching to SC conditions).

Utilising PL measurements to understand the impact of mobile ions on device performance subcell-selectively might be advantageous, because it allows to study the subcells in the tandem device while it is being operated under balanced illumination, ideally even under conditions where the subcells are current-matched [ii]. This as opposed

[ii]Although it is complicated to calibrate a setup in such a way that two laser beams both homogeneously illuminate the active device area of the sample with the exact 1 sun equivalent intensity. But this is just a practical challenge, rather than a fundamental limitation.

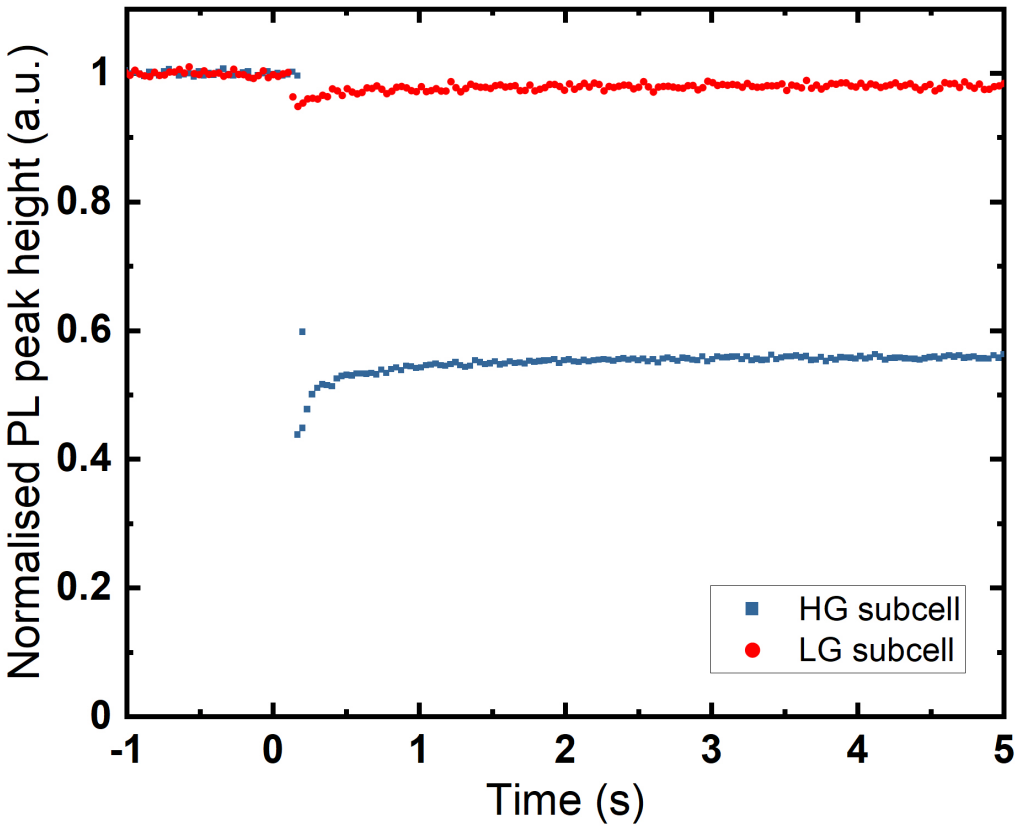

Figure 7.7: The maximum height of the subcell-selectively measured PL peak a function of time, where t = 0 is the moment where the bias of the device was switched from OC to SC. Data is normalalised to the average PL peak height at OC. Measured with assistance of Lucas Holte.

to the methods described above, where, to perform subcell-selective current-decay and fast hysteresis measurements, the device needs to be brought into disbalance. Subcell-selective mobile ion measurements using PL, therefore, are not at risk of being disturbed by artefacts or changes in device behaviour arising from the artificial creation of a current imbalance, and allow the subcells to be measured under realistic operating conditions. On the other hand, however, although PL measurements can provide important information about charge extraction efficiency[243] and recombination at short circuit conditions, to date, it does not provide a direct value for the mobile-ion-induced current losses, like the other optoelectronic measurements[244].

7.2.3 Voltage-dependent photoluminescence time series and device ageing

To investigate the fundamental link between mobile ion-induced losses and the PL at SC conditions more in-depth, a simple and reproducible system is needed. Therefore, the measurements presented in the following section were performed on single junction triple cation (83/17) solar cells.

With increasing mobile ion densities upon ageing, the PL response of ageing devices upon switching to SC is also expected to change. Figure 7.8 displays the PL peak height as a function of time upon switching the device bias of a single junction device to SC. The device has been aged under light at OC conditions for different amounts of time. The curves have been normalised to the PL at OC conditions. It can be seen that, with ageing, the relative height of the PL peak at SC increases, indicating increased radiative recombination at short circuit conditions, which in turn points towards a reduced charge extraction efficiency.

In order to more in-depth understand what happens to the output of subcells upon ageing, we next try to link the PL at SC directly to current losses. When the sample is illuminated at 1 sun equivalent intensity, the generated carrier density, J_{gen}, is known. At SC, all generated carriers are either extracted or recombine, hence, $J_{\mathsf{gen}} = J_{\mathsf{SC}} + J_{\mathsf{rec}}$, where $J_{\mathsf{rec}} = J_{\mathsf{rad}} + J_{\mathsf{nrad}}$. From this formula, if the radiative and non-radiative recombination currents are known, the short circuit current can be determined from the PL measurements.

However, establishing the exact relationship between radiative and non-radiative recombination at SC in tandem subcells is challenging. One possibility to tackle this challenge would be to measure, in single junction solar cells based on different perovskite compositions, the J_{rad}. For these single junctions, where $J_{\mathsf{ext}} = J_{\mathsf{SC}}$, the extracted current can simply be measured during the experiment, and related to the PL at every voltage. The radiative current can be determined from PLQY,

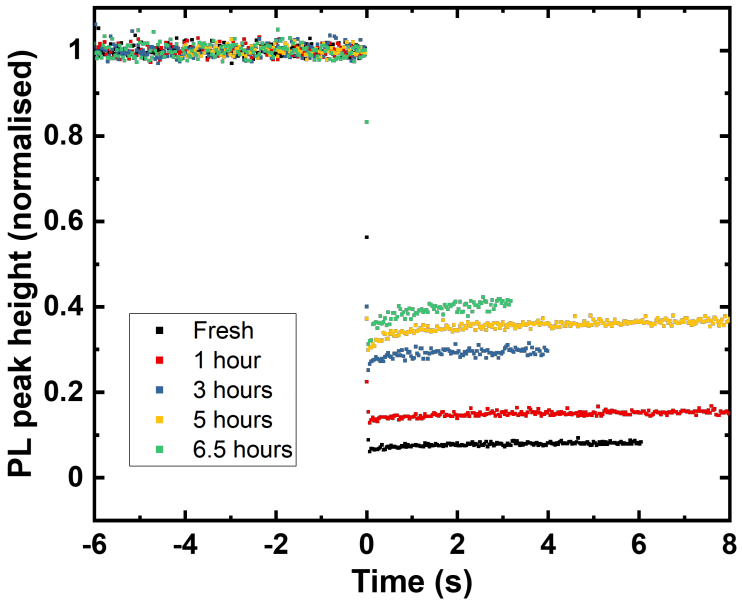

Figure 7.8: PL peak height as a function of time upon switching the device bias from OC to SC for a single junction device. The curves are normalised to the PL at OC conditions to allow for a direct comparison of the ratio PL_{SC}/PL_{OC}. Measurements were taken after the device had been aged under 1 sun illumination at open circuit conditions for different amounts of time.

and since $J_{gen} = J_{ext} + J_{rad} + J_{nrad}$, $J_{nrad} = J_{gen} - J_{ext} - J_{rad}$[245]. By performing these measurements for a range of different perovskite compositions, and for various degradation stages, the ratio of J_{rad}/J_{nrad} might be estimated, and used in tandem devices to determine J_{SC} for the different subcells. Although such a first estimate of the short circuit current in the device already can provide some useful insights, this method does rely on the assumption that J_{rad}/J_{nrad} ratios change similarly in tandem subcells and single junctions, and is a gross oversimplification. On top of that, it would require a significant number of measurements in order to build up a data set which would allow for the determination of J_{rad}/J_{nrad} ratios. Every perovskite composition would require additional measurements.

In order to figure out a more direct way to include non-radiative recombination in the determination of current losses from PL, we investigate the ratio between radiative

and non-radiative recombination as a function of voltage. Data displayed in Figure 7.9 can be processed further by linking the absolute PLQY of the device at a known laser fluence at OC (measured using the integrating sphere) to the number of PL counts at a known laser fluence at OC (measured using the linear setup). Next, with J_{gen} and J_{ext} known, $J_{\text{rad}}/J_{\text{nrad}}$ can then be calculated for different applied voltages. We note that optical effects are not taken into account, and outcoupling of light is assumed to remain constant. This assumption should be valid as long as the location of the PL emission in the device does not change significantly. Unfortunately, due to time limitations, the data processing to obtain the final $J_{\text{rad}}/J_{\text{nrad}}$ ratios as a function of applied voltage could not be finalised before completion of this thesis and is still pending.

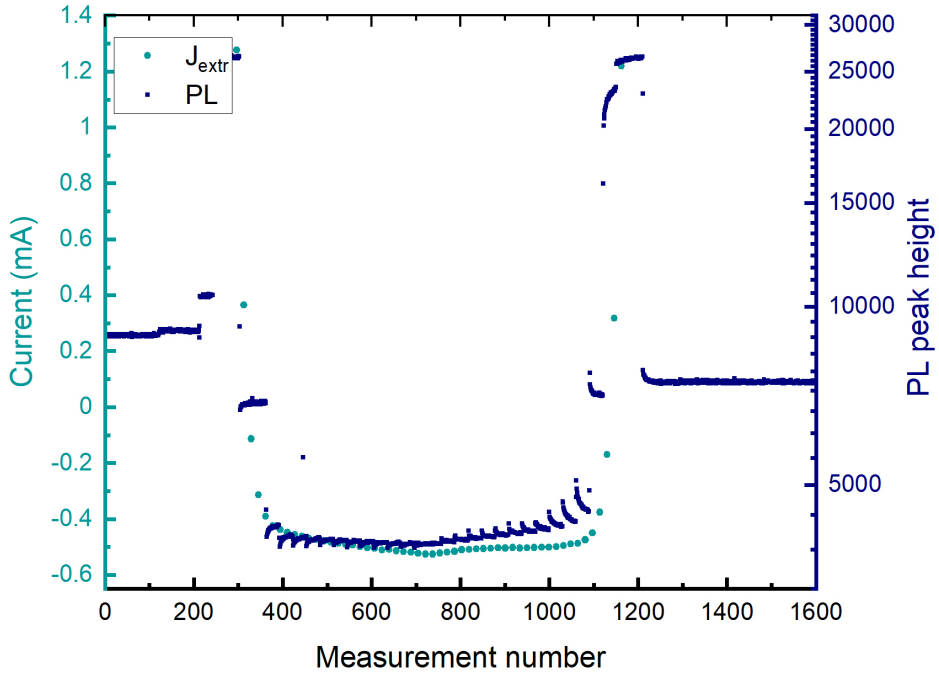

Figure 7.9: PL peak height and extracted current as a function of voltage. This data, upon further processing, can be used to determine the $J_{\text{nrad}}/J_{\text{nrad}}$ ratio.

In another attempt to directly determine J_{nrad} in subcells, TRPL measurements were carried out under SC conditions. The results, displayed in Figure 7.10, show a

decrease in decay time, as expected. However, although in principle the monomolecular and bimolecular recombination rates k1 and k2 could be determined by fitting this TRPL decay, such a fit is not directly valid since the extracted carriers need to be taken into account. However, due to experimental issues, the extracted current could not yet be recorded. Therefore, additional measurements are needed to determine the number of extracted carriers during the TRPL measurements and understand better how the relationship between k1 and k2 changes at SC.

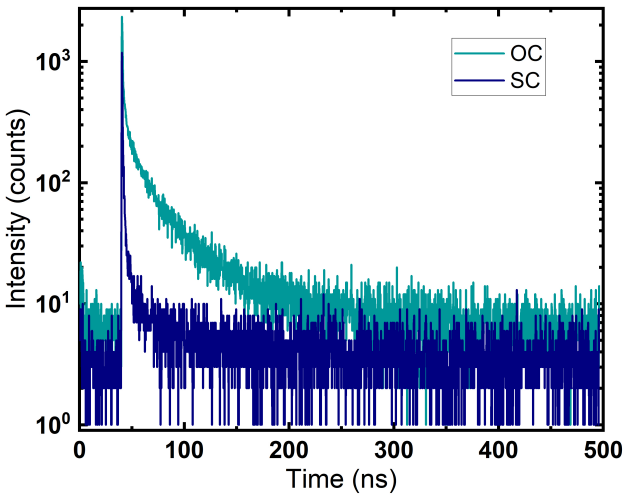

Figure 7.10: TRPL at OC and SC conditions for a single junction device

The intensity dependent PL, which can be used at OC conditions to determine the ideality factor, and gain further insights into radiative and non-radiative loss processes, can also be measured at SC. The results, displayed in Figure 7.11, show that the increase of PLQY with intensity is much slower at SC conditions, as expected. However, we note that also in this case, it is important to take into account the number of extracted carriers, and determine the increase of PLQY with intensity corrected for the number of extracted carriers. It is possible to fit the PLQY as a function of intensity and extract values for k1 and k2. However, as this work is ongoing, analysis of the recombination rates is still pending.

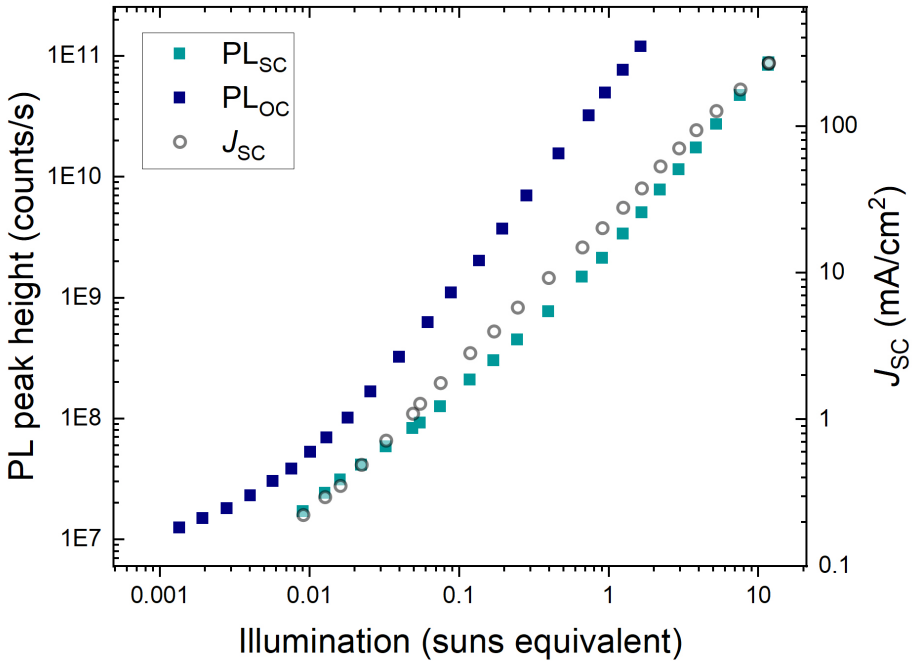

Figure 7.11: Intensity dependent PLQY measurements at SC and OC conditions for a single junction device, as well as the J_{SC} measured during the intensity dependent measurements at SC.

Overall, a direct determination of short circuit losses from PL at SC could not be established yet. Hence, although using subcell selective luminescence based measurements would be superior to the use of fast hysteresis or current decay measurements, a more in-depth analysis of the preliminary results presented here is needed to determine whether there is a way to directly assess the ratio of non-radiative losses to radiative losses at SC conditions.

7.3 Conclusion

Understanding mobile-ion-induced current losses is especially crucial in perovskite-based 2-terminal tandems, since current matching is vital to enable these tandem devices to reach their efficiency potentials. Measuring losses directly in the subcells is important, since things like additional free charges, processing differences and the presence of a different chemical environment can impact ageing in the tandem device, meaning that the mobile ion densities in the subcells do not necessarily develop in the same way as in their single junction counterparts.

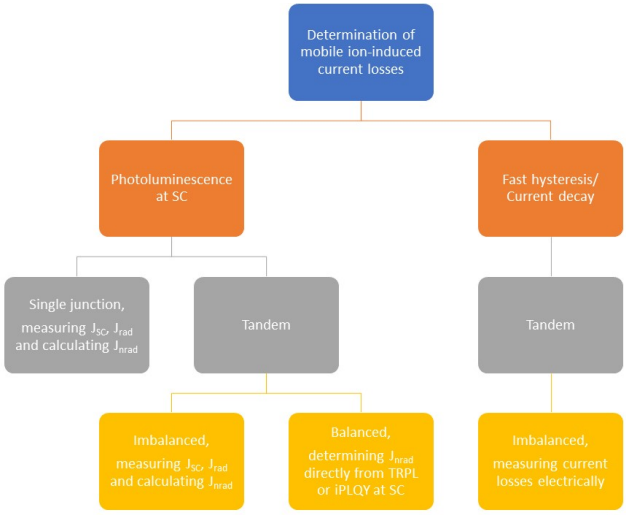

Figure 7.12: Schematic overview of the different methods proposed to investigate mobile-ion-induced losses in perovskite-based tandem solar cells, either electronically, or using photoluminescence.

In order to gain insights into the effects of mobile ions on the performance of the subcells, we developed two subcell-selective measurement techniques in this chapter, and explored their robustness and applicability. An overview of the different methods discussed can be seen in Figure 7.12. The first method, based on an adaptation of the techniques previously described in chapter 4, relies on purposely making one of the subcells current limiting, such that the current losses in this subcell can be determined directly. The second method employs photoluminescence measurements to investigate charge extraction efficiency upon switching the device bias to short-circuit. This is a more indirect method, which does not directly provide values for ion-induced current losses. However, the fact that the measurement does, in some cases, not require a current imbalance means measurements can be taken of devices under realistic operating conditions.

Both techniques provide consistent results, and trends observed in the subcells of freshly fabricated tandem devices are in line with those observed in their corresponding single junctions. The photoluminescence method can be improved further - with additional investigation, it might be possible to establish a direct link between the photoluminescence at SC and the total amount of current losses in the subcell, provided the ideality factor is known. This would allow current losses in both subcells to be

determined while the device is kept under operating conditions, thereby providing a powerful tool to understand, and manage, mobile ions and ageing-related degradation in perovskite-based tandem solar cells.

CHAPTER 8

On the oxidation of lead-tin perovskite solar cells

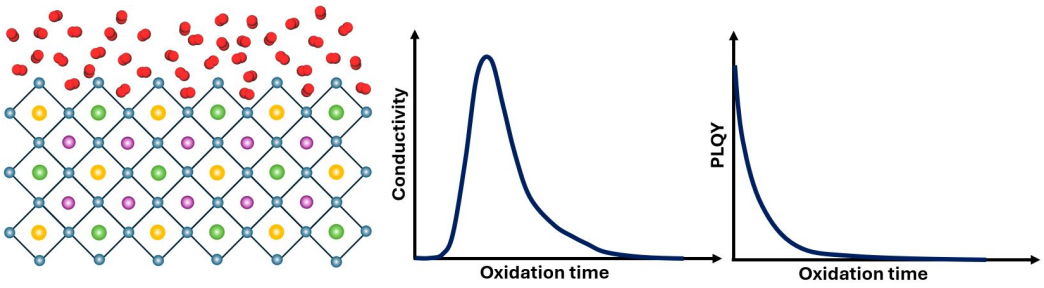

8.1 Introduction

It is well known that mixed-metal lead-tin perovskites can undergo tremendous changes upon exposure to oxygen due to the oxidation of tin atoms in the material. The oxidation pathways have been well established; however, a thorough investigation of the different ways oxygen exposure influences the different material properties and the resulting device performance of these lead-tin perovskites is still lacking. This

chapter presents some results from ongoing work investigating the oxidation of lead-tin perovskites. We provide insight into the different effects of oxygen exposure on low bandgap lead-tin perovskite solar cells. We look into self-doping and the generation of trap states, but also investigate the role of mobile ions in this process, as well as energy level changes that may affect device performance. We show that increased trap state and mobile ion densities upon prolonged oxygen exposure undermine device performance, but also that limited amounts of oxygen exposure can have beneficial effects on open circuit voltage and overall power conversion efficiency.

8.2 Results

To investigate the effects of oxidation on the device performance of low bandgap, mixed-metal lead-tin ($FA_{0.83}Cs_{0.17}Pb_{0.5}Sn_{0.5}I_3$) perovskite solar cells, devices, films and partial device stacks were fabricated as described in Chapter 3.

8.2.1 V_{OC} Increase

To investigate the effect of oxidation of the perovskite on device performance, a set of half-cells (ITO / PEDOT:PSS / perovskite) was exposed to oxygen in a dry air box for different amounts of time before the ETL and electrode were deposited on top. Initially, oxidation of the half stacks causes an increase in V_{OC} and a corresponding efficiency enhancement. The V_{OC} of the cells, and with that also the PCE peak for air exposure times of around 30 to 45 minutes. Thereafter, the V_{OC} starts to slowly decrease. Furthermore, after 90 minutes the J_{SC} and FF of the cells decline rapidly, eventually causing a complete deterioration of the cell performance.

We have two different hypotheses as to what might cause this slight increase in the V_{OC}: we suspect that either the energy level alignments in the device stack improve, or that moderate amounts of doping improve reduce recombination at the perovskite-HTL interface. In order to investigate why the V_{OC} initially slightly increases, photoluminescence (PL) measurements are performed on different partial stacks (neat

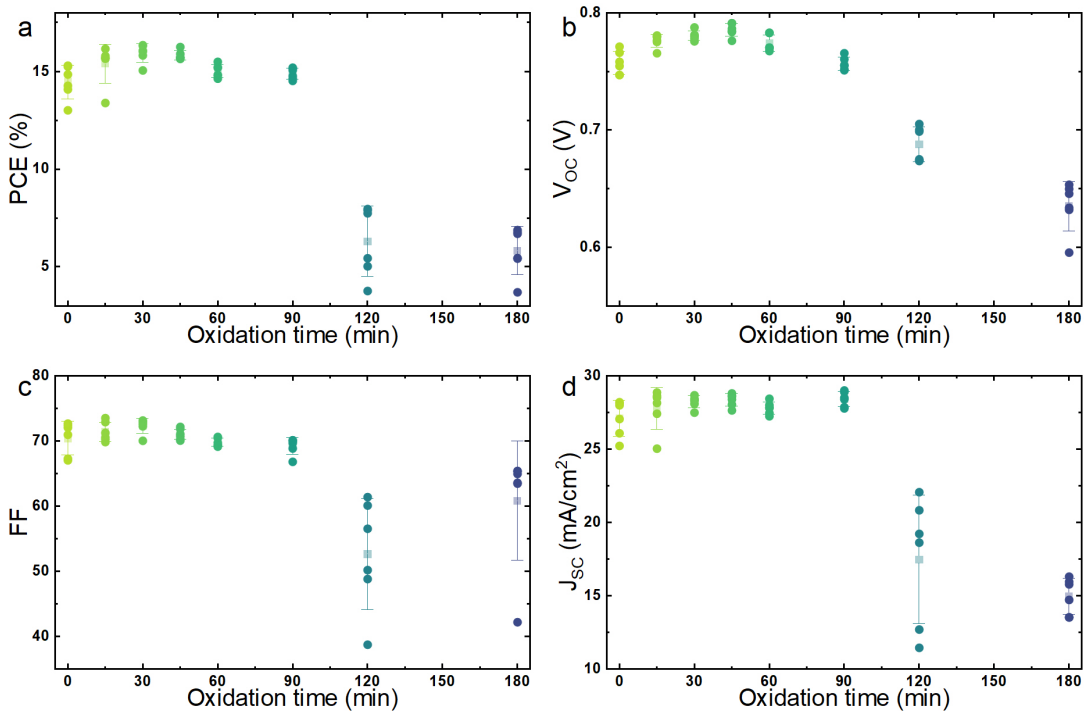

Figure 8.1: JV parameters, (a) PCE, (b) V_{OC}, (c) FF and (d) J_{SC} of lead-tin perovskite solar cells which have been oxidised for different amounts of time, before deposition of the ETL and metal contact. Semi-transparent squares indicate the average value of the performance metrics for each of the oxidation durations.

perovskite, PEDOT:PSS / perovskite, perovskite / C60, and PEDOT:PSS / perovskite / C60) that were oxidised for different amounts of time, but due to issues with the precursor materials, this experiment has to be repeated. Furthermore, Kelvin probe measurements on perovskite samples oxidised for different amounts of time show a slight change in work function. However, since the work function of the tip drifted strongly over time, the change in work function of the perovskite and that drifting work function of the tip itself could not be disentangled. In order to further investigate the origin of the V_{OC} increase, additional PL and KPFM measurements are needed, as well as additional simulations investigating the effect of doping on the device V_{OC}, especially in the presence of mobile ions.

8.2.2 Doping and Trap States

In order to quantify doping densities as a function of oxidation time, 4-point probe and transient photoconductivity measurements were carried out. The results, displayed in Figure 8.2a and b, show a very strong increase in conductivity – up to 3 orders of magnitude. This rapid increase in conductivity starts to take place as soon as the sample is exposed to air. Upon prolonged exposure, the conductivity reaches a peak after around 60 minutes, after which it starts to slowly decline. Interestingly, the peak conductivity is reached at timescales similar to those on which the V_{OC} and PCE reach their maximum. We note that the difference in light conductivity determined from the 4-point probe measurements displayed in Figure 8.2a versus the TPC measurements in Figure 8.2b can be attributed to the difference in illumination intensity between the two different experiments.

Our hypothesis is that this quick increase in conductivity can be linked to a strong increase in background charge density (doping), caused by the oxidation of Sn^{2+} ions to Sn^{4+}. Assuming the mobility of the charge carriers remains constant during the initial moments of exposure, the increase in charge carrier density can be calculated using:

$$\sigma = q\mu n \tag{8.1}$$

$$\Delta n = \frac{\sigma_1 - \sigma_2}{q\mu} \tag{8.2}$$

where σ is the conductivity at times 1 and 2, respectively, μ is the mobility, q is the elementary charge, and Δn is the change in carrier density between times 1 and 2. Considering that the conductivity increases by over 3 orders of magnitude, this would imply that the background carrier density also increased by over 3 orders of magnitude, provided the mobility of the charge carriers did not change. As shown previously in

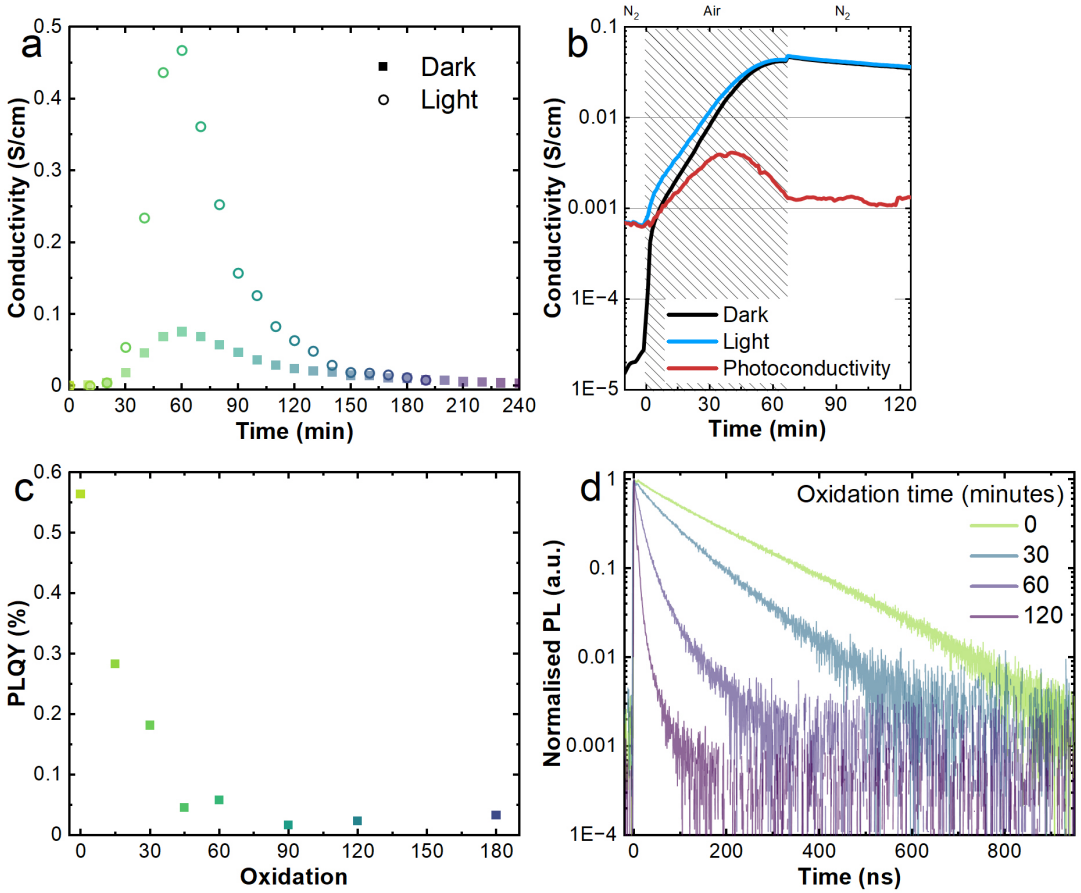

Figure 8.2: a) Perovskite conductivity upon oxidation in ambient air, measured using a 4-point probe technique. Meausrements were carried out in dark conditions as well as under ambient light. b) Transient photoconductivity upon oxidation of the perovskite in dry air. Following the initial oxidation, the atmosphere is exchanged back to nitrogen. c) Photoluminescence quantum yield measured upon oxidation of the perovskite in ambient air. d) Transient photoluminescence upon oxidation of the perovskite in dry air. TPC and TRPL data measured by Jongchul Lim and Manuel Kober-Czerny, respectively.

Chapter 4 (Figure 4.14), such a strong increase in doping densities could lead to significant fill factor losses in the device.

It is unlikely that the doping density in the perovskite suddenly strongly decreases after the conductivity reaches its peak. Rather, the evolving conductivity is likely the product of an interplay between increased doping densities on the one hand, and increased trap densities and carrier scattering reducing the carrier mobility on the other hand. In order to investigate whether this is indeed the case, we perform TRPL measurements, as well as PLQY measurements, in an attempt to calculate the trap densities as well as carrier densities for samples in different oxidation states. As can

be seen in Figure 8.2c, the PLQY of perovskite films decreases with increasing oxygen exposure time, indicating enhanced non-radiative recombination, which points to an increased trap density. Figure 8.2d shows that oxidation of the perovskite leads to a strong reduction in carrier lifetimes, further suggesting an increase in trap-assisted recombination.

We note that photo-oxidation can also alter the photoluminescence[246], although the exact impact of this effect on lead-tin perovskites has not been investigated yet. In order to minimise the occurence of any photo-induced chemical reactions at the surface of the lead-tin perovskites, illumination times were kept as low as possible, and TRPL measurements were carried out at low fluences. We note that the dark conductivities measured from TPC and 4-point probe measurements (Figure 8.2a and b) are consistent with each other, despite the fact that the TPC sample was subject to light pulses during oxidation. Therefore, we assume that the influence of photo-induced chemical reactions on the conductivity to be negligible.

In order to get an idea of the trap density as a function of oxidation time, in a next step, carrier densities and lifetimes can be calculated from the lifetimes obtained from the TRPL measurements following:

$$\tau = \frac{1}{N_t \sigma v_{th}} \tag{8.3}$$

Where τ is the carrier lifetime, N_t is the trap density, σ is the capture cross-section, and v_{th} is the thermal velocity (valid if no significant transfer).

Similarly, PLQY is related to these carrier densities and traps:

$$k_2 n^2 / ((k_1 n) + (k_2 n^2)) \tag{8.4}$$

However, as the work presented in this chapter is still in progress, calculations of carrier densities and lifetimes from TRPL and PQLY, as well as the subsequent

determination of long range charge carrier mobilities from TPC are still pending.

Interestingly, TPC results, displayed in Figure 8.2b, show that the photoconductivity can be stabilised by bringing the sample back into a nitrogen atmosphere, indicating that the oxidation process can be halted quickly. Furthermore, TPC measurements also show that, although dark- and light-conductivity peak at slightly longer timescales of around 60 minutes, the difference between the dark- and light-conductivity, which we will refer to as 'photoconductivity' here, peaks slightly earlier, at timescales corresponding exactly to the timescales at which the V_{OC} and PCE peak.

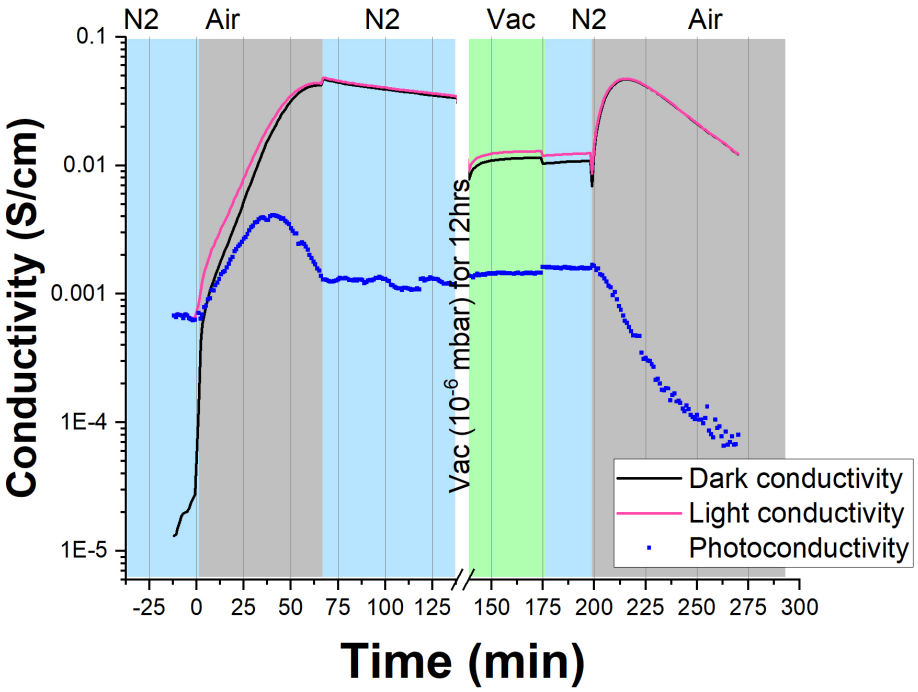

Figure 8.3: TPC results upon bringing samples into vacuum.

We also note that the photoconductivity can be partially increased again by storing the sample under vacuum overnight (see Figure 8.3a). We hypothesise that this might be explained by the extraction of SnI_4 or I_2 under vacuum. Leijtens et al. proposed the following reaction mechanism for the oxidation of lead-tin perovskites[75]:

$$2APb_{0.5}Sn_{0.5}I_3 + O_2 \longrightarrow 2AI + SnO_2 + PbI_2 + I_2\ (g) \tag{8.5}$$

Small amounts of SnI_4 are likely also formed, but in perovskites with a 50/50 lead/tin ratio, the predominant degradation mechanism produces I_2 rather than SnI_4[75]. Both I_2 or SnI_4 could act as deep trap states (the latter especially when it is present at the surface of the perovskite). Therefore, extracting SnI_4 or I_2 could reduce the trap density, thereby increasing the photoconductivity slightly. This hypothesis is supported by TRPL decays displayed in Figure 8.4a, which show an increase in carrier lifetimes when a previously oxidised sample is brought under vacuum. The PLQY, displayed in Figure 8.4b, also slightly increases again after the sample is brought under vacuum, further indicating a reduction in non-radiative recombination which would be consistent with a reduced trap density.

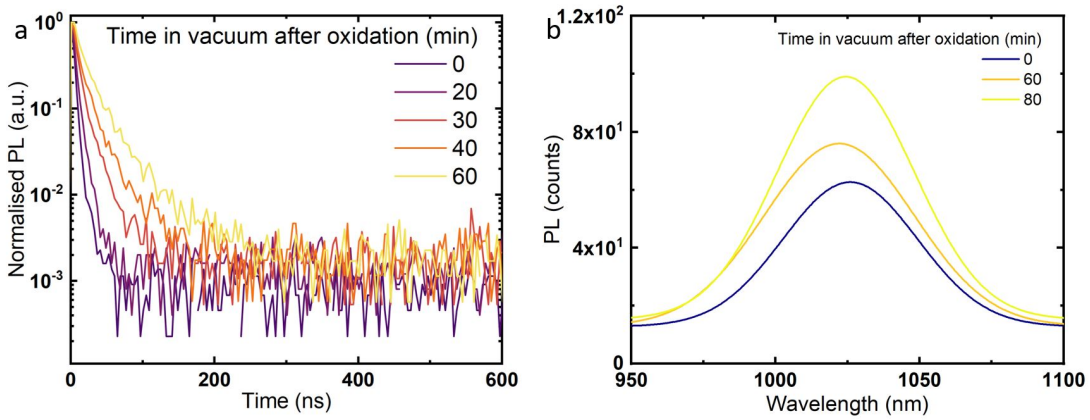

Figure 8.4: Evaluation of TRPL decay of an oxidised sample which is put under vacuum (a) and PLQY (b) for an oxidised sample which is put under vacuum for 30 minutes.

To investigate changes in the carrier mobility, as well as to get an idea about what happens with the minority carrier densities, we carried out photo hall measurements, the results of which can be seen in Figure 8.5.

The results of these photo-Hall measurements indicate that upon oxidation, carrier densities increase, while carrier mobility decreases. These results are consistent with

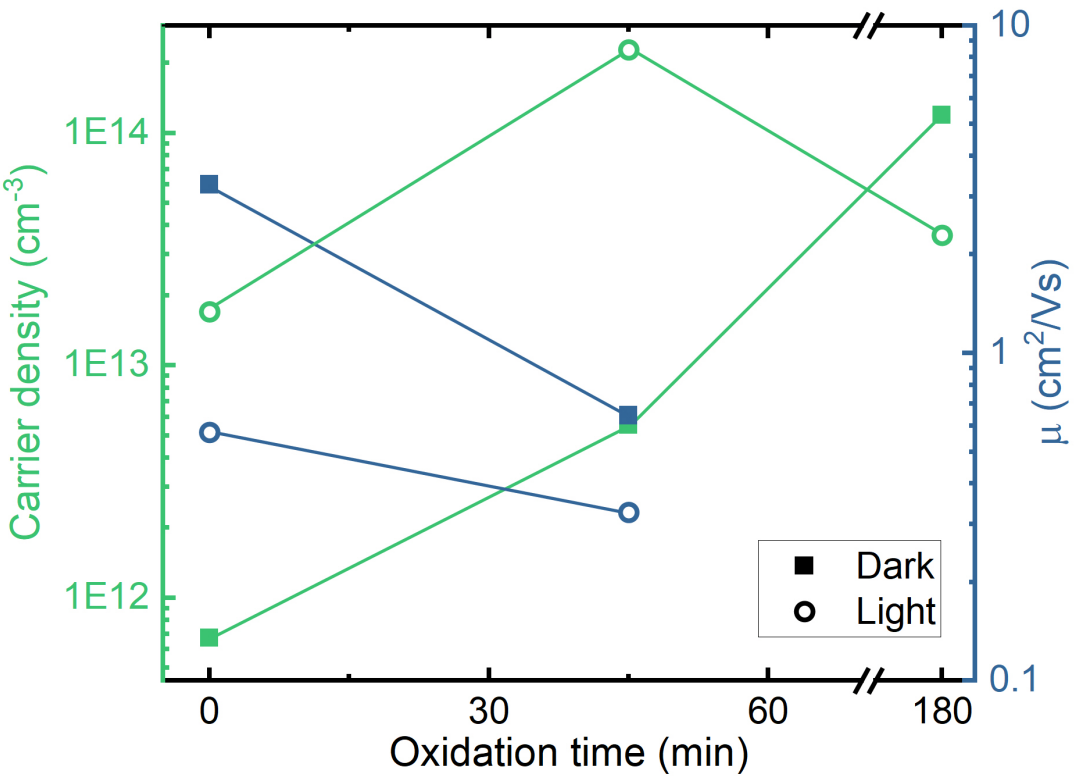

Figure 8.5: Carrier density (green) and mobility (blue) from photo Hall measurements of fresh samples, samples oxidised for 45 minutes to reach peak conductivity, and samples oxidised for 3 hours, for which the conductivity has decreased again. Measurement and analysis by Oki Gunawan, IBM. Results for both dark (filled squares) and light (open circles) measurements are displayed.

the hypothesis that oxygen-induced self-doping of the perovskite causes an increased background carrier density. The observed decreasing mobilities with increasing oxidation time would explain why the (photo) conductivity decreases after reaching an initial peak. However, we note a significant discrepancy between the increase in conductivity levels upon oxidation measured during the photo-Hall experiment, and the increase in conductivity which would be expected from the measurements presented in Figure 8.2a and b. Due to the long duration of the photo-Hall measurements, needed to reach sufficiently high signal-to-noise levels, the photo-Hall effect could not be measured in real time during oxidation. Instead, the perovskite was oxidised using dry air following deposition, after which the samples were encapsulated in a N_2-filled glovebox and transferred to IBM to be measured. Several measurement techniques show a significant difference between outcomes for samples measured during real-time oxidation, versus

samples which were encapsulated and stored after oxidation to be measured (some examples are displayed in Figure 8.6). One reason for this might be the fact that samples which are encapsulated undergo some extent of vacuum treatment when they are brought into the glovebox for encapsulation. Furthermore, altered surface chemistry of the perovskite, and potentially the presence of some remaining oxygen atoms, may also impact the way oxygen exposure affects the sample in the long term. Therefore, although the photo-Hall results may indicate trends in carrier density and mobility upon oxidation, these results should be interpreted with caution, and cannot be directly compared to results from real-time measurements presented in Figures 8.2, 8.3 and 8.4.

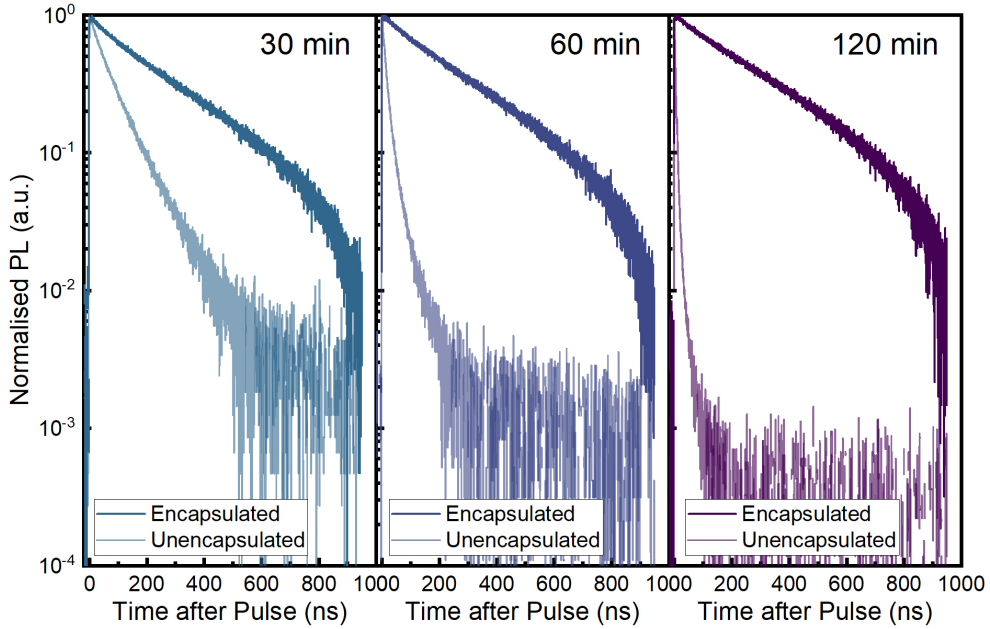

Figure 8.6: TRPL results of samples with and without encapsulation for different amounts of oxidation time. Samples were oxidised in real time (light), or oxidised, brought into the glovebox (including vacuum (90 mbar) in the antechamber for 5 minutes), and encapsulated. It should be noted that the samples were prepared (and, in the case of the encapsulated samples, oxidised) two days before measurement. An attempt to reduce the vacuum that the samples are exposed to in the antechamber before encapsulation to about 500 mbar yielded less reproducible results, although the general trend of increasing decay times upon increased oxygen exposure corresponded with that of the encapsulated samples which had been in vacuum in the antechamber for 5 minutes. Measured by Manuel Kober-Czerny.

8.2.3 Mobile Ions

From the oxidation pathways which have previously been established by Leijtens et al., it can be inferred that, upon oxidation of lead-tin perovskites, several species are formed which can act as mobile ions if they are not extracted from the perovskite[75]. Indeed, Figure 8.7a shows BACE results which indicate that upon oxidation, mobile ion densities strongly increase. Current decay measurements displayed in Figure 8.7b, show that this increased mobile ion density in turn leads to increased current losses due to enhanced field screening, an effect we described more in-depth in Chapters 4 and 5. On top of the increased mobile ion densities resulting in more severe current losses, worsening interfaces (as observed from PLQY) and reduced lifetimes (determined from TRPL) cause those mobile ions that are present in the perovskite to also have a stronger negative impact on the device performance.

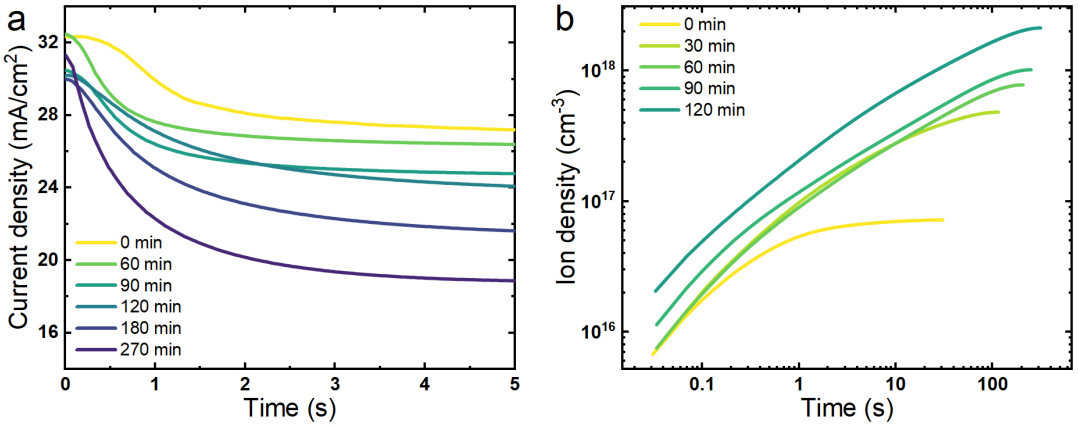

Figure 8.7: a) Current decay and b) integrated mobile ion densities from BACE measurements for a sample oxidised for different amounts of time. Oxidised samples display an increased concentration of mobile ions. We note that the device used for these experiments had been stored in N_2 for 12 months before these measurements. Additional experiments on fresh devices are still pending.

8.3 Conclusion

Looking at the device performance as a function of oxidation time, combined with the analysis of a range of optoelectronic measurements to extract trap- and doping densities, we found that the increase in trap density upon exposure to oxygen eventually

causes a strong deterioration in device performance. Although doping densities also increase upon oxidation, we hypothesise that a small amount of self-doping in the perovskite can actually improve device performance by reducing recombination at the HTL, which results in an observed increase in V_{OC}. Larger amounts of doping, however, still undermine device performance, mainly by causing increased fill factor and current losses. Exposure of perovskite layers to vacuum after oxidation revives conductivity to some extent, and seems to lead to a partial reduction in the density of trap states. However, further investigation is needed to shed light on the mechanism resulting in these changes upon vacuum treatment. Besides affecting the doping- and trap state density, oxygen exposure also leads to a clear increase in the concentration of mobile ions in the mixed lead-tin perovskites. This, in combination with increased interface recombination and strongly reduced carrier lifetimes, leads to significant current losses, as well as a decrease in fill factor. However, in order to fully understand how the different effects of oxidation impact the device performance of lead-tin perovskite solar cells, additional experiments and simulations are needed. Carrier densities and mobilities need to be determined as a function of oxidation time, and changes in radiative and non-radiative recombination also should be quantified. The changes in device performance upon oxidation are likely dictated by a complex interplay of changing doping densities, charge carrier mobilities, trap densities and mobile ions, and possibly complicated further by changes in energy level alignments.

CHAPTER 9

Conclusion and outlook

Although perovskite solar cells have undergone tremendous development over the past years, many of the mechanisms dictating device performance and stability are still not thoroughly understood. Properly understanding where efficiency losses come from, and how to design evidence-based optimisation approaches, is key to ultimately enable up-scaling and commercialisation of these devices.

This thesis aimed to investigate different aspects of perovskite solar cell physics in order to ultimately enable more efficient, stable devices. The two main topics at the heart of this investigation were firstly the impact of mobile ions on device performance and stability, and secondly the subcell selective investigation of losses in perovskite-based tandems. Ultimately, these two topics were combined in an attempt to also understand mobile-ion-induced losses in perovskite-based tandem solar cells.

The presence of mobile ions in perovskite solar cells has long been recognised, and linked to, for example, hysteresis and the degradation of electrodes and transport layers. However, the impact of mobile ions on current losses has not been investigated

as extensively. In Chapter 4, the discrepancy between the current which should in theory be generated based on the device optics, and the actual output current of mixed lead-tin perovskite solar cells is investigated. Rather than these current losses being caused by doping of the perovskite, which is often assumed to be a loss mechanism in these devices, we find that mobile ions are responsible for these current losses. Using time-dependent PL measurements, we show that field screening by these mobile ions leads to a reduced charge extraction efficiency, and an increased carrier density in the device under operating conditions. This eventually results in an increased recombination current, and a decreased extracted current density. This effect does not only occur in mixed-metal lead-tin perovskite solar cells, but also in lead-based devices. We show examples of different compositions, where in every case, decreased extraction current is accompanied by an increase in photoluminescence at short circuit. Next, we also investigate these mobile-ion-induced losses by looking at different charge extraction measurements, and link the time scales of these effects to the presence of mobile ions, rather than doping-induced charges. We perform scan speed dependent current-voltage measurements and show that the 'mobile-ion-free' PCE for these devices is significantly higher, mostly due to the absence of ion-induced current losses. Interestingly, different devices exhibit different extents of ion-induced current losses. Although the presence of mobile ions is required to create such losses in the first place, the extent of the current losses not only depends on the mobile ion density, but is also influenced by things like the transport layers that are present in the device stack, and non-radiative recombination at the device interfaces. Understanding which aspects of the device determine the impact of mobile ions on the its performance will be vital for future device optimisation. This research, by highlighting how mobile ions cause current losses, paves the way to develop more efficient devices with reduced current losses.

Next, the impact of device ageing on performance is investigated. Improved stability is key for the commercialisation of perovskite solar cells. Silicon solar cells are normally required to provide stable performance for at least 20 years - with

perovskite based tandem solar cells only really becoming economically advantageous if the perovskite (sub)cells last 15 years while retaining at least 80 % of their original PCE. However, many perovskite solar cells do not reach this target yet. Therefore, understanding how and why device performance degrades upon ageing is of vital importance. Hence we decided to investigate this topic in Chapter 5. We monitored device performance of solar cells with a range of different perovskite compositions, while they were subject to different stressors to accelerate ageing, and found that the initial reduction in performance was mostly governed by current losses. The findings presented in Chapter 4 prompted us to investigate whether mobile-ion-induced losses might be at the root of this performance reduction, or whether there might be other issues at play, such as increased surface recombination. Using the same charge extraction techniques as before, in combination with photoluminescence measurements, we were able to rule out increased surface recombination, and found that an increase in mobile ion densities upon ageing dominates early-onset performance reduction. Interestingly, mobile ion densities mostly increased when devices were stressed in such a way that there were additional electronic charges present, for example under light at open circuit, or in the dark with a bias applied to the device. Ageing at elevated temperature or at MPP conditions lead to less rapid device degradation and performance losses. Furthermore, although the same loss mechanism was observed in all perovskite compositions that were studied, some devices seem to be more strongly affected, and display larger efficiency losses, than others. Finally, a previously reported effect was observed, where the performance losses can, partially or even fully, recover when the stressor is removed and the device is placed in the dark. We were able to link this recovery to a reduction in the mobile ion density in the perovskite. When the stressor is reapplied, however, degradation quickly returns to the point it was at before the stressor was removed. This might have interesting implications as perovskite solar cells will be subject to a dark/light cycle under normal operating conditions. The results obtained in this chapter, for the first time, directly link the performance degradation of perovskite solar cells upon ageing to an increase in the

mobile ion densities in the device. This is an important finding, as it provides clear directions for future research: to prevent performance losses upon device ageing, and ultimately enable commercialisation of stable perovskite solar cells, the increase in mobile ion densities and their corresponding negative impacts need to be prevented. Finally, the 'recovery effect' should be investigated further, as this can provide vital clues on the creation and dynamics of mobile ions in perovskite solar cells.

After having investigated mobile ions and device degradation in perovskite solar cells in the first part of this thesis, we then turned our attention to 2-terminal all-perovskite tandem devices in the second half of the thesis. Just like for the single junctions investigated in the first part, gaining a better understanding of where the different losses in these tandems originate from is key to improving them in an evidence-based manner. Traditionally, 2-terminal tandem devices are often optimised by looking at the single-junction equivalents of both subcells. However, a better approach would be to directly characterise the performance of these subcells in the tandem device. In Chapter 6, we show how subcell selective characterisation of all-perovskite solar cells can pinpoint different losses, which then allows for an evidence-based optimisation approach. Comparing data from single junctions to data from the subcells, we find that the interconnect we used is quasi-lossless, and the voltage from both subcells directly adds up to the tandem voltage. However, both the HG, as well as the LG subcell can benefit from optimisation: reduced voltage losses in the HG subcell, as well as an increased current in the LG subcell, eventually lead to an optimised all-perovskite tandem with a stabilised efficiency of 25.9%. The work in this chapter demonstrates a generalisable evidence-based optimisation strategy utilising optoelectronic subcell characterisation. In doing so, it paves the way for accelerated improvement of all-perovskite tandem solar cells.

Finally, Chapters 7 and 8 present some results from ongoing research projects. In Chapter 7, knowledge obtained throughout the first chapters of this thesis is

combined to investigate the role of mobile ions in perovskite-based tandem solar cells. To this end, different subcell selective measurement techniques are explored, and their validity is discussed. Furthermore, the use of photoluminescence measurements for the determination of mobile-ion-induced losses is examined more in-depth, ultimately raising the question whether non-radiative losses can be determined directly from optoelectronic measurements in devices at short-circuit conditions. However, to fully answer this question, additional research is required. Chapter 8 seeks to understand the impact of oxidation on the device performance of low bandgap lead-tin perovskite solar cells. It highlights the presence of increased mobile ion densities in the perovskite upon oxidation alongside increased trap densities. However, additional measurements are required to better understand for example why the V_{OC} can slightly increase with oxidation, and why non-radiative recombination in the perovskite can be reduced through vacuum treatment.

Overall, this thesis demonstrates that gaining a better understanding of the device physics of perovskite solar cells is crucial to identify, and understand, different loss mechanisms. These insights can then be used to design an evidence-based optimisation approach, eliminating losses in a targeted manner. The work presented in this thesis marks a significant step forward in recognising the importance of mobile ions in perovskite solar cells, and their role in device degradation. Still, many open questions remain to be investigated. For example, for future device optimisation, it will be crucial to understand where the mobile ions in the perovskite originate from, and why they have a stronger impact on device performance in some systems than in others. Furthermore, moving forward, the impact of transport layers on mobile-ion-induced losses should critically be addressed. This thesis also highlighted the importance of subcell-selective measurements in perovskite-based tandems to pinpoint losses and develop effective and evidence-based optimisation strategies for perovskite-based tandem solar cells. This is key to accelerating the development of tandem devices towards commercialisation, as these evidence-based optimisation

strategies enable more resource-effective and targeted research. Ultimately, the impact of mobile ions on these tandem solar cells should also be investigated further, as current matching requirements in 2T devices imply that mobile ion-induced losses in perovskite subcells can have a significant impact on the overall device performance.

APPENDIX A

Appendix A, Supporting information to Chapter 3

A.1 Materials and Device Fabrication

A.1.1 p-i-n devices

The majority of devices presented in this thesis are p-i-n devices, meaning the devices are illuminated through the HTL side. A schematic overview of the general p-i-n device structure can be found in Figure A.1. Different HTLs and perovskite compositions were used for different experiments, most notably PEDOT:PSS, PTAA, 2-PACz for the HTL, and lead-tin perovskite (PbSn), various triple cation perovskites (TC), double cation perovskites (FACs), methylammonium lead iodide (MAPI) for the perovskites.

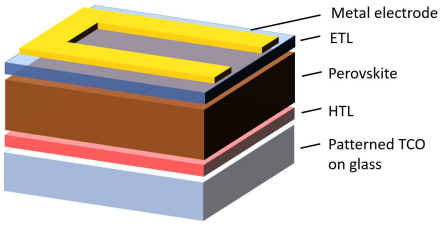

Figure A.1: A schematic overview of a p-i-n device stack

A.1.1.1 Substrate Cleaning

Pre-patterned (2.5×2.5 cm2, 15 Ω/sq) ITO substrates (Psiotec, UK) were sonicated for 10 minutes subsequently in acetone, 3% Hellmanex solution in deionised (DI) water, DI water, and isopropanol in order to clean them. After an oxygen plasma treatment (4 minutes, 120 W), the substrates for the mixed-metal lead-tin perovskite devices were transferred to a laminar flow bench, while the other substrates were transferred into an N_2-filled glovebox.

A.1.1.2 Hole Transport Layers

A.1.1.2.1 PEDOT:PSS For the mixed-metal perovskite solar cells described in this thesis, PEDOT:PSS (poly(3,4-ethylenedioxythiophene) polystyrene sulfonate) (Heraeus, AL3083) layer was spin-coated in air from a 1:2 (PEDOT:PSS):methanol solution, that had been filtered using a 0.45 µm GMF filter. The PEDOT:PSS/methanol solution was spin-coated at 4000 rpm for 45 seconds at a ramp of 1500 rpm/s After 20 minutes of annealing on a pre-heated hotplate at 150 °C, the films were transferred immediately to a N_2 filled glovebox.

A.1.1.2.2 PTAA For the pin-type Pb-based cells described in this thesis, 60 µL of PTAA (Poly-[bis-(4-phenyl)-(2,4,6-trimethylphenyl)-amin]) solution (Sigma-Aldrich, 1.75 mg/mL in toluene) was spin-coated at 6000 rpm for 30 seconds with a ramp of 2000 rpm/s After 10 min annealing on a hotplate at 100 °C, the films were cooled down to room temperature. This process resulted in the formation of a PTAA layer with an estimated thickness of 8 nm. After the deposition of the PTAA layer, 60 µL

of PFN-Br (Poly(9,9-bis(3'-(N,N-dimethyl)-N-ethylammoinium-propyl-2,7-fluorene)-alt-2,7-(9,9-dioctylfluorene))dibromide) solution (1-Material, 0.5 mg/mL in methanol) was deposited on top of the PTAA layer dynamically at 4000 rpm for 30 s resulting in a film with thickness below the detection limit of our AFM ($<$ 5 nm). No further annealing of the HTL took place after this.

A.1.1.2.3 2PACz Some of the optimised pin-type Pb-based cells described in this thesis are based on the use of SAMs instead of a conventional HTL. For these devices, a previously sonicated solution of 2PACz (TCI, 1.0 mg/mL, in ethanol) was spin-coated at 3000 rpm for 30 seconds with a ramp of 3000 rpm/s. The substrates were annealed at 100 °C for 10 minutes and cooled down to room temperature before the deposition of the perovskite layer.

A.1.1.3 Perovskite Absorber Layers

A.1.1.3.1 Mixed-metal lead-tin perovskite (LG) The 1.2 M mixed-metal lead-tin perovskite solutions were prepared by dissolving FAI, CsI, SnI_2 and PbI_2, together with, relative to their respective metals, 6 molar% $Pb(SCN)_2$ and 10 molar & SnF_2 in a 4:1 DMF:DMSO mixture. We note that all precursors used for this solution were stored and weighed in a N_2-filled glovebox, to prevent contamination of the solution with O_2 or H_2O. The solution was stirred for 2 hours at room temperature. Finally, the solution was filtered using a 0.45 µm PTFE filter.

The mixed-metal $FA_{0.83}Cs_{0.17}Pb_{0.5}Sn_{0.5}I_3$ perovskite films were deposited by spin-coating at 3000 rpm for 45 s with a ramp of 1000 rpm/s. 25 s after the start of the spinning process, the spinning substrate was washed with 200 µL anisole, which was deposited in the centre of the film. By the end of the spinning process, the perovskite films turned dark brown. The perovskite films were then annealed at 100 °C for 10 minutes on a preheated hotplate inside the N_2 filled glovebox. During the annealing process, the perovskite films turned black.

For the improved, thicker lead-tin perovskite presented in the second half of Chapter 6, a preparation method based on work by Hu et al.[238] was used, with the following adaptations: - instead of ammonium thiocyanate, 0.036 mmol/mL guanidinium thiocyanate was added - after the perovskite precursors were dissolved, metallic tin powder was added to the solution, which was continuously stirred. Just before deposition of the perovskite, the solution was filtered to remove the metallic tin.

A.1.1.3.2 Triple cation perovskites The triple cation perovskites presented in this thesis were fabricated by Francisco Peña-Camargo, Emilio Gutierrez-Partida, Sahil Shah and myself. The solutions for the lead-based perovskites layers were prepared as follows: 1.2 M $FAPbI_3$ solution was prepared by dissolving FAI and PbI_2 in DMF:DMSO (4:1 volume ratio) which contains a 10%-molar excess of PbI_2. The 1.2 M $MAPbBr_3$ solution was made by dissolving MABr and $PbBr_2$ in DMF:DMSO (4:1 volume ratio) which contains a 10 %-molar excess of $PbBr_2$. The solutions were stirred overnight at room temperature. By mixing these $FAPbI_3$ and $MAPbBr_3$ solutions in a ratio of 60:40 or 83:17 respectively, we obtain "MAFA" solutions. Lastly, 42 µL of a 1.5 M CsI solution in DMSO was mixed with 958 µL of each one of the MAFA solutions resulting in nominal triple cation perovskite stoichiometries of $Cs_{0.05}(FA_{0.60}MA_{0.40})_{0.95}Pb(I_{0.60}Br_{0.40})_3$ and $Cs_{0.05}(FA_{0.83}MA_{0.17})_{0.95}Pb(I_{0.83}Br_{0.17})_3$. These 2 triple cation perovskites are throughout the thesis referred to as '60/40' and '83/17', respectively.

All triple cation perovskite films were prepared by statically depositing 120 µL perovskite solution and spin-coating at 4000 rpm for 40 s at a ramp of 1334 rpm/s. 10 s after the start of the spinning process, the spinning substrate was washed with 300 µL ethylacetate for approximately 1 s (the anti-solvent was deposited in the centre of the film). We note that by the end of the spin coating process, the perovskite film turned dark brown. The perovskite film was then annealed at 100 °C for 1 h on a preheated hotplate, where the film turned slightly darker.

A.1.1.3.3 MAPI The MAPI devices used for measurements presented in this thesis were fabricated by Francisco Peña-Camargo. MAPI solution was prepared by dissolution of MAI powder (Dysol 1.3 M) with PbI_2 (TCI, 1.3 M) in a γ-butyrolactone/dimethyl sulfoxide mixed solvent (7:3 by volume), stirring at 60 °C for 10 min.

The MAPI solution (80 µL) was then spin-coated at 1000 rpm for 5 s followed by 3000 rpm for 80 s. 100 µL toluene was added dropwise after 40 s to form a transparent perovskite film. After spin-coating, the films were dried for 2 minutes in the glovebox at room temperature, during which the films changed their colour from yellow to light brown. The MAPI perovskite layers were then subsequently annealed for 2 minutes at 100 °C on a hotplate where the films turned black immediately.

A.1.1.4 Electron Transport Layers and Top Electrode

After annealing of the perovskite, the samples were transferred to an evaporation chamber where fullerene C_{60} (25 nm), (Bathocuproine, BCP) (8 nm) and copper (100 nm) were deposited under vacuum (p $= 10^{-7}$ mbar). The overlap of the copper with the ITO electrodes defined the active area of the pixel (6 mm^2).

A.1.2 n-i-p devices

The n-i-p devices presented in this thesis were fabricated by Max Grischek and Emilio Gutierrez-Partida.

A.1.2.1 Substrate Cleaning

Pre-patterned (2.5×2.5 cm^2) FTO substrates (Advanced Election Technology Co. Ltd., China) were sonicated for 10 minutes subsequently in 2% Mucasol solution in deionised (DI) water (Schülke & Mayr GmbH, Germany), acetone and isopropanol. After each sonication in Mucasol solution and acetone, the substrates were thoroughly rinsed with DI water. After sonication in isopropanol, the substrates were dried with a

nitrogen gun and further cleaned using a UV-ozone cleaner for 20 minutes just before the deposition of the compact TiO_2 layer.

A.1.2.2 TiO_2 layer

Deposition of compact TiO_2 layer The compact TiO_2 layer was deposited by spray pyrolysis. The solution consisted of 0.72 mL titanium diisopropoxide bis(acetylacetonate) (75 wt.% in isopropanol, Sigma Aldrich) and 0.48 mL acetylacetone (Sigma Aldrich) in 10.8 mL of ethanol. The sides of the substrates were covered with glass to ensure direct contact with the FTO for the evaporated electrodes. After heating the substrates to 450 °C and letting the temperature stabilise for 15 min, the full volume of solution was sprayed with oxygen gas flow on 32 substrates (4 rows and 8 columns) by slowly moving over the substrates once every 30 s in a distance of approximately 20 cm at an angle of approximately 45 °C. The substrates were then kept at 450 °C for 30 min and taken off the hot plate after cooling down to below 150 °C.

Deposition of mesoporous TIO_2 layer The substrates with compact TiO_2 layer were cleaned using a UV-ozone cleaner for 15 minutes. TiO_2 paste (30NR-T, Greatcell Solar Materials Pty Ltd., Australia) was dissolved in ethanol with a weight ratio of 1:6. It was stirred overnight before spin-coating. The mesoporous TiO_2 layer was prepared by spin-coating 50 µL of the dispersion on the compact TiO_2 layer at a speed of 4000 rpm for 10 s with a ramp of 2000 rpm/s, followed by annealing at 100 °C for a minimum of 5 min. The substrates were then annealed on a hot plate programmed to hold a temperature of 125 °C for 5 min, 325 °C for 5 min, 375 °C for 5 min, and 450 °C for 30 min with 5 min ramping time between each temperature.

LiTFSI-doping of mesoporous TiO_2 layer 80 µL of a fresh solution consisting of bis(trifluoromethane)sulfonimide lithium salt (LiTFSI, 99.95 %; Sigma-Aldrich) in acetonitrile (10 mg/mL) were spin-coated on the mesoporous TiO_2 layer at a speed of 3000 rpm for 10 s with a ramp of 1000 rpm/s, followed by annealing at 100 °C for a

minimum of 5 min. The substrates were then annealed on a hot plate using the same program as for the mesoporous TiO_2 layer. Both TiO_2 layers and the LiTFSI were deposited and annealed in a flow box in ambient air. The surface of the annealed film was finally cleaned using a UV-ozone cleaner for 15 minutes.

A.1.2.3 Perovskite absorber layers

1.5 M nominal PbI_2 and $PbBr_2$ stock solutions were prepared in DMF:DMSO = 4:1 volume and shaken overnight at 60 °C. PbI_2 was added to FAI solution with 9% PbI_2 excess and $PbBr_2$ was added to MABr with 9 % $PbBr_2$ excess. The resulting $FAPbI_3$ and $MAPbBr_3$ solutions were then mixed in an 85:15 volume ratio. Finally, 5 vol-% of 1.5 M nominal CsI in DMSO was added to the perovskite precursor. The CsI stock solution was prepared one day before mixing.

The perovskite layer was prepared by spreading 100 µL of perovskite solution on the substrate and then spinning it with one step of 3500 rpm for 35 s with 5 s acceleration time. 10 s before the end of the program, 300 µL of the anti-solvent Anisole was dripped on the film. The films were then annealed at 100 °C for 40 minutes.

A.1.2.4 Hole Transport Layers and Top Electrode

For the HTL solution, 36.15 mg of 2,2‘7,7‘-tetrakis(N,N-di-p-methoxyphenylamin)-9,9‘- spirobifluoren (Spiro-OMeTAD; Sigma Aldrich) was dissolved in 1 mL of Chlorobenzene. 8.8µL of a bis(trifluoro-methane) sulfonimide lithium salt, (LiTFSI, 99.95%; Sigma-Aldrich) stock solution (520 mg/mL in acetonitrile), 14.6 µL of a tris(bis(trifluoromethyl-sulfonyl)imide) (FK209, Dyenamo) stock solution (300 mg/mL in acetonitrile), and 14.4 µL of 4-tert-butyl-pyridine (Sigma-Aldrich) were added as dopants. 70 µL of the Spiro-OMeTAD solution containing the doping agents was spin-coated onto the spinning samples at a speed of 1800 rpm for 30 s to form 150 nm thick layers. After spin-coating, the samples were stored in a dry air box overnight at a relative humidity below 0.3 %. The next day, the samples were transferred to an

evaporation chamber where 80 nm of gold was deposited under vacuum (p= 10^{-6} mbar). The overlap of the gold electrodes and the FTO defined the active area of the pixel (18 mm^2). Both the perovskite and Spiro-OMeTAD layers were spin-coated and annealed in a glove box under a nitrogen atmosphere.

A.1.3 Device fabrication of 2-terminal all-perovskite tandem devices

To fabricate tandem devices, the high gap perovskite cells were prepared by Francisco Peña-Camargo as described above, up until the deposition of the C60 layer. Hereafter, aluminium zinc oxide (AZO) nanoparticle dispersion (N21X from Avantama) was diluted in a 1:2 ratio with isopropanol and spin-coated in a nitrogen filled glovebox at 4000 rpm for 20s with a ramp of 6 s, followed by a 90 min annealing step at 80 °C. Thereafter the samples were transferred into a Beneq TFS-200 system without inert break. SnOx and InOx layers were sequentially grown from tetrakis(dimethylamino)tin(IV) (TDMA-Sn, Strem) + water and Cyclopentadienylindium (CpIn, Strem), oxygen (purity 99.999%) + water respectively. TDMA-Sn and CpIn were used from hot sources kept at 45 °C, and 50 °C respectively. Water was kept in a liquid source at room temperature. Reactor temperature during both deposition processes was set to 80 °C. All interconnects for the tandem devices described in this thesis were deposited by Kai O. Brinkmann. After the deposition of the interconnect, the tandems were finished by myself in the same manner as described above for the low-gap perovskite single junctions, by deposition of PEDOT:PSS, low-gap perovskite and ETL & top contact. A schematic overview of a 2-terminal all-perovskite tandem solar cell is displayed in Figure A.2.

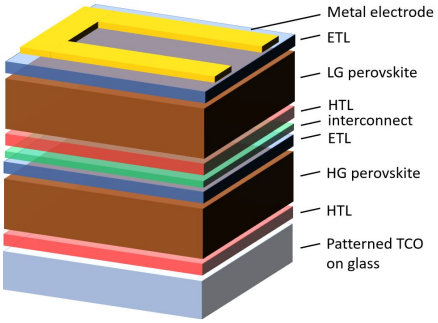

Figure A.2: A schematic overview of a 2-terminal all-perovskite tandem stack.

A.2 Simulation parameters

Simulations of lead-tin perovskites presented in Chapter 4 were carried out using Setfos version 5.1, whereas simulations of the all-perovskite tandems presented in Chapter 6 were carried out using Setfos version 5.2.

Table A.1: Parameter values for the simulation of lead-tin perovskites as used in Chapter 4 and 6

Parameter	Symbol	Value	Unit	Comment
Majority carrier band offset between perovskite and C60	$\Delta E_{\text{maj,c}}$	0	eV	Due to near QFLS=V_{OC} match in these devices
Majority carrier band offset between perovskite and PEDOT	$\Delta E_{\text{maj,v}}$	0	eV	Due to near QFLS=V_{OC} match in these devices
Ionised acceptors in PEDOT:PSS	$N^{-}_{\text{A,p}}$	6.2×10^{19}	cm^{-3}	PEDOT:PSS is considered to be highly doped.
Ionised donors in C60	$N^{+}_{\text{D,n}}$	0	cm^{-3}	No doping used
Thickness of PEDOT:PSS	$d_{\text{PEDOT:PSS}}$	25	nm	Measured with profilometer
Thickness of perovskite	d_{pero}	470	nm	Measured with profilometer
Thickness of C60	d_{C60}	30	nm	Measured with profilometer
Thickness of BCP	d_{BCP}	8	nm	Measured with profilometer
Offset between metal and PEDOT:PSS	$\Delta E_{\text{F,metal-p}}$	0.0	eV	Assumption
Offset between metal and C60	$\Delta E_{\text{F,metal-n}}$	0.0	eV	Assumption
Device built-in voltage	V_{BI}	0.8	V	Fit to experimental data
Bandgap PEDOT:PSS	$E_{\text{G,PEDOT:PSS}}$	2.5	eV	Assumption

Continued on next page

Table A.1 – *Continued from previous page*

Parameter	Symbol	Value	Unit	Comment
Electron affinity PEDOT:PSS	$E_{\mathrm{A,PEDOT:PSS}}$	2.5	eV	Consider aligned PEDOT:PSS HOMO with perovskite valence band
Bandgap perovskite	$E_{\mathrm{G,pero}}$	1.2	eV	Measured by UV-Vis
Electron affinity perovskite	$E_{\mathrm{A,pero}}$	3.9	eV	Assumption
Electron affinity C60	$E_{\mathrm{A,C60}}$	3.9	eV	Consider aligned C60 LUMO with perovskite conduction band
Bandgap C60	$E_{\mathrm{G,C60}}$	2.0	eV	Measured by UV-Vis
Electron mobility in C60	$\mu_{\mathrm{n,C60}}$	1×10^{-2}	$\mathrm{cm}^2/\mathrm{Vs}$	1.5×10^{-2} $\mathrm{cm}^2/\mathrm{Vs}$ measured with SCLC in ref.[247].
Hole mobility in PEDOT:PSS	$\mu_{\mathrm{p,PEDOT:PSS}}$	1.5×10^{-2}	$\mathrm{cm}^2/\mathrm{Vs}$	Assumption, due to doping the mobility in the HTL is less important.
Electron mobility in perovskite	$\mu_{\mathrm{n,pero}}$	1	$\mathrm{cm}^2/\mathrm{Vs}$	Thz perovskite mobility sums of around 35 $\mathrm{cm}^2/\mathrm{Vs}$ were measured for lead-tin perovskites in ref.[106], lowered to account for grain boundaries
Hole mobility in perovskite	$\mu_{\mathrm{p,pero}}$	1	$\mathrm{cm}^2/\mathrm{Vs}$	
Electron trap density in perovskite	$N_{\mathrm{t,n}}$	4×10^{15}	cm^{-3}	Fit to experimental data
Hole trap density in perovskite	$N_{\mathrm{t,p}}$	4×10^{15}	cm^{-3}	Fit to experimental data

Continued on next page

Table A.1 – *Continued from previous page*

Parameter	Symbol	Value	Unit	Comment
Hole trap density at perovskite interface with the HTL	$N_{t,n,pi}$	1×10^{16}	cm^{-3}	In order to simulate interface effects, a 1 nm thick perovskite layer with a higher trap density is used at both perovskite – TL interfaces. Other parameters were kept the same as in the bulk perovskite
Electron trap density at perovskite interface with the ETL	$N_{t,n,in}$	1×10^{16}	cm^{-3}	
Electron trap depth in perovskite	$E_{t,n}$	0.6	eV	Fit to experimental data
Hole trap depth in perovskite	$E_{t,p}$	0.6	eV	Fit to experimental data
Electron capture rate in perovskite	$r_{t,n}$	5×10^{-10}	cm^3/s	Fit to experimental data
Hole capture rate in perovskite	$r_{t,p}$	5×10^{-10}	cm^3/s	Fit to experimental data
Relative dielectric constant PEDOT:PSS	$\epsilon_{PEDOT:PSS}$	2.7		Typical value for organic conjugated polymers[248].
Relative dielectric constant perovskite	ϵ_{pero}	40		Measured value from dark-CELIV.
Relative dielectric constant C60	ϵ_{C60}	3.5		A relative permittivity of 5 was measured at lowest frequencies (1kHz) at 300 K, ref.[249]
Effective electron density of states in HTL	$N_{C/V,PEDOT:PSS}$	1×10^{20}	cm^{-3}	ref.[180]

Continued on next page

Table A.1 – *Continued from previous page*

Parameter	Symbol	Value	Unit	Comment
Effective electron density of states in C60	$N_{C/V,C60}$	1×10^{20}	cm^{-3}	ref.[180]
Effective electron density of states in perovskite	$N_{C/V,pero}$	2.2×10^{18}	cm^{-3}	Assumed for lead-tin perovskite based on lead-based perovskite value in ref.[250]
Anion mobility in perovskite	$\mu_{A,pero}$	5×10^{-9}	cm^2/Vs	Fit to experimental data
Anion density in perovskite	$n_{A,pero}$	3.6×10^{16}	cm^{-3}	Fit to experimental data

For the simulations of triple cation '83/17' perovskites, presented in Chapter 5, a newer version of Setfos (5.2) was used, which allowed for the direct simulation of interface effects. Therefore, the 1 nm thick perovskite layers with higher trap densities, which were used for the simulations presented in Chapter 4, were omitted. Instead, trap densities and electron- and hole capture rates at the interfaces of the perovskite with the HTL and ETL were directly implemented in Setfos. Simulation parameters for the 83/17 perovskites were originally adapted for use in Setfos by Jonas Diekmann and Vincent Le Corre. Many of the parameters used for the simulation of triple cation perovskites are the same as those listed in Table A.1. Where parameters differed, the parameters specific to the triple cation simulations are listed in Table A.2.

Table A.2: Parameter values for the simulation of 83/17 triple cation perovskites as used in Chapter 5

Parameter	Symbol	Value	Unit	Comment
Ionised acceptors in HTL	$N_{A,p}^-$	0	cm^{-3}	No doping used.
Thickness of PTAA	$d_{PEDOT:PSS}$	10	nm	Measured with profilometer

Continued on next page

Table A.2 – *Continued from previous page*

Parameter	Symbol	Value	Unit	Comment
Thickness of perovskite	d_{pero}	500	nm	Measured with profilometer
Thickness of C60	d_{C60}	25	nm	Measured with profilometer
Offset between metal and PEDOT:PSS	$\Delta E_{\text{F,metal-p}}$	0.1	eV	
Offset between metal and C60	$\Delta E_{\text{F,metal-n}}$	0.1	eV	
Device built-in voltage	V_{BI}	1.4	V	
Bandgap PTAA	$E_{\text{G,PTAA}}$	3.0	eV	Assumption
Electron affinity PTAA	$E_{\text{A,PTAA}}$	2.5	eV	Consider aligned PTAA HOMO with perovskite valence band
Bandgap perovskite	$E_{\text{G,pero}}$	1.62	eV	Measured by UV-Vis
Hole mobility in PTAA	$\mu_{\text{p,PTAA}}$	1.5×10^{-4}	cm^2/Vs	
Electron trap density in perovskite	$N_{\text{t,n}}$	4×10^{15}	cm^{-3}	Fit to experimental data
Hole trap density in perovskite	$N_{\text{t,p}}$	4×10^{15}	cm^{-3}	Fit to experimental data
Hole trap density at perovskite interface with the HTL	$N_{\text{t,n,pi}}$	1×10^{16}	cm^{-3}	
Electron trap density at perovskite interface with the ETL	$N_{\text{t,n,in}}$	1×10^{16}	cm^{-3}	
Electron trap depth in perovskite	$E_{\text{t,n}}$	0.6	eV	Fit to experimental data
Hole trap depth in perovskite	$E_{\text{t,p}}$	0.6	eV	Fit to experimental data

Continued on next page

Table A.2 – *Continued from previous page*

Parameter	Symbol	Value	Unit	Comment
Electron capture rate in perovskite	$r_{\text{t,n}}$	5×10^{-10}	cm^3/s	Fit to experimental data
Hole capture rate in perovskite	$r_{\text{t,p}}$	5×10^{-10}	cm^3/s	Fit to experimental data
Relative dielectric constant PTAA	$\epsilon_{\text{PEDOT:PSS}}$	3.5		
Relative dielectric constant perovskite	ϵ_{pero}	22		Measured value from dark-CELIV.
Relative dielectric constant C60	ϵ_{C60}	5		A relative permittivity of 5 was measured at lowest frequencies (1kHz) at 300 K, ref.[249]
Anion mobility in perovskite	$\mu_{\text{A,pero}}$	5×10^{-9}	cm^2/Vs	Fit to experimental data
Anion density in perovskite	$n_{\text{A,pero}}$	3.6×10^{16}	cm^{-3}	Fit to experimental data

For the simulation of all-perovskite tandems, presented in Chapter 6, a HG perovskite subcell with a 1.85 eV bandgap was simulated, using mostly the same parameters used for the '83/17' simulations detailed in Table A.2. The HG and LG subcell were connected using an interface at which charges could recombine through hopping, with an attempt frequency of 5x10^{-7} m^2/s. We note, however, that these simulations were carried out using version 5.2.5 of Setfos. In more recent versions of Setfos (5.3 and 5.4), due changes in the way carrier recombination at interfaces is simulated, these input parameters yield different results than they did in Version 5.2.5. For a full overview of the parameters used to simulate all-perovskite tandems, we refer to[237].

APPENDIX B

Appendix B, Supporting information to Chapter 5

B.1 Material characterisation

This appendix contains additional figures, which relate to mechanical and chemical changes to the materials upon ageing.

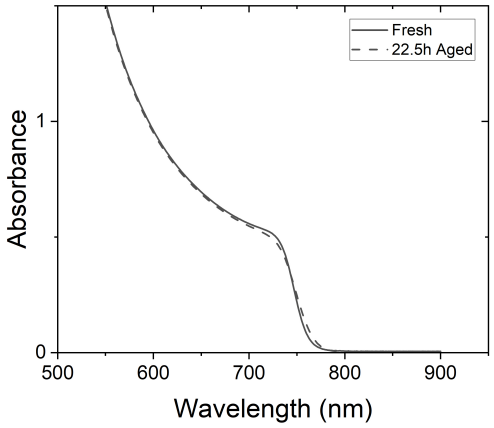

Figure B.1: Absorption spectroscopy of fresh and degraded triple cation films after 22.5 hours of illumination. Measured by Sahil Shah.

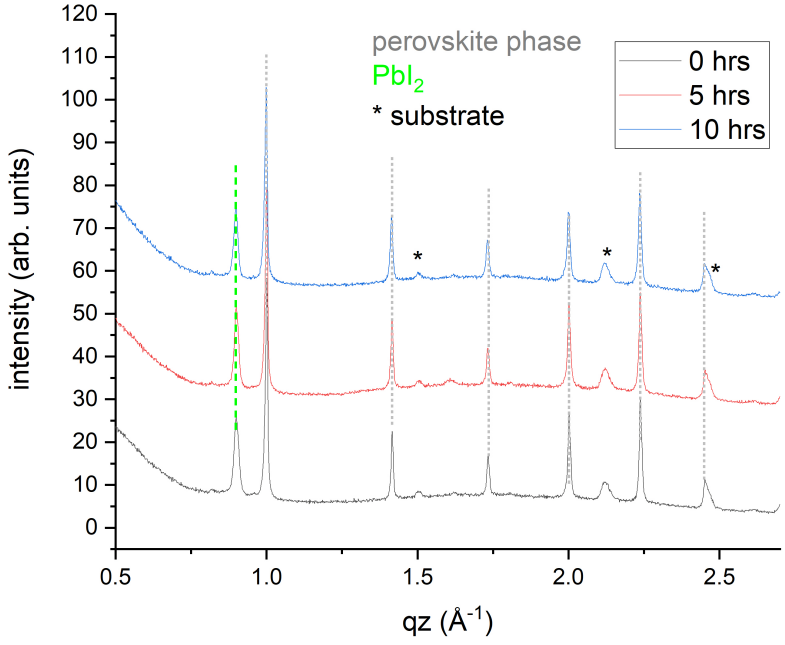

Figure B.2: X-ray diffraction measurements of fresh and degraded triple cation films after different durations of illumination revealed no apparent change during the illumination within the first hours of degradation. Measured by Fengshuo Zu.

B.2 Different perovskite compositions and ageing methods

This appendix contains additional ageing data, from devices with different perovskite compositions (Part 1) and devices which were aged using different ageing methods

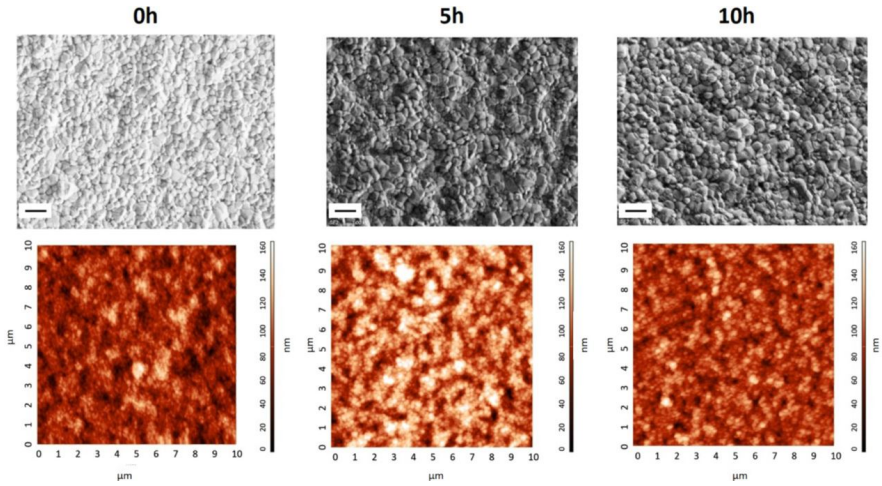

Figure B.3: SEM and AFM of fresh and degraded triple cation films after different durations of illumination. The scale bar in the SEM images is 500 nm. Measured by Burkhard Stiller.

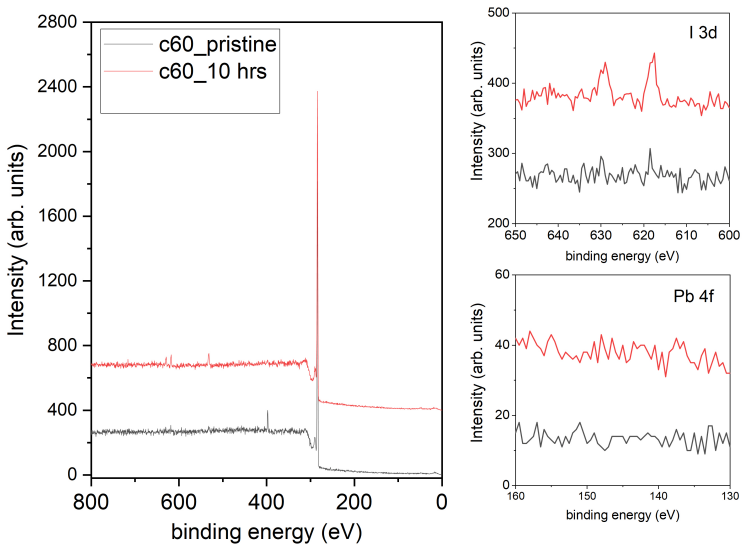

Figure B.4: XPS survey of Si wafers suspended on top (at a distance of ca. 1 mm) of different perovskite films, i.e. the neat 83-17 triple cation (TC) film, TC capped with C_{60} and TC capped with C_{60} and 1 nm (100 nm) of Cu, after 10 hours of illumination. We observe the capture of iodine for the bare perovskite sample, evidencing the release of iodine under illumination but no other perovskite species (e.g., iodine or lead) for all other sample stacks suggesting an effective diffusion barrier on these short timescales. Measured by Fengshuo Zu.

(Part 2).

B.2.1 Different perovskite compositions

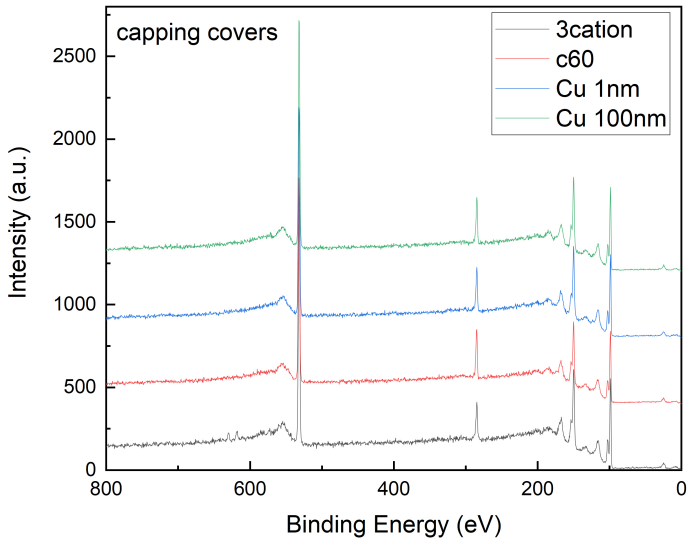

Figure B.5: XPS survey of Si wafers suspended on top (at a distance of ca. 1 mm) of different perovskite films, i.e. the neat 83-17 triple cation (TC) film, TC capped with C_{60} and TC capped with C_{60} and 1 nm (100 nm) of Cu, after 10 hours of illumination. We observe the capture of iodine for the bare perovskite sample, evidencing the release of iodine under illumination but no other perovskite species (e.g., iodine or lead) for all other sample stacks suggesting an effective diffusion barrier on these short timescales. Measured by Fengshuo Zu.

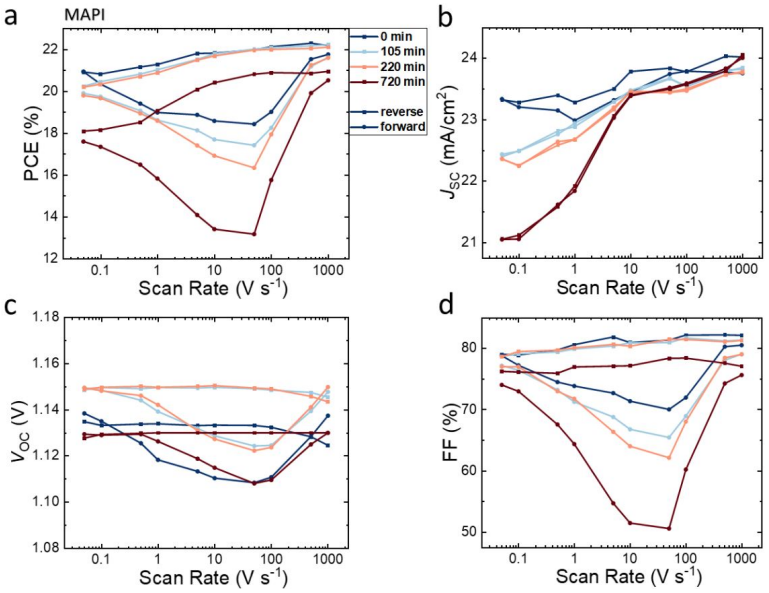

Figure B.6: a The power conversion efficiency (PCE), b short-circuit current density (J_{SC}), c open-circuit voltage (V_{OC}) and d fill factor (FF) from current-voltage characteristics measured at different scan speeds for $MAPbI_3$ perovskite solar cells after different ageing times.

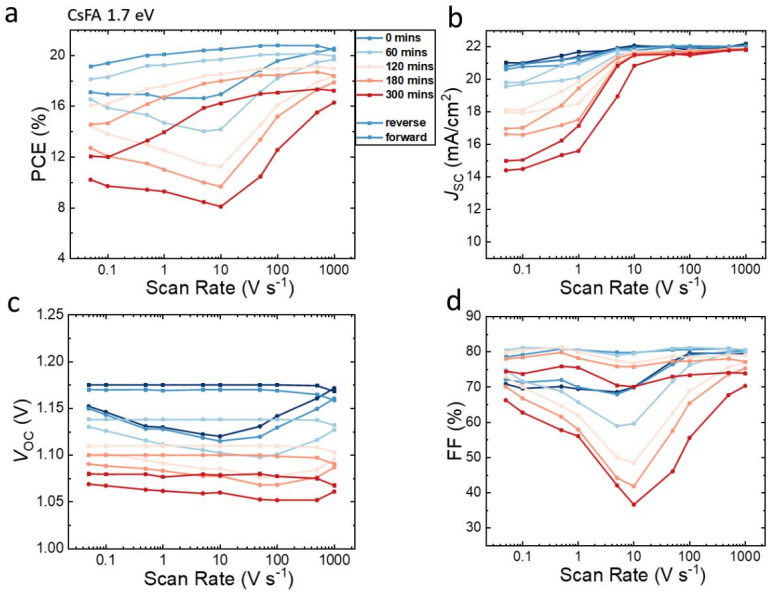

Figure B.7: a The power conversion efficiency (PCE), b short-circuit current density (J_{SC}), c open-circuit voltage (V_{OC}) and d fill factor (FF) from current-voltage characteristics measured at different scan speeds for $FA_{0.85}Cs_{0.15}Pb(I_{0.77}Br_{0.23})_3$ perovskite solar cells after different ageing times. Measured by Sahil Shah and Francisco Peña-Camargo.

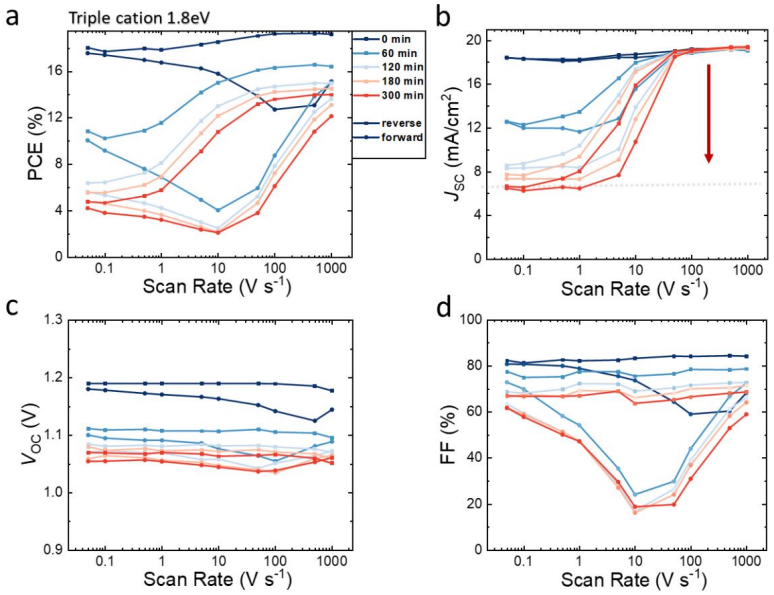

Figure B.8: a The power conversion efficiency (PCE), b short-circuit current density (J_{SC}), c open-circuit voltage (V_{OC}) and d fill factor (FF) from current-voltage characteristics measured at different scan speeds for 1.8eV wide gap $Cs_{0.05}(FA_{0.60}MA_{0.40})_{0.95}Pb(I_{0.60}Br_{0.40})_3$ perovskite solar cells after different ageing times. Measured by Sahil Shah and Francisco Peña-Camargo.

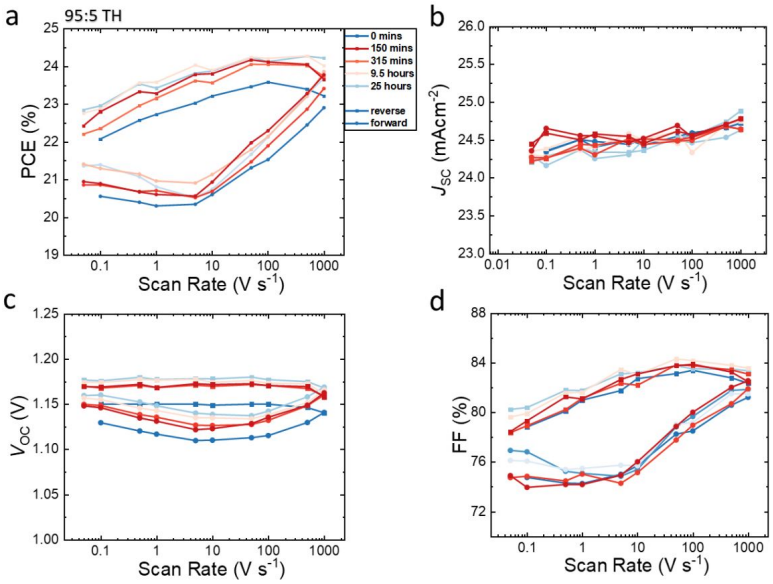

Figure B.9: a The power conversion efficiency (PCE), b short-circuit current density (J_{SC}), c open-circuit voltage (V_{OC}) and d fill factor (FF) from current-voltage characteristics measured at different scan speeds for triple halide $Cs_{0.05}(FA_{0.95}MA_{0.05})_{0.95}Pb(I_{0.95}Br_{0.05})_3$ + 20 mol% MACl perovskite solar cells after different ageing times.

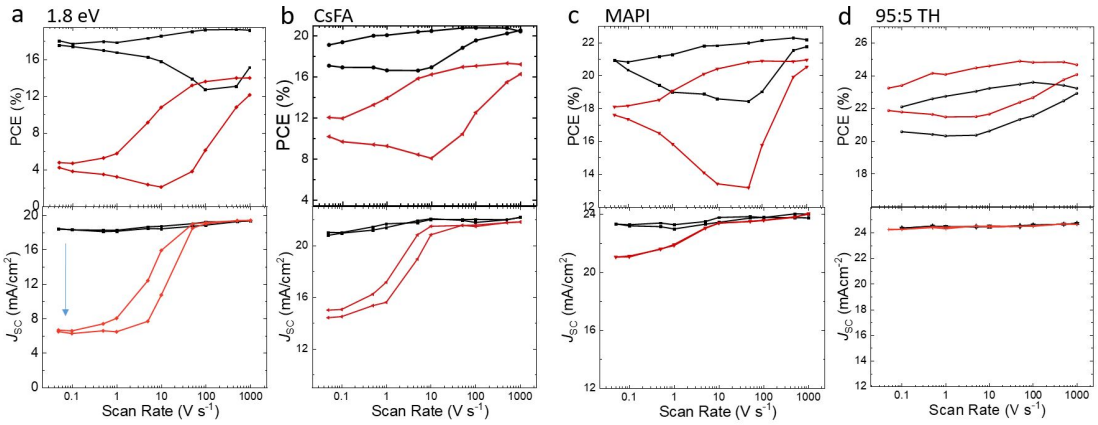

Figure B.10: The power conversion efficiency (PCE) and short-circuit current density (J_{SC}) measured at different scan speeds for different perovskite systems before and after 5h of illumination (12h in case of MAPI). Measured by Sahil Shah, Francisco Peña-Camargo, Fanyuan Ye, Emilio Gutierrez-Partida and myself.

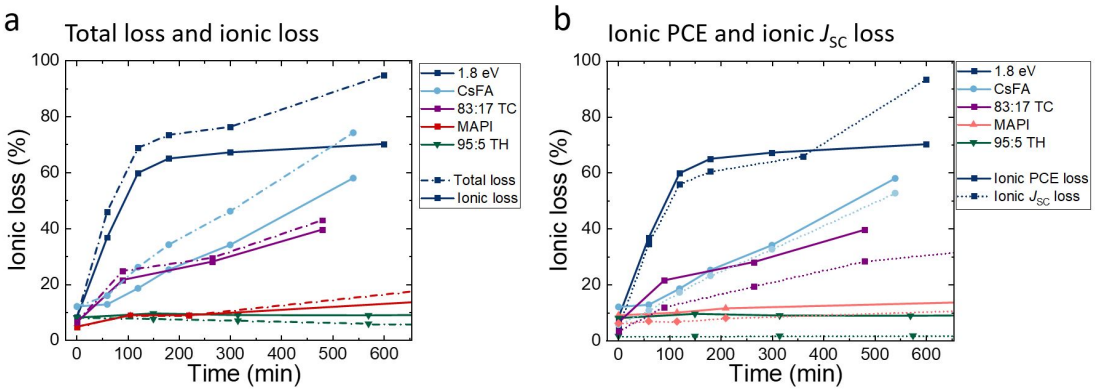

Figure B.11: a) Fraction of total- and ionic loss and b) ionic PCE versus ionic J_{SC} loss for various systems. Measured by Sahil Shah, Francisco Peña-Camargo, Fanyuan Ye, Emilio Gutierrez-Partida and myself.

B.2.2 Different ageing methods

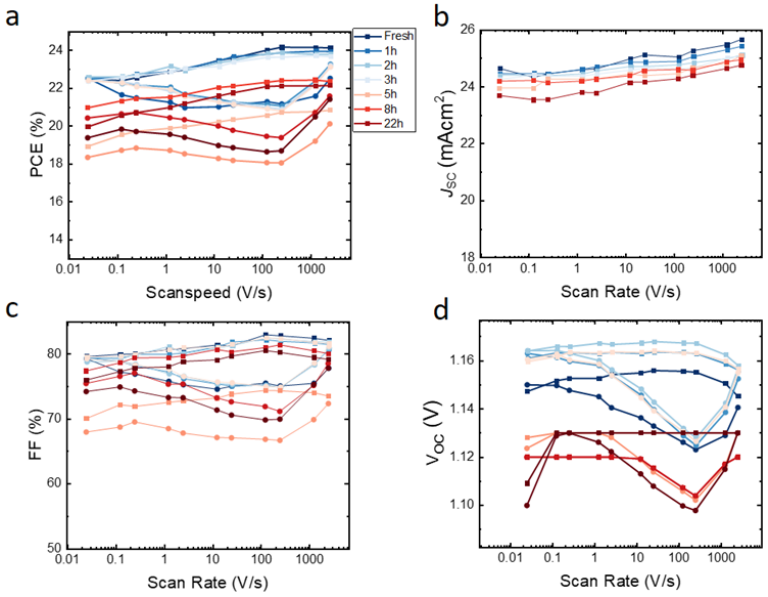

Figure B.12: a The power conversion efficiency (PCE), b short-circuit current density (J_{SC}), c open-circuit voltage (V_{OC}) and d fill factor (FF) measured at different scan speeds for $Cs_{0.05}(FA_{0.83}MA_{0.17})_{0.95}Pb(I_{0.83}Br_{0.17})_3$ perovskite solar cells after different ageing times. Accelerated ageing was carried out by keeping the cell at 75 °C in the dark. Cells were cooled down to 25 °C before measurement. We note the measurement at 5h is an outlier, probably caused by the cell not being properly cooled down, and being at a temperature higher than 25 °C during the measurement.

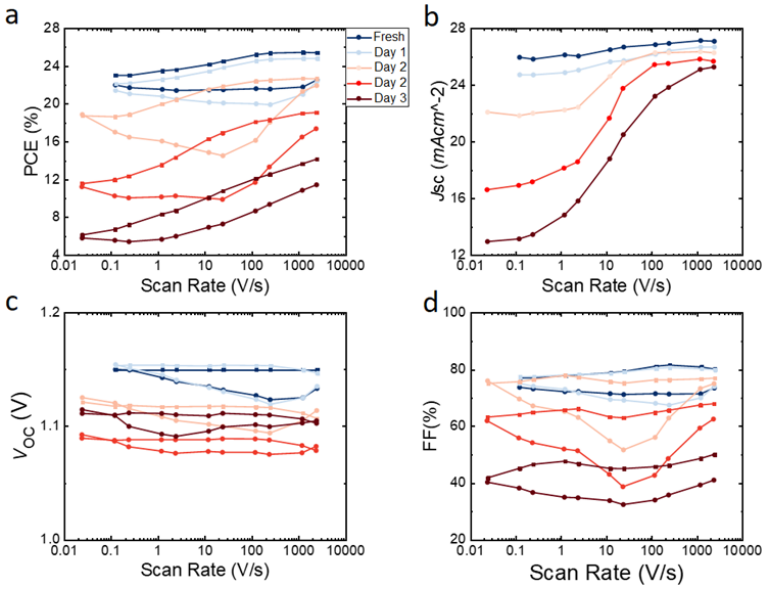

Figure B.13: a The power conversion efficiency (PCE), b short-circuit current density (J_{SC}), c open-circuit voltage (V_{OC}) and d fill factor (FF) measured at different scan speeds for $Cs_{0.05}(FA_{0.83}MA_{0.17})_{0.95}Pb(I_{0.83}Br_{0.17})_3$ perovskite solar cells after different ageing times. Ageing was carried out at MPP conditions under 1 sun equivalent illumination with a white LED in a glovebox.

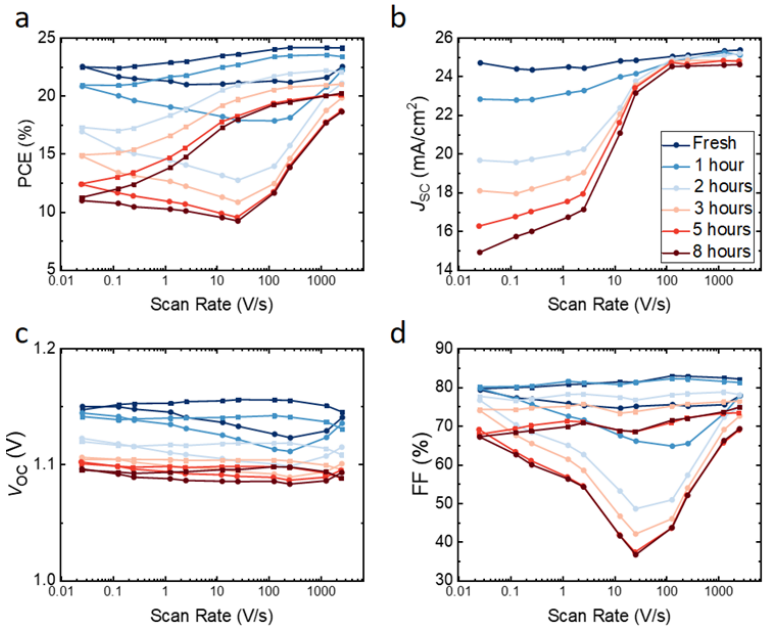

Figure B.14: a The power conversion efficiency (PCE), b short-circuit current density (J_{SC}), c open-circuit voltage (V_{OC}) and d fill factor (FF) measured at different scan speeds for $Cs_{0.05}(FA_{0.83}MA_{0.17})_{0.95}Pb(I_{0.83}Br_{0.17})_3$ perovskite solar cells after different ageing times. Ageing was carried out by keeping the device in the dark and in the glovebox and applying a forward bias to it.

APPENDIX C

Appendix C, Supporting information to Chapter 6

C.1 Note on current matching

In case of the 1.80/1.27eV tandem combination, the integrated EQE of the LG subcell is significantly lower than the corresponding HG subcell leading to a current mismatched device, see also Figure C.3. Although there is no current matching, the performance and J_{SC} of the devices - measured using an additional illumination mask to avoid parasitic effects and avoid overestimation of J_{SC} - is still good. We believe this is due to the fact that the LG subcell has a low shunt resistance – which allows for the tandem to operate without strict current matching. To substantiate our hypothesis we measured subcell selective resistive photovoltage (RPV) of our perovskite tandem and corresponding single junction devices. In this measurement, samples are excited with a 5 ns long laser pulse and the photovoltage is recorded as a function of time. Using a load resistance of 1MΩ, and a correspondingly long RC time means that charge

carriers will accumulate at the respective electrodes after transit through the whole device, allowing us to extract and compare transit times. As shown in Figure C.2a and b, we observe relatively fast and comparable transit times (10^{-7}s) in HG and LG perovskite single junctions. We then measured RPV of the individual subcells, using appropriate laser wavelengths that are selectively absorbed. In this case, we expect longer transit times, as we have a much thicker layer stack the charge carriers need to transit through. Indeed, we observe longer transit times when exciting the PbSn subcell. However, the transit time remains short when exciting the HG subcell, indicating some shunts within the PbSn subcell, leading to a faster photovoltage buildup.

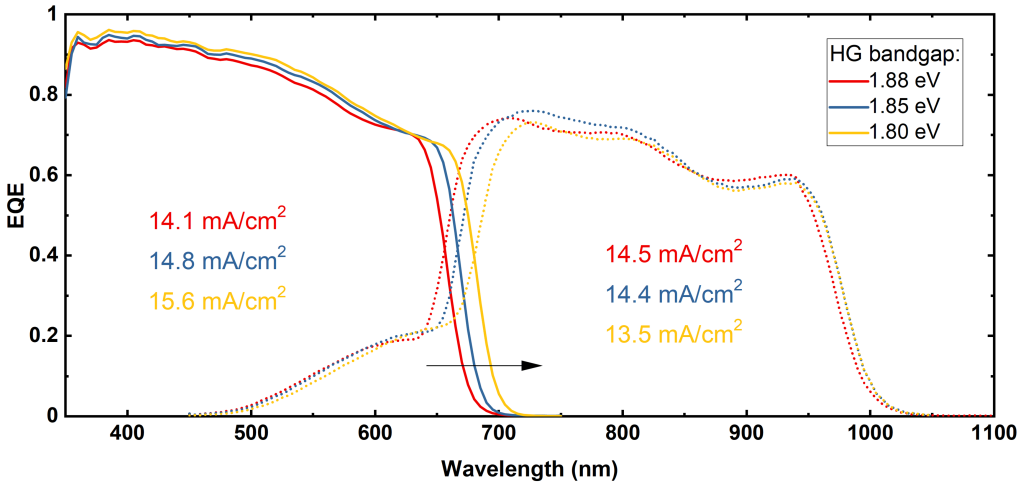

Figure C.1: EQE and integrated currents for tandems with three different HG perovskite bandgaps.

To corroborate this hypothesis further we performed electrical simulations in LTspice using a simplistic equivalent circuit comprising two diodes with parallel shunt resistances. A relatively low shunt resistance in the range of 0.1-5 kΩ/cm^2 hereby allows to accurately describe the observed JV characteristics and reproduces our observation - that the J_{SC} must not be limited by the normally current limiting subcell in case of pinholes and/or low shunt resistances. We show simulations for various shunt resistances, in Figure C.3, and further note that this phenomenon lowers the fill factor (FF) and thus may rather reduce the PCE compared to shunt-free current-matched

devices. The effect therefore represents a loss mechanism, limiting performance, and consequently, our measured PCE values are not overestimated due to this effect. Robustness against current mismatching on the other hand is highly interesting for tandem photovoltaics considering spectral variations throughout the day and hence could increase the overall energy yield in real-world applications.

In better current matched devices e.g. the 1.85/1.27 and 1.88/1.27 eV HG/LG combinations, the mismatch between integrated EQE of the HG and LG subcells is smaller, see Figure C.5, with less impact of the above described effect.

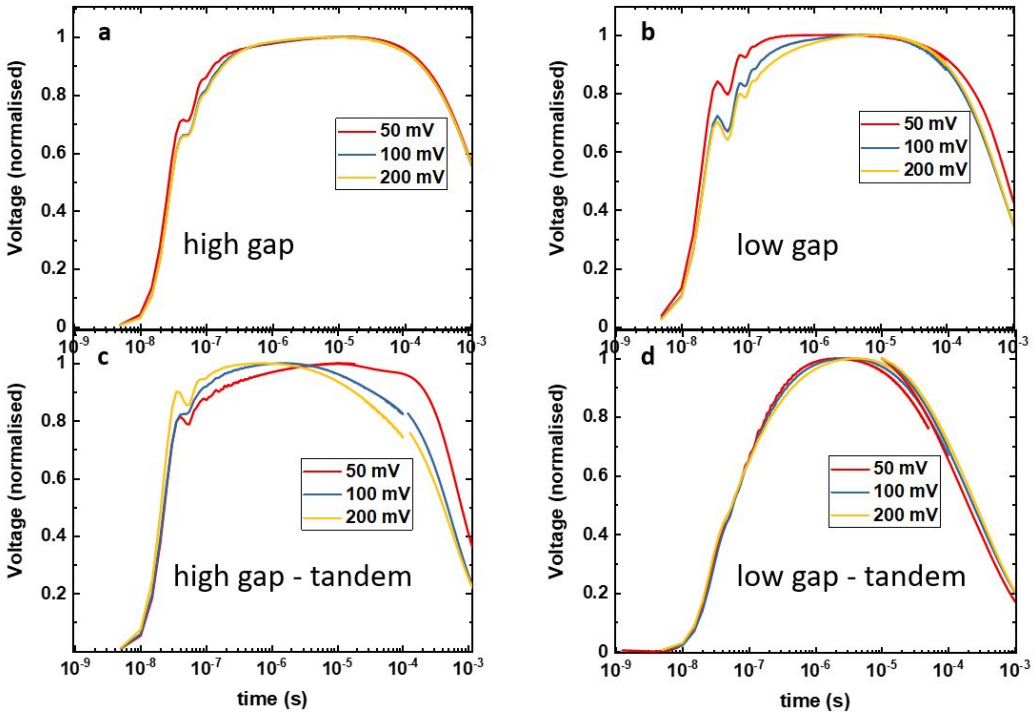

Figure C.2: Resistance dependent Photovoltage (RPV) measurements for a) a high gap single junction, b) a low gap single junction, c) a high gap subcell in a 2T all-perovskite cell and d) a low gap subcell in a 2T all-perovskite cell.

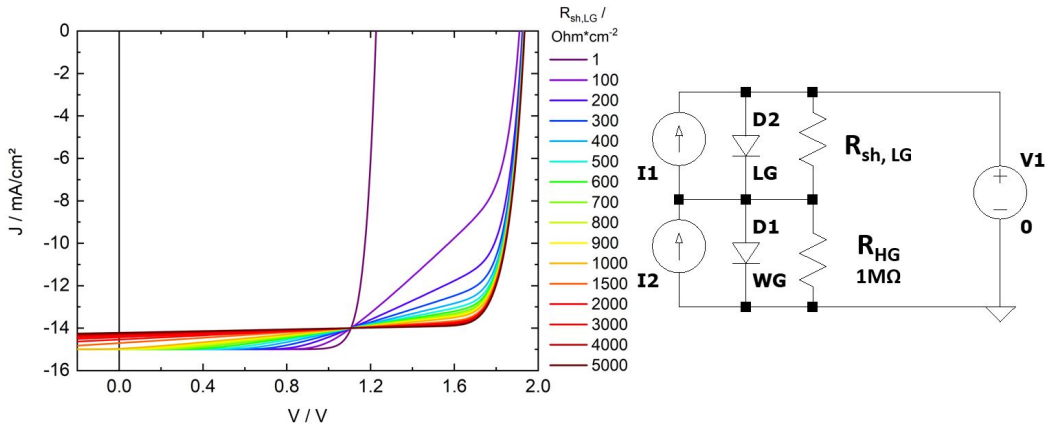

Figure C.3: Simulations carried out using the LTspice electric circuit simulation tool to demonstrate the increasing reduction in FF of the tandem JV upon decreasing shunt resistance. On the right, the equivalent circuit used for these simulations is displayed. Simulations performed by Kai O. Brinkmann.

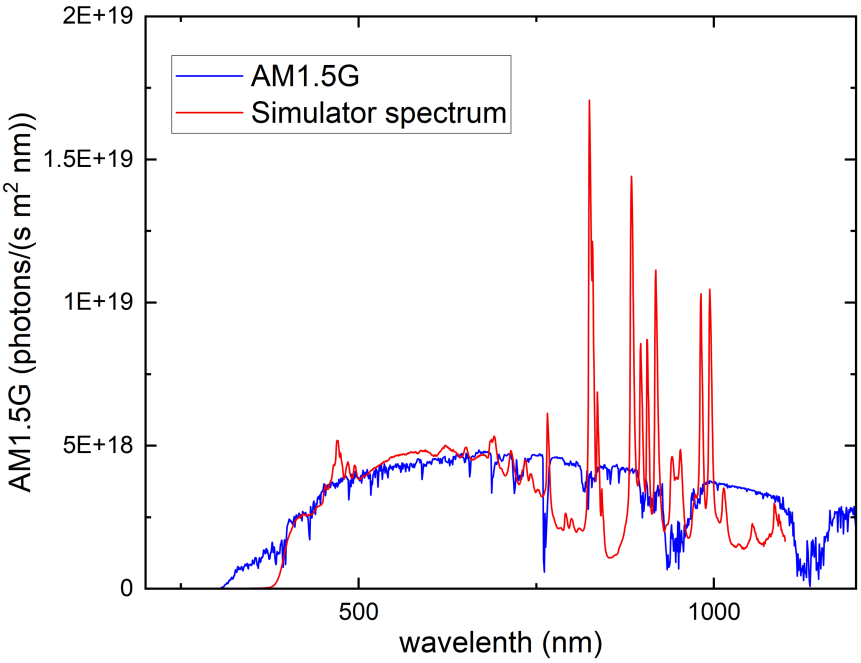

Figure C.4: Measured solar simulator spectrum compared with the AM1.5G spectrum. Spectral mismatch values were calculated for the different HG bandgaps by integrating and multiplying the measured EQE with our solar simulator spectrum and the AM1.5G spectrum, respectively, and dividing the two integrated currents obtained by each other. The spectral mismatch values obtained were 1.0019, 1.0003 and 1.0004 for HG perovskites with bandgaps of 1.80, 1.85 and 1.88 eV, respectively.

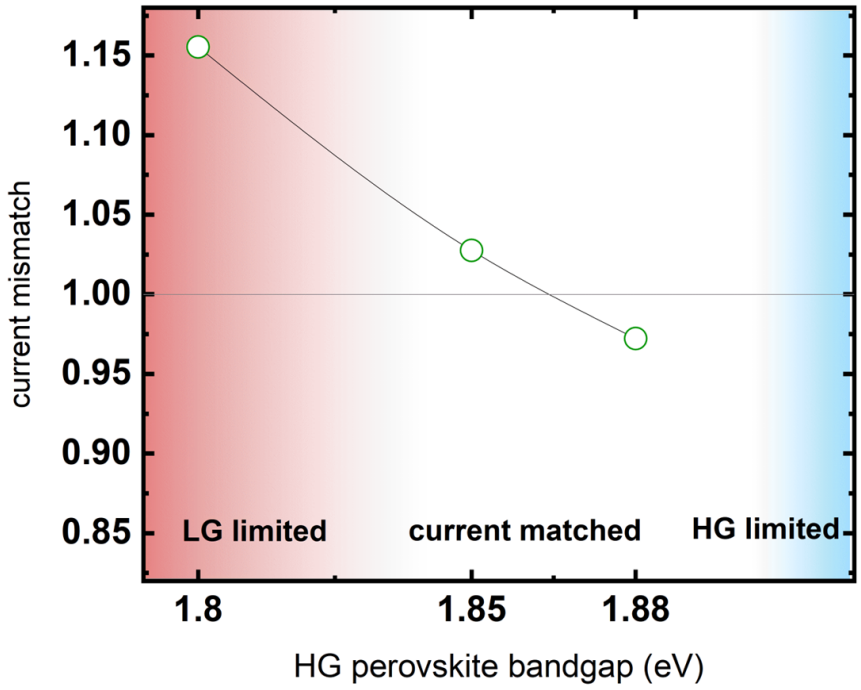

Figure C.5: Current mismatch of optimised all-perovskite tandem solar cells based on 1.80/1.27 eV, 1.85/1.27 eV, and 1.88/1.27 eV bandgap combinations. The mismatch is calculated from the integrated EQE currents

C.2 Data on HG optimisation

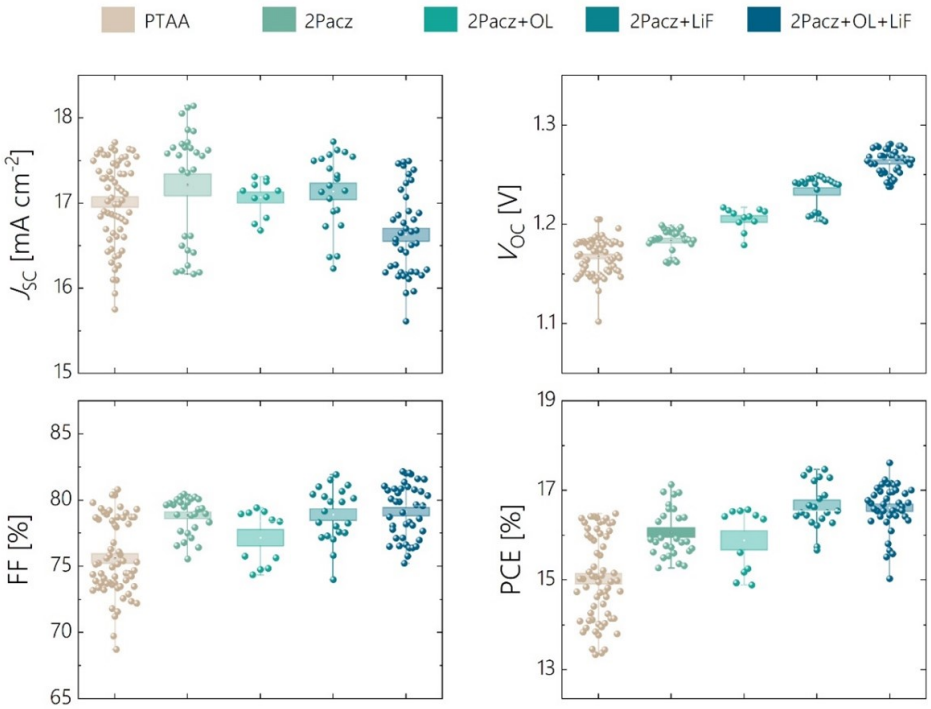

Figure C.6: Device statistics for the different optimisation steps, for the 1.80 eV HG perovskite. Measurement and analysis by Francisco Peña-Camargo.

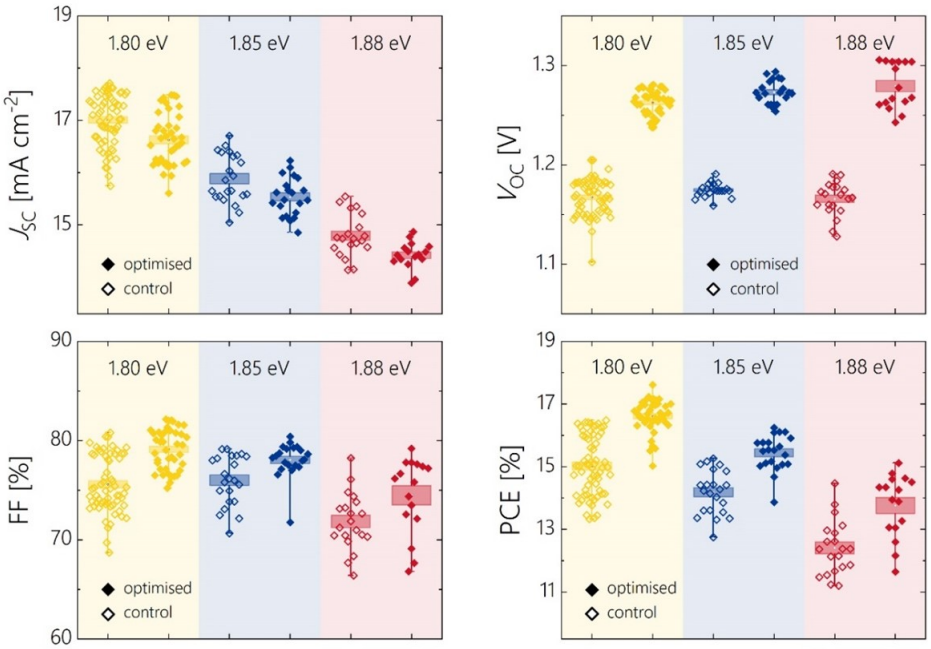

Figure C.7: Device statistics for control (open symbol) and fully optimised (closed symbol) single junction perovskite solar cells with bandgaps of 1.80, 1.85, and 1.88 eV. Measurement and analysis by Francisco Peña-Camargo.

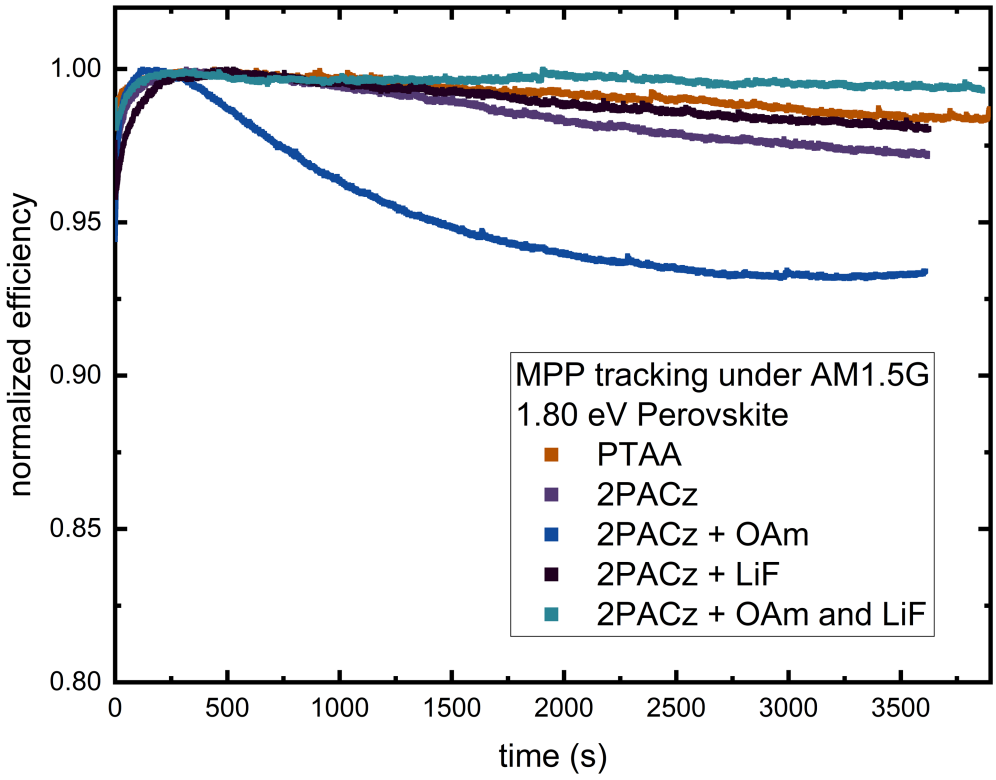

Figure C.8: Long-term MPP tracking under AM1.5G illumination of control and optimised 1.8 eV-based HG single junction solar cells. (AM1.5G sun simulator, T=25°C, under N_2 atmosphere). Measurement and analysis by Francisco Peña-Camargo.

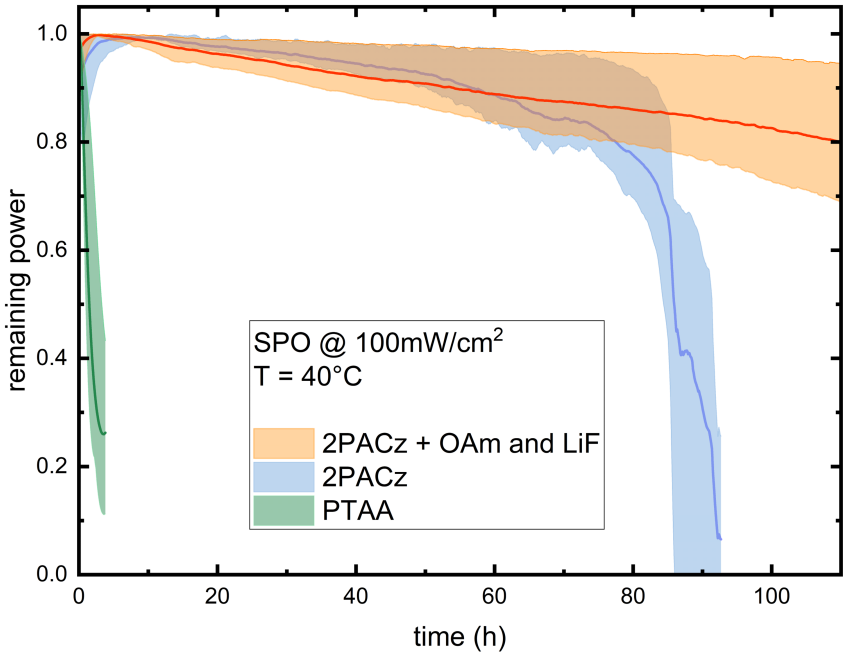

Figure C.9: Long-term SPO tracking of PTAA control, 2PACz control and fully optimised 2PACz + OAm and LiF 1.80 eV-based HG single junction solar cells. (100mW/cm^2 while light LED (3000K Cree CXB3590) illumination, T=40°C, ambient atmosphere) Lines and envelopes refer to the mean and Min/Max values of 4 tested pixels on each device configuration. Measurement and analysis by Francisco Peña-Camargo.

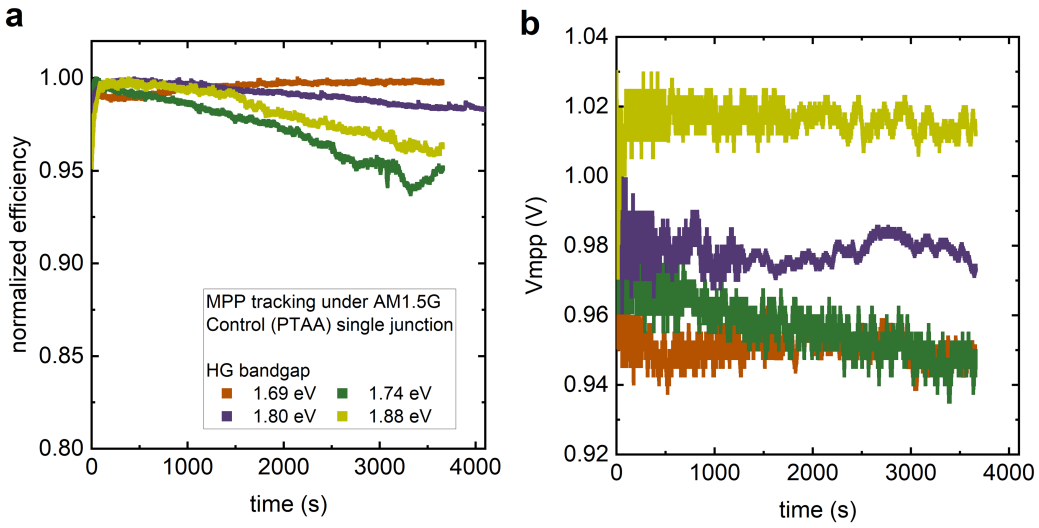

Figure C.10: Long-term MPP tracking under AM1.5G illumination of control (PTAA) based HG single junction solar cells with various bandgaps from 1.69 eV to 1.88 eV. Panel (a) displays the evolution of the normalised efficiency, and (b) displays the voltage at MPP (V_{MPP}). Interestingly we find the V_{MPP} to be relatively stable for most bandgaps, indicating that halide segregation plays only a minor role for the voltage and QFLS. (T=25°C, under N_2 atmosphere).Measurement and analysis by Francisco Peña-Camargo.

Bibliography

1. Intergovernmental Panel on Climate Change (IPCC), "Climate change 2021: The sixth assessment report," 2021.

2. M. Rantanen, A. Y. Karpechko, A. Lipponen, K. Nordling, O. Hyvärinen, K. Ruosteenoja, T. Vihma, and A. Laaksonen, "The arctic has warmed nearly four times faster than the globe since 1979," *Communications Earth & Environment*, vol. 3, no. 1, p. 168, 2022.

3. S. Dangendorf, C. Hay, F. M. Calafat, M. Marcos, C. G. Piecuch, K. Berk, and J. Jensen, "Persistent acceleration in global sea-level rise since the 1960s," *Nature Climate Change*, vol. 9, no. 9, pp. 705–710, 2019.

4. R. A. Feely, S. C. Doney, and S. R. Cooley, "Ocean acidification: Present conditions and future changes in a high-CO_2 world," *Oceanography*, vol. 22, no. 4, pp. 36–47, 2009.

5. N. G. I. for Space Studies, "GISS Surface Temperature Analysis (GISTEMP), version 4," 2023. Accessed on: August 20, 2023.

6. N. Lenssen, G. Schmidt, J. Hansen, M. Menne, A. Persin, R. Ruedy, and D. Zyss, "Improvements in the GISTEMP uncertainty model," *J. Geophys. Res. Atmos.*, vol. 124, no. 12, pp. 6307–6326, 2019.

7. X. Lan, P. Tans, and K. W. Thoning, "Trends in globally-averaged CO_2 determined from noaa global monitoring laboratory measurements." Version 2023-09, 2023. DOI: 10.15138/9N0H-ZH07.

8. I. E. Agency, *Key World Energy Statistics 2021*. 2021.

9. C. E. Fritts, "On the Fritts selenium cells and batteries," *Journal of the Franklin Institute*, vol. 119, no. 3, pp. 221–232, 1885.

10. Bellincat, "Untangling the mystery of the world's first rooftop solar panel," August 16 2023.

11. R. S. Ohl, "Light-sensitive electric device," *US Patent*, vol. 240252, 1941.

12. D. M. Chapin, C. S. Fuller, and G. L. Pearson, "A new silicon p-n junction photocell for converting solar radiation into electrical power," *Journal of Applied Physics*, vol. 25, no. 5, pp. 676–677, 1954.

13. A. not specified, "Vast power of the sun is tapped by battery using sand ingredient," *The New York Times*, April 1954.

14. R. L. Easton and M. J. Votaw, "Vanguard I IGY Satellite (1958 Beta)," *Review of Scientific Instruments*, vol. 30, pp. 70–75, 12 2004.

15. International Renewable Energy Agency, "Renewable energy statistics 2023," 2023.

16. Z. Sun, X. Chen, Y. He, J. Li, J. Wang, H. Yan, and Y. Zhang, "Toward efficiency limits of crystalline silicon solar cells: Recent progress in high-efficiency silicon heterojunction solar cells," *Advanced Energy Materials*, vol. 12, no. 23, p. 2200015, 2022.

17. C. Kittel, *Introduction to Solid State Physics*. Wiley, 2004.

18. P. Würfel, *Physics of Perovskite Solar Cells*. John Wiley & Sons, 2019.

19. K. W. Böer and U. W. Pohl, *Semiconductor Physics*. Springer Nature, 2023.

20. P. C. Y. Chow, S. Gélinas, A. Rao, and R. H. Friend, "Quantitative bimolecular recombination in organic photovoltaics through triplet exciton formation," *Journal of the American Chemical Society*, vol. 136, no. 9, pp. 3424–3429, 2014.

21. W. Shockley and W. T. Read, "Statistics of the recombinations of holes and electrons," *Physical Review*, vol. 87, pp. 835–842, Sep 1952.

22. R. N. Hall, "Electron-hole recombination in Germanium," *Physical Review*, vol. 87, pp. 387–387, Jul 1952.

23. U. Rau, "Reciprocity relation between photovoltaic quantum efficiency and electroluminescent emission of solar cells," *Physical Review B - Condensed Matter and Materials Physics*, vol. 76, p. 085303, 8 2007.

24. T. Kirchartz, J. A. Márquez, M. Stolterfoht, and T. Unold, "Photoluminescence-based characterization of halide perovskites for photovoltaics," *Advanced Energy Materials*, vol. 10, no. 26, p. 1904134, 2020.

25. T. P. Weiss, B. Bissig, T. Feurer, R. Carron, S. Buecheler, and A. N. Tiwari, "Bulk and surface recombination properties in thin film semiconductors with different surface treatments from time-resolved photoluminescence measurements," *Scientific Reports*, vol. 9, no. 1, p. 5385, 2019.

26. P. T. Landsberg and V. Badescu, "Carnot factor in solar cell efficiencies," *Journal of Physics D: Applied Physics*, vol. 33, p. 3004, nov 2000.

27. L. C. Hirst and N. J. Ekins-Daukes, "Fundamental losses in solar cells," *Progress in Photovoltaics: Research and Applications*, vol. 19, no. 3, pp. 286–293, 2011.

28. M. A. Green, A. Ho-Baillie, and H. J. Snaith, "The emergence of perovskite solar cells," *Nature Photonics*, vol. 8, pp. 506–514, 2014.

29. E. L. Warren, W. E. McMahon, M. Rienäcker, K. T. VanSant, R. C. Whitehead, R. Peibst, and A. C. Tamboli, "A taxonomy for three-terminal tandem solar cells," *ACS Energy Letters*, vol. 5, no. 4, pp. 1233–1242, 2020.

30. E. A. Katz, "Perovskite: Name puzzle and German-Russian odyssey of discovery," *Helvetica Chimica Acta*, vol. 103, no. 6, p. e2000061, 2020.

31. V. M. Goldschmidt, "Die Gesetze der Krystallochemie," *Naturwissenschaften*, vol. 14, no. 21, pp. 477–485, 1926.

32. W. Bao, J. Axe, C. Chen, and S. Cheong, "Impact of charge ordering on magnetic correlations in perovskite (Bi, Ca)MnO_3," *Physical Review Letters*, vol. 78, no. 3, p. 543, 1997.

33. Y. Moritomo, H. Kuwahara, Y. Tomioka, and Y. Tokura, "Pressure effects on charge-ordering transitions in perovskite manganites," *Physical Review B*, vol. 55, no. 12, p. 7549, 1997.

34. Y. Moritomo, A. Asamitsu, H. Kuwahara, and Y. Tokura, "Giant magnetoresistance of manganese oxides with a layered perovskite structure," *Nature*, vol. 380, no. 6570, pp. 141–144, 1996.

35. A. Ramirez, "Colossal magnetoresistance," *Journal of Physics: Condensed Matter*, vol. 9, no. 39, p. 8171, 1997.

36. Y.-M. You, W.-Q. Liao, D. Zhao, H.-Y. Ye, Y. Zhang, Q. Zhou, X. Niu, J. Wang, P.-F. Li, D.-W. Fu, Z. Wang, S. Gao, K. Yang, J.-M. Liu, J. Li, Y. Yan, and R.-G. Xiong, "An organic-inorganic perovskite ferroelectric with large piezoelectric response," *Science*, vol. 357, no. 6348, pp. 306–309, 2017.

37. Y. Maeno, H. Hashimoto, K. Yoshida, S. Nishizaki, T. Fujita, J. Bednorz, and F. Lichtenberg, "Superconductivity in a layered perovskite without copper," *Nature*, vol. 372, no. 6506, pp. 532–534, 1994.

38. J. G. Bednorz and K. A. Müller, "Perovskite-type oxides—the new approach to high-T_c superconductivity," *Reviews of Modern Physics*, vol. 60, pp. 585–600, Jul 1988.

39. A. W. Sleight, J. Gillson, and P. Bierstedt, "High-temperature superconductivity in the $BaPb_{1-x}Bi_xO_3$ systems," *Solid State Communications*, vol. 17, no. 1, pp. 27–28, 1975.

40. H. Lu, J. Wang, C. Xiao, X. Pan, X. Chen, R. Brunecky, J. J. Berry, K. Zhu, M. C. Beard, and Z. V. Vardeny, "Spin-dependent charge transport through 2D chiral hybrid lead-iodide perovskites," *Science Advances*, vol. 5, no. 12, p. eaay0571, 2019.

41. A. Bhalla, R. Guo, and R. Roy, "The perovskite structure—a review of its role in ceramic science and technology," *Materials Research Innovations*, vol. 4, no. 1, pp. 3–26, 2000.

42. C. Møller, "Crystal structure and photoconductivity of caesium plumbohalides," *Nature*, vol. 182, no. 4647, pp. 1436–1436, 1958.

43. H. L. Wells, "Über die Cäsium- und Kalium-Bleihalogenide," *Zeitschrift für anorganische Chemie*, vol. 3, no. 1, pp. 195–210, 1893.

44. D. Weber, "CH3NH3PbX3, ein Pb(II)-System mit kubischer Perowskitstruktur / CH3NH3PbX3, a Pb(II)-System with Cubic Perovskite Structure," *Zeitschrift für Naturforschung B*, vol. 33, no. 12, pp. 1443–1445, 1978.

45. D. Weber, "Ch3nh3snbrxi3-x (x = 0-3), ein sn(ii)-system mit kubischer perowskitstruktur / ch3nh3snbrxi3-x(x = 0-3), a sn(ii)-system with cubic perovskite structure," *Zeitschrift für Naturforschung B*, vol. 33, no. 8, pp. 862–865, 1978.

46. A. Kojima, K. Teshima, Y. Shirai, and T. Miyasaka, "Organometal halide perovskites as visible-light sensitizers for photovoltaic cells," *Journal of the American Chemical Society*, vol. 131, pp. 6050–6051, 2009.

47. M. M. Lee, J. Teuscher, T. Miyasaka, T. N. Murakami, and H. J. Snaith, "Efficient hybrid solar cells based on meso-superstructured organometal halide perovskites," *Science*, vol. 338, pp. 643–647, 2012.

48. A. Walsh, "Principles of chemical bonding and band gap engineering in hybrid organic–inorganic halide perovskites," *The Journal of Physical Chemistry C*, vol. 119, no. 11, pp. 5755–5760, 2015.

49. E. L. Unger, L. Kegelmann, K. Suchan, D. Sörell, L. Korte, and S. Albrecht, "Roadmap and roadblocks for the band gap tunability of metal halide perovskites," *Journal of Materials Chemistry A*, vol. 5, pp. 11401–11409, 2017.

50. A. J. Barker, A. Sadhanala, F. Deschler, M. Gandini, S. P. Senanayak, P. M. Pearce, E. Mosconi, A. J. Pearson, Y. Wu, A. R. Srimath Kandada, T. Leijtens, F. De Angelis, S. E. Dutton, A. Petrozza, and R. H. Friend, "Defect-assisted photoinduced halide segregation in mixed-halide perovskite thin films," *ACS Energy Letters*, vol. 2, no. 6, pp. 1416–1424, 2017.

51. M. Baranowski and P. Plochocka, "Excitons in metal-halide perovskites," *Advanced Energy Materials*, vol. 10, no. 26, p. 1903659, 2020.

52. P. Umari, E. Mosconi, and F. De Angelis, "Infrared dielectric screening determines the low exciton binding energy of metal-halide perovskites," *The Journal of Physical Chemistry Letters*, vol. 9, no. 3, pp. 620–627, 2018.

53. J. Yan, T. J. Savenije, L. Mazzarella, and O. Isabella, "Progress and challenges on scaling up of perovskite solar cell technology," *Sustainable Energy Fuels*, vol. 6, pp. 243–266, 2022.

54. Z. Xiao and Y. Yan, "Progress in theoretical study of metal halide perovskite solar cell materials," *Advanced Energy Materials*, vol. 7, no. 22, p. 1701136, 2017.

55. D. Meggiolaro, S. G. Motti, E. Mosconi, A. J. Barker, J. Ball, C. Andrea Riccardo Perini, F. Deschler, A. Petrozza, and F. De Angelis, "Iodine chemistry determines the defect tolerance of lead-halide perovskites," *Energy& Environmental Science*, vol. 11, pp. 702–713, 2018.

56. G.-W. Kim and A. Petrozza, "Defect tolerance and intolerance in metal-halide perovskites," *Advanced Energy Materials*, vol. 10, no. 37, p. 2001959, 2020.

57. Y.-C. Hsiao, T. Wu, M. Li, Q. Liu, W. Qin, and B. Hu, "Fundamental physics behind high-efficiency organo-metal halide perovskite solar cells," *Journal of Materials Chemistry A*, vol. 3, pp. 15372–15385, 2015.

58. B. P. Finkenauer, Akriti, K. Ma, and L. Dou, "Degradation and self-healing in perovskite solar cells," *ACS Applied Materials & Interfaces*, vol. 14, no. 21, pp. 24073–24088, 2022.

59. F. Lang, N. H. Nickel, J. Bundesmann, S. Seidel, A. Denker, S. Albrecht, V. V. Brus, J. Rappich, B. Rech, G. Landi, and H. C. Neitzert, "Radiation hardness and self-healing of perovskite solar cells," *Advanced Materials*, vol. 28, no. 39, pp. 8726–8731, 2016.

60. C. Eames, J. M. Frost, P. R. Barnes, B. C. O'regan, A. Walsh, and M. S. Islam, "Ionic transport in hybrid lead iodide perovskite solar cells," *Nature Communications*, vol. 6, no. 1, p. 7497, 2015.

61. Y. Zhao, W. Zhou, H. Tan, R. Fu, Q. Li, F. Lin, D. Yu, G. Walters, E. H. Sargent, and Q. Zhao, "Mobile-ion-induced degradation of organic hole-selective layers in perovskite solar cells," *Journal of Physical Chemistry C*, vol. 121, pp. 14517–14523, 2017.

62. B. Rivkin, P. Fassl, Q. Sun, A. D. Taylor, Z. Chen, and Y. Vaynzof, "Effect of ion migration-induced electrode degradation on the operational stability of perovskite solar cells," *ACS Omega*, vol. 3, no. 8, pp. 10042–10047, 2018.

63. S. Kim, S. Bae, S.-W. Lee, K. Cho, K. D. Lee, H. Kim, S. Park, G. Kwon, S.-W. Ahn, H.-M. Lee, Y. Kang, H.-S. Lee, and D. Kim, "Relationship between ion migration and interfacial

degradation of $CH_3NH_3PbI_3$ perovskite solar cells under thermal conditions," *Scientific Reports*, vol. 7, no. 1, p. 1200, 2017.

64. W. Tress, N. Marinova, T. Moehl, S. M. Zakeeruddin, M. K. Nazeeruddin, and M. Grätzel, "Understanding the rate-dependent J-V hysteresis, slow time component, and aging in $CH_3NH_3PbI_3$ perovskite solar cells: The role of a compensated electric field," *Energy& Environmental Science*, vol. 8, pp. 995–1004, 3 2015.

65. Y. Cheng, H. W. Li, J. Qing, Q. D. Yang, Z. Guan, C. Liu, S. H. Cheung, S. K. So, C. S. Lee, and S. W. Tsang, "The detrimental effect of excess mobile ions in planar $CH_3NH_3PbI_3$ perovskite solar cells," *Journal of Materials Chemistry A*, vol. 4, pp. 12748–12755, 2016.

66. N. Wu, D. Walter, A. Fell, Y. Wu, and K. Weber, "The impact of mobile ions on the steady-state performance of perovskite solar cells," *The Journal of Physical Chemistry C*, vol. 124, no. 1, pp. 219–229, 2020.

67. J. M. Cave, N. E. Courtier, I. A. Blakborn, T. W. Jones, D. Ghosh, K. F. Anderson, L. Lin, A. A. Dijkhoff, G. J. Wilson, K. Feron, M. S. Islam, J. M. Foster, G. Richardson, and A. B. Walker, "Deducing transport properties of mobile vacancies from perovskite solar cell characteristics," *Journal of Applied Physics*, vol. 128, p. 184501, 11 2020.

68. S. Chen, X. Zhang, J. Zhao, Y. Zhang, G. Kong, Q. Li, N. Li, Y. Yu, N. Xu, J. Zhang, K. Liu, Q. Zhao, J. Cao, J. Feng, X. Li, and J. Qi, "Atomic scale insights into structure instability and decomposition pathway of methylammonium lead iodide perovskite," *Nature Communications*, vol. 9, no. 1, p. 4807, 2018.

69. E. J. Juarez-Perez, L. K. Ono, M. Maeda, Y. Jiang, Z. Hawash, and Y. Qi, "Photodecomposition and thermal decomposition in methylammonium halide lead perovskites and inferred design principles to increase photovoltaic device stability," *Journal of Materials Chemistry A*, vol. 6, pp. 9604–9612, 2018.

70. Y.-H. Kye, C.-J. Yu, U.-G. Jong, Y. Chen, and A. Walsh, "Critical role of water in defect aggregation and chemical degradation of perovskite solar cells," *The Journal of Physical Chemistry Letters*, vol. 9, no. 9, pp. 2196–2201, 2018.

71. E. Mosconi, J. M. Azpiroz, and F. De Angelis, "Ab initio molecular dynamics simulations of

methylammonium lead iodide perovskite degradation by water," *Chemistry of Materials*, vol. 27, no. 13, pp. 4885–4892, 2015.

72. L. Meng, J. You, and Y. Yang, "Addressing the stability issue of perovskite solar cells for commercial applications," *Nature Communications*, vol. 9, 12 2018.

73. N. Li, X. Niu, Q. Chen, and H. Zhou, "Towards commercialization: the operational stability of perovskite solar cells," *Chem. Soc. Rev.*, vol. 49, pp. 8235–8286, 2020.

74. Y. Cheng and L. Ding, "Pushing commercialization of perovskite solar cells by improving their intrinsic stability," *Energy& Environmental Science*, vol. 14, pp. 3233–3255, 2021.

75. T. Leijtens, R. Prasanna, A. Gold-Parker, M. F. Toney, and M. D. McGehee, "Mechanism of tin oxidation and stabilization by lead substitution in tin halide perovskites," *ACS Energy Letters*, vol. 2, pp. 2159–2165, 2017.

76. M. I. Saidaminov, I. Spanopoulos, J. Abed, W. Ke, J. Wicks, M. G. Kanatzidis, and E. H. Sargent, "Conventional solvent oxidizes sn(ii) in perovskite inks," *ACS Energy Letters*, vol. 5, pp. 1153–1155, 4 2020.

77. L. Lanzetta, T. Webb, N. Zibouche, X. Liang, D. Ding, G. Min, R. J. Westbrook, B. Gaggio, T. J. Macdonald, M. S. Islam, and S. A. Haque, "Degradation mechanism of hybrid tin-based perovskite solar cells and the critical role of tin (iv) iodide," *Nature Communications*, vol. 12, no. 1, p. 2853, 2021.

78. K. Dey, D. Ghosh, M. Pilot, S. R. Pering, B. Roose, P. Deswal, S. P. Senanayak, P. J. Cameron, M. S. Islam, and S. D. Stranks, "Substitution of lead with tin suppresses ionic transport in halide perovskite optoelectronics," 2023.

79. R. Lin, K. Xiao, Z. Qin, Q. Han, C. Zhang, M. Wei, M. I. Saidaminov, Y. Gao, J. Xu, M. Xiao, A. Li, J. Zhu, E. H. Sargent, and H. Tan, "Monolithic all-perovskite tandem solar cells with 24.8% efficiency exploiting comproportionation to suppress Sn(ii) oxidation in precursor ink," *Nature Energy*, vol. 4, pp. 864–873, 2019.

80. K. Xiao, R. Lin, Q. Han, Y. Hou, Z. Qin, H. T. Nguyen, J. Wen, M. Wei, V. Yeddu, M. I. Saidaminov, Y. Gao, X. Luo, Y. Wang, H. Gao, C. Zhang, J. Xu, J. Zhu, E. H. Sargent, and H. Tan, "All-perovskite tandem solar cells with 24.2% certified efficiency and area over 1 cm2 using surface-anchoring zwitterionic antioxidant," *Nature Energy*, vol. 5, pp. 870–880, 2020.

81. A. Mahata, D. Meggiolaro, L. Gregori, and F. De Angelis, "Suppression of tin oxidation by 3D/2D perovskite interfacing," *The Journal of Physical Chemistry C*, vol. 125, no. 20, pp. 10901–10908, 2021.

82. S. Hu, M. A. Truong, K. Otsuka, T. Handa, T. Yamada, R. Nishikubo, Y. Iwasaki, A. Saeki, R. Murdey, Y. Kanemitsu, and A. Wakamiya, "Mixed lead–tin perovskite films with $>$7 µs charge carrier lifetimes realized by maltol post-treatment," *Chem. Sci.*, vol. 12, pp. 13513–13519, 2021.

83. S. Gu, R. Lin, Q. Han, Y. Gao, H. Tan, and J. Zhu, "Tin and mixed lead–tin halide perovskite solar cells: Progress and their application in tandem solar cells," *Advanced Materials*, vol. 32, p. 1907392, 2 2020.

84. J. Wang, Z. Gao, J. Yang, M. Lv, H. Chen, D.-J. Xue, X. Meng, and S. Yang, "Controlling the crystallization kinetics of lead-free tin halide perovskites for high performance green photovoltaics," *Advanced Energy Materials*, vol. 11, no. 39, p. 2102131, 2021.

85. J. Wang, K. Datta, J. Li, M. A. Verheijen, D. Zhang, M. M. Wienk, and R. A. J. Janssen, "Understanding the film formation kinetics of sequential deposited narrow-bandgap Pb–Sn hybrid perovskite films," *Advanced Energy Materials*, vol. 10, no. 22, p. 2000566, 2020.

86. H. Liu, L. Wang, R. Li, B. Shi, P. Wang, Y. Zhao, and X. Zhang, "Modulated crystallization and reduced V_{OC} deficit of mixed lead–tin perovskite solar cells with antioxidant caffeic acid," *ACS Energy Letters*, vol. 6, no. 8, pp. 2907–2916, 2021.

87. P. Würfel, "The chemical potential of radiation," *Journal of Physics C: Solid State Physics*, vol. 15, no. 18, p. 3967, 1982.

88. W. Shockley and H. J. Queisser, "Detailed Balance Limit of Efficiency of p-n Junction Solar Cells," *Journal of Applied Physics*, vol. 32, pp. 510–519, 06 2004.

89. J. Lim, M. Kober-Czerny, Y.-H. Lin, J. M. Ball, N. Sakai, E. A. Duijnstee, M. J. Hong, J. G. Labram, B. Wenger, and H. J. Snaith, "Long-range charge carrier mobility in metal halide perovskite thin-films and single crystals via transient photo-conductivity," *Nature Communications*, vol. 13, no. 1, p. 4201, 2022.

90. O. Gunawan, S. R. Pae, D. M. Bishop, Y. Virgus, J. H. Noh, N. J. Jeon, Y. S. Lee, X. Shao, T. Todorov, D. B. Mitzi, and B. Shin, "Carrier-resolved photo-Hall effect," *Nature*, vol. 575, pp. 151–155, 2019.

91. M. Burgelman, P. Nollet, and S. Degrave, "Modelling polycrystalline semiconductor solar cells," *Thin Solid Films*, vol. 361-362, pp. 527–532, 2000.

92. J. M. Ball, S. D. Stranks, M. T. Hörantner, S. Hüttner, W. Zhang, E. J. W. Crossland, I. Ramirez, M. Riede, M. B. Johnston, R. H. Friend, and H. J. Snaith, "Optical properties and limiting photocurrent of thin-film perovskite solar cells," *Energy& Environmental Science*, vol. 8, pp. 602–609, 2015.

93. G. E. Eperon, T. Leijtens, K. A. Bush, R. Prasanna, T. Green, J. T. W. Wang, D. P. McMeekin, G. Volonakis, R. L. Milot, R. May, A. Palmstrom, D. J. Slotcavage, R. A. Belisle, J. B. Patel, E. S. Parrott, R. J. Sutton, W. Ma, F. Moghadam, B. Conings, A. Babayigit, H. G. Boyen, S. Bent, F. Giustino, L. M. Herz, M. B. Johnston, M. D. McGehee, and H. J. Snaith, "Perovskite-perovskite tandem photovoltaics with optimized band gaps," *Science*, vol. 354, pp. 861–865, 2016.

94. NREL, "NREL best research-cell efficiency chart," 2020.

95. C. C. Stoumpos, C. D. Malliakas, and M. G. Kanatzidis, "Semiconducting tin and lead iodide perovskites with organic cations: Phase transitions, high mobilities, and near-infrared photoluminescent properties," *Inorganic Chemistry*, vol. 52, pp. 9019–9038, 2013.

96. F. Hao, C. C. Stoumpos, D. H. Cao, R. P. Chang, and M. G. Kanatzidis, "Lead-free solid-state organic-inorganic halide perovskite solar cells," *Nature Photonics*, vol. 8, pp. 489–494, 2014.

97. M. Jošt, S. Albrecht, L. Kegelmann, C. M. Wolff, F. Lang, B. Lipovšek, J. Krč, L. Korte, D. Neher, B. Rech, and M. Topič, "Efficient light management by textured nanoimprinted layers for perovskite solar cells," *ACS Photonics*, vol. 4, pp. 1232–1239, 5 2017.

98. G. Martínez-Denegri, S. Colodrero, Q. Liu, J. Toudert, G. Kozyreff, and J. Martorell, "Ergodic light propagation in a half-cylinder photonic plate for optimal absorption in perovskite solar cells," *Advanced Optical Materials*, vol. 7, p. 1900018, 2019.

99. M. Long, Z. Chen, T. Zhang, Y. Xiao, X. Zeng, J. Chen, K. Yan, and J. Xu, "Ultrathin efficient perovskite solar cells employing a periodic structure of a composite hole conductor for elevated plasmonic light harvesting and hole collection," *Nanoscale*, vol. 8, pp. 6290–6299, 3 2016.

100. M. M. Tavakoli, K. H. Tsui, Q. Zhang, J. He, Y. Yao, D. Li, and Z. Fan, "Highly efficient flexible perovskite solar cells with antireflection and self-cleaning nanostructures," *ACS Nano*, vol. 9, pp. 10287–10295, 8 2015.

101. U. W. Paetzold, W. Qiu, F. Finger, J. Poortmans, and D. Cheyns, "Nanophotonic front electrodes for perovskite solar cells," *Applied Physics Letters*, vol. 106, 4 2015.

102. N. K. Noel, S. D. Stranks, A. Abate, C. Wehrenfennig, S. Guarnera, A. A. Haghighirad, A. Sadhanala, G. E. Eperon, S. K. Pathak, M. B. Johnston, A. Petrozza, L. M. Herz, and H. J. Snaith, "Lead-free organic-inorganic tin halide perovskites for photovoltaic applications," *Energy& Environmental Science*, vol. 7, pp. 3061–3068, 2014.

103. M. Kim, G. H. Kim, T. K. Lee, I. W. Choi, H. W. Choi, Y. Jo, Y. J. Yoon, J. W. Kim, J. Lee, D. Huh, H. Lee, S. K. Kwak, J. Y. Kim, and D. S. Kim, "Methylammonium chloride induces intermediate phase stabilization for efficient perovskite solar cells," *Joule*, vol. 3, pp. 2179–2192, 2019.

104. H. Min, M. Kim, S. U. Lee, H. Kim, G. Kim, K. Choi, J. H. Lee, and S. I. Seok, "Efficient, stable solar cells by using inherent bandgap of a-phase formamidinium lead iodide," *Science*, vol. 366, pp. 749–753, 2019.

105. K. D. Jayawardena, R. M. Bandara, M. Monti, E. Butler-Caddle, T. Pichler, H. Shiozawa, Z. Wang, S. Jenatsch, S. J. Hinder, M. G. Masteghin, M. Patel, H. M. Thirimanne, W. Zhang, R. A. Sporea, J. Lloyd-Hughes, and S. R. Silva, "Approaching the Shockley-Queisser limit for fill factors in lead-tin mixed perovskite photovoltaics," *Journal of Materials Chemistry A*, vol. 8, pp. 693–705, 2020.

106. M. T. Klug, R. L. Milot, R. L. Milot, J. B. Patel, T. Green, H. C. Sansom, M. D. Farrar, A. J. Ramadan, S. Martani, Z. Wang, B. Wenger, J. M. Ball, L. Langshaw, A. Petrozza, M. B. Johnston, L. M. Herz, and H. J. Snaith, "Metal composition influences optoelectronic quality in mixed-metal lead-tin triiodide perovskite solar absorbers," *Energy& Environmental Science*, vol. 13, pp. 1776–1787, 2020.

107. M. Zhang, D. Chi, J. Wang, F. Wu, and S. Huang, "Improved performance of lead-tin mixed perovskite solar cells with pedot:pss treated by hydroquinone," *Solar Energy*, vol. 201, pp. 589–595, 5 2020.

108. X. Xu, C. C. Chueh, P. Jing, Z. Yang, X. Shi, T. Zhao, L. Y. Lin, and A. K. Jen, "High-performance near-IR photodetector using low-bandgap $MA_{0.5}FA_{0.5}Pb_{0.5}Sn_{0.5}I_3$ perovskite," *Advanced Functional Materials*, vol. 27, pp. 1–6, 2017.

109. W. Li, J. Li, J. Li, J. Fan, Y. Mai, and L. Wang, "Additive-assisted construction of all-inorganic $CsSnIBr_2$ mesoscopic perovskite solar cells with superior thermal stability up to 473 K," *Journal of Materials Chemistry A*, vol. 4, pp. 17104–17110, 2016.

110. M. H. Kumar, S. Dharani, W. L. Leong, P. P. Boix, R. R. Prabhakar, T. Baikie, C. Shi, H. Ding, R. Ramesh, M. Asta, M. Graetzel, S. G. Mhaisalkar, and N. Mathews, "Lead-free halide perovskite solar cells with high photocurrents realized through vacancy modulation," *Advanced Materials*, vol. 26, pp. 7122–7127, 2014.

111. Y. Takahashi, H. Hasegawa, Y. Takahashi, and T. Inabe, "Hall mobility in tin iodide perovskite $CH_3NH_3SnI_3$: Evidence for a doped semiconductor," *Journal of Solid State Chemistry*, vol. 205, pp. 39–43, 2013.

112. S. J. Lee, S. S. Shin, J. Im, T. K. Ahn, J. H. Noh, N. J. Jeon, S. I. Seok, and J. Seo, "Reducing carrier density in formamidinium tin perovskites and its beneficial effects on stability and efficiency of perovskite solar cells," *ACS Energy Letters*, vol. 3, pp. 46–53, 2018.

113. R. L. Milot, M. T. Klug, C. L. Davies, Z. Wang, H. Kraus, H. J. Snaith, M. B. Johnston, and L. M. Herz, "The effects of doping density and temperature on the optoelectronic properties of formamidinium tin triiodide thin films," *Advanced Materials*, vol. 30, 11 2018.

114. A. R. Bowman, M. T. Klug, T. A. Doherty, M. D. Farrar, S. P. Senanayak, B. Wenger, G. Divitini, E. P. Booker, Z. Andaji-Garmaroudi, S. Macpherson, E. Ruggeri, H. Sirringhaus, H. J. Snaith, and S. D. Stranks, "Microsecond carrier lifetimes, controlled p-doping, and enhanced air stability in low-bandgap metal halide perovskites," *ACS Energy Letters*, vol. 4, pp. 2301–2307, 2019.

115. Z. Yang, Z. Yu, H. Wei, X. Xiao, Z. Ni, B. Chen, Y. Deng, S. N. Habisreutinger, X. Chen, K. Wang, J. Zhao, P. N. Rudd, J. J. Berry, M. C. Beard, and J. Huang, "Enhancing electron

diffusion length in narrow-bandgap perovskites for efficient monolithic perovskite tandem solar cells," *Nature Communications*, vol. 10, pp. 1–9, 2019.

116. S. Shao, J. Liu, G. Portale, H. H. Fang, G. R. Blake, G. H. ten Brink, L. J. A. Koster, and M. A. Loi, "Highly reproducible Sn-based hybrid perovskite solar cells with 9% efficiency," *Advanced Energy Materials*, vol. 8, 2 2018.

117. K. J. Savill, A. M. Ulatowski, M. D. Farrar, M. B. Johnston, H. J. Snaith, and L. M. Herz, "Impact of tin fluoride additive on the properties of mixed tin-lead iodide perovskite semiconductors," *Advanced Functional Materials*, vol. 30, pp. 1–13, 2020.

118. H. Yao, F. Zhou, Z. Li, Z. Ci, L. Ding, and Z. Jin, "Strategies for improving the stability of tin-based perovskite ($ASnX_3$) solar cells," *Advanced Science*, vol. 7, 2020.

119. R. A. Belisle, W. H. Nguyen, A. R. Bowring, P. Calado, X. Li, S. J. Irvine, M. D. McGehee, P. R. Barnes, and B. C. O'Regan, "Interpretation of inverted photocurrent transients in organic lead halide perovskite solar cells: Proof of the field screening by mobile ions and determination of the space charge layer widths," *Energy& Environmental Science*, vol. 10, pp. 192–204, 2017.

120. L. Bertoluzzi, R. A. Belisle, K. A. Bush, R. Cheacharoen, M. D. McGehee, and B. C. O'Regan, "In situ measurement of electric-field screening in hysteresis-free PTAA/$FA_{0.83}Cs_{0.17}Pb(I_{0.83}Br_{0.17})_3$/C60 perovskite solar cells gives an ion mobility of $\sim 3 \times 10^{-7}$ $cm^2/(v\ s)$, 2 orders of magnitude faster than reported for metal-oxide-contacted perovskite cells with hysteresis," *Journal of the American Chemical Society*, vol. 140, pp. 12775–12784, 2018.

121. L. Bertoluzzi, C. C. Boyd, N. Rolston, J. Xu, R. Prasanna, B. C. O'Regan, and M. D. McGehee, "Mobile ion concentration measurement and open-access band diagram simulation platform for halide perovskite solar cells," *Joule*, vol. 4, pp. 109–127, 2020.

122. M. H. Futscher, J. M. Lee, L. McGovern, L. A. Muscarella, T. Wang, M. I. Haider, A. Fakharuddin, L. Schmidt-Mende, and B. Ehrler, "Quantification of ion migration in $CH_3NH_3PbI_3$ perovskite solar cells by transient capacitance measurements," *Materials Horizons*, vol. 6, pp. 1497–1503, 2019.

123. J. Herterich, M. Unmüssig, G. Loukeris, M. Kohlstädt, and U. Würfel, "Ion movement explains

huge V_{OC} increase despite almost unchanged internal quasi-Fermi-level splitting in planar perovskite solar cells," *Energy Technology*, vol. 9, p. 2001104, 2021.

124. S. van Reenen, M. Kemerink, and H. J. Snaith, "Modeling anomalous hysteresis in perovskite solar cells," *The Journal of Physical Chemistry Letters*, vol. 6, no. 19, pp. 3808–3814, 2015.

125. Y. Zhang, M. Liu, G. E. Eperon, T. C. Leijtens, D. McMeekin, M. Saliba, W. Zhang, M. D. Bastiani, A. Petrozza, L. M. Herz, M. B. Johnston, H. Lin, and H. J. Snaith, "Charge selective contacts, mobile ions and anomalous hysteresis in organic-inorganic perovskite solar cells," *Materials Horizons*, vol. 2, pp. 315–322, 2015.

126. M. V. Khenkin, K. M. Anoop, E. A. Katz, and I. Visoly-Fisher, "Bias-dependent degradation of various solar cells: Lessons for stability of perovskite photovoltaics," *Energy& Environmental Science*, vol. 12, pp. 550–558, 2019.

127. T. Cheng, G. Tumen-Ulzii, D. Klotz, S. Watanabe, T. Matsushima, and C. Adachi, "Ion migration-induced degradation and efficiency roll-off in quasi-2D perovskite light-emitting diodes," *ACS Applied Materials and Interfaces*, vol. 12, pp. 33004–33013, 2020.

128. S. P. Senanayak, B. Yang, T. H. Thomas, N. Giesbrecht, W. Huang, E. Gann, B. Nair, K. Goedel, S. Guha, X. Moya, C. R. McNeill, P. Docampo, A. Sadhanala, R. H. Friend, and H. Sirringhaus, "Understanding charge transport in lead iodide perovskite thin-film field-effect transistors," *Science Advances*, vol. 3, pp. 1–11, 2017.

129. X. Liu, D. Yu, X. Song, and H. Zeng, "Metal halide perovskites: Synthesis, ion migration, and application in field-effect transistors," *Small*, vol. 14, pp. 1–20, 2018.

130. M. A. Green, E. D. Dunlop, J. Hohl-Ebinger, M. Yoshita, N. Kopidakis, and X. Hao, "Solar cell efficiency tables (version 56)," *Progress in Photovoltaics: Research and Applications*, vol. 28, pp. 629–638, 2020.

131. J. J. Yoo, G. Seo, M. R. Chua, T. G. Park, Y. Lu, F. Rotermund, Y. K. Kim, C. S. Moon, N. J. Jeon, J. P. Correa-Baena, V. Bulović, S. S. Shin, M. G. Bawendi, and J. Seo, "Efficient perovskite solar cells via improved carrier management," *Nature*, vol. 590, pp. 587–593, 2021.

132. A. Polman, M. Knight, E. C. Garnett, B. Ehrler, and W. C. Sinke, "Photovoltaic materials – present efficiencies and future challenges," *Science*, vol. 352, p. 307, 2016.

133. G. F. Burkhard, E. T. Hoke, and M. D. McGehee, "Accounting for interference, scattering, and electrode absorption to make accurate internal quantum efficiency measurements in organic and other thin solar cells," *Advanced Materials*, vol. 22, pp. 3293–3297, 2010.

134. M. Stolterfoht, V. M. Le Corre, M. Feuerstein, P. Caprioglio, L. J. A. Koster, and D. Neher, "Voltage-dependent photoluminescence and how it correlates with the fill factor and open-circuit voltage in perovskite solar cells," *ACS Energy Letters*, vol. 4, no. 12, pp. 2887–2892, 2019.

135. M. Stolterfoht, P. Caprioglio, C. M. Wolff, J. A. Márquez, J. Nordmann, S. Zhang, D. Rothhardt, U. Hörmann, Y. Amir, A. Redinger, L. Kegelmann, F. Zu, S. Albrecht, N. Koch, T. Kirchartz, M. Saliba, T. Unold, and D. Neher, "The impact of energy alignment and interfacial recombination on the internal and external open-circuit voltage of perovskite solar cells," *Energy& Environmental Science*, vol. 12, pp. 2778–2788, 2019.

136. J. Diekmann, P. Caprioglio, M. H. Futscher, V. M. L. Corre, S. Reichert, F. Jaiser, M. Arvind, L. P. Toro, E. Gutierrez-Partida, F. Peña-Camargo, C. Deibel, B. Ehrler, T. Unold, T. Kirchartz, D. Neher, and M. Stolterfoht, "Pathways toward 30% efficient single-junction perovskite solar cells and the role of mobile ions," *Solar RRL*, vol. 5, p. 2100219, 8 2021.

137. V. M. L. Corre, J. Diekmann, F. Peña-Camargo, J. Thiesbrummel, N. Tokmoldin, E. Gutierrez-Partida, K. P. Peters, L. Perdigón-Toro, M. H. Futscher, F. Lang, J. Warby, H. J. Snaith, D. Neher, and M. Stolterfoht, "Quantification of efficiency losses due to mobile ions in perovskite solar cells via fast hysteresis measurements," *Solar RRL*, vol. 6, 4 2022.

138. G. Juška, K. Arlauskas, M. Viliunas, and J. Kočka, "Extraction current transients: New method of study of charge transport in microcrystalline silicon," *Physical Review Letters*, vol. 84, pp. 4946–4949, 2000.

139. M. Stolterfoht, C. M. Wolff, Y. Amir, A. Paulke, L. Perdigón-Toro, P. Caprioglio, and D. Neher, "Approaching the fill factor Shockley–Queisser limit in stable, dopant-free triple cation perovskite solar cells," *Energy& Environmental Science*, vol. 10, pp. 1530–1539, 2017.

140. X. Deng, X. Wen, J. Zheng, T. Young, C. F. J. Lau, J. Kim, M. Green, S. Huang, and A. Ho-Baillie, "Dynamic study of the light soaking effect on perovskite solar cells by in-situ photoluminescence microscopy," *Nano Energy*, vol. 46, pp. 356–364, 4 2018.

141. Y. Rong, Y. Hu, A. Mei, H. Tan, M. I. Saidaminov, S. I. Seok, M. D. McGehee, E. H. Sargent, and H. Han, "Challenges for commercializing perovskite solar cells," *Science*, vol. 361, 9 2018.

142. J. K. Ling, P. K. K. Kizhakkedath, T. M. Watson, I. Mora-Seró, L. Schmidt-Mende, T. M. Brown, and R. Jose, "A perspective on the commercial viability of perovskite solar cells," *Solar RRL*, vol. 5, 11 2021.

143. S. Ruan, M. A. Surmiak, Y. Ruan, D. P. McMeekin, H. Ebendorff-Heidepriem, Y. B. Cheng, J. Lu, and C. R. McNeill, "Light induced degradation in mixed-halide perovskites," *Journal of Materials Chemistry C*, vol. 7, pp. 9326–9334, 2019.

144. F. Lang, G. E. Eperon, K. Frohna, E. M. Tennyson, A. Al-Ashouri, G. Kourkafas, J. Bundesmann, A. Denker, K. G. West, L. C. Hirst, H. C. Neitzert, and S. D. Stranks, "Proton-radiation tolerant all-perovskite multijunction solar cells," *Advanced Energy Materials*, vol. 11, p. 2102246, 11 2021.

145. R. K. Misra, S. Aharon, B. Li, D. Mogilyansky, I. Visoly-Fisher, L. Etgar, and E. A. Katz, "Temperature- and component-dependent degradation of perovskite photovoltaic materials under concentrated sunlight," *Journal of Physical Chemistry Letters*, vol. 6, pp. 326–330, 2 2015.

146. B. Conings, J. Drijkoningen, N. Gauquelin, A. Babayigit, J. D'Haen, L. D'Olieslaeger, A. Ethirajan, J. Verbeeck, J. Manca, E. Mosconi, F. D. Angelis, and H. G. Boyen, "Intrinsic thermal instability of methylammonium lead trihalide perovskite," *Advanced Energy Materials*, vol. 5, 8 2015.

147. Y. Ouyang, Y. Li, P. Zhu, Q. Li, Y. Gao, J. Tong, L. Shi, Q. Zhou, C. Ling, Q. Chen, Z. Deng, H. Tan, W. Deng, and J. Wang, "Photo-oxidative degradation of methylammonium lead iodide perovskite: Mechanism and protection," *Journal of Materials Chemistry A*, vol. 7, pp. 2275–2282, 2019.

148. D. Bryant, N. Aristidou, S. Pont, I. Sanchez-Molina, T. Chotchunangatchaval, S. Wheeler, J. R. Durrant, and S. A. Haque, "Light and oxygen induced degradation limits the operational stability of methylammonium lead triiodide perovskite solar cells," *Energy& Environmental Science*, vol. 9, pp. 1655–1660, 5 2016.

149. Q. Wang, B. Chen, Y. Liu, Y. Deng, Y. Bai, Q. Dong, and J. Huang, "Scaling behavior of moisture-induced grain degradation in polycrystalline hybrid perovskite thin films," *Energy& Environmental Science*, vol. 10, pp. 516–522, 2 2017.

150. M. Salado, L. Contreras-Bernal, L. Caliò, A. Todinova, C. López-Santos, S. Ahmad, A. Borras, J. Idígoras, and J. A. Anta, "Impact of moisture on efficiency-determining electronic processes in perovskite solar cells," *Journal of Materials Chemistry A*, vol. 5, pp. 10917–10927, 2017.

151. S.-H. Turren-Cruz, A. Hagfeldt, and M. Saliba, "Methylammonium-free, high-performance, and stable perovskite solar cells on a planar architecture," *Science*, vol. 362, no. 6413, pp. 449–453, 2018.

152. G. E. Eperon, S. D. Stranks, C. Menelaou, M. B. Johnston, L. M. Herz, and H. J. Snaith, "Formamidinium lead trihalide: a broadly tunable perovskite for efficient planar heterojunction solar cells," *Energy& Environmental Science*, vol. 7, p. 982, 2014.

153. I. S. Yang and N. G. Park, "Dual additive for simultaneous improvement of photovoltaic performance and stability of perovskite solar cell," *Advanced Functional Materials*, vol. 31, 5 2021.

154. F. Zhang and K. Zhu, "Additive engineering for efficient and stable perovskite solar cells," *Advanced Energy Materials*, vol. 10, 4 2020.

155. J. Byeon, J. Kim, J. Y. Kim, G. Lee, K. Bang, N. Ahn, and M. Choi, "Charge transport layer-dependent electronic band bending in perovskite solar cells and its correlation to light-induced device degradation," *ACS Energy Letters*, vol. 5, pp. 2580–2589, 8 2020.

156. F. Wang, M. Endo, S. Mouri, Y. Miyauchi, Y. Ohno, A. Wakamiya, Y. Murata, and K. Matsuda, "Highly stable perovskite solar cells with an all-carbon hole transport layer," *Nanoscale*, vol. 8, pp. 11882–11888, 6 2016.

157. L. Huang and Z. Ge, "Simple, robust, and going more efficient: Recent advance on electron transport layer-free perovskite solar cells," *Advanced Energy Materials*, vol. 9, 6 2019.

158. Y. Li, H. Xie, E. L. Lim, A. Hagfeldt, and D. Bi, "Recent progress of critical interface engineering for highly efficient and stable perovskite solar cells," *Advanced Energy Materials*, vol. 12, 2 2022.

159. Y. Lin, Y. Bai, Y. Fang, Z. Chen, S. Yang, X. Zheng, S. Tang, Y. Liu, J. Zhao, and J. Huang, "Enhanced thermal stability in perovskite solar cells by assembling 2D/3D stacking structures," *Journal of Physical Chemistry Letters*, vol. 9, pp. 654–658, 2 2018.

160. P. Chen, Y. Bai, S. Wang, M. Lyu, J. H. Yun, and L. Wang, "In situ growth of 2D perovskite capping layer for stable and efficient perovskite solar cells," *Advanced Functional Materials*, vol. 28, 4 2018.

161. G. Grancini, C. Roldán-Carmona, I. Zimmermann, E. Mosconi, X. Lee, D. Martineau, S. Narbey, F. Oswald, F. D. Angelis, M. Graetzel, and M. K. Nazeeruddin, "One-year stable perovskite solar cells by 2D/3D interface engineering," *Nature Communications*, vol. 8, 6 2017.

162. T. Gahlmann, K. O. Brinkmann, T. Becker, C. Tückmantel, C. Kreusel, F. van gen Hassend, S. Weber, and T. Riedl, "Impermeable charge transport layers enable aqueous processing on top of perovskite solar cells," *Advanced Energy Materials*, vol. 10, 3 2020.

163. K. O. Brinkmann, J. Zhao, N. Pourdavoud, T. Becker, T. Hu, S. Olthof, K. Meerholz, L. Hoffmann, T. Gahlmann, R. Heiderhoff, M. F. Oszajca, N. A. Luechinger, D. Rogalla, Y. Chen, B. Cheng, and T. Riedl, "Suppressed decomposition of organometal halide perovskites by impermeable electron-extraction layers in inverted solar cells," *Nature Communications*, vol. 8, p. 13938, 2017.

164. J. Zhao, K. O. Brinkmann, T. Hu, N. Pourdavoud, T. Becker, T. Gahlmann, R. Heiderhoff, A. Polywka, P. Görrn, Y. Chen, B. Cheng, and T. Riedl, "Self-encapsulating thermostable and air-resilient semitransparent perovskite solar cells," *Advanced Energy Materials*, vol. 7, no. 14, p. 1602599, 2017.

165. N. Arora, M. I. Dar, A. Hinderhofer, N. Pellet, F. Schreiber, S. M. Zakeeruddin, and M. Grätzel, "Perovskite solar cells with cuscn hole extraction layers yield stabilized efficiencies greater than 20%," *Science*, vol. 358, no. 6364, pp. 768–771, 2017.

166. S. Wu, R. Chen, S. Zhang, B. H. Babu, Y. Yue, H. Zhu, Z. Yang, C. Chen, W. Chen, Y. Huang, S. Fang, T. Liu, L. Han, and W. Chen, "A chemically inert bismuth interlayer enhances long-term stability of inverted perovskite solar cells," *Nature Communications*, vol. 10, no. 1, p. 1161, 2019.

167. R. Cheacharoen, C. C. Boyd, G. F. Burkhard, T. Leijtens, J. A. Raiford, K. A. Bush, S. F. Bent, and M. D. McGehee, "Encapsulating perovskite solar cells to withstand damp heat and thermal cycling," *Sustainable Energy Fuels*, vol. 2, pp. 2398–2406, 2018.

168. W. Meng, K. Zhang, A. Osvet, J. Zhang, W. Gruber, K. Forberich, B. Meyer, W. Heiss, T. Unruh, N. Li, and C. J. Brabec, "Revealing the strain-associated physical mechanisms impacting the performance and stability of perovskite solar cells," *Joule*, vol. 6, 2022.

169. J. A. Steele, H. Jin, I. Dovgaliuk, R. F. Berger, T. Braeckevelt, H. Yuan, C. Martin, E. Solano, K. Lejaeghere, S. M. J. Rogge, C. Notebaert, W. Vandezande, K. P. F. Janssen, B. Goderis, E. Debroye, Y.-K. Wang, Y. Dong, D. Ma, M. Saidaminov, H. Tan, Z. Lu, V. Dyadkin, D. Chernyshov, V. V. Speybroeck, E. H. Sargent, J. Hofkens, and M. B. J. Roeffaers, "Thermal unequilibrium of strained black cspbi$_3$ thin films," *Science*, vol. 365, no. 6454, pp. 679–684, 2019.

170. E. T. Hoke, D. J. Slotcavage, E. R. Dohner, A. R. Bowring, H. I. Karunadasa, and M. D. McGehee, "Reversible photo-induced trap formation in mixed-halide hybrid perovskites for photovoltaics," *Chemical Science*, vol. 6, pp. 613–617, 1 2015.

171. T. Zhang, C. Hu, and S. Yang, "Ion migration: A "double-edged sword" for halide-perovskite-based electronic devices," *Small Methods*, vol. 4, no. 5, p. 1900552, 2020.

172. F. Penã-Camargo, P. Caprioglio, F. Zu, E. Gutierrez-Partida, C. M. Wolff, K. Brinkmann, S. Albrecht, T. Riedl, N. Koch, D. Neher, and M. Stolterfoht, "Halide segregation versus interfacial recombination in bromide-rich wide-gap perovskite solar cells," *ACS Energy Letters*, vol. 5, pp. 2728–2736, 8 2020.

173. A. J. Knight, J. B. Patel, H. J. Snaith, M. B. Johnston, and L. M. Herz, "Trap states, electric fields, and phase segregation in mixed-halide perovskite photovoltaic devices," *Advanced Energy Materials*, vol. 10, pp. 1–11, 2020.

174. M. De Bastiani, G. Armaroli, R. Jalmood, L. Ferlauto, X. Li, R. Tao, G. T. Harrison, M. K. Eswaran, R. Azmi, M. Babics, A. S. Subbiah, E. Aydin, T. G. Allen, C. Combe, T. Cramer, D. Baran, U. Schwingenschlögl, G. Lubineau, D. Cavalcoli, and S. De Wolf, "Mechanical reliability of fullerene/tin oxide interfaces in monolithic perovskite/silicon tandem cells," *ACS Energy Letters*, vol. 7, no. 2, pp. 827–833, 2022.

175. G. Y. Kim, A. Senocrate, T.-Y. Yang, G. Gregori, M. Grätzel, and J. Maier, "Large tunable photoeffect on ion conduction in halide perovskites and implications for photodecomposition," *Nature Materials*, vol. 17, no. 5, pp. 445–449, 2018.

176. A. Walsh, D. O. Scanlon, S. Chen, X. G. Gong, and S.-H. Wei, "Self-regulation mechanism for charged point defects in hybrid halide perovskites," *Angewandte Chemie International Edition*, vol. 54, no. 6, pp. 1791–1794, 2015.

177. S. A. Weber, I. M. Hermes, S. H. Turren-Cruz, C. Gort, V. W. Bergmann, L. Gilson, A. Hagfeldt, M. Graetzel, W. Tress, and R. Berger, "How the formation of interfacial charge causes hysteresis in perovskite solar cells," *Energy& Environmental Science*, vol. 11, pp. 2404–2413, 2018.

178. G. Richardson, S. E. J. O'Kane, R. G. Niemann, T. A. Peltola, J. M. Foster, P. J. Cameron, and A. B. Walker, "Can slow-moving ions explain hysteresis in the current–voltage curves of perovskite solar cells?," *Energy& Environmental Science*, vol. 9, pp. 1476–1485, 2016.

179. P. Calado, A. M. Telford, D. Bryant, X. Li, J. Nelson, B. C. O'Regan, and P. R. Barnes, "Evidence for ion migration in hybrid perovskite solar cells with minimal hysteresis," *Nature Communications*, vol. 7, pp. 1–10, 2016.

180. N. Tessler and Y. Vaynzof, "Insights from device modeling of perovskite solar cells," *ACS Energy Letters*, vol. 5, pp. 1260–1270, 2020.

181. F. Fu, S. Pisoni, Q. Jeangros, J. Sastre-Pellicer, M. Kawecki, A. Paracchino, T. Moser, J. Werner, C. Andres, L. Duchêne, P. Fiala, M. Rawlence, S. Nicolay, C. Ballif, A. N. Tiwari, and S. Buecheler, "I_2 vapor-induced degradation of formamidinium lead iodide based perovskite solar cells under heat–light soaking conditions," *Energy& Environmental Science*, vol. 12, pp. 3074–3088, 2019.

182. D. A. Jacobs, C. M. Wolff, X.-Y. Chin, K. Artuk, C. Ballif, and Q. Jeangros, "Lateral ion migration accelerates degradation in halide perovskite devices," *Energy& Environmental Science*, vol. 15, pp. 5324–5339, 2022.

183. S. P. Dunfield, L. Bliss, F. Zhang, J. M. Luther, K. Zhu, M. F. A. M. van Hest, M. O. Reese, and J. J. Berry, "From defects to degradation: A mechanistic understanding of degradation in perovskite solar cell devices and modules," *Advanced Energy Materials*, vol. 10, no. 26, p. 1904054, 2020.

184. A. Mei, Y. Sheng, Y. Ming, Y. Hu, Y. Rong, W. Zhang, S. Luo, G. Na, C. Tian, X. Hou, Y. Xiong, Z. Zhang, S. Liu, S. Uchida, T.-W. Kim, Y. Yuan, L. Zhang, Y. Zhou, and H. Han, "Stabilizing perovskite solar cells to IEC61215:2016 standards with over 9,000-h operational tracking," *Joule*, vol. 4, no. 12, pp. 2646–2660, 2020.

185. T.-Y. Yang, G. Gregori, N. Pellet, M. Grätzel, and J. Maier, "The significance of ion conduction in a hybrid organic–inorganic lead-iodide-based perovskite photosensitizer," *Angewandte Chemie International Edition*, vol. 54, no. 27, pp. 7905–7910, 2015.

186. Y. Kato, L. K. Ono, M. V. Lee, S. Wang, S. R. Raga, and Y. Qi, "Silver iodide formation in methyl ammonium lead iodide perovskite solar cells with silver top electrodes," *Advanced Materials Interfaces*, vol. 2, no. 13, p. 1500195, 2015.

187. J. Thiesbrummel, V. M. L. Corre, F. Peña-Camargo, L. Perdigón-Toro, F. Lang, F. Yang, M. Grischek, E. Gutierrez-Partida, J. Warby, M. D. Farrar, S. Mahesh, P. Caprioglio, S. Albrecht, D. Neher, H. J. Snaith, and M. Stolterfoht, "Universal current losses in perovskite solar cells due to mobile ions," *Advanced Energy Materials*, vol. 11, 9 2021.

188. M. Stolterfoht, C. M. Wolff, J. A. Márquez, S. Zhang, C. J. Hages, D. Rothhardt, S. Albrecht, P. L. Burn, P. Meredith, T. Unold, and D. Neher, "Visualization and suppression of interfacial recombination for high-efficiency large-area pin perovskite solar cells," *Nature Energy*, vol. 3, pp. 847–854, 10 2018.

189. D. A. Jacobs, Y. Wu, H. Shen, C. Barugkin, F. J. Beck, T. P. White, K. Weber, and K. R. Catchpole, "Hysteresis phenomena in perovskite solar cells: the many and varied effects of ionic accumulation," *Phys. Chem. Chem. Phys.*, vol. 19, pp. 3094–3103, 2017.

190. J. Kniepert, A. Paulke, L. Perdigón-Toro, J. Kurpiers, H. Zhang, F. Gao, J. Yuan, Y. Zou, V. M. Le Corre, L. J. A. Koster, and D. Neher, "Reliability of charge carrier recombination data determined with charge extraction methods," *Journal of Applied Physics*, vol. 126, p. 205501, 11 2019.

191. S. Reichert, Q. An, Y.-W. Woo, A. Walsh, Y. Vaynzof, and C. Deibel, "Probing the ionic defect landscape in halide perovskite solar cells," *Nature Communications*, vol. 11, no. 1, p. 6098, 2020.

192. J. Thiesbrummel, S. Shah, E. Gutierrez-Partida, F. Zu, F. Camargo, S. Zeiske, J. Diekmann, F. Ye, K. Peters, K. O. Brinkmann, J. Warby, Q. Jeangros, F. Lang, Y. Wu, S. Albrecht, T. Riedl, A. Armin, D. Neher, N. Koch, V. L. Corre, H. J. Snaith, and M. Stolterfoht, "Ion induced field screening governs the early performance degradation of perovskite solar cells," *ResearchSquare*, 2023. Preprint.

193. S. G. Motti, D. Meggiolaro, A. J. Barker, E. Mosconi, C. A. R. Perini, J. M. Ball, M. Gandini, M. Kim, F. De Angelis, and A. Petrozza, "Controlling competing photochemical reactions stabilizes perovskite solar cells," *Nature Photonics*, vol. 13, no. 8, pp. 532–539, 2019.

194. J. Holovský, A. Peter Amalathas, L. Landová, B. Dzurňák, B. Conrad, M. Ledinský, Z. Hájková, O. Pop-Georgievski, J. Svoboda, T. C.-J. Yang, and Q. Jeangros, "Lead halide residue as a source of light-induced reversible defects in hybrid perovskite layers and solar cells," *ACS Energy Letters*, vol. 4, no. 12, pp. 3011–3017, 2019.

195. F. Zu, T. Schultz, C. M. Wolff, D. Shin, L. Frohloff, D. Neher, P. Amsalem, and N. Koch, "Position-locking of volatile reaction products by atmosphere and capping layers slows down photodecomposition of methylammonium lead triiodide perovskite," *RSC Adv.*, vol. 10, pp. 17534–17542, 2020.

196. M. De Bastiani, E. Van Kerschaver, Q. Jeangros, A. Ur Rehman, E. Aydin, F. H. Isikgor, A. J. Mirabelli, M. Babics, J. Liu, S. Zhumagali, E. Ugur, G. T. Harrison, T. G. Allen, B. Chen, Y. Hou, S. Shikin, E. H. Sargent, C. Ballif, M. Salvador, and S. De Wolf, "Toward stable monolithic perovskite/silicon tandem photovoltaics: A six-month outdoor performance study in a hot and humid climate," *ACS Energy Letters*, vol. 6, no. 8, pp. 2944–2951, 2021.

197. F. Sahli, J. Werner, B. A. Kamino, M. Bräuninger, R. Monnard, B. Paviet-Salomon, L. Barraud, L. Ding, J. J. D. Leon, D. Sacchetto, G. Cattaneo, M. Despeisse, M. Boccard, S. Nicolay, Q. Jeangros, B. Niesen, and C. Ballif, "Fully textured monolithic perovskite/silicon tandem solar cells with 25.2% power conversion efficiency," *Nature Materials*, vol. 17, no. 9, pp. 820–826, 2018.

198. P. Yadav, D. Prochowicz, E. A. Alharbi, S. M. Zakeeruddin, and M. Grätzel, "Intrinsic and interfacial kinetics of perovskite solar cells under photo and bias-induced degradation and recovery," *Journal of Materials Chemistry C*, vol. 5, pp. 7799–7805, 2017.

199. K. "Domanski, B. Roose, T. Matsui, M. Saliba, S.-H. Turren-Cruz, J.-P. Correa-Baena, C. R. Carmona, G. Richardson, J. M. Foster, F. De Angelis, J. M. Ball, A. Petrozza, N. Mine, M. K. Nazeeruddin, W. Tress, M. Grätzel, U. Steiner, A. Hagfeldt, and A. Abate, "Migration of cations induces reversible performance losses over day/night cycling in perovskite solar cells," *Energy& Environmental Science*, vol. 10, no. 2, pp. 604–613, 2017.

200. A. Onno, C. Chen, and Z. C. Holman, "Electron and hole partial specific resistances: a framework to understand contacts to solar cells," in *2019 IEEE 46th Photovoltaic Specialists Conference (PVSC)*, pp. 2329–2333, 2019.

201. S. Kavadiya, A. Onno, C. C. Boyd, X. Wang, A. Cetta, M. D. McGehee, and Z. C. Holman, "Investigation of the selectivity of carrier transport layers in wide-bandgap perovskite solar cells," *Solar RRL*, vol. 5, p. 2100107, 7 2021.

202. Z. Yang, A. Rajagopal, C. C. Chueh, S. B. Jo, B. Liu, T. Zhao, and A. K. Jen, "Stable low-bandgap Pb–Sn binary perovskites for tandem solar cells," *Advanced Materials*, vol. 28, pp. 8990–8997, 10 2016.

203. A. Rajagopal, Z. Yang, S. B. Jo, I. L. Braly, P. W. Liang, H. W. Hillhouse, and A. K. Jen, "Highly efficient perovskite–perovskite tandem solar cells reaching 80% of the theoretical limit in photovoltage," *Advanced Materials*, vol. 29, pp. 1–10, 2017.

204. T. Todorov, T. Gershon, O. Gunawan, Y. S. Lee, C. Sturdevant, L. Y. Chang, and S. Guha, "Monolithic perovskite-CIGS tandem solar cells via in situ band gap engineering," *Advanced Energy Materials*, vol. 5, pp. 1–6, 2015.

205. C. D. Bailie, M. G. Christoforo, J. P. Mailoa, A. R. Bowring, E. L. Unger, W. H. Nguyen, J. Burschka, N. Pellet, J. Z. Lee, M. Grätzel, R. Noufi, T. Buonassisi, A. Salleo, and M. D. McGehee, "Semi-transparent perovskite solar cells for tandems with silicon and CIGS," *Energy& Environmental Science*, vol. 8, pp. 956–963, 2015.

206. F. Lang, M. A. Gluba, S. Albrecht, J. Rappich, L. Korte, B. Rech, and N. H. Nickel, "Perovskite solar cells with large-area CVD-graphene for tandem solar cells," *Journal of Physical Chemistry Letters*, vol. 6, pp. 2745–2750, 7 2015.

207. S. Albrecht, M. Saliba, J. P. C. Baena, F. Lang, L. Kegelmann, M. Mews, L. Steier, A. Abate, J. Rappich, L. Korte, R. Schlatmann, M. K. Nazeeruddin, A. Hagfeldt, M. Grätzel, and B. Rech,

"Monolithic perovskite/silicon-heterojunction tandem solar cells processed at low temperature," *Energy& Environmental Science*, vol. 9, pp. 81–88, 1 2016.

208. J. P. Mailoa, C. D. Bailie, E. C. Johlin, E. T. Hoke, A. J. Akey, W. H. Nguyen, M. D. McGehee, and T. Buonassisi, "A 2-terminal perovskite/silicon multijunction solar cell enabled by a silicon tunnel junction," *Applied Physics Letters*, vol. 106, p. 121105, 3 2015.

209. D. N. Weiss, "Tandem solar cells beyond perovskite-silicon," *Joule*, vol. 5, pp. 2247–2250, 2021.

210. R. Lin, J. Xu, M. Wei, Y. Wang, Z. Qin, Z. Liu, J. Wu, K. Xiao, B. Chen, S. M. Park, G. Chen, H. R. Atapattu, K. R. Graham, J. Xu, J. Zhu, L. Li, C. Zhang, E. H. Sargent, and H. Tan, "All-perovskite tandem solar cells with improved grain surface passivation," *Nature*, 2022.

211. T. Leijtens, R. Prasanna, K. A. Bush, G. E. Eperon, J. A. Raiford, A. Gold-Parker, E. J. Wolf, S. A. Swifter, C. C. Boyd, H. P. Wang, M. F. Toney, S. F. Bent, and M. D. McGehee, "Tin-lead halide perovskites with improved thermal and air stability for efficient all-perovskite tandem solar cells," *Sustainable Energy and Fuels*, vol. 2, pp. 2450–2459, 2018.

212. T. J. Jacobsson, A. Hultqvist, A. García-Fernández, A. Anand, A. Al-Ashouri, A. Hagfeldt, A. Crovetto, A. Abate, A. G. Ricciardulli, A. Vijayan, A. Kulkarni, A. Y. Anderson, B. P. Darwich, B. Yang, B. L. Coles, C. A. Perini, C. Rehermann, D. Ramirez, D. Fairen-Jimenez, D. D. Girolamo, D. Jia, E. Avila, E. J. Juarez-Perez, F. Baumann, F. Mathies, G. S. González, G. Boschloo, G. Nasti, G. Paramasivam, G. Martínez-Denegri, H. Näsström, H. Michaels, H. Köbler, H. Wu, I. Benesperi, M. I. Dar, I. B. Pehlivan, I. E. Gould, J. N. Vagott, J. Dagar, J. Kettle, J. Yang, J. Li, J. A. Smith, J. Pascual, J. J. Jerónimo-Rendón, J. F. Montoya, J. P. Correa-Baena, J. Qiu, J. Wang, K. Sveinbjörnsson, K. Hirselandt, K. Dey, K. Frohna, L. Mathies, L. A. Castriotta, M. H. Aldamasy, M. Vasquez-Montoya, M. A. Ruiz-Preciado, M. A. Flatken, M. V. Khenkin, M. Grischek, M. Kedia, M. Saliba, M. Anaya, M. Veldhoen, N. Arora, O. Shargaieva, O. Maus, O. S. Game, O. Yudilevich, P. Fassl, Q. Zhou, R. Betancur, R. Munir, R. Patidar, S. D. Stranks, S. Alam, S. Kar, T. Unold, T. Abzieher, T. Edvinsson, T. W. David, U. W. Paetzold, W. Zia, W. Fu, W. Zuo, V. R. Schröder, W. Tress, X. Zhang, Y. H. Chiang, Z. Iqbal, Z. Xie, and E. Unger, "An open-access database and analysis tool for perovskite solar cells based on the fair data principles," *Nature Energy*, vol. 7, pp. 107–115, 2022.

213. R. Sheng, M. T. Hörantner, Z. Wang, Y. Jiang, W. Zhang, A. Agosti, S. Huang, X. Hao, A. Ho-Baillie, M. Green, and H. J. Snaith, "Monolithic wide band gap perovskite/perovskite tandem solar cells with organic recombination layers," *Journal of Physical Chemistry C*, vol. 121, pp. 27256–27262, 2017.

214. D. Zhao, C. Chen, C. Wang, M. M. Junda, Z. Song, C. R. Grice, Y. Yu, C. Li, B. Subedi, N. J. Podraza, X. Zhao, G. Fang, R. G. Xiong, K. Zhu, and Y. Yan, "Efficient two-terminal all-perovskite tandem solar cells enabled by high-quality low-bandgap absorber layers," *Nature Energy*, vol. 3, pp. 1093–1100, 2018.

215. A. F. Palmstrom, G. E. Eperon, T. Leijtens, R. Prasanna, S. N. Habisreutinger, W. Nemeth, E. A. Gaulding, S. P. Dunfield, M. Reese, S. Nanayakkara, T. Moot, J. Werner, J. Liu, B. To, S. T. Christensen, M. D. McGehee, M. F. van Hest, J. M. Luther, J. J. Berry, and D. T. Moore, "Enabling flexible all-perovskite tandem solar cells," *Joule*, vol. 3, pp. 2193–2204, 9 2019.

216. J. Tong, Z. Song, D. H. Kim, X. Chen, C. Chen, A. F. Palmstrom, P. F. Ndione, M. O. Reese, S. P. Dunfield, O. G. Reid, J. Liu, F. Zhang, S. P. Harvey, Z. Li, S. T. Christensen, G. Teeter, D. Zhao, M. M. Al-Jassim, M. F. V. Hest, M. C. Beard, S. E. Shaheen, J. J. Berry, Y. Yan, and K. Zhu, "Carrier lifetimes of $>$1 ms in Sn-Pb perovskites enable efficient all-perovskite tandem solar cells," *Science*, vol. 364, pp. 475–479, 2019.

217. Z. Yu, Z. Yang, Z. Ni, Y. Shao, B. Chen, Y. Lin, H. Wei, Z. J. Yu, Z. Holman, and J. Huang, "Simplified interconnection structure based on C60/SnO_{2-x} for all-perovskite tandem solar cells," *Nature Energy*, vol. 5, pp. 657–665, 2020.

218. H. Gao, Q. Lu, K. Xiao, Q. Han, R. Lin, Z. Liu, H. Li, L. Li, X. Luo, Y. Gao, Y. Wang, J. Wen, Z. Zou, Y. Zhou, and H. Tan, "Thermally stable all-perovskite tandem solar cells fully using metal oxide charge transport layers and tunnel junction," *Solar RRL*, vol. 5, p. 2100814, 12 2021.

219. K. Datta, J. Wang, D. Zhang, V. Zardetto, W. H. Remmerswaal, C. H. Weijtens, M. M. Wienk, and R. A. Janssen, "Monolithic all-perovskite tandem solar cells with minimized optical and energetic losses," *Advanced Materials*, vol. 34, p. 2110053, 3 2022.

220. T. Kirchartz, U. Rau, M. Hermle, A. W. Bett, A. Helbig, and J. H. Werner, "Internal voltages in GaIn/PGaInAs/Ge multijunction solar cells determined by electroluminescence measurements," *Applied Physics Letters*, vol. 92, 2008.

221. S. Roensch, R. Hoheisel, F. Dimroth, and A. W. Bett, "Subcell I-V characteristic analysis of GaInP/GaInAs/Ge solar cells using electroluminescence measurements," *Applied Physics Letters*, vol. 98, 6 2011.

222. S. Chen, L. Zhu, M. Yoshita, T. Mochizuki, C. Kim, H. Akiyama, M. Imaizumi, and Y. Kanemitsu, "Thorough subcells diagnosis in a multi-junction solar cell via absolute electroluminescence-efficiency measurements," *Scientific Reports*, vol. 5, 1 2015.

223. D. Alonso-Álvarez and N. Ekins-Daukes, "Photoluminescence-based current-voltage characterization of individual subcells in multijunction devices," *IEEE Journal of Photovoltaics*, vol. 6, pp. 1004–1011, 7 2016.

224. A. Al-Ashouri, A. Magomedov, M. Roß, M. Jošt, M. Talaikis, G. Chistiakova, T. Bertram, J. A. Márquez, E. Köhnen, E. Kasparavičius, S. Levcenco, L. Gil-Escrig, C. J. Hages, R. Schlatmann, B. Rech, T. Malinauskas, T. Unold, C. A. Kaufmann, L. Korte, G. Niaura, V. Getautis, and S. Albrecht, "Conformal monolayer contacts with lossless interfaces for perovskite single junction and monolithic tandem solar cells," *Energy& Environmental Science*, vol. 12, pp. 3356–3369, 11 2019.

225. J. Dagar, M. Fenske, A. Al-Ashouri, C. Schultz, B. Li, H. Köbler, R. Munir, G. Parmasivam, J. Li, I. Levine, A. Merdasa, L. Kegelmann, H. Näsström, J. A. Marquez, T. Unold, D. M. Többens, R. Schlatmann, B. Stegemann, A. Abate, S. Albrecht, and E. Unger, "Compositional and interfacial engineering yield high-performance and stable p-i-n perovskite solar cells and mini-modules," *ACS Applied Materials and Interfaces*, vol. 13, pp. 13022–13033, 3 2021.

226. Z. Liu, J. Siekmann, B. Klingebiel, U. Rau, and T. Kirchartz, "Interface optimization via fullerene blends enables open-circuit voltages of 1.35 V in $CH_3NH_3Pb(I_{0.8}Br_{0.2})_3$ solar cells," *Advanced Energy Materials*, 4 2021.

227. J. Seo, S. Park, Y. C. Kim, N. J. Jeon, J. H. Noh, S. C. Yoon, and S. I. Seok, "Benefits of very thin PCBM and LiF layers for solution-processed p-i-n perovskite solar cells," *Energy& Environmental Science*, vol. 7, pp. 2642–2646, 2014.

228. X. Zheng, Y. Hou, C. Bao, J. Yin, F. Yuan, Z. Huang, K. Song, J. Liu, J. Troughton, N. Gasparini, C. Zhou, Y. Lin, D. J. Xue, B. Chen, A. K. Johnston, N. Wei, M. N. Hedhili, M. Wei, A. Y. Alsalloum, P. Maity, B. Turedi, C. Yang, D. Baran, T. D. Anthopoulos, Y. Han,

Z. H. Lu, O. F. Mohammed, F. Gao, E. H. Sargent, and O. M. Bakr, "Managing grains and interfaces via ligand anchoring enables 22.3%-efficiency inverted perovskite solar cells," *Nature Energy*, vol. 5, pp. 131–140, 2 2020.

229. E. L. Unger, L. Kegelmann, K. Suchan, D. Sörell, L. Korte, and S. Albrecht, "Roadmap and roadblocks for the band gap tunability of metal halide perovskites," *Journal of Materials Chemistry A*, vol. 5, pp. 11401–11409, 2017.

230. S. Mahesh, J. M. Ball, R. D. Oliver, D. P. McMeekin, P. K. Nayak, M. B. Johnston, and H. J. Snaith, "Revealing the origin of voltage loss in mixed-halide perovskite solar cells," *Energy& Environmental Science*, vol. 13, pp. 258–267, 1 2020.

231. K. O. Brinkmann, T. Becker, F. Zimmermann, C. Kreusel, T. Gahlmann, M. Theisen, T. Haeger, S. Olthof, C. Tückmantel, M. Günster, T. Maschwitz, F. Göbelsmann, C. Koch, D. Hertel, P. Caprioglio, F. Peña-Camargo, L. Perdigón-Toro, A. Al-Ashouri, L. Merten, A. Hinderhofer, L. Gomell, S. Zhang, F. Schreiber, S. Albrecht, K. Meerholz, D. Neher, M. Stolterfoht, and T. Riedl, "Perovskite–organic tandem solar cells with indium oxide interconnect," *Nature*, vol. 604, pp. 280–286, 2022.

232. K. O. Brinkmann, T. Becker, F. Zimmermann, C. Kreusel, T. Gahlmann, T. Haeger, and T. Riedl, "The optical origin of near-unity external quantum efficiencies in perovskite solar cells," *Solar RRL*, vol. 5, p. 2100371, 2021.

233. P. Caprioglio, S. Caicedo-Dávila, T. C. J. Yang, C. M. Wolff, F. Peña-Camargo, P. Fiala, B. Rech, C. Ballif, D. Abou-Ras, M. Stolterfoht, S. Albrecht, Q. Jeangros, and D. Neher, "Nano-emitting heterostructures violate optical reciprocity and enable efficient photoluminescence in halide-segregated methylammonium-free wide bandgap perovskites," *ACS Energy Letters*, vol. 6, pp. 419–428, 2 2021.

234. M. Stolterfoht, M. Grischek, P. Caprioglio, C. M. Wolff, E. Gutierrez-Partida, F. Peña-Camargo, D. Rothhardt, S. Zhang, M. Raoufi, J. Wolansky, M. Abdi-Jalebi, S. D. Stranks, S. Albrecht, T. Kirchartz, and D. Neher, "How to quantify the efficiency potential of neat perovskite films: Perovskite semiconductors with an implied efficiency exceeding 28%," *Advanced Materials*, vol. 32, p. 2000080, 4 2020.

235. K. Tvingstedt, O. Malinkiewicz, A. Baumann, C. Deibel, H. J. Snaith, V. Dyakonov, and H. J.

Bolink, "Radiative efficiency of lead iodide based perovskite solar cells," *Scientific Reports*, vol. 4, pp. 1–7, 2014.

236. A. Onno, C. Chen, P. Koswatta, M. Boccard, and Z. C. Holman, "Passivation, conductivity, and selectivity in solar cell contacts: Concepts and simulations based on a unified partial-resistances framework," *Journal of Applied Physics*, vol. 126, p. 183103, 11 2019.

237. J. Thiesbrummel, F. Peña-Camargo, K. O. Brinkmann, E. Gutierrez-Partida, F. Yang, J. Warby, S. Albrecht, D. Neher, T. Riedl, H. J. Snaith, M. Stolterfoht, and F. Lang, "Understanding and minimizing V_{OC} losses in all-perovskite tandem photovoltaics," *Advanced Energy Materials*, vol. 13, no. 3, p. 2202674, 2023.

238. S. Hu, K. Otsuka, R. Murdey, T. Nakamura, M. A. Truong, T. Yamada, T. Handa, K. Matsuda, K. Nakano, A. Sato, K. Marumoto, K. Tajima, Y. Kanemitsu, and A. Wakamiya, "Optimized carrier extraction at interfaces for 23.6% efficient tin-lead perovskite solar cells," *Energy& Environmental Science*, vol. 15, pp. 2096–2107, 2022.

239. A. R. Bowman, F. Lang, Y. H. Chiang, A. Jiménez-Solano, K. Frohna, G. E. Eperon, E. Ruggeri, M. Abdi-Jalebi, M. Anaya, B. V. Lotsch, and S. D. Stranks, "Relaxed current matching requirements in highly luminescent perovskite tandem solar cells and their fundamental efficiency limits," *ACS Energy Letters*, vol. 6, pp. 612–620, 2 2021.

240. A. Farooq, M. R. Khan, T. Abzieher, A. Voigt, D. C. Lupascu, U. Lemmer, B. S. Richards, and U. W. Paetzold, "Photodegradation of triple-cation perovskite solar cells: The role of spectrum and bias conditions," *ACS Applied Energy Materials*, vol. 4, no. 4, pp. 3083–3092, 2021.

241. S. Guarnera, A. Abate, W. Zhang, J. M. Foster, G. Richardson, A. Petrozza, and H. J. Snaith, "Improving the long-term stability of perovskite solar cells with a porous Al_2O_3 buffer layer," *The Journal of Physical Chemistry Letters*, vol. 6, no. 3, pp. 432–437, 2015.

242. S. Daliento, V. d'Alessandro, P. Guerriero, and O. Tari, "An approach to the measurement of shunt resistance of individual subcells in thin-film tandem devices," *Progress in Photovoltaics: Research and Applications*, vol. 23, no. 2, pp. 194–200, 2015.

243. U. Rau, V. Huhn, and B. E. Pieters, "Luminescence analysis of charge-carrier separation and internal series-resistance losses in $\mathrm{Cu(In,Ga)Se_2}$ solar cells," *Physical Reviews Applied*, vol. 14, p. 014046, Jul 2020.

244. A. Dasgupta, S. Mahesh, P. Caprioglio, Y.-H. Lin, K.-A. Zaininger, R. D. Oliver, P. Holzhey, S. Zhou, M. M. McCarthy, J. A. Smith, M. Frenzel, M. G. Christoforo, J. M. Ball, B. Wenger, and H. J. Snaith, "Visualizing macroscopic inhomogeneities in perovskite solar cells," *ACS Energy Letters*, vol. 7, no. 7, pp. 2311–2322, 2022.

245. W. Xu, L. J. F. Hart, B. Moss, P. Caprioglio, T. J. Macdonald, F. Furlan, J. Panidi, R. D. J. Oliver, R. A. Pacalaj, M. Heeney, N. Gasparini, H. J. Snaith, P. R. F. Barnes, and J. R. Durrant, "Impact of interface energetic alignment and mobile ions on charge carrier accumulation and extraction in p-i-n perovskite solar cells," *Advanced Energy Materials*, vol. 13, no. 36, p. 2301102, 2023.

246. M. Anaya, J. F. Galisteo-López, M. E. Calvo, J. P. Espinós, and H. Míguez, "Origin of light-induced photophysical effects in organic metal halide perovskites in the presence of oxygen," *The Journal of Physical Chemistry Letters*, vol. 9, no. 14, pp. 3891–3896, 2018.

247. N. Mendil, M. Daoudi, Z. Berkai, and A. Belghachi, "Disorder effect on carrier mobility in fullerene organic semiconductor," *Journal of Physics: Conference Series*, vol. 647, p. 012057, 10 2015.

248. S. Torabi, F. Jahani, I. V. Severen, C. Kanimozhi, S. Patil, R. W. Havenith, R. C. Chiechi, L. Lutsen, D. J. Vanderzande, T. J. Cleij, J. C. Hummelen, and L. J. A. Koster, "Strategy for enhancing the dielectric constant of organic semiconductors without sacrificing charge carrier mobility and solubility," *Advanced Functional Materials*, vol. 25, pp. 150–157, 2015.

249. G. Chern, H. Mathias, L. R. Testardi, L. Seger, and J. Schlenoff, "Low-frequency dielectric permittivity of C60," *Journal of Superconductivity*, vol. 8, pp. 207–210, 1995.

250. F. Staub, H. Hempel, J. C. Hebig, J. Mock, U. W. Paetzold, U. Rau, T. Unold, and T. Kirchartz, "Beyond bulk lifetimes: Insights into lead halide perovskite films from time-resolved photoluminescence," *Physical Review Applied*, vol. 6, pp. 1–13, 2016.